Mathematical problems relating to the fabrication of organic photovoltaic devices



Matthew G. Hennessy
St Catherine's College
University of Oxford

A thesis submitted for the degree of
Doctor of Philosophy

Trinity 2014

To P., D., and J.

Acknowledgements

First and foremost, I would like to extend my sincerest gratitude to my three supervisors: Andreas Münch, Chris Breward, and Colin Please. Their never-ending support, encouragement, and patience, in combination with their time for countless discussions, made the doctoral journey a truly enjoyable, productive, and enlightening one.

In addition to my official supervisors, I am also deeply indebted to Barbara Wagner, John Ockendon, Peter Howell, Jon Chapman, Victor Burlakov, and Alain Goriely for the invaluable guidance and suggestions they have so kindly provided while I was working on this thesis. I have also benefited from many fruitful discussions with Tobias Ahnert and Maciek Korzec.

I am forever grateful to the many outstanding friends, new and old, who have shared this incredible journey with me. Mark, Mo, Ben, Ingrid, Amy, and Marya made being in the department an absolute blast. Tom and the Manchester crew, with their appearance at numerous conferences and study groups, ensured there were never any shortages of social activities at these events. A warm and special thanks goes to Iain for all of his help during my time in Oxford and his natural ability to act as a constant source of inspiration. I also express my gratitude to Paul D. for always being around when I was in Canada and for making home still feel like a home. Lastly, I give my deepest thanks to Johnny, Martin, Kamil, Adam, Emre, and the Michaels for all of the indescribable experiences we have shared over the years.

Finally, none of this would have been possible without the unceasing love and support from my family. I thank you all so much for this.

Abstract

The photoactive component of a polymeric organic solar cell can be produced by drying a mixture consisting of a volatile solvent and non-volatile polymers. As the solvent evaporates, the polymers demix and self-assemble into microscale structures, the morphology of which plays a pivotal role in determining the efficiency of the resulting device. Thus, a detailed understanding of the physical mechanisms that drive and influence structure formation in evaporating solvent-polymer mixtures is of high scientific and industrial value.

This thesis explores several problems that aim to produce novel insights into the dynamics of evaporating solvent-polymer mixtures. First, the role of compositional Marangoni instabilities in slowly evaporating binary mixtures is studied using the framework of linear stability theory. The analysis is non-trivial because evaporative mass loss naturally leads to a time-dependent base state. In the limit of slow evaporation compared to diffusion, a separation of time scales emerges in the linear stability problem, allowing asymptotic methods to be applied. In particular, an asymptotic solution to linear stability problems that have slowly evolving base states is derived. Using this solution, regions of parameter space where an oscillatory instability occurs are identified and used to formulate appropriate conditions for observing this phenomenon in future experiments.

The second topic of this thesis is the use of multiphase fluid models to study the dynamics of evaporating solvent-polymer mixtures. A two-phase model is used to assess the role of compositional buoyancy and to examine the formation of a polymer-rich skin at the free surface. Then, a three-phase model is used to conduct a preliminary investigation of the link between evaporation and phase separation.

Finally, this thesis explores the dynamics of a binary mixture that is confined between two horizontal walls using a diffusive phase-field model and its sharp-interface and thin-film approximations. We first determine the conditions under which a homogeneous mixture undergoes phase separation to form a metastable bilayer. We then present a novel mechanism for generating a repeating lateral sequence of alternating A-rich and B-rich domains from this bilayer.

Statement of Originality

All of the work that is presented in this thesis has been carried out by the author. The key results from Chapter 2 on evaporation-driven Marangoni instabilities in binary mixtures have been published in Hennessy & Münch [74, 75]. All of the material on bilayer formation and breakup that is presented in Chapter 4, with the exception of the analysis in Section 4.3.2 and the three-dimensional numerical simulations in Section 4.4.4.1, appears in Hennessy *et al.* [72, 73]. The derivation of the multiphase model in Chapter 3 closely follows that of Drew [56] and Drew & Passman [57], but the subsequent analysis is original and unpublished.

Contents

1 Introduction **1**

1.1 Principles of organic solar cell operation 2

1.2 Fabrication of organic solar cells 5

1.3 Relevant physical mechanisms 7

1.4 Scope of thesis 8

1.5 Mathematical studies of spin coating 11

2 Marangoni instabilities in an evaporating solvent-polymer mixture **12**

2.1 Introduction 12

2.1.1 Linear stability of time-dependent base states 14

2.1.2 The Marangoni instability 16

2.1.3 Summary and outline of chapter 19

2.2 Mathematical model 19

2.2.1 Non-dimensionalisation 22

2.3 Formulation 25

2.3.1 Computation of the base state 25

2.3.1.1 Solutions in the first time regime 26

2.3.1.2 Solution in the large-time regime 28

2.3.1.3 Comparison with numerical solutions 30

2.3.2 Linear stability 32

2.3.2.1 Frozen-time analysis 33

2.3.2.2 Asymptotic analysis 36

2.3.3 Chapter outlook 37

2.4 Dynamics with a non-deformable fluid surface 38

2.4.1 Frozen-time analysis 38

2.4.2 Asymptotic analysis 41

2.5 Dynamics with a deformable fluid surface 50

2.5.1 Long-wave expansion 51

2.5.2 Initial neutral stability curves 55
2.5.3 Competing modes of instability 60
2.5.4 Evolution of the neutral stability curves 61
2.5.5 Asymptotic analysis 65
2.6 Application to experiments 69
2.6.1 Interpreting the experimental results of Bassou & Rharbi 69
2.6.2 Observing the oscillatory instability 73
2.7 Discussion and conclusion 75

3 Multiphase models of solvent-polymer mixtures 80
3.1 Introduction 80
3.1.1 Aims and outline 82
3.2 Mathematical modelling 83
3.2.1 Microscopic model 83
3.2.1.1 Caveats of the microscopic model 87
3.2.2 Averaging and the macroscopic model 87
3.2.2.1 The indicator function 88
3.2.2.2 Averaged equations 90
3.2.2.3 Averaged variables 92
3.2.2.4 Caveats of the macroscopic model 94
3.2.3 Constitutive laws and model closure 95
3.2.4 Summary of model 97
3.2.4.1 Initial and boundary conditions 98
3.3 Two-phase flow in a gravitational field 100
3.3.1 Non-dimensionalisation 101
3.3.2 The dilute polymer approximation 102
3.3.2.1 Solution in one dimension 103
3.3.3 The full one-dimensional problem 109
3.3.3.1 Small-time solution 113
3.3.3.2 Solution with weak drag and gravity 116
3.3.3.3 Dynamics with strong gravity 117
3.3.3.4 Dynamics with strong drag 121
3.3.3.5 Dynamics with strong drag and gravity 128
3.4 Three-phase flow in the absence of gravity 128
3.4.1 Non-dimensionalisation 130
3.4.2 Reduction of the system 131

3.4.3 The slow-flow limit . . . 133
3.4.3.1 Large-time regime . . . 135
3.4.4 The strong-drag limit . . . 136
3.4.4.1 The inner problem . . . 137
3.4.4.2 The outer problem . . . 138
3.4.4.3 A comment on the matching . . . 138
3.4.4.4 Numerical solutions . . . 139
3.4.5 Skin formation . . . 140
3.5 Discussion and conclusion . . . 142

4 Bilayer formation and topological transformations in a confined binary mixture 147

4.1 Introduction . . . 147
4.1.1 Thermodynamics background . . . 149
4.1.2 Phase separation in confined geometries . . . 151
4.1.3 Phase-field models . . . 153
4.1.4 Aims and assumptions . . . 154
4.1.5 Summary of key results and outline of chapter . . . 155
4.2 Mathematical formulation . . . 156
4.2.1 Free energy of the system . . . 156
4.2.2 Evolution equations . . . 158
4.2.3 Non-dimensionalisation . . . 159
4.2.4 The near-criticality approximation . . . 161
4.2.5 Surface interaction potentials and their relation to wetting properties 162
4.2.6 Model summary . . . 164
4.2.7 Numerical methods . . . 164
4.3 Bilayer formation . . . 166
4.3.1 Dynamics at constant temperature with weakly biased walls . . . 167
4.3.1.1 Morphology selection . . . 169
4.3.2 Dynamics at constant temperature with strongly biased walls . . . 173
4.3.3 Dynamics of a slowly cooled mixture . . . 179
4.4 Bilayer stability and topological transformations . . . 182
4.4.1 Sharp-interface asymptotics . . . 182
4.4.1.1 The outer problem . . . 185
4.4.1.2 The inner problem . . . 185
4.4.1.3 Approximation of the free energy . . . 188

4.4.1.4 Summary of sharp-interface model . . . 189
4.4.1.5 Reformulation of the sharp-interface model . . . 189
4.4.2 Reduction to a thin-film problem . . . 190
4.4.3 Linear stability of a bilayer . . . 191
4.4.4 Dynamics of a punctured bilayer . . . 192
4.4.4.1 Extensions to three dimensions . . . 200
4.5 Discussion and conclusion . . . 200

5 Conclusions **204**
5.1 Summary and discussion of thesis . . . 204
5.2 Future directions . . . 209
5.3 Final thoughts . . . 212

A Supplementary material for Chapter 2 **214**
A.1 Derivation of the asymptotic solution . . . 214
A.1.1 An alternative derivation using the WKB method . . . 218
A.2 The adjoint problem . . . 221
A.2.1 Formulation . . . 221
A.2.2 Small-wavenumber asymptotics . . . 223

B Supplementary material for Chapter 3 **224**
B.1 Properties of the indicator function . . . 224

C Supplementary material for Chapter 4 **227**
C.1 Proof of monotonically decreasing energy . . . 227
C.2 Calculation of the equilibrium contact angle . . . 228
C.3 Details of the sharp-interface limit . . . 230

Bibliography **232**

List of Figures

1.1 Top (a): The absorption of photons by the donor polymer generates excitons, which are electron-hole pairs that are bound together by the Coulomb force. Bottom left (b): To separate the electron and the hole, the exciton must travel to the donor-acceptor interface via diffusion, where a strong electric field splits it apart. The electron is transferred to the acceptor polymer and the charges travel to the electrodes via drift. Bottom right (c): The diffusion length of an exciton is small ($\sim$ 10 nm), so it might not reach the donor-acceptor interface. If this is the case, then the electron and the hole recombine and the energy is lost. 3

1.2 A schematic diagram of the spin-coating process. The polymers are blended in a common solvent and spread onto a substrate (a). The system is rotated with a high angular velocity which thins the film and enhances the evaporation of solvent (b). Recent experiments by Heriot & Jones [76] and Mokarian-Tabari *et al.* [107] suggest that the polymers undergo phase separation and form a horizontal bilayer (c). An instability at the bilayer interface leads to it becoming corrugated (d) and continued growth of the finger-like protrusions leads to a laterally phase separated film (e). 6

1.3 Bird's-eye views of spin-cast polymer blends showing typical morphologies that arise in experiments. Regions of different contrast denote different polymers. (a): The striation-type morphology showing rays, or striations, of polymers that emanate from the axis of rotation. The domains are aligned with the radial direction, shown as a dashed line. (b): In some cases, the striations break up and form islands of one type of polymer that appear to be embedded within a sea of the other. (c): The filament-type morphology showing long, curved structures that branch and intersect with one another. The experimental conditions in panels (a) and (b) are the same except for differing polymer ratios in the initial mixture. Panels (a)–(b) are reprinted with permission from Wu *et al.* [159]. Copyright 2006 American Chemical Society. Panel (c) is reprinted with permission from Ebbens *et al.* [60]. Copyright 2011 American Chemical Society. 7

2.1 The evaporation-driven solutal Marangoni instability. Non-uniform evaporation of solvent leads to composition-induced surface-tension gradients which pull fluid from regions of low to high surface tension, γ. Converging fluid sinks to the substrate and fluid rises beneath regions of low surface tension. The uprising fluid is rich in solvent whereas the sinking fluid has been depleted of such due to the evaporation that has occurred. Left (a): The short-wavelength non-deformable mode of instability. Right (b): Long-wavelength mode associated with interface deformations. Note the diagram is not drawn to scale. 17

2.2 A schematic diagram of the system under consideration, showing a two-dimensional layer of fluid resting on a non-permeable substrate. The fluid is composed of a non-volatile polymer and a volatile solvent. The layer has thickness $h(x,t)$ and the mixture has horizontal and vertical components of velocity given by u and w, respectively. 20

2.3 Numerical (solid lines) and asymptotic (symbols) solutions to the base state problem. (a): The short-term behaviour of the base state solvent volume fraction showing, in particular, the growth of a boundary layer from the surface of the fluid layer. (b): The quasi-static evolution of the solvent volume fraction. (c): The evolution of the film thickness. (d): The two time regimes and their regions of overlap are clearly shown by plotting the average concentration gradient across the film. The asymptotic solution in (2.27) is used in panel (a), whereas the $t = O(\delta^{-1})$ asymptotic solution given in (2.44) is used in panels (b)–(d). The $t = O(1)$ solution presented in (2.30) is denoted by open circles in panel (d). Parameter values are $\beta = 0.85$ and $\delta = 0.01$. 31

2.4 Left (a): The neutral stability curve (solid) traces out a path in parameter space where the top frozen-time eigenvalue is equal to zero. The top eigenvalue is positive and negative above and below this curve, respectively. Therefore, the neutral stability curve defines the boundary between stable and unstable regions of parameter space. Here, M and a denote the rescaled Marangoni number and wavenumber, respectively; see (2.51) and (2.53). The dashed line gives an example of how these effective parameters change from their initial values (denoted by the star) as the slow time τ increases. Right (b): The top frozen-time eigenvalue σ as a function of the rescaled wavenumber a when $\tau = 0$ and $M = 105$. These parameters correspond to the dashed-dot line shown in panel (a). 40

2.5 Left (a): Amplification of a long-wavelength perturbation by the stationary Marangoni instability. The asymptotic amplifications, A_{asy} and $A^{(0)}_{\text{asy}}$, are defined in (2.83a) and (2.83b), respectively. The numerical amplification is computed from time-stepping the linearised problem. Right (b): The relative error between the numerical and asymptotic solution defined according to (2.87). The initial condition was taken to be the top eigenfunction and the parameters are Ma = 105, $k = 0.3$, $\beta = 0.85$, and $\delta = 0.01$. 44

2.6 Amplification of a short-wavelength perturbation by the stationary Marangoni instability. Left (a): Comparison of the asymptotic and numerical amplifications. The asymptotic curves are based on the single-mode expressions in (2.77) and (2.79) with eigenvalues and eigenfunctions that have been computed numerically for each value of the slow time τ. Right (b): The relative error between the numerical and asymptotic solution defined according to (2.87). The initial condition was taken to be the top eigenfunction and the parameters are Ma = 105, $k = 1.67$, $\beta = 0.85$, and $\delta = 0.01$. For these parameter values, the system evolves according to the dashed line show in Figure 2.4 (a). 46

2.7 Top (a)–(b): Eigenfunction coefficients in a two-mode asymptotic approximation of the solution to the linearised problem. The initial condition was taken to be the top eigenfunction. Despite the solution not having any component along the second eigenfunction at time $t = 0$, this mode does become active, although its contributions to the asymptotic solution remain small. The exact expressions for α_1 and α_2 are given in (2.89). Bottom (c)–(d): Relative error between numerical and asymptotic approximations to the functions α_1 and α_2. Parameter values are $k = 1.67$, Ma = 105, $\beta = 0.85$, and $\delta = 0.01$. 48

2.8 Left (a): Amplifications of a perturbation that initially composed of many eigenfunctions. The exact form of the initial condition is given by (2.90). The amplifications given by $A_{\text{asy,N}}$ are computed asymptotically using the top N modes; see (2.92). The numerical solution is captured remarkably well by even the single-mode asymptotic approximation. Right (b): Effective growth rates of the amplifications. These are computed by taking the time derivative of the logarithm of the amplification. Parameter values are the same as in Figure 2.6; in particular, $k = 1.67$, Ma = 105, $\beta = 0.85$, and $\delta = 0.01$. . . . 50

2.9 Progression of the oscillatory instability. Shown are the perturbations to the surface solvent concentration (dashed), $\tilde{C}$, and the film thickness (solid), $\tilde{H}$, both of which are defined in (2.111). The arrows indicate the instantaneous direction of flow and γ_+ and γ_- denote regions of high and low surface tension, respectively. Furthermore, $\omega = (M/2)^{1/2}$ represents the frequency of oscillation. See text for a detailed explanation of the dynamics. 55

2.10 Neutral stability curves for non-deformable systems (solid black) and deformable systems (dashed and dashed-dot). The solid and dashed curves correspond to locations in parameter space where the top eigenvalue is zero. The dashed-dot line corresponds to where the top eigenvalue is purely imaginary. See text for definitions of M_s, M_o, and the a_i. 57

2.11 The dependence of the top two eigenvalues on the disturbance wavenumber for various effective Marangoni numbers. The values of C and G are chosen to coincide with the neutral stability diagram in Figure 2.10, thus $C = 0.01$ and $G = 100$. Each value of M illustrates a qualitatively distinct behaviour of the eigenvalues and each behaviour characterises a subregion of the neutral stability diagram. See text for full details. The definitions of the $R_{u,i}$ are given in (2.115). 57

2.12 Left (a): Critical Marangoni numbers as a functions of the effective Galileo number G and the effective capillary number C. The solid black line denotes the Marangoni numbers associated with the onset of an oscillatory instability and is given analytically by (2.116). The dashed lines with symbols denote Marangoni numbers associated with the onset of stationary instabilities. For each value of C these curves intersect at one particular value of G denoted by G_p. Right (b): The dependence of the function G_p on the capillary number C. For $G < G_p$, the inequality $M_o < M_s$ is satisfied. Thus, the region below this curve corresponds to parameter regimes where it is possible to only induce the oscillatory mode of instability. The grey area is defined by the parameters $C < 10^{-2}$ and $G < 47$. The grey area denotes the parameter regime where it is possible to isolate the oscillatory instability if $M < 80$; see text for further details. 62

2.13 Evolution of the neutral stability curves in the upper-quarter plane in terms of the base state film thickness $\bar{h}$. Stationary neutral stability curves are shown as solid black lines and oscillatory ones as dashed lines. Parameter values are Ca = 0.01, Ga = 30, and $\beta = 0.85$. As $\bar{h} \to 1 - \beta = 0.15$ the curves tend to infinity. 64

2.14 The evolution of the minima of the stationary (solid) and oscillatory (dashed) neutral stability curves. The parameter values are (a): Ca = 0.01, Ga = 30, $\beta = 0.85$; (b): Ca = 0.01, Ga = 30, $\beta = 0.25$. Note the difference in scales in panel (b). 64

2.15 The oscillatory instability. Top (a): The evolution of the real and imaginary parts of the top two eigenvalues. Middle (b): Evolution of the real part of the disturbance to the film thickness relative to its initial value. Bottom (c): Disturbance amplification as a function of time. The asymptotic solution in Section 2.3.2.2 breaks down and diverges as the imaginary parts of the eigenvalues tend toward zero. Parameter values are Ma = 70, Ca = 0.01, Ga = 30, $\beta = 0.85$, $\delta = 0.01$, and $k = 0.21$. The top eigenfunction at $\tau = 0$ is used as the initial condition. 67

2.16 Numerically computed amplifications of stationary (solid) and oscillatory (dashed) modes when Ma = 100, Ga = 30, Ca = 0.01, $\beta = 0.85$, and $\delta = 0.01$. The stationary mode has wavenumber $k = 1.65$ whereas the oscillatory mode has $k = 0.33$ and the initial condition is taken to be the top eigenfunction at time $\tau = 0$. While the oscillatory mode obtains a larger overall amplification, the rapid growth of the stationary mode means that it can obtain much larger initial amplifications. 68

3.1 Left (a): We consider a three-component mixture consisting of a volatile solvent, a dispersed or partially dissolved polymer phase (short lines), and demixed polymers that have separated from the solvent (pink). This fluid is assumed to form a long layer of height $h(x,t)$ on a flat substrate. Right (b): The microscopic geometry between two phases. Regions of phase j and k are denoted as $R_j(t)$ and $R_k(t)$, respectively. The interface between these domains is given by $\partial R_j(t) \cap \partial R_k(t)$. The unit vector $\boldsymbol{e}_n^j$ points out of phase j and $\boldsymbol{v}$ describes the velocity of the j-k interface. 84

3.2 A schematic diagram of the functions f_1 (dashed) and f_2 (solid) that correspond to the left- and right-hand sides of (3.91), respectively. Solutions of this equation are given by the non-trivial intersections of these curves. When $r > 1$, the two curves only intersect if $a > a_c$, where a_c is defined in (3.95). . 108

3.3 Comparison of the asymptotic solution as $t \to 1$ with numerical solutions to (3.82) when both R and D are large. The left column shows polymer volume fractions and the right column displays the corresponding vertical velocity. Parameter values are $t = 0.95$, $D = 100$, and $R = 25$, 75, and 125 for panels (a)–(b), (c)–(d), and (e)–(f), respectively. Panels (a)–(b) corresponds to the drag-dominated region of parameter space given by $R < D/2$. Panels (c)–(f) represent the gravity-dominated behaviour that occurs when $R > D/2$. This can be subdivided into two regimes. If $D/2 < R < D$, the volume fraction has an interior minimum and there is some accumulation of polymer near the surface (c). If $R > D$, gravity is so strong that the volume fraction decreases monotonically (e). 110

3.4 Flow chart showing the parameter and time regimes that are considered in the analysis of the one-dimensional two-phase problem given by (3.104). The key dynamics that occur in the various regimes are also summarised. The case with strong drag and strong gravity is briefly mentioned in Section 3.3.3.5 but is not shown in this diagram. 112

3.5 Comparison of approximate and numerical solutions for the film thickness when both drag and gravity are weak. The small-time approximation corresponds to the asymptotic solution for h given in Section 3.3.3.1. The $R, D \ll 1$ approximation corresponds to the implicit solution in (3.125). Parameter values are: (a) $A = 0.1$, $R = 2$, $D = 1$; (b) $A = 0.5$, $R = 0.6$, $D = 0.5$. In both cases, $\mu = 1$. 118

3.6 Dynamics when gravitational effects are strong. In this case, an initially homogeneous mixture rapidly evolves into a bilayer, with the denser polymer on the bottom and the solvent on the top (a). The velocity of polymers (b) is small near the substrate, where they are tightly packed. Little evaporation of solvent occurs during the rapid formation of the bilayer so the film thickness is approximately constant during this time interval (c). Once the bilayer has formed, the solvent-rich upper layer freely evaporates at a constant rate (d). The parameters used in the simulation are $A = 0.5$, $\mu = 1$, $D = 0$, $R = 1000$. 122

3.7 Dynamics in the limit of strong drag, $D \gg 1$, and moderate gravity, $R = O(1)$. An asymptotic analysis reveals three time regimes. The first is when $t = O(D^{-1/2})$, during which evaporation-induced drag leads to the rapid formation of a compositional boundary layer at the free surface. When $t = O(1)$, gravitational effects lead to the slow accumulation of polymers on the substrate and the development of a second boundary layer. For $t \gg 1$, layers that are nearly pure in polymer have developed at the surface and the substrate, leaving a two-phase core in the interior of the layer. Gravity is expected to slowly break up the polymer-rich skin at the free surface, after which the remaining solvent evaporates from the layer. Parameters values were taken to be $A = 1/2$, $D = 1000$, $R = 1$, $\mu = 1$. The initial condition was $\alpha_p(z, 0) \equiv 1$. 125

3.8 Evolution of the film thickness during the simulation shown in Figure 3.7. After a short period of rapid thinning, the development of a polymer-rich layer below the free surface decreases the evaporation rate. The near-surface composition changes slowly, leading to a film that decreases at a roughly uniform rate. The parameter used in the simulation were $A = 1/2$, $D = 1000$, $R = 1$, $\mu = 1$. The dashed line corresponds to when $t = D^{1/2}$. 128

3.9 Flow chart showing the parameter and time regimes that are considered in the analysis of the one-dimensional three-phase problem given by (3.173)–(3.175). The key dynamics that occur in the various regimes are also summarised. . 133

3.10 Dynamics of a three-phase mixture consisting of a solvent, dispersed polymers, and demixed polymers. The left column shows the volume fraction of the polymer phases and the right shows the corresponding velocities. Strong drag forces between the solvent and the dispersed polymers lead to the rapid formation of a compositional boundary layer (b) because the polymers, which are advected with the solvent, do not evaporate at the free surface. The accumulation of dispersed polymers enhances their demixing, leading to the formation of a polymer-rich layer at the top of the film (c). The simulation was computed using the following parameter values: $D = \beta = 1$, and $\varepsilon = 1/1000$. The initial conditions were $\alpha_{pi} = \alpha_{di} = 0.1$. The asymptotic approximations for the velocities are composite solutions formed from the inner and outer problems discussed in Sections 3.4.4.1–3.4.4.3. 141

3.11 The corresponding film thickness for the simulation show in in Figure 3.10. The film rapidly thins for small times, but the build up of a polymer-rich skin at the surface significantly reduces the evaporation rate. In this case, amount 89% of the solvent remains trapped within the bulk. The parameter values were $D = \beta = 1$, and $\varepsilon = 1/1000$. The initial conditions were $\alpha_{pi} = \alpha_{di} = 0.1$. 142

3.12 Steady-state solvent mass fractions as functions of the relative evaporation rate β and the drag coefficient D for two different values of the drag ratio ε. Parameters values that lie above the 0.5 contour (black) lead to more than half of the solvent remaining in the layer. The steady-state mass fraction is defined as the mass of solvent when $|\mathrm{d}h/\mathrm{d}t|$ first decreases to 10^{-3} divided by the initial solvent mass. Larger values of the mass fraction correspond to more solvent being trapped in the bulk. Decreasing ε leads to a significant increase in the formation of a skin. Note the change in scales between panels (a) and (b). The initial conditions in the simulations were $\alpha_{di} = \alpha_{pi} = 0.1$. . 143

4.1 Typical cross sections of polymer films that are created by spin coating a mixture of two polymers, A and B, and a common solvent. The two colours represent A-rich and B-rich regions. As the solvent evaporates, the polymers undergo phase separation to either form a bilayer (a) or a laterally separated structure (b). 148

4.2 Two potential routes that lead to a laterally separated film morphology. Top (a)–(c): An instability develops at the bilayer interface, leading to corrugations that grow until they come in contact with the surface or substrate. The new contact lines move under the action of interface minimisation to form columnar structures. Bottom (d)–(f): An instability occurs at the top of the mixture while it is still homogeneous (the homogeneous regions are shown in purple). This leads to localised phase separation that proceeds from the surface down to the substrate. 149

4.3 Left (a): The homogeneous free energy of mixing for binary mixture as a function of composition. If the temperature T is above the bulk critical temperature T_c, the free energy is convex. When $T < T_c$, the free energy has a double-well structure. Right (b): A typical binary phase diagram for an unconfined mixture. For a given temperature, the binodal and spinodal points correspond to compositions where f has a minimum and a vanishing second derivative, respectively. If the initial composition φ_i lies in the region above the binodal (the white region), which is always the case above the bulk critical point, the mixture will tend to a homogeneous state. However, if φ_i is below the spinodal (blue region), the mixture can separate into two co-existing phases with compositions given by $\varphi_\pm$ that lie on the binodal. . 151

4.4 We consider a binary mixture consisting of material A and material B that is confined between two walls that are a distance d apart. If the temperature is below the critical point, a homogeneous mixture will separate into A-rich and B-rich phases, which are labelled as A and B, respectively. The walls interact with the mixture, causing each component to be preferentially attracted to one of the two surfaces. The strength of this attraction is measured through the equilibrium contact angle θ. 156

4.5 Characteristic temperature dependence of the equilibrium contact angle θ. For temperatures above a wetting temperature (dashed line), the walls are perfectly wetting. In this example, the bias of the walls is $\breve{\beta} = 1/2$ and the wetting temperature corresponds to $T/T_c \simeq 0.63$. Details of the calculation used to determine θ are given in Appendix C.2. 163

4.6 Top (a)–(c): Numerical simulation showing the homogenisation of a perturbed 50:50 mixture and the formation of enrichment layers when the system lies above the spinodal and the temperature is constant. Bottom (d)–(f): Evolution of the laterally averaged order parameter (see (4.42) for a definition of $\langle\phi\rangle_l$). Solid lines and stars depict numerical and asymptotic solutions, respectively. The circles in panel (f) denote the asymptotic approximation to the steady-state solution computed using (4.41). Parameter values are $\psi = 0$, $\chi = -1$, $\delta = 0.06$, and $\beta = \delta/2$. The initial condition was uniformly distributed random numbers between ± 0.2. 171

4.7 (a)–(d): Dynamics of a 50:50 mixture in the spinodal regime of the phase diagram when the temperature is constant in time and the bias of the walls is weak. (a) Spinodal decomposition quickly amplifies fluctuations in the initial condition and leads to the formation of small domains within the bulk. (b)–(d): These domains coarsen until a laterally separated columnar morphology is obtained. (e)–(f): Comparison of the laterally averaged and vertically averaged order parameters that have been computed numerically (solid line) and asymptotically (stars). Parameter values are $\psi = 0$, $\chi = 1$, $\delta = 0.06$ and $\beta = \delta/2$. The initial condition is uniformly distributed random numbers between ± 0.2. 174

4.8 Top (a): The early time similarity solution when the walls strongly interact with the materials. See text for definitions of $\check{\tau}$, η, and the function p. Middle (b)–(d): Comparison of the early time similarity solution (dashed line) to one-dimensional numerical solutions (solid line) when $\beta = 1$ ($\theta = 0$). Bottom (e)–(g): Two-dimensional simulations showing the formation of layered structures when the walls are perfectly wetting. The initial condition for panels (b)–(d) was taken to be a homogeneous 50:50 mixture corresponding to $\phi \equiv 0$, and for panels (e)–(g) it was a random perturbation of size 0.2 to the same state. In both cases a value of $\delta = 0.06$ was used. 177

4.9 When the bias of the walls is strong, the layers satisfy a $\check{\tau}^{1/4}$ growth law for early times. The thickness of the bottom layer, ℓ, is measured using the first zero of the laterally averaged order parameter. The numerical values of ℓ have been averaged over several simulations using random initial conditions and fixed values of $\delta = 0.06$ and $\beta = 1$. See text for further details. 179

4.10 Top (a)–(c): A simulation of the phase-field model showing that a bilayer morphology can be induced by slowly cooling the system. In this case, the temperature evolves according to $\chi(t) = 1 - \exp(-t/\tau_c)$, where $\tau_c = 100$. The solution is shown at times $t = 1$, $t = 20$, and $t = 500$, corresponding to $\chi = 0.01$, 0.18, and 1, respectively. Middle (d)–(f): Comparison of the laterally averaged order parameter (line) computed from the numerical solutions shown in (a)–(c) with the instantaneous steady states (stars) associated with each value of χ. Bottom (g)–(i): Growth rate of perturbations to the steady -state profiles shown in (d)–(f). The parameters are $\delta = 0.06$ and $\beta = \delta/2$, which correspond to weakly biased walls. 183

4.11 Schematic diagram of the sharp-interface model. The domains $\Omega_\pm$ correspond to the outer regions where the composition is approximately constant and given by $\phi \simeq \pm 1$, respectively. These domains are separated by a thin transition region of width $O(\delta)$. The transition region is described by the coordinates s and η, where s is the arclength along the centerline of this region $\boldsymbol{r}(s)$, and the coordinate η lies along the vector that is normal to the centerline, $\boldsymbol{\nu}(s)$. The centerline is precisely defined as the curve where $\phi(\boldsymbol{r}(s)) \equiv 0$. 184

4.12 Dynamics of a punctured bilayer when the walls are not biased. In this case, the equilibrium contact angle is $\theta = 90^\circ$ ($\beta = 0$). The motion of the initial contact line displaces material B (blue) and forms a growing ridge (b) that eventually hits the top wall (c). This creates a hole in the upper layer of material A (red) which rapidly opens (d)–(e). The rightmost of the newly created contact lines moves further to the right, displacing material A and creating a dip (f) that grows until it hits the bottom wall (g). The process repeats itself (h) until the bilayer is transformed into a sequence of columns (i). The other parameter values are $\delta = 0.06$ and $\chi = 1$. The figure is assumed to be symmetric about $x = 0$. The black line corresponds to the $\phi = 0$ contour. 194

4.13 Evolution of the rescaled free energy (4.77) during the sequence of topological transformations shown in Figure 4.12. The dashed lines correspond to the times shown in panels (c) and (g) in this figure. Each sharp change in the free energy marks the creation of new contact lines and the rapid opening of the associated hole. 195

4.14 When the walls are biased ($\beta \neq 0$), introducing a hole in the bilayer results in a sequence of topological transformations that is similar to that shown in Figure 4.12. As shown here, however, the columns that emerge are now trapezoidal instead of rectangular because the equilibrium contact angle is less than 90°. The trapezoids are always oriented so the long horizontal edge is in contact with the preferred wall. The irregularities in the widths of the last two columns are due to the finite length of the computational domain. Parameter values are $\beta = 0.64$, corresponding to $\theta = 50^\circ$, and $\delta = 0.1$. The solution is shown at time $\tau = 107$. Red and blue corresponds to material A and B, respectively. The black line denotes the $\phi = 0$ contour. 196

4.15 Comparison of the perturbed bilayer interface computed using the phase-field model (line) and the thin-film equation (stars) when the equilibrium contact angle is 20° and $\delta = 0.1$. The agreement between the two models is excellent before the system is close to a topological transformation (a)–(b). However, the two models begin to differ significantly when the ridge gets within an $O(\delta)$ distance from the upper wall (c). The source of this discrepancy is a "suction" effect in the phase-field model that is not present in the thin-film equation. This causes the bilayer interface to be rapidly pulled towards the upper wall in the phase-field model, thus accelerating the topological transformation. Here, $\bar{x} = \theta x$, $\bar{s} = \theta s$, $\bar{L} = \theta L$, and $\bar{\tau} = \theta^4 \tau$. 197

4.16 Topological transformations in a bilayer with unequal composition ratios. In this case, the height ratio of the upper to lower layer is $r : 1$ with $r = 10$. The corresponding composition ratio is $9 : 1$. Distances have been scaled by r so that the height of the undisturbed lower layer has unity thickness. When a hole is introduced into the lower layer, it opens further to create a growing ridge (a). However, the dip in front of the ridge now comes into contact with the lower wall before the ridge hits the upper wall (b). The ridge then detaches from the retracting layer and forms a drop (c). The process repeats itself resulting in an array of droplets (d). Parameter values are $\delta = 0.03$ and $\theta = 45°$. Red and blue corresponds to material A and B, respectively. The black line denotes the $\phi = 0$ contour. 199

4.17 Three-dimensional simulation of a punctured bilayer when the equilibrium contact angle is 90°. (a): The two-dimensional sharp interface that separates the two layers, defined implicitly by the equation $\phi(x, y, z) = 0$, just before the first topological transformation occurs. (b): Two-dimensional slices of the solution along the bottom wall ($z = 0$), the top wall ($z = 1$), and at mid-height ($z = 1/2$) showing a cylinder of material A (red) surrounded by annulus of material B (blue). The material in the corners corresponds to developing ridges. Parameter values are $\delta = 0.06$ and $\beta = 0$. 201

Chapter 1

Introduction

The surface of our planet is constantly absorbing an enormous amount of solar radiation. The estimate in Morton [110] places this value to be approximately 120 petajoules per second. The global energy consumption in 2010, on the other hand, has been estimated to be 504,000 petajoules [27]. Using these values, a quick "back of the envelope" calculation can produce one very astonishing fact: the amount of solar energy that is absorbed in one *hour* is nearly enough to power the entire planet for one *year*. This naturally leads to the realisation that our planet could be completely powered by solar energy if only a small percentage of it ($\sim 0.01\%$) could be captured and fed into the global power infrastructure. With historical data showing annual increases in the amount of energy that our civilisation consumes each year [27], the need for a clean, safe, and renewable source of energy has never been more pressing.

The idea to generate electricity using incoming solar radiation is not a novel one. In fact, people have been thinking about it for over a century. The first solar cell was created sometime around 1883 [136]. The first *practical* solar cell, however, was built at Bell Laboratories in 1954 [39]. Despite photovoltaic technology existing for more than fifty years, the amount of energy that is harnessed from solar radiation accounts for only a small fraction of the total energy that is produced throughout the world. It has been estimated that, of the total energy produced in 2010, only 1% of this was generated from photovoltaic devices [27]. Although there are many reasons for why this contribution is relatively low, two of the most important factors relate to the efficiency and the cost of photovoltaic devices.

The first solar cells were manufactured using inorganic materials such as selenium and crystalline silicon. These breakthrough devices had efficiencies that were on the order of a few percent [69, 136] and, consequently, were of little practical use. However, further development of inorganic photovoltaic devices led to improved efficiencies in the 10%–20% range [69, 77]. Unfortunately, the cost of manufacturing inorganic solar cells remains high

in comparison with the cost of producing electricity via alternative methods [16], which ultimately inhibits the large scale use of this technology.

A breakthrough in materials science came in 1987 when Tang and VanSlyke [148] produced light by sending an electrical current through a layer of organic material. As this is essentially the opposite process that takes place in a solar cell, it was not much longer until organic materials were being used as the photoactive components of photovoltaic devices [136]. Organic solar cells have since been gaining attention because they offer several advantages over traditional silicon-based technologies. Firstly and most importantly, the organic materials that are required in such devices are cheap to synthesise [70]. Moreover, photovoltaic cells that are constructed using thin films of organic material are relatively easy to manufacture. These two factors significantly reduce the overall production cost of such a device. Organic materials also provide new levels of versatility, allowing organic solar cells to be used in an increasing number of applications.

Despite the many benefits of organic photovoltaic (OPV) devices, they suffer from relatively low efficiencies in comparison with their inorganic counterparts [70, 77]. In order for organic-based devices to become an attractive source of renewable energy, further performance enhancements are required to make them competitive with existing and emerging technologies.

1.1 Principles of organic solar cell operation

The inefficiency of organic solar cells is intimately linked to the fundamental operating principles of such devices. Thus, to understand the source of inefficiency, one must understand the physics behind OPV devices. The proceeding discussion about the physics of polymeric organic cells will closely follow that found in many review papers on the subject; see, for example, Goetzberger *et al.* [69], Günes *et al.* [70], Hoppea & Sariciftci [77], and Shevaleevskiy [136].

The photoactive component of a polymeric organic solar cell often consists of two interpenetrating polymers phases, each with different electrical characteristics. One of these polymers acts as an electron donor, whereas the other polymer acts as an electron acceptor. The absorption of photons occurs exclusively within the donor layer of the solar cell, as shown in Figure 1.1 (a). The energy of an absorbed photon creates an excited state consisting of an electron-hole pair. The electron and the hole are bound together by the Coulomb force and they can be considered to behave as a single collective unit, commonly referred to as an exciton [70].

Excitons are electrically neutral and, as such, their motion will not generate an electric current. Therefore, each exciton must be split apart and the constituent electron and hole

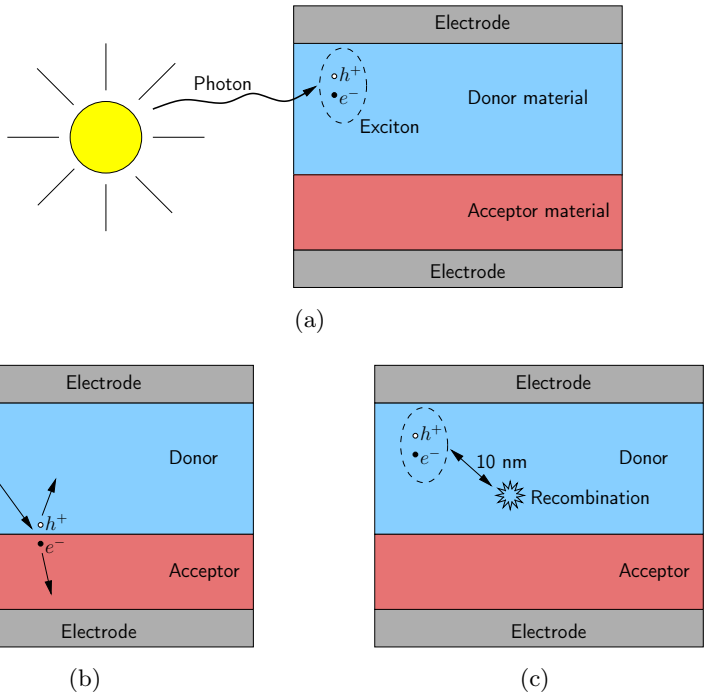


Figure 1.1: Top (a): The absorption of photons by the donor polymer generates excitons, which are electron-hole pairs that are bound together by the Coulomb force. Bottom left (b): To separate the electron and the hole, the exciton must travel to the donor-acceptor interface via diffusion, where a strong electric field splits it apart. The electron is transferred to the acceptor polymer and the charges travel to the electrodes via drift. Bottom right (c): The diffusion length of an exciton is small ($\sim$ 10 nm), so it might not reach the donor-acceptor interface. If this is the case, then the electron and the hole recombine and the energy is lost.

must be collected independently. Separating the electron from the hole is not an easy task, as the Coulomb force acts strongly on small scales. However, the introduction of a second layer of polymer (the acceptor layer) can produce an electric field that is localised about the donor-acceptor interface and strong enough to overcome the Coulomb interaction. The caveat of this approach is that it requires the exciton to reach the interface that forms between the two polymers. The electroneutrality of excitons prevents their motion from being affected by the presence of an external electric field. Therefore, diffusion is the primary means of exciton transport. This further implies that the distance to an interface must be within the exciton diffusion length (typically 10–20 nm [70]), otherwise the electron and the hole will recombine and the energy will be lost[1]; see Figure 1.1 (c).

If an exciton makes it to the donor-acceptor interface and is split apart, then the electron is transferred (donated) to the acceptor material. The hole stays within the donor material; see Figure 1.1 (b). An internal electric field within the donor and acceptor layers directs the separated electric charges towards the electrodes where they are collected and used to power some external device. In order for the charges to reach the electrodes, the donor and acceptor materials must form continuous pathways.

It is now widely accepted that the performance of OPV devices and other technologies that are based on thin polymer films is significantly influenced by the internal structure of the film [38, 42]. In the context of organic solar cells, it is desirable for the polymers to interpenetrate on a length scale that is commensurate with the exciton diffusion length while forming continuous pathways to the electrodes. An idealised morphology that is optimal in these regards could be formed by creating finger-like layers of donor material that penetrate the acceptor material, where the width of each finger is on the order of the exciton diffusion length. The close proximity of the interface to the donor material means there is an increased likelihood of the excitons diffusing to the interface before recombining. It is currently estimated that only 10% of the excitons that are generated actually lead to the creation of free electric charges [70]. Although this figure also accounts for the fact that some excitons do not separate upon reaching the interface, it does show how there is significant room for improvement in this aspect of organic solar cell design. The difficulty in optimising the donor-acceptor interface lies in the inability to control its morphology during the fabrication processes. This is partly due to an incomplete understanding of the precise physical mechanisms which govern this interface.

[1] Although the exciton diffusion length is a useful construct to explain the relationship between recombination and diffusion to the interface, it is slightly misleading because technically the exciton recombines after a certain amount of *time* has passed and not after a certain *distance* has been travelled. However, the diffusion length of an exciton can be related to its lifetime via $\ell = \sqrt{DT_e}$, where ℓ is the diffusion length, D is the diffusion coefficient, and T_e is the lifetime of an exciton.

1.2 Fabrication of organic solar cells

One method for creating the photoactive component of organic solar cells is by spin coating a mixture of two organic polymers that have been blended in a common volatile solvent. The mixture is spread onto a substrate and the system is spun at a high angular velocity; see Figure 1.2 (a). The centrifugal force that is generated rapidly thins the fluid layer and the enhanced airflow above the layer aids in the evaporation of solvent, as shown in Figure 1.2 (b). The end result is a thin coating of polymers on top of the substrate.

During spin coating, several intricate physical processes, which will be described below, cause the polymers to separate from the mixture and self-assemble into nano- and microscale domains. Generally, the process by which a homogeneous mixture decomposes into its constituent phases is referred to as phase separation. The self-assembly of small, polymer-rich domains due to the action of phase separation can give rise to thin films with complex internal interfaces [76, 101, 108, 159]. From a nanoscience perspective, the self-organising behaviour of polymeric mixtures is especially exciting because it may offer an inexpensive route for fabricating polymer films with optimal morphological characteristics if it can be systematically controlled. Herein lies the main challenge in producing polymer films from spin-cast mixtures: it is not always clear which experimental conditions should be used to create a film with a given morphology. This has motivated a number of recent experimental investigations that strive to elucidate the key physical mechanisms that influence the morphological characteristics of dried polymer films [8, 82, 107, 149, 154].

Experimental studies show that the domains in the resulting film are often pure in one polymer and laterally separated. Each domain extends from the substrate to the air so that the composition is approximately uniform in the vertical direction. However, the composition of the domains alternates in the horizontal directions, as shown schematically in Figure 1.2 (e). When the films are viewed from above, their morphology can be divided into two main classes, which we will refer to as the striation and filament types.

The striation type of morphology is, in some sense, the most ordered of the two. In this case, the polymer domains form rays, or striations, that emanate from the axis of rotation to give the film the appearance of a bicycle wheel when viewed from above. One polymer forms the spokes of the wheel while the other fills the gaps between them. A bird's-eye view of this configuration is shown in Figure 1.3 (a). In some cases, the striations break up to form what appear to be islands of one of the two polymers that are embedded within a sea of the other. An example of this topology is shown in Figure 1.3 (b). Wu *et al.* [159] have shown that simply varying the ratio of the two polymers in the initial mixture, leaving the solvent concentration fixed, is enough to switch between topologies with fully developed

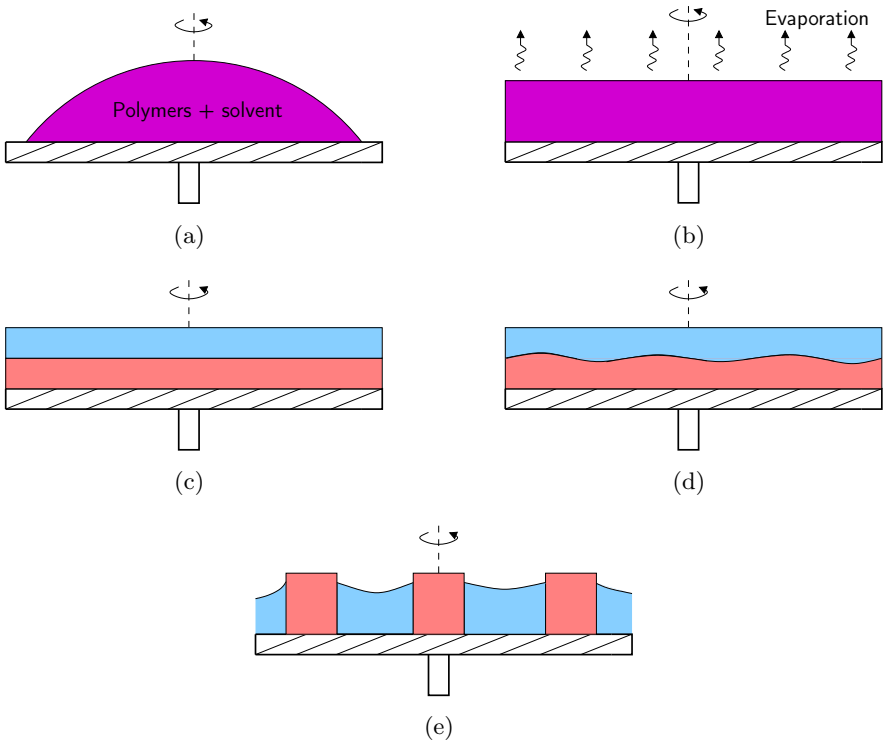
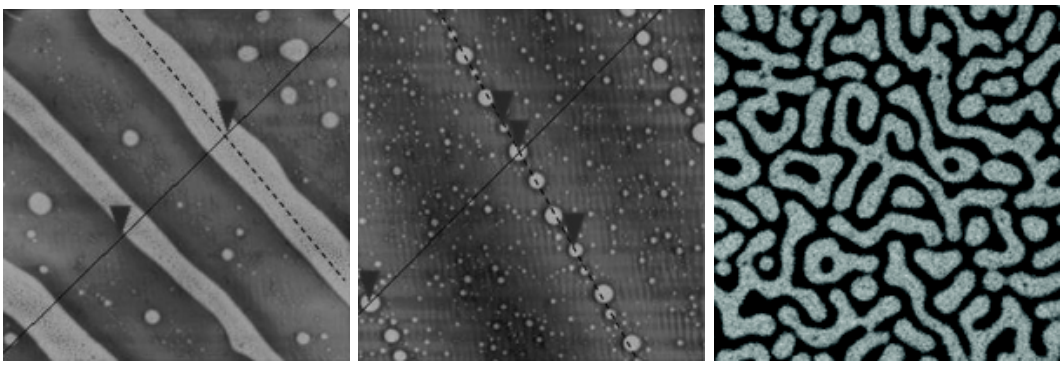


Figure 1.2: A schematic diagram of the spin-coating process. The polymers are blended in a common solvent and spread onto a substrate (a). The system is rotated with a high angular velocity which thins the film and enhances the evaporation of solvent (b). Recent experiments by Heriot & Jones [76] and Mokarian-Tabari *et al.* [107] suggest that the polymers undergo phase separation and form a horizontal bilayer (c). An instability at the bilayer interface leads to it becoming corrugated (d) and continued growth of the finger-like protrusions leads to a laterally phase separated film (e).



(a) (b) (c)

Figure 1.3: Bird's-eye views of spin-cast polymer blends showing typical morphologies that arise in experiments. Regions of different contrast denote different polymers. (a): The striation-type morphology showing rays, or striations, of polymers that emanate from the axis of rotation. The domains are aligned with the radial direction, shown as a dashed line. (b): In some cases, the striations break up and form islands of one type of polymer that appear to be embedded within a sea of the other. (c): The filament-type morphology showing long, curved structures that branch and intersect with one another. The experimental conditions in panels (a) and (b) are the same except for differing polymer ratios in the initial mixture. Panels (a)–(b) are reprinted with permission from Wu *et al.* [159]. Copyright 2006 American Chemical Society. Panel (c) is reprinted with permission from Ebbens *et al.* [60]. Copyright 2011 American Chemical Society.

striations and those with small islands. It has been shown by Birnie [22] that some films can simultaneously exhibit both topologies, with the islands forming near the centre of the film and striations away from it.

The filament type of morphology is similar to the striation type in the sense that the domains are long and generally well connected. However, the domains of the filament morphology form highly curved bicontinuous structures that branch and intersect with each other rather than aligning themselves with the radial direction. An example of this is shown in Figure 1.3 (c). Two-dimensional Fourier analyses of typical filament-type morphologies reveal that they can often be characterised by a single length scale corresponding to the width of the filaments [60]. Moreover, the pattern is found to be isotropic in the sense that it has the same size and shape characteristics across the polymer film.

1.3 Relevant physical mechanisms

Determining the physical processes that are responsible for the lateral separation of the domains and, in particular, selecting the type of film morphology has been hindered by the tremendous difficulties that are faced when attempting to obtain experimental data about the transient dynamics. However, significant progress has been made within the last decade. The data from Ebbens *et al.* [60] suggests that a hydrodynamic instability at the air-mixture interface triggers the localised onset of phase separation which leads to a

demixing of polymers that proceeds from the surface of the fluid down to the substrate. Thus, the laterally separated structures are grown from the top down in a manner that is analogous to directional solidification [53, 64]. Heriot & Jones [76] and Mokarian-Tabari [107], on the other hand, give experimental evidence to suggest that spin-cast polymer blends pass through an intermediate state consisting of a vertically stratified bilayer, as shown in Figure 1.2 (c), which then decomposes into laterally separated structures. The formation of this bilayer is thought to be caused by a combination of phase separation and preferential attraction between the substrate and one of the polymers. More specifically, it is suspected that the mixture undergoes phase separation during the drying process and energetically favourable interactions between the substrate and its preferred polymer lead to the development of a wetting layer.

There is some debate over how the bilayer breaks up into laterally separated domains. Several authors have proposed that a hydrodynamic instability occurs at the bilayer interface, causing it to form finger-like protrusions that grow towards the surface and the substrate [76, 82, 87, 107]; see Figure 1.2 (d). The growth of these fingers, in combination with the thinning of the layer due to centrifugal effects and evaporative mass loss, form laterally separated domains. Dunbar *et al.* [58] give compelling experimental evidence of this instability through their detection of bilayers with undulating polymer-polymer interfaces. Alternatively, Sprenger *et al.* [142] suggests that the upper surface of the bilayer, *i.e.*, the polymer-air interface, may also undergo an instability that acts in conjunction with the one at the polymer-polymer interface. Jaczewska *et al.* [82] argue that, in addition to hydrodynamic instabilities playing a role in transitioning from the bilayer to a laterally separated state, the phenomenon of dewetting may also be important. In this case, the bilayer is suspected to destabilise because it has become energetically unfavourable to maintain the polymer-polymer and polymer-substrate interfaces. Thus, the bottom layer "dewets" from the substrate by creating holes that are filled with the other polymer, thus reducing the overall energy of the configuration.

1.4 Scope of thesis

The roles of phase separation, hydrodynamic instability, and wetting/dewetting in the context of structure formation in spin-cast polymer blends can be further understood by systematic mathematical investigations of these systems. The attractiveness of a mathematical study comes from its potential to provide detailed quantitative insights into the relationships between experimental parameters and film morphologies. The aim of this thesis is, therefore, to investigate mathematically the role of these physical mechanisms in the context of evaporating mixtures by decomposing the spin-coating process into several simpler

problems. Many of these problems are idealisations of the various hypothetical stages of film evolution shown in Figure 1.2. We now give an overview of the problems addressed in this thesis, their motivation, as well as the key results that have been obtained.

Nearly all of the proposed routes that lead to the formation of a laterally separated morphology involve the onset of a hydrodynamic instability. Several experimental and theoretical studies have focused on determining the important modes of instability in evaporating mixtures [8, 55, 104]. A strong consensus has emerged which argues that composition-driven instabilities due to surface-tension gradients, *i.e.*, solutal Marangoni instabilities, play the largest role [8, 22, 76, 104, 107].

With this as motivation, in Chapter 2 we explore the onset of solutal Marangoni instabilities in non-rotating, isothermal binary mixtures with one volatile component. This is obviously a significant simplification of the ternary mixtures considered in spin-coating experiments; however, it turns out that even in this highly simplified system, the mathematical analysis is not straightforward. The main difficulty stems from the fact that evaporative mass loss introduces a natural time dependence in the solutions, which complicates a linear stability analysis of the system. In many binary mixtures, however, there is a significant difference between the time scale of evaporation and that of diffusion. The film thins according to the evaporative time scale, whereas the Marangoni instability typically evolves on the diffusive time scale. This naturally leads to the question of whether there is an asymptotic approach that can be used to study the linear stability problem and, in particular, that can also capture long-term changes in the stability that occur as the film slowly thins.

In our study of an evaporating binary mixture, we derive a fairly general asymptotic solution to linear stability problems with slowly varying base states. This is used to explore the onset of solutal Marangoni instabilities in films that are subject to the stabilising mechanisms of gravity and mean surface tension. Two main modes of instability are found. The first is a short-wave stationary instability associated with steady convection cells which is analogous to the thermal-Marangoni instability first studied by Pearson [121]. The second is a long-wave oscillatory mode of instability associated with surface deformations that we believe is related to the periodic behaviour seen in drying paint films [63, 79]. The generality of our approach to studying the linear stability problem means that it may be used to study more complicated systems with time-dependent solutions, such as those arising in the context of spin coating.

The depletion of solvent due to evaporation can lead to the formation of a polymer-rich fluid layer beneath the free surface, which may play several important roles during spin coating. For example, a viscous skin can form at the surface if the concentration of polymer is sufficiently high. This skin can prevent further removal of solvent, thus ending the drying

process prematurely. On one hand, this skin may also lead to a stabilisation of the system, as Marangoni effects would be weakened due to the increase in the mixture viscosity near the surface. On the other, the polymers are often more dense than the solvent, and the creation of a polymer-rich layer of fluid on top of a solvent-rich layer may lead to Rayleigh–Taylor instabilities if gravitational effects are sufficiently strong. However, gravity might prevent this skin from forming in the first place if the polymers sink more rapidly than they accumulate the free surface. If gravitational effects are not too strong and a polymer-rich region does indeed form, phase separation might occur within this layer if the solvent concentration falls below a critical value, causing the growth of domains from the surface down to the substrate.

In Chapter 3, we aim to explore these possibilities through the use of multiphase fluid models for evaporating solvent-polymer blends. Starting from a microscopic description of the mixture, we derive a macroscopic model that accounts for density differences between the phases, gravitational effects, and phase separation. Rotation of the system is not considered. A two-phase fluid model for a mixture consisting of a solvent and a single polymer is first used to explore the interplay between gravity, evaporation, and skin formation. Analytical conditions are derived in certain asymptotic limits that can be used to determine whether or not a skin is likely to form. The focus then turns to using a three-phase fluid model to explore the relationship between skin formation and phase separation. Our model predicts that the accumulation of polymer beneath the free surface leads to a local increase in the rate at which polymers demix from the solvent, therefore suggesting that phase separation first occurs at the top of the fluid layer.

In Chapter 4, we focus on the formation of a transient bilayer and its subsequent break up, which are thought to be key stages in the evolution of spin-cast polymer films. To simplify our study, we consider a binary mixture that is confined to a non-rotating thin-film geometry. More specifically, the mixture is placed between two vertically separated walls of infinite horizontal extent. Each component of the mixture is assumed to be preferentially attracted to one, but not the same, wall. A phase-field model that describes the composition of the mixture is derived and used to investigate the effects of geometrical confinement on the dynamics of phase separation and, in particular, to determine conditions under which a bilayer can form. Having established this, we then examine how the bilayer responds to a localised perturbation of finite size that brings the bilayer interface in contact with one of the walls. This perturbation can be imagined as being caused by an interfacial instability.

Our results indicate that when the temperature of the mixture is slowly cooled, which is thermodynamically similar to removing solvent from a ternary mixture, even a small amount of preferential attraction between the walls and the components is enough to induce a bilayer

morphology. We also find that a single, localised perturbation to this bilayer can initiate a self-sustaining sequence of ruptures that causes it to break up into a laterally separated structure with a well-ordered morphology.

The domains of the bilayer are found to be nearly uniform in composition and separated by a very thin transition region where the composition changes rapidly. This length-scale separation is exploited to reduce the phase-field model to a sharp-interface model that is mathematically identical to the types of Stefan problems that are commonly encountered in studies of solidification [53, 111]. A further asymptotic analysis is carried out to reduce the sharp-interface model to a thin-film equation, which is then used to efficiently explore the dynamics of bilayer break up.

The thesis concludes in Chapter 5, where the results are summarised and further discussed, and interesting avenues of future work are mentioned.

1.5 Mathematical studies of spin coating

All of the models considered in this thesis are posed in stationary, non-rotating, systems. Consequently, any effects due to centrifugal or Coriolis forces are neglected. The reason for this is due to our belief that rotation does not fundamentally alter the key physical mechanisms that drive the evolution of evaporating polymer films. This claim is partially justified by the experimental results of Mokarian–Tabari *et al.* [107], where similar film morphologies are found close to and far away from the axis of rotation. That being said, there is an extensive and interesting literature on the mathematics of spin coating, which we now briefly discuss. The first mathematical study of spin coating was performed by Emslie *et al.* [62], who showed that shocks can form if the initial thickness of the layer is non-uniform. Moriarty *et al.* [109] later showed these shocks are regularised by surface tension. Bornside [26] showed that a highly viscous polymer-rich skin can form at the fluid surface, and this was investigated in detail by Münch *et al.* [112]. The linear stability of spin-cast fluids has been studied by Reisfeld *et al.* [128, 129], who found that evaporation and inertial effects stabilise and destabilise surface deformations, respectively. Acrivos *et al.* [2], Charpin *et al.* [40], and Lawrence & Zhou [102] investigate the spin coating of non-Newtonian fluids.

Chapter 2

Marangoni instabilities in an evaporating solvent-polymer mixture

2.1 Introduction

Thin layers of evaporating solvent-polymer mixtures are commonly encountered in a number of industrial contexts ranging from painting, inkjet printing, and the fabrication of polymer-based photovoltaic devices [54, 70, 76, 79, 141]. In all of these applications, the quality of the resulting polymer film or coating is directly related to its morphology and composition. As a consequence, these applications often seek films with specific morphologies that are optimal in some sense. For example, paint coatings should be highly uniform in thickness to minimise the scattering of light [63]. In the case of organic solar cells, the polymers that constitute the photoactive component of the device should interpenetrate on nanometer scales to minimise exciton recombination [108]. Fabricating polymer films that have specific morphologies in a manner that is both robust and inexpensive remains a major technical challenge in many applications. Therefore, it is of great practical interest to further understand the relationship between the physical processes that occur during the drying process and the morphological characteristics of the resulting film.

As a solvent-polymer mixture dries, it is influenced by several factors including, but not limited to, surface tension, surface-tension gradients, gravity, and van der Waals interactions. The situation is even more complicated when the evaporating blend consists of multiple polymers: the change in temperature and composition that occurs during the drying process can trigger the onset of phase separation within the bulk, resulting in films with complex heterogeneous compositions [108]. These physical factors affect the morphology of a thin film in different ways; some of them act as stabilising mechanisms whereas others are destabilising. For instance, surface tension has the tendency to flatten the film

surface so it might be considered a source of stabilisation. On the other hand, van der Waals forces between the substrate and the fluid molecules can lead to ruptures in the film and the formation of dry spots on the substrate. Comprehensive reviews on the dynamics of thin layers of fluid that evolve under the influence of such factors are given by Myers [115], Oron *et al.* [119], and Craster & Matar [49].

Evaporation is intimately linked to many of the aforementioned physical effects. As the film thins due to solvent loss, van der Waals forces become more prominent whereas gravitational effects are generally weakened. Furthermore, surface-tension gradients, which can be induced by non-uniformities in the surface temperature and composition, are commonly caused by evaporation. The loss of solvent near the surface can also lead to the formation of highly viscous crusts which freeze in transient morphologies. Thus, the key to understanding how a dried polymer film acquires its morphology lies partially in determining the relationship between evaporation and the many well-known processes that influence the dynamics of thin films.

There are many parallels between an evaporating solvent-polymer mixture that is assumed to be isothermal and a layer of pure liquid that is heated from below. The vertical concentration gradient that is induced by evaporation is analogous to the thermal gradient that a layer of fluid on top of a heated substrate experiences. If the solvent and the polymer do not have the same density, a concentration gradient may lead to buoyancy effects in much the same way that the thermal expansion of a pure liquid can. As alluded to previously, the surface tension of a fluid can be affected by the composition and temperature in similar ways. Therefore, it is tempting to treat layers of pure fluid that are heated from below as a proxy for isothermal evaporating mixtures, in which case the vast literature on the former system can provide useful insight into the dynamics that can be expected in the latter.

The first systematic studies of a pure liquid layer subject to heating from below are attributed to Bénard [9, 11, 10]. His early experiments indicate that sufficiently large temperature gradients can lead to the onset of convection within the layer. A subsequent mathematical analysis of Bénard's experiments by Rayleigh [127] showed that this convection could be driven by thermally induced density variations within the fluid layer. However, further experiments by Block [23] led to the realisation that Bénard's films were, in fact, too thin for convection to be caused by density differences. Block then proposed an alternative mechanism for convection based on thermally induced gradients in the surface tension. A mathematical analysis by Pearson [121] that followed roughly two years later verified Block's claims. Pearson's analysis was then extended by Scriven & Sternling [132] to consider how surface deformations affect the onset of convection. Their analysis predicted that long-wavelength convection patterns should be observed regardless of the relative strength

of surface-tension gradients, and this contradicted several experimental results [97]. Smith [139] reconciled the discrepancy between experiment and theory by showing that gravity stabilises long-wavelength convection. Subsequent experiments by Berg *et al.* [14] highlight how evaporation can lead to the onset of thermal convection in fluid layers that are not heated from below. The temperature gradient in these systems is the result of evaporative cooling at the surface of the fluid. An extensive theoretical investigation of evaporating layers of pure fluid has been carried out by Burelbach *et al.* [30]. This work was then extended by Sultan *et al.* [144], who considered the diffusion of vapour in the overlying gas. For reviews on recent developments in the field of convective instabilities in liquid films, see Bodenschatz *et al.* [24] and Colinet *et al.* [45].

2.1.1 Linear stability of time-dependent base states

A mathematical analysis of an evaporating layer of fluid is complicated by the evaporative mass loss, which naturally leads to solutions that depend on time. In the context of linear stability theory, this often implies that the base state which the system is linearised about is time dependent. As a result, the linear problem for the perturbations to the base state becomes non-autonomous in the time variable which generally means that the solution will no longer simply be proportional to $\exp(\lambda t)$. In some instances, such as in Burelbach *et al.* [30], this is not an issue and the linear stability problem can still be solved analytically. In other cases, the stability problem can be simplified by seeking a transformation that separates the space and time variables or by seeking a similarity solution in certain time regimes; see Smolka & Witelski [140] and Kang & Choi [88]. As mentioned by Davis [52] in the context of hydrodynamic stability, Floquet theory can be used when the base state is periodic in time.

In the situation where the linear stability problem cannot be treated analytically, one must turn to an approximate method or make some simplifying assumptions about the base state. One possibility is to treat the linearised problem as an initial value problem which is then solved numerically. The stability of the system is then inferred by taking a suitable norm of the perturbation. In some instances, this norm can be associated with a physical quantity such as energy; see, for example, Doumenc *et al.* [55], Shen [135], or Warner *et al.* [155]. Such a numerical approach was taken by Foster [66] to study convection in a layer of fluid that is uniformly cooled from above. The same method was used by Machrafi *et al.* [105] to study instabilities in an evaporating binary mixture. A shortcoming of this approach is that the growth of a perturbation will depend sensitively on its initial condition. This issue was addressed by Doumenc *et al.* [55], who describe how to find the optimal initial condition that maximises the perturbation amplitude at a given time.

They show that their numerical results for an evaporating mixture are in good agreement with experiment. Numerical approaches to linear stability problems can quickly become prohibitive if the parameter space is large. In such instances, it becomes highly desirable to have a systematic method for determining the stability of the system over a wide range of parameter values.

One method for circumventing the difficulties associated with a time-dependent base state is to modify the problem in some manner that removes this dependence. To study the stability of an evaporating solvent-polymer mixture, Souche & Clarke [141] introduce an artificial in-flux boundary condition at the substrate which compensates for the loss of solvent due to evaporation. A similar approach was also taken by Sultan *et al.* [144]. The shortcoming of this approach is that it is not always trivial to assess how the artificial modification of the problem influences the stability of the system.

An alternative method for simplifying a non-autonomous stability problem is the so-called frozen-time approximation, which is based around the assumption that the base state evolves so slowly in comparison to the perturbations that it can be frozen. The time variable in base state is then treated as an additional parameter of the system. This reduces the stability problem to one that is autonomous and it has the advantage of allowing the usual techniques from linear stability theory to be applied. However, this approach only provides information about the instantaneous stability of the problem for a given base state; therefore, it is difficult to assess how the stability of the problem changes over the long times on which the base state evolves. Despite this shortcoming, the frozen-time method has been used in a number of studies of evaporating mixtures; see, for example, Eres *et al.* [63], Haut & Colinet [71], Machrafi *et al.* [104], or Serpetsi & Yiantsios [134].

Several authors have noticed a close connection between the eigenvalues of the frozen-time linear stability problem and the approximate solutions that are obtained by solving the non-autonomous stability problem numerically [55, 103, 114, 155]. Benney & Rosenblat [13] investigated the stability of slowly varying flows and used the WKB method to show that the solution to the linearised problem can be approximated by integrating the largest frozen-time eigenvalue in time and then taking the exponential. Lick [103] also found this was the case when studying the dynamics of a fluid layer subject to time-varying heating. A similar result has been noted by Doumenc *et al.* [55]. The WKB approximation has been used by Seminara & Hall [133] to examine the stability of slowly varying flows in curved channels. In this chapter, we systematically generalise Lick's result to obtain an asymptotic solution to linear stability problems with slowly varying base states. In addition, we compute the next-order correction to this solution, which provides interesting insights into its validity. We derive our solution using two different approaches, one based on the method of multiple

scales and the other using the WKB approximation. Both of these approaches exploit the fact that the evolution of the base state occurs on a vastly different characteristic time scale compared to the perturbations. Using this asymptotic solution to the linearised problem, we are able to track the long-term evolution of perturbations and, in particular, capture the stabilisation that occurs as the fluid layer is eventually depleted of solvent. A similar approach has recently been adopted by Dziwnik *et al.* [59] to study contact-line instabilities in dewetting films.

2.1.2 The Marangoni instability

The hydrodynamic instability that is caused by surface-tension gradients does not bear the name of Pearson, who was the first to study this theoretically, but rather it has been termed the Bénard–Marangoni instability, or simply the Marangoni instability for short [97]. This instability comes in two flavours, the thermal and solutal type, depending on whether the surface-tension gradients are induced by variations in the surface temperature or composition, respectively.

Recent experimental and theoretical studies of evaporating binary mixtures have given evidence to suggest that convection is primarily driven by a solutal Marangoni instability rather than its thermal counterpart or by density differences across the fluid layer [8, 104]. Furthermore, there is experimental evidence to suggest that solutal Marangoni instabilities play an important role in setting the morphology of spin-cast polymer blends, a relevant process that is used in the fabrication organic solar cells [76, 107]. Thus, this chapter will focus on the evaporation-driven solutal Marangoni instability.

The process of evaporation is linked to the solutal Marangoni instability through the fact that non-uniform removal of solvent can generate the necessary gradients in composition that drive the formation and preservation of convection cells. To understand why this is so, let us first consider the case when the surface of the fluid is non-deformable. Non-uniform evaporation of solvent will generate composition-induced surface-tension gradients that effectively lead to a game of tug-of-war being played at the surface, with regions of high surface tension pulling on regions of lower surface tension. The surface shear is transmitted into the bulk by viscosity which, in turn, causes fluid near the surface to be dragged to regions of higher surface tension. By conservation of mass, the fluid that converges at regions of high surface tension must sink towards the substrate. Similarly, fluid must rise from the substrate in order to replace the fluid that has been dragged away. This convection motion can be sustained for two reasons. Firstly, removal of solvent from the surface will generate a vertical gradient in the composition that leads to uprising fluid being rich in solvent. This maintains the regions of low surface tension. Secondly, as this fluid is pulled

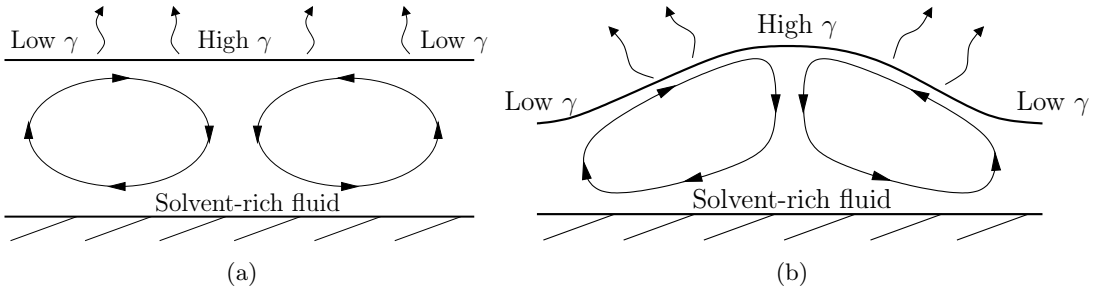


Figure 2.1: The evaporation-driven solutal Marangoni instability. Non-uniform evaporation of solvent leads to composition-induced surface-tension gradients which pull fluid from regions of low to high surface tension, γ. Converging fluid sinks to the substrate and fluid rises beneath regions of low surface tension. The uprising fluid is rich in solvent whereas the sinking fluid has been depleted of such due to the evaporation that has occurred. Left (a): The short-wavelength non-deformable mode of instability. Right (b): Long-wavelength mode associated with interface deformations. Note the diagram is not drawn to scale.

across the surface, evaporation depletes it of solvent. Thus, regions of high surface tension persist as well, allowing convection to continue. A schematic of this process is shown in Figure 2.1 (a).

The situation just described is characteristic of the case when the wavelength of the convection cells is sufficiently small that surface tension acts to keep the air-mixture interface relatively flat. If, on the other hand, the wavelength of the instability is long, then the interface can deform. In this case, the same basic situation described above also occurs; however, the build-up of fluid near regions of high surface tension leads to a local increase in the film thickness. Similarly, the transport of fluid from regions of low surface tension creates a local decrease in the thickness. This scenario is shown schematically in Figure 2.1 (b). By drawing on the analogy between binary mixtures and single-phase fluids subject to temperature gradients with or without evaporation, the same arguments can be used to understand the thermal Marangoni instability as well.

In layers of single-phase fluids, the thermal Marangoni instability can either be stationary or oscillatory in nature. Stationary instabilities are associated with the monotonic growth of small disturbances, whereas oscillatory instabilities lead to disturbances that grow in a modulated fashion. In the case of fluid layers with non-deformable upper surfaces, numerical studies by Vidal & Acrivos [151] suggested the Marangoni instability had to be stationary. This conjecture was later proven by Vrentas & Vrentas [153]. However, when the surface of the fluid is deformable, Takashima [146] showed that an oscillatory Marangoni instability is possible if the bottom of the fluid layer is cooler than the top. Subsequent studies by Pérez-García & Carneiro [123] and Shklyaev *et al.* [137] found that this was also possible in systems that are heated from below. Shklyaev *et al.* [138] has shown the

existence of thermally driven long-wavelength oscillatory instabilities in layers of pure fluid when the temperature gradient is induced by evaporation at the free surface.

The close connection between a layer of single-phase fluid that is subject to a vertical temperature gradient and an evaporating isothermal binary mixture naturally leads to the question of whether oscillatory Marangoni instabilities can occur in the latter system as well. The experiments with waterborne coatings by Kojima *et al.* [96] might support such a claim. During the drying process, the crests of the initial surface deformation can become troughs and troughs can become crests. This crest-to-trough reversal has been reported to happen several times during a given experiment and it could represent a standing wave solution of the governing equations. This reversal has also been seen in drying paint layers, although usually only one reversal occurs during a given experiment; see Overdiep [120], Howison *et al.* [79], or Wilson [156] for more details. Further mathematical investigations of the reversal have been carried out by Eres *et al.* [63] in the framework of lubrication theory and under the assumption that the solute concentration is uniform across the height of the fluid layer. Their frozen-time analysis indicates that, for sufficiently large evaporation rates, oscillatory modes can be linearly unstable. However, their nonlinear simulations show that the system is stabilised due to the viscosity of the mixture increasing as solvent is removed and hence the oscillations decay. As a consequence of working within lubrication theory, Eres *et al.* are unable to capture possible interactions and competition between long-wavelength oscillatory and short-wavelength stationary instabilities. The recent work by Serpetsi & Yiantsios [134] extends the analysis of Eres *et al.* by working outside of the lubrication approximation and allowing the solute concentration to vary in the vertical direction. However, only mixtures with constant viscosities and diffusivities in the absence of gravity are considered. Using a combination of frozen-time linear stability theory and numerical simulations, they find that long-wavelength oscillatory Marangoni instabilities do, indeed, exist in evaporating binary mixtures, but only if the Marangoni number is sufficiently small. If the Marangoni number is too large, the long-wave oscillatory mode is overwhelmed by the short-wave stationary one. However, no attempt was made to determine the dominant mode of instability for a given set of parameter values. In this chapter, we pay particular attention to the competition between the oscillatory and stationary modes of instability and we identify parameter regimes where each mode dominates. The development of a systematic method for analysing the linear stability of evaporating mixtures allows us goes beyond the frozen-time approximation, which enables us to determine how the two instabilities may interact and overtake each other on long time scales. Furthermore, gravity is included in our model so that we can explore whether it leads to a stabilisation of the long-wavelength oscillatory instability.

2.1.3 Summary and outline of chapter

In this chapter we study the role of solutal Marangoni instabilities in evaporating binary mixtures. In addition to evaporation and surface-tension gradients influencing the dynamics of the mixture, we include the action of gravity and mean surface tension in the mathematical model. Diffusion of the two components is assumed to occur on a much faster time scale than evaporation. The evolution of the base state, which occurs on the evaporative time scale, is much slower than the growth or decay of perturbations, which occurs on the diffusive time scale. The separation of these two scales is exploited and used to study the linear stability using a frozen-time analysis and to construct an asymptotic solution to the linearised problem. The frozen-time analysis facilitates the identification of unstable parameter regimes and the asymptotic solution enables the stability of the system to be monitored over the long time intervals on which the base state evolves. Using these techniques, we examine the competitive behaviour between stationary and oscillatory modes of instability.

The chapter is outlined as follows. In Section 2.2, the mathematical model is developed. In Section 2.3, we formulate the problems for the base state and its linear stability. The frozen-time method and the asymptotic solution are presented here. However, the detailed derivations of the asymptotic solution are given in Appendix A.1. In Section 2.4, we consider the dynamics of a fluid surface with a non-deformable upper surface. This is used as a toy model to understand how linear stability problems with slowly varying base states can be analysed. Moreover, we use this toy problem to explore the accuracy of the asymptotic solution. In Section 2.5, we consider the realistic case of a fluid with a deformable surface. The results from the analyses are interpreted in an experimental context in Section 2.6. The chapter ends with a discussion and conclusion in Section 2.7.

2.2 Mathematical model

We are interested in the dynamics of an evaporating layer of fluid that is composed of a volatile solvent and a non-volatile polymer. The fluid layer is assumed to be of infinite horizontal extent and it rests on a non-permeable substrate; see Figure 2.2. Above the fluid layer we assume the existence of a passive gas layer; that is, we neglect any interactions between this gas layer and the underlying fluid. Neglecting this gas layer can be made systematic by taking the so-called one-sided limit of a two-layer (fluid and gas) model; see Burelbach *et al.* [30] for more details. We base our theoretical mixture on the polystyrene-toluene blends considered experimentally by Bassou & Rharbi [8], who argue that thermal effects are not important. Recent work by Chauvet *et al.* [41] has also shown that evaporation can dampen thermocapillary effects. Thus, it is assumed that the fluid is isothermal. However,

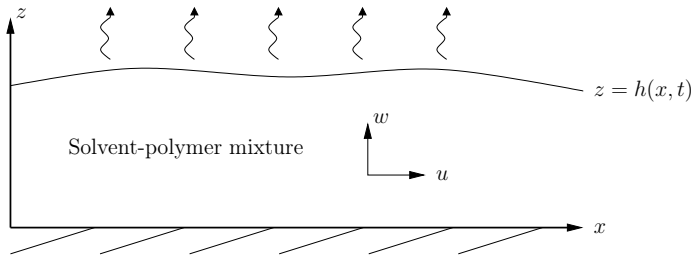


Figure 2.2: A schematic diagram of the system under consideration, showing a two-dimensional layer of fluid resting on a non-permeable substrate. The fluid is composed of a non-volatile polymer and a volatile solvent. The layer has thickness $h(x,t)$ and the mixture has horizontal and vertical components of velocity given by u and w, respectively.

we return to this assumption in Section 2.6. The mathematical model, therefore, considers the horizontal and vertical components of the mixture velocity, u and w, respectively; the hydrodynamic pressure p; and the volume fraction of solvent c; all of which are functions of the horizontal coordinate x, the vertical coordinate z, and time t.

Conservation of solvent and polymer within the fluid layer implies

$$\partial_t \rho_s + \nabla \cdot \boldsymbol{q}_s = 0, \tag{2.1a}$$

$$\partial_t \rho_p + \nabla \cdot \boldsymbol{q}_p = 0, \tag{2.1b}$$

where ρ_s and ρ_p denote the density of the solvent and polymer, respectively, and $\boldsymbol{q}_s$ and $\boldsymbol{q}_p$ denote the corresponding mass fluxes. We assume the density of the mixture $\rho = \rho_s + \rho_p$ is constant and, consequently, we neglect any effects due to compositional buoyancy; these will be studied in Chapter 3. The mixture flux is defined as $\boldsymbol{q} = \rho \boldsymbol{u} = \boldsymbol{q}_s + \boldsymbol{q}_p$, where $\boldsymbol{u} = u\boldsymbol{e}_x + w\boldsymbol{e}_z$ is the mixture velocity written in terms of the basis vectors $\boldsymbol{e}_x$ and $\boldsymbol{e}_z$ pointing in the x and z direction, respectively. Adding the two equations in (2.1) implies the mixture velocity is divergence-free, thus

$$\nabla \cdot \boldsymbol{u} = 0. \tag{2.2}$$

The solvent mass flux is assumed to have two contributions: one from the bulk motion of the mixture and the other from diffusion into the polymer. Therefore, we take $\boldsymbol{q}_s = \rho_s \boldsymbol{u} - D\nabla\rho_s$, where D is the diffusion coefficient of solvent into polymer (assumed constant). By writing the solvent density in terms of the solvent volume fraction, $\rho_s = \rho c$, the conservation equation in (2.1a) becomes

$$\partial_t c + \boldsymbol{u} \cdot \nabla c = D\nabla^2 c, \tag{2.3}$$

where (2.2) has been used. The fluid is assumed to have Newtonian rheology and we suppose that its bulk motion can be adequately described by the Stokes equations,

$$-\nabla p + \mu \nabla^2 \boldsymbol{u} - \rho g \boldsymbol{e}_z = 0, \tag{2.4}$$

where μ denotes the kinematic viscosity of the mixture, and g is the acceleration due to gravity.

The assumption that the mixture is Newtonian with constant viscosity and diffusivity is only expected to be valid during the early stages of the drying process when the polymer phase is dilute. For later times, the nonlinear dependence of the viscosity and diffusivity on the polymer concentration and non-Newtonian behaviour due to shear thinning are expected to influence the dynamics of the evaporating mixture. If the initial polymer concentration is sufficiently small, the mixture will behave Newtonian during the first stages of the drying process and, in particular, when the instability is first developing. Thus, a Newtonian fluid model with constant viscosity is a useful approximation that can be used to gain basic insight into the role of Marangoni instabilities in evaporating mixtures. Therefore, we neglect these complicated rheological features for the time being but will discuss them further in the conclusion.

The underlying substrate at $z = 0$ is assumed to be non-permeable; therefore, the usual no-flux and no-slip conditions apply,

$$u = w = \partial_z c = 0, \quad z = 0. \tag{2.5}$$

The surface of the fluid layer is denoted by $z = h(x, t)$ and it is assumed that only the solvent evaporates. A rigorous mathematical description of the evaporation process cannot be obtained from our one-sided model because it neglects the effects of the overlying gas layer. Instead, we take a phenomenological approach and assume the evaporative mass flux is proportional to the solvent concentration at the surface,

$$q_{\text{evap}} = k_m \rho c(x, h(x, t), t), \tag{2.6}$$

where k_m is a mass transfer coefficient. Such relations are common in studies involving evaporating solvent-solute systems; see Bornside *et al.* [26] and Souche & Clarke [141].

Conservation of total mass across the surface of the fluid layer implies that

$$\rho(\boldsymbol{u} \cdot \boldsymbol{e}_n - v_n) = q_{\text{evap}}, \quad z = h(x, t), \tag{2.7}$$

where $\boldsymbol{e}_n$ and v_n are the unit normal vector to the surface and the normal velocity of the surface, respectively. These can be written explicitly as

$$\boldsymbol{e}_n = \frac{-\partial_x h \boldsymbol{e}_x + \boldsymbol{e}_z}{\sqrt{1 + (\partial_x h)^2}}, \quad v_n = \frac{\partial_t h}{\sqrt{1 + (\partial_x h)^2}}. \tag{2.8}$$

Conservation of solvent across the surface yields the condition

$$-\rho D \nabla c \cdot \boldsymbol{e}_n + \rho c(\boldsymbol{u} \cdot \boldsymbol{e}_n - v_n) = q_{\text{evap}}, \quad z = h(x, t). \tag{2.9}$$

By combining (2.7) and (2.9), a simplified mass-balance condition for the solvent can be obtained, namely

$$-\rho D \nabla c \cdot \boldsymbol{e}_n = q_{\text{evap}}(1-c), \quad z = h(x,t). \tag{2.10}$$

Deformations in the surface of the fluid layer and gradients in the surface tension both induce stresses that must be balanced by the pressure and the viscous stress in the fluid at the surface. The normal and tangential stress balances at the interface are given by

$$-p + \mu\, \boldsymbol{e}_n \cdot (\nabla \boldsymbol{u} + \nabla \boldsymbol{u}^T) \cdot \boldsymbol{e}_n = -\gamma \nabla \cdot \boldsymbol{e}_n, \quad z = h(x,t), \tag{2.11a}$$

$$\mu\, \boldsymbol{e}_t \cdot (\nabla \boldsymbol{u} + \nabla \boldsymbol{u}^T) \cdot \boldsymbol{e}_n = \partial_s \gamma, \qquad z = h(x,t), \tag{2.11b}$$

respectively, where $\boldsymbol{e}_t$ denotes the unit tangent vector to the surface; ∂_s denotes differentiation with respect to the arclength of the surface; and γ is the surface tension of the fluid, which we take to be a linearly decreasing function of the solvent concentration at the surface, $\gamma = \gamma_r - \gamma_c \rho (c - c_r)$. Here, γ_c and c_r are reference values and γ_c characterises how the surface tension varies with the solvent volume fraction. The unit tangent vector is given by

$$\boldsymbol{e}_t = \frac{\boldsymbol{e}_x + \partial_x h \boldsymbol{e}_z}{\sqrt{1 + (\partial_x h)^2}}. \tag{2.12}$$

Using the expression for the surface tension in (2.11b) yields the boundary condition

$$\mu\, \boldsymbol{e}_t \cdot (\nabla \boldsymbol{u} + \nabla \boldsymbol{u}^T) \cdot \boldsymbol{e}_n = -\gamma_c \rho \nabla c \cdot \boldsymbol{e}_t, \quad z = h(x,t). \tag{2.13}$$

The initial conditions for the solvent volume fraction and the film thickness are given by

$$c(x,z,0) = c_i(x,z), \quad h(x,0) = h_i(x). \tag{2.14}$$

We define the mean values of the initial conditions as

$$\beta = \lim_{L\to\infty} \frac{1}{2L} \int_{-L}^{L} \frac{1}{h_i(x)} \int_0^{h_i(x)} c_i(x,z)\, \mathrm{d}z \mathrm{d}x, \quad h_m = \lim_{L\to\infty} \frac{1}{2L} \int_{-L}^{L} h_i(x)\, \mathrm{d}x, \tag{2.15}$$

and these will be used in the non-dimensionalisation below.

2.2.1 Non-dimensionalisation

We scale the spatial dimensions of the problem with the mean initial thickness of the film so that $x = h_m x'$ and $z = h_m z'$, where primes are used to denote dimensionless quantities. Time is scaled according to the diffusive time scale, $t = (h_m^2/D)t'$, and from these we can define a velocity scale so that $\boldsymbol{u} = (D/h_m)\boldsymbol{u}'$. The pressure scale is chosen

to be $\mu D/h_m^2$ and we write the pressure as the deviation from its hydrostatic component, $p = (\mu D/h_m^2)(p' - \mathrm{Ga}\, z')$, where Ga is the Galileo number defined as

$$\mathrm{Ga} = \frac{\rho g h_m^3}{\mu D}. \tag{2.16}$$

The solvent volume fraction is written as the deviation from its mean initial value, $c = \beta + Sc'$, where the scale S is determined from the boundary condition (2.10), with c replaced by β on the right-hand side of this condition. This gives $S = \delta\beta(1-\beta)$, where

$$\delta = \frac{k_m h_m}{D} \tag{2.17}$$

defines an evaporative Biot number.

With these scalings, the bulk equations can be written as (after dropping the primes)

$$-\nabla p + \nabla^2 \boldsymbol{u} = 0, \tag{2.18a}$$

$$\nabla \cdot \boldsymbol{u} = 0, \tag{2.18b}$$

$$\partial_t c + \boldsymbol{u} \cdot \nabla c = \nabla^2 c. \tag{2.18c}$$

The boundary conditions along the substrate are given by

$$u = w = \partial_z c = 0, \quad z = 0, \tag{2.18d}$$

and at the free surface they are

$$\boldsymbol{u} \cdot \boldsymbol{e}_n - v_n = \delta\beta[1 + \delta(1-\beta)c], \qquad z = h(x,t), \tag{2.18e}$$

$$-\nabla c \cdot \boldsymbol{e}_n = [1 + \delta(1-\beta)c](1 - \delta\beta c), \qquad z = h(x,t), \tag{2.18f}$$

$$-p + \boldsymbol{e}_n \cdot (\nabla \boldsymbol{u} + \nabla \boldsymbol{u}^T) \cdot \boldsymbol{e}_n = -\mathrm{Ga}\, h - \mathrm{Ca}^{-1}(1 - \mathrm{MaCa}\, c)\nabla \cdot \boldsymbol{e}_n, \quad z = h(x,t), \tag{2.18g}$$

$$\boldsymbol{e}_t \cdot (\nabla \boldsymbol{u} + \nabla \boldsymbol{u}^T) \cdot \boldsymbol{e}_n = -\mathrm{Ma} \nabla c \cdot \boldsymbol{e}_t, \qquad z = h(x,t), \tag{2.18h}$$

where we have chosen $c_r = \beta$. The non-dimensional initial conditions are given by

$$c(x,z,0) = c_i(x,z), \quad h(x,0) = h_i(x), \tag{2.18i}$$

where c_i now has a mean value of zero. For a flat and spatially uniform (well-mixed) initial state, the initial conditions are $c_i(x,z) \equiv 0$ and $h_i(x) \equiv 1$. The additional non-dimensional numbers that appear are the capillary number Ca and the Marangoni number Ma. These are defined as

$$\mathrm{Ca} = \frac{\mu D}{\gamma_r h_m}, \quad \mathrm{Ma} = \frac{\delta\beta(1-\beta)\rho\gamma_c h_m}{\mu D}. \tag{2.19}$$

Table 2.1: Example parameter values taken from the experiments of [8]

Quantity	Value	Unit
ρ	1000	$\mathrm{kg \cdot m^{-3}}$
μ	0.15	$\mathrm{Pa \cdot s}$
g	9.81	$\mathrm{m \cdot s^{-2}}$
D	1.38×10^{-9}	$\mathrm{m^2 \cdot s^{-1}}$
k_m	3.53×10^{-7}	$\mathrm{m \cdot s^{-1}}$
γ_r	0.03	$\mathrm{N \cdot m^{-1}}$
γ_c	9.2×10^{-6}	$\mathrm{N \cdot m^2 \cdot kg^{-1}}$
h_m	10^{-4}–1.4×10^{-3}	m
β	0.85	–

In this chapter, we assume that $\gamma_c > 0$ so that the Marangoni numbers are positive. However, it is possible for binary mixtures to have negative Marangoni numbers if the solute has the effect the lowering the surface tension of the fluid.

To estimate the size of the non-dimensional numbers, we base the parameters values on the evaporating toluene-polystyrene systems studied by Bassou & Rharbi [8]. Their mixtures often had an initial solvent volume fraction of $\beta = 0.85$ and they imposed an evaporative flux of $q_{\mathrm{evap}} = 3 \times 10^{-4}\ \mathrm{kg \cdot m^{-2} \cdot s^{-1}}$. With these two parameter values, the mass transfer coefficient k_m can be inferred via (2.6) if c is replaced by β. The density of polystyrene and toluene are $1050\ \mathrm{kg \cdot m^{-3}}$ and $867\ \mathrm{kg \cdot m^{-3}}$, respectively, so we approximate the net density of the mixture as $\rho = 1000\ \mathrm{kg \cdot m^{-3}}$. A diffusion coefficient for their system can be obtained by interpolating the values found in NaNagara *et al.* [117]. A list of the physical parameters in our model, along with their values, can be found in Table 2.1.

By inserting these parameter values into the expressions for the non-dimensional numbers, we find that δ, which can be interpreted as the ratio of the diffusive time scale to the evaporative time scale h_m/k_m, is bounded between $0.026 < \delta < 0.36$. This suggests a separation of time scales in the problem and we will assume throughout the remainder of this chapter that $\delta \ll 1$. The Galileo and Marangoni numbers can vary by several orders of magnitude owing to their nonlinear dependence on the mean initial film thickness; note that Ma scales like h_m^2 because of the factor of h_m contained within δ. We find that $14 < \mathrm{Ma} < 3 \times 10^3$ and $47 < \mathrm{Ga} < 1.3 \times 10^5$. The capillary numbers always remain small, however, and these are bounded by $5 \times 10^{-6} < \mathrm{Ca} < 7 \times 10^{-5}$. The product MaCa is always expected to be small so we drop these terms from the normal stress balance (2.18g). Moreover, we only consider the case $\mathrm{Ca} \ll 1$ in the calculations below.

2.3 Formulation

In this chapter we focus on carrying out a linear stability analysis of the governing equations. This requires examining how infinitesimal perturbations to a simplified base state evolve in time. In this problem, the base state corresponds to a flat film and the fluid velocity, pressure, and the concentration are assumed to vary only in the vertical direction. The perturbations are decomposed into Fourier modes with wavenumber k. Therefore, we seek solutions to (2.18) of the form

$$\boldsymbol{u}(x,z,t) = \bar{\boldsymbol{u}}(z,t) + \varepsilon\tilde{\boldsymbol{u}}(z,t)e^{ikx}, \tag{2.20a}$$

$$p(x,z,t) = \bar{p}(z,t) + \varepsilon\tilde{p}(z,t)e^{ikx}, \tag{2.20b}$$

$$c(x,z,t) = \bar{c}(z,t) + \varepsilon\tilde{c}(z,t)e^{ikx}, \tag{2.20c}$$

$$h(x,t) = \bar{h}(t) + \varepsilon\tilde{h}(t)e^{ikx}, \tag{2.20d}$$

where $\varepsilon \ll \delta \ll 1$ is a small parameter representing the initial size of the perturbation. The $O(1)$ contribution to this solution corresponds to the base state and the associated variables are denoted with bars. The $O(\varepsilon)$ contribution corresponds to the perturbation and this is denoted by variables with tildes. Systems of equations that govern the evolution of the base state and the perturbations can be obtained by inserting (2.20) into (2.18) and expanding about $\varepsilon \ll 1$. The base state is obtained from the nonlinear $O(1)$ problem whereas the evolution of perturbations is determined from the linear $O(\varepsilon)$ problem.

2.3.1 Computation of the base state

The hydrodynamic part of the $O(1)$ problem is given by

$$\partial_z^2\bar{u} = 0, \tag{2.21a}$$

$$-\partial_z\bar{p} + \partial_z^2\bar{w} = 0, \tag{2.21b}$$

$$\partial_z\bar{w} = 0. \tag{2.21c}$$

subject to the boundary conditions

$$\bar{\boldsymbol{u}} = 0, \quad z = 0, \tag{2.21d}$$

along the substrate and

$$\bar{w} - \partial_t\bar{h} = \delta\beta[1 + \delta(1-\beta)\bar{c}], \quad z = \bar{h}(t), \tag{2.21e}$$

$$-\bar{p} + 2\partial_z\bar{w} = -\mathrm{Ga}\,\bar{h}, \quad z = \bar{h}(t), \tag{2.21f}$$

$$\partial_z\bar{u} = 0, \quad z = \bar{h}(t), \tag{2.21g}$$

at the free surface. From these expressions, it can be deduced that the fluid is motionless so that $\bar{\boldsymbol{u}} \equiv 0$ and $\bar{p}(z,t) = \mathrm{Ga}\,\bar{h}(t)$. The problem for the solvent volume fraction is then given by

$$\partial_t \bar{c} = \partial_z^2 \bar{c} \tag{2.22a}$$

with boundary conditions

$$\partial_z \bar{c} = 0, \qquad z = 0, \tag{2.22b}$$

$$\partial_z \bar{c} = -[1 + \delta(1-\beta)\bar{c}](1 - \delta\beta\bar{c}), \quad z = \bar{h}(t). \tag{2.22c}$$

The initial condition for the base state is taken to be $\bar{c}(z,0) \equiv 0$ so that mixture is initially homogeneous in composition. The kinematic boundary condition in (2.21e) provides an expression for the evolution of the free boundary:

$$\partial_t \bar{h} = -\delta\beta[1 + \delta(1-\beta)\bar{c}(\bar{h}(t),t)]. \tag{2.22d}$$

The corresponding initial condition for the film thickness is $\bar{h}(0) = 1$.

An examination of (2.22) shows that there are at least two time regimes to consider. The first corresponds to $O(1)$ times, during which evaporation leads to the formation of a compositional boundary layer at the surface of the film. This layer grows in thickness until it reaches the substrate, after which the concentration profile begins to settle into a quasi-equilibrium. In this time regime, the small loss of solvent leads to the film thickness remaining approximately constant. The second regime corresponds to large times, namely when $t = O(\delta^{-1})$. On this time scale, the fluid layer thins by an appreciable amount and the concentration field evolves quasi-statically owing to the fast relative rate of diffusion. We will use matched asymptotic expansions to obtain solutions that are valid within each region.

2.3.1.1 Solutions in the first time regime

It is insightful to decompose the first time regime into a small-time regime and an $O(1)$ time regime. In the small-time regime, it is possible to obtain a closed-form solution that clearly captures the development of the compositional boundary layer which forms at the surface due to evaporation. To obtain this solution, we first introduce a fast time given by $T = \delta^{-q}t$, where $q > 0$ is arbitrary. The evolution of the film thickness is exceptionally slow on this time scale and hence we can set $\bar{h}(T) \equiv 1$. As we expect a boundary layer to only form near the surface of the layer, we consider the solution in an outer region away from the surface and in an inner region close to the surface.

The leading-order problem in the outer region is given by

$$\partial_T \bar{c} = \delta^q \partial_z^2 \bar{c}, \tag{2.23}$$

with $\partial_z \bar{c} = 0$ at $z = 0$ and $\bar{c} = 0$ at $T = 0$. Thus, the solution is given trivially by $\bar{c} \equiv 0$. In physical terms, this simply means the solvent in the bulk has yet to feel the effects of evaporation.

To obtain the problem in the inner region, we introduce the coordinate $\eta = (1 - z)/\delta^{q/2}$ and scale the volume fraction according to $\bar{c} = \delta^{q/2}\bar{C}$. The leading-order problem in the inner region is given by

$$\partial_T \bar{C} = \partial_\eta^2 \bar{C}, \tag{2.24}$$

subject to $\partial_\eta \bar{C} = 1$ at $\eta = 0$, $\bar{C} \to 0$ as $\eta \to \infty$, and $\bar{C} = 0$ at $T = 0$. We seek a similarity solution to this problem of the form $\bar{C}(\eta, T) = T^{1/2} f(\xi)$, where $\xi = \eta/T^{1/2}$. It is easy to show that f satisfies

$$f(\xi) - \xi f'(\xi) = 2f''(\xi), \tag{2.25}$$

subject to $f'(0) = 1$ and $f \to 0$ as $\xi \to \infty$. The solution to this boundary value problem can obtained by first noting that $f(\xi) = \xi$ solves the differential equation. Thus, by seeking a solution of the form $f(\xi) = \xi r(\xi)$, the order of (2.25) can effectively be reduced. The problem for r boils down to solving a separable, first-order equation and then integrating the solution. Both are straightforward tasks. Upon obtaining the general solution for f and applying the boundary conditions, we find that

$$f(\xi) = \xi \text{erfc}\left(\frac{\xi}{2}\right) - \frac{2}{\sqrt{\pi}} e^{-\xi^2/4}. \tag{2.26}$$

Thus, the uniformly valid composite solution for the solvent volume fraction, written in terms of the original independent variables, is given by

$$\bar{c}(z, t) = (1 - z)\text{erfc}\left(\frac{1 - z}{\sqrt{4t}}\right) - \sqrt{\frac{4t}{\pi}} e^{-(1-z)^2/4t}, \quad t \ll 1. \tag{2.27}$$

We now consider the problem for $O(1)$ times. In this case, we pose an asymptotic expansion of the form

$$\bar{c}(z, t) = \bar{c}_0(z, t) + \delta \bar{c}_1(z, t) + O(\delta^2), \tag{2.28a}$$

$$\bar{h}(t) = \bar{h}_0(t) + \delta \bar{h}_1(t) + O(\delta^2), \tag{2.28b}$$

and insert this into (2.22). The leading-order problem for the concentration is given by

$$\partial_t \bar{c}_0 = \partial_z^2 \bar{c}_0 \tag{2.29a}$$

subject to

$$\partial_z \bar{c}_0 = 0, \qquad z = 0, \tag{2.29b}$$

$$\partial_z \bar{c}_0 = -1, \quad z = \bar{h}_0(t) \tag{2.29c}$$

$$\bar{c}_0 = 0, \qquad t = 0. \tag{2.29d}$$

The corresponding problem for the film thickness is simply $\partial_t \bar{h}_0 = 0$ with $\bar{h}_0(0) = 1$. Therefore, $\bar{h}_0(t) \equiv 1$, which allows the concentration field to be computed using a series expansion. In particular, the leading-order solvent concentration is given by

$$\bar{c}_0(z,t) = \frac{1}{6} - \frac{1}{2}\, z^2 - t + \frac{2}{\pi^2} \sum_{n=1}^{\infty} \frac{(-1)^n}{n^2}\, e^{-n^2\pi^2 t} \cos(n\pi z). \tag{2.30}$$

The boundary layer solution in (2.27) is, in fact, contained within this solution, so that (2.30) provides a complete description of the solution in the first time regime.

2.3.1.2 Solution in the large-time regime

The second regime corresponds to the slow evolution of the concentration and thinning of the fluid layer. This occurs over long $O(\delta^{-1})$ time scales; hence, to capture this regime, we introduce a slow time given by $\tau = \delta t$. The problem for the base-state concentration then reads

$$\delta \partial_\tau \bar{c} = \partial_z^2 \bar{c}, \tag{2.31a}$$

subject to

$$\partial_z \bar{c} = 0, \qquad z = 0, \tag{2.31b}$$

$$\partial_z \bar{c} = -[1 + \delta(1-\beta)\bar{c}](1 - \delta\beta\bar{c}), \quad z = \bar{h}(\tau). \tag{2.31c}$$

The film thickness evolves according to

$$\partial_\tau \bar{h} = -\beta[1 + \delta(1-\beta)\bar{c}(\bar{h}(\tau), \tau)]. \tag{2.32}$$

Initial conditions for this problem are determined by matching to the solution in the previous time regime. This results in the conditions

$$\bar{h}(\tau) \sim 1, \tag{2.33a}$$

$$\bar{c}(z,\tau) \sim 1/6 - z^2/2 - \tau/\delta, \tag{2.33b}$$

as $\tau \to 0$. In order to obtain a sensible balance among terms, the concentration field and the film thickness are expanded as

$$\bar{c}(z,\tau) = \delta^{-1}\bar{c}_0(z,\tau) + \bar{c}_1(z,\tau) + O(\delta), \tag{2.34a}$$

$$\bar{h}(\tau) = \bar{h}_0(\tau) + \delta\bar{h}_1(\tau) + O(\delta^2). \tag{2.34b}$$

The leading-order problem is given by

$$\partial_z^2 \bar{c}_0 = 0, \tag{2.35}$$

with the conditions $\partial_z \bar{c}_0 = 0$ at both $z = 0$ and $z = \bar{h}_0(\tau)$, and $\bar{c}_0 \sim -\tau$ as $\tau \to 0$. It can be immediately deduced that the leading-order solvent volume fraction is independent of the vertical coordinate z; hence, we may write $\bar{c}_0(z, \tau) = \bar{c}_0(\tau)$. The functional form of $\bar{c}_0$ will be determined by a higher-order problem. The leading-order equation for the film thickness reads

$$\partial_\tau \bar{h}_0 = -\beta[1 + (1 - \beta)\bar{c}_0]. \tag{2.36}$$

To make further progress, we proceed to the $O(1)$ problem. The equation in the bulk reads

$$\partial_\tau \bar{c}_0 = \partial_z^2 \bar{c}_1, \tag{2.37}$$

which is supplemented with the boundary conditions

$$\partial_z \bar{c}_1 = 0, \qquad z = 0, \tag{2.38a}$$

$$\partial_z \bar{c}_1 = -[1 + (1 - \beta)\bar{c}_0](1 - \beta\bar{c}_0), \quad z = \bar{h}_0(\tau), \tag{2.38b}$$

and the initial condition $\bar{c}_1 \sim 1/6 - z^2/2$ as $\tau \to 0$. As $\bar{c}_0$ is only a function of τ, (2.37) can be integrated in space and the boundary condition at $z = 0$ can be applied to yield

$$\bar{c}_1(z, \tau) = \frac{1}{2} \frac{\mathrm{d}\bar{c}_0}{\mathrm{d}\tau} z^2 + \bar{c}_1(0, \tau). \tag{2.39}$$

This expression can be inserted into (2.38b) and, by using (2.36), it can be shown that

$$\bar{c}_0(\tau) = \frac{\bar{h}_0(\tau) - 1}{\beta \bar{h}_0(\tau)}. \tag{2.40}$$

By re-inserting this solution for $\bar{c}_0$ into (2.36), an implicit expression for the leading-order film thickness can be obtained:

$$\bar{h}_0 - 1 + (1 - \beta) \log\left(\frac{\bar{h}_0 - 1 + \beta}{\beta}\right) = -\tau. \tag{2.41}$$

Using this solution, it can be deduced that $\bar{h}_0 \to 1 - \beta$ as $\tau \to \infty$; thus, all of the solvent evaporates and the remaining film is pure in polymer. These leading-order solutions can be used in (2.39) to show that

$$\bar{c}_1(z, \tau) = -\frac{\bar{h}_0(\tau) - 1 + \beta}{2\beta \bar{h}_0^3(\tau)} z^2 + \bar{c}_1(0, \tau). \tag{2.42}$$

For this to match with the appropriate initial data as $\tau \to 0$, the condition $\bar{c}_1(0, 0) = 1/6$ must be imposed. Obtaining a functional form for $\bar{c}_1(0, \tau)$ comes from solving the $O(\delta)$ problem. However, this is not actually required in the linear stability analysis so it will be left unspecified.

2.3.1.3 Comparison with numerical solutions

The asymptotic solutions to the base state are compared with numerical solutions in Figure 2.3 for the example parameter values $\beta = 0.85$ and $\delta = 0.01$. Although this hypothetical value of δ is slightly smaller than the experimental values from Bassou & Rharbi [8], we find that increasing δ does not affect the qualitative features of the dynamics. The numerical scheme is based on a method-of-lines approach where spatial derivatives are discretised using finite differences and the resulting equations are treated as a system of ordinary differential equations. Figure 2.3 (a) shows the asymptotic solution for small times given in (2.27) and it highlights the fast growth of a solutal boundary layer from the free upper surface. The quasi-steady solution to the solvent volume fraction (2.44a) is presented in Figure 2.3 (b), where it can be seen that the concentration profiles differ mainly by an additive constant. The evolution of the film thickness and a comparison of the quasi-steady solution (2.41) is shown in Figure 2.3 (c). The film thickness remains relatively constant up to $O(1)$ times, after which it slowly decreases to its equilibrium value of $1 - \beta$.

It is enlightening to examine the evolution of the mean concentration gradient across the film, which we define as

$$\frac{\bar{c}(\bar{h}(t), t) - \bar{c}(0, t)}{\bar{h}(t)}. \tag{2.43}$$

Numerical and asymptotic approximations of this quantity are shown in Figure 2.3 (d). The numerical approximation clearly shows two distinct time regimes which are perfectly captured by the two asymptotic solutions. In the early time regime corresponding to $O(1)$ times, the concentration gradient slowly builds due the development of the compositional boundary layer at the surface. The gradient then begins to plateau when the boundary layer has penetrated the depth of the layer. This is also associated with the concentration settling into its quasi-steady profile. Around this time, the thickness begins to decrease which strengthens the gradient. On $O(\delta^{-1})$ time scales, the concentration gradient slowly diminishes due to the loss of solvent.

Recalling that the solutal Marangoni instability is driven, in part, by the presence of a vertical composition gradient, we can use Figure 2.3 (d) to understand how this instability may evolve in time. The initial build-up of the concentration gradient suggests that an observable instability is unlikely to develop straight away. However, the persistence and amplification of this gradient over long time scales is indicative that an instability could amplify perturbations to a level that would make them detectable. The eventual decay of the concentration gradient implies that the system will stabilise in the long-term.

Throughout the remainder of the chapter, the initial transients in the base state that occur in the first time regime will be neglected and we will only consider its quasi-steady

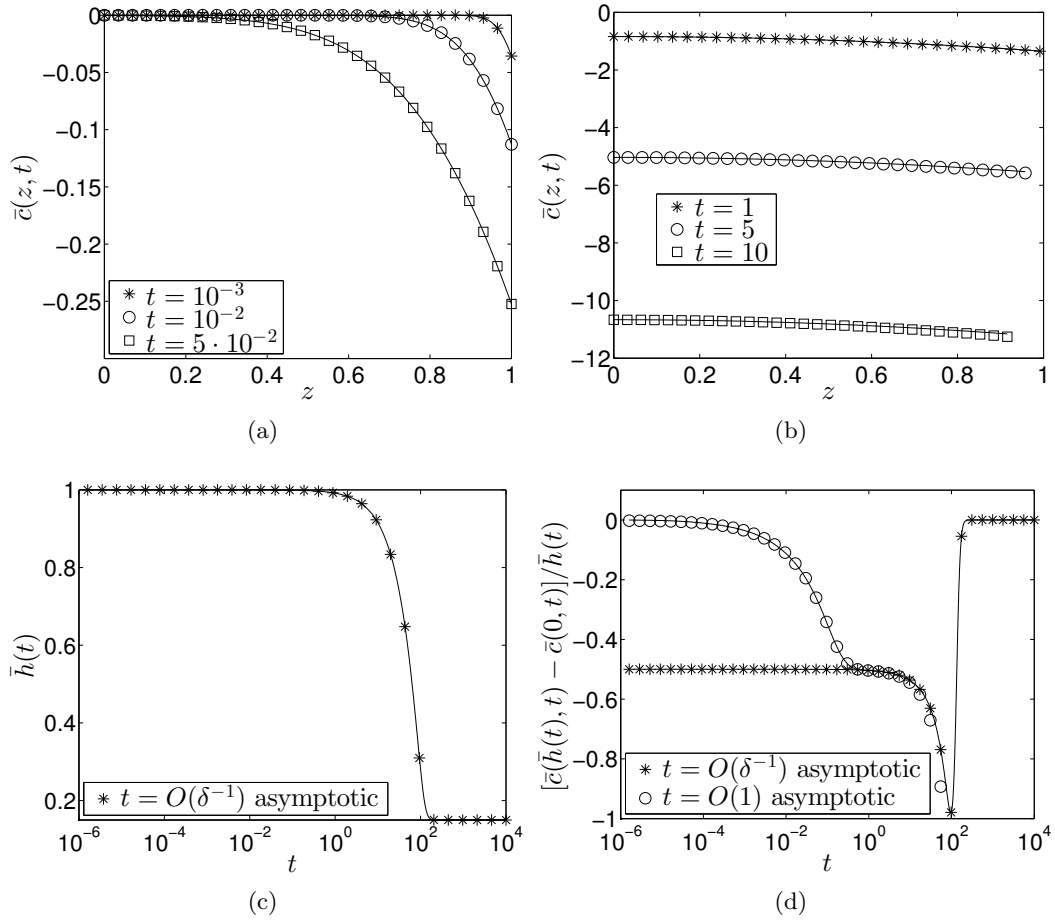


Figure 2.3: Numerical (solid lines) and asymptotic (symbols) solutions to the base state problem. (a): The short-term behaviour of the base state solvent volume fraction showing, in particular, the growth of a boundary layer from the surface of the fluid layer. (b): The quasi-static evolution of the solvent volume fraction. (c): The evolution of the film thickness. (d): The two time regimes and their regions of overlap are clearly shown by plotting the average concentration gradient across the film. The asymptotic solution in (2.27) is used in panel (a), whereas the $t = O(\delta^{-1})$ asymptotic solution given in (2.44) is used in panels (b)–(d). The $t = O(1)$ solution presented in (2.30) is denoted by open circles in panel (d). Parameter values are $\beta = 0.85$ and $\delta = 0.01$.

evolution. More specifically, we assume that the base state is given by the asymptotic solution in the $O(\delta^{-1})$ time regime for all times. The solution for the solvent volume fraction is written as

$$\bar{c}(z,\tau) = \delta^{-1}\left(\frac{\bar{h}(\tau)-1}{\beta\bar{h}(\tau)}\right) - \frac{1}{2}F(\tau)z^2 + \bar{c}_1(0,\tau) + O(\delta), \tag{2.44a}$$

where the function F, which gives a measure of the concentration gradient, is given by

$$F(\tau) = \frac{\bar{h}(\tau)-1+\beta}{\beta\bar{h}^3(\tau)}. \tag{2.44b}$$

The film thickness, $\bar{h}$, is given implicitly by (2.41).

As Figure 2.3 shows, the quasi-steady solution captures much of the base state evolution, even for $O(1)$ times, so neglecting the transient dynamics is not too unreasonable. Moreover, the slow evolution of this base-state solution can be exploited to study the linear stability problem using asymptotic methods for slowly varying systems. We note that considering only the quasi-steady solution is not inconsistent with a traditional linear stability analysis, where the system is typically linearised about a steady-state solution. Moreover, the effects of neglecting these transients will be discussed in Section 2.4.2.

2.3.2 Linear stability

The $O(\varepsilon)$ problem describes the linear stability of the base state. The perturbation to the horizontal velocity, $\tilde{u}$, can be eliminated from this problem via the $O(\varepsilon)$ incompressibility condition which reads $ik\tilde{u} + \partial_z\tilde{w} = 0$. The remaining bulk equations for this problem can be written as

$$-k^2\tilde{p} + \partial_z^2\tilde{p} = 0, \tag{2.45a}$$

$$-\partial_z\tilde{p} - k^2\tilde{w} + \partial_z^2\tilde{w} = 0, \tag{2.45b}$$

$$\partial_t\tilde{c} + \tilde{w}\partial_z\bar{c} = -k^2\tilde{c} + \partial_z^2\tilde{c}. \tag{2.45c}$$

These are subject to the boundary conditions on the substrate given by

$$\tilde{w} = \partial_z\tilde{w} = \partial_z\tilde{c} = 0, \quad z = 0. \tag{2.45d}$$

The corresponding boundary conditions at the free surface are linearised about the base state film thickness; therefore, we impose

$$\tilde{w} - \partial_t\tilde{h} = \delta^2\beta(1-\beta)[\tilde{c} + (\partial_z\bar{c})\tilde{h}], \qquad z = \bar{h}(\tau), \tag{2.45e}$$

$$(\partial_z^2\bar{c})\tilde{h} + \partial_z\tilde{c} = -\delta[1-2\beta-2\delta\beta(1-\beta)\bar{c}][\tilde{c} + (\partial_z\bar{c})\tilde{h}], \quad z = \bar{h}(\tau), \tag{2.45f}$$

$$-\tilde{p} + 2\partial_z\tilde{w} = -(k^2\mathrm{Ca}^{-1} + \mathrm{Ga})\tilde{h}, \qquad z = \bar{h}(\tau), \tag{2.45g}$$

$$\partial_z^2\tilde{w} + k^2\tilde{w} = -k^2\mathrm{Ma}[\tilde{c} + (\partial_z\bar{c})\tilde{h}], \qquad z = \bar{h}(\tau). \tag{2.45h}$$

The pressure disturbance $\tilde{p}$ can also be eliminated from this problem by combining (2.45a) and (2.45b) to yield $\tilde{p} = k^{-2}\partial_z^3\tilde{w} - \partial_z\tilde{w}$. This implies that (2.45b) can be written as

$$(\partial_z^2 - k^2)^2\tilde{w} = 0 \tag{2.46}$$

and the boundary condition (2.45g) becomes

$$-\partial_z^3\tilde{w} + 3k^2\partial_z\tilde{w} = -k^2(k^2\mathrm{Ca}^{-1} + \mathrm{Ga})\tilde{h}, \quad z = \bar{h}(\tau). \tag{2.47}$$

Initial conditions for the problem are given by

$$\tilde{c}(z,0) = \tilde{c}_i(z), \quad \tilde{h}(0) = \tilde{h}_i. \tag{2.48}$$

Throughout the remainder of the chapter, we neglect terms of $O(\delta)$ and higher that appear in the linear stability problem (2.45) and, in particular, in its boundary conditions. This is asymptotically consistent with using a solution for the base state that is $O(1)$ accurate.

2.3.2.1 Frozen-time analysis

In the frozen-time analysis, we treat the slow time τ as a parameter and not as a time variable. The interpretation of this approximation is that if the base state evolves slow enough, then it looks approximately constant in time. This can be made asymptotically rigorous by treating τ as a time variable, taking the limit $\delta \to 0$ with t fixed and $\tau = \tau' + \delta t$, and then considering the leading-order problem. Under this assumption the linear problem given in (2.45)–(2.47) becomes autonomous and the dynamics can be deduced from an eigenvalue analysis. Thus, we seek solutions of the form

$$\tilde{w}(z,t) = \hat{w}(z;\tau)e^{\lambda(\tau)t}, \tag{2.49a}$$

$$\tilde{c}(z,t) = \hat{c}(z;\tau)e^{\lambda(\tau)t}, \tag{2.49b}$$

$$\tilde{h}(t) = \hat{h}(\tau)e^{\lambda(\tau)t}, \tag{2.49c}$$

where λ is an eigenvalue corresponding to the instantaneous growth rate of the disturbances at time τ. Inserting (2.49) into (2.45)–(2.47), using (2.22) for the base state, and neglecting the $O(\delta)$ terms yields the eigenvalue problem given by

$$(\partial_z^2 - k^2)^2\hat{w} = 0, \tag{2.50a}$$

$$\lambda\hat{c} - Fz\hat{w} = -k^2\hat{c} + \partial_z^2\hat{c}, \tag{2.50b}$$

where the τ dependence of λ and F has not been written for brevity. Boundary conditions for this problem are

$$\hat{w} = \partial_z\hat{w} = \partial_z\hat{c} = 0, \quad z = 0, \tag{2.50c}$$

at the substrate and

$$\hat{w} - \lambda\hat{h} = 0, \qquad z = \bar{h}(\tau), \tag{2.50d}$$

$$-F\hat{h} + \partial_z\hat{c} = 0, \qquad z = \bar{h}(\tau), \tag{2.50e}$$

$$-\partial_z^3\hat{w} + 3k^2\partial_z\hat{w} = -k^2(k^2\mathrm{Ca}^{-1} + \mathrm{Ga})\hat{h}, \quad z = \bar{h}(\tau), \tag{2.50f}$$

$$\partial_z^2\hat{w} + k^2\hat{w} = -\mathrm{Ma}\,k^2(\hat{c} - F\bar{h}\hat{h}), \qquad z = \bar{h}(\tau), \tag{2.50g}$$

at the linearised free surface.

To simplify the eigenvalue problem in (2.50), we rescale the variables and parameters according to

$$z = \bar{h}(\tau)\zeta, \qquad k = \bar{h}(\tau)^{-1}a, \quad \lambda = \bar{h}(\tau)^{-2}\sigma, \tag{2.51a}$$

$$\hat{w} = F(\tau)^{-1}\bar{h}(\tau)^{-3}\check{w}, \quad \hat{c} = \check{c}, \qquad \hat{h} = F(\tau)^{-1}\bar{h}(\tau)^{-1}\check{h}. \tag{2.51b}$$

The corresponding rescaled eigenvalue problem is given by

$$(\partial_\zeta^2 - a^2)^2\check{w} = 0, \tag{2.52a}$$

$$\sigma\check{c} - \zeta\check{w} = -a^2\check{c} + \partial_\zeta^2\check{c}. \tag{2.52b}$$

The boundary conditions along the substrate read

$$\check{w} = \partial_\zeta\check{w} = \partial_\zeta\check{c} = 0, \quad \zeta = 0, \tag{2.52c}$$

and at the surface we have

$$\check{w} - \sigma\check{h} = 0, \qquad \zeta = 1, \tag{2.52d}$$

$$-\check{h} + \partial_\zeta\check{c} = 0, \qquad \zeta = 1, \tag{2.52e}$$

$$-\partial_\zeta^3\check{w} + 3a^2\partial_\zeta\check{w} = -a^2(a^2C^{-1} + G)\check{h}, \quad \zeta = 1, \tag{2.52f}$$

$$\partial_\zeta^2\check{w} + a^2\check{w} = -a^2M(\check{c} - \check{h}) \qquad \zeta = 1. \tag{2.52g}$$

The numbers M, C, and G that appear in the boundary conditions denote effective, time-dependent non-dimensional numbers given by

$$M = F(\tau)\bar{h}^3(\tau)\mathrm{Ma}, \quad C = \bar{h}(\tau)^{-1}\mathrm{Ca}, \quad G = \bar{h}^3(\tau)\mathrm{Ga}. \tag{2.53}$$

When $\tau = 0$ these numbers are equivalent to the original non-dimensional parameters Ma, Ca, and Ga.

The τ dependence now enters this problem through the rescaled wavenumber a and the effective non-dimensional numbers G, C, and M. Thus, understanding how the stability of the base state evolves under changes in τ is equivalent to understanding how the eigenvalue

σ changes with a, G, C, and M. From the rescaling in (2.53) and the definition of F in (2.44b), we have that the effective Marangoni number M monotonically decreases to zero as $\bar{h} \to 1-\beta$. Thus, the destabilising Marangoni stresses weaken as the system evolves and we expect that the system will eventually stabilise.

An examination of (2.52) shows that the problem for the vertical velocity $\check{w}$ decouples from the solvent problem; thus, it can be solved, in principle, to find

$$\check{w}(\zeta) = W_c(\zeta)\check{c}(1) + W_h(\zeta)\check{h}, \tag{2.54}$$

where W_c and W_h are complicated functions of ζ, the parameters, and the wavenumber a. This solution can be inserted into the bulk equation for the solvent volume fraction (2.52b) and the corresponding eigenvalue problem reduces to

$$\sigma\check{c} = \zeta W_c(\zeta)\check{c}(1) + \zeta W_h(\zeta)\check{h} - a^2\check{c} + \partial_\zeta^2\check{c}, \tag{2.55a}$$

$$\sigma\check{h} = W_c(1)\check{c}(1) + W_h(1)\check{h}, \tag{2.55b}$$

subject to the boundary conditions

$$\partial_\zeta\check{c} = 0, \quad \zeta = 0, \tag{2.55c}$$

$$\partial_\zeta\check{c} - \check{h} = 0, \quad \zeta = 1. \tag{2.55d}$$

The characteristic equation that determines the eigenvalues can, in theory, be obtained by integrating (2.55a) and imposing the relevant conditions. However, there is a more direct route to obtaining the characteristic equation using the adjoint eigenvalue problem. In particular, it is relatively straightforward to show that the eigenvalues σ satisfy the relation

$$\begin{aligned}[W_h(1;a) - \sigma]\left[\chi_c(\sigma;a) - \sqrt{a^2+\sigma}\sinh(\sqrt{a^2+\sigma})\right] \\ -W_c(1;a)\left[\cosh(\sqrt{a^2+\sigma}) + \chi_h(\sigma;a)\right] = 0,\end{aligned} \tag{2.56a}$$

where the functions χ_c and χ_h are defined as

$$\chi_c(\sigma;a) := \int_0^1 \zeta W_c(\zeta;a)\cosh(\sqrt{a^2+\sigma}\zeta)\,d\zeta, \tag{2.56b}$$

$$\chi_h(\sigma;a) := \int_0^1 \zeta W_h(\zeta;a)\cosh(\sqrt{a^2+\sigma}\zeta)\,d\zeta. \tag{2.56c}$$

Details of the adjoint problem and the calculation of the characteristic equation are given in Appendix A.2. In practice, this highly nonlinear equation is solved numerically. However, it is possible to obtain asymptotic solutions to the eigenvalue problem when $a \ll 1$ and this will be discussed further below.

2.3.2.2 Asymptotic analysis

If the base state is "unfrozen" so that τ is treated properly as a time variable, then it is possible to construct an asymptotic solution to the non-autonomous linear stability problem (2.45) using the method of multiple scales [91] or using the WKB approximation [12]. These solutions will be uniformly valid over long periods of time. Both cases begin by first eliminating $\tilde{w}$ so that (2.45) (without its $O(\delta)$ and higher contributions) reduces to an evolution problem of the form

$$\partial_t \tilde{U} = L(\tau)\tilde{U}, \tag{2.57}$$

where L is a slowly varying linear operator and $\tilde{U}(z,t) = [\tilde{c}(z,t), \tilde{h}(t)]^T$. We write the boundary conditions as $B(\tau)\tilde{U} = 0$, where B denotes a linear boundary operator, and the initial conditions as $\tilde{U}(z,0) = \tilde{U}_i(z) = [\tilde{c}_i(z), \tilde{h}_i]^T$.

The two different asymptotic treatments of this problem are given in Appendix A.1 so the details will not be presented here. The results of the two methods are the same, and in both cases the solution $\tilde{U}$ is written as an eigenfunction expansion of the form

$$\tilde{U}(z,t) = \sum_{l=1}^{\infty} \alpha_l(t) v_l(z;\tau), \tag{2.58}$$

where v_l denotes the l-th eigenfunction which satisfies

$$L(\tau)v_l = \lambda_l(\tau)v_l, \tag{2.59}$$

with $B(\tau)v_l = 0$ on the boundary. The normalisation of these eigenfunctions will be discussed below and the eigenvalues are labelled according to the size of their real part: $\mathrm{Re}\{\lambda_1\} > \mathrm{Re}\{\lambda_2\} > \ldots > \mathrm{Re}\{\lambda_n\}$ as $n \to \infty$. Note that the eigenvalues and eigenfunctions of (2.59) exactly correspond to those of the original frozen-time problem (2.50).

The asymptotic expression for the coefficients α_l in (2.58) is given by

$$\begin{aligned}\alpha_l(t) = \alpha_{li} e^{T_l(t)} &+ \delta \sum_{j \neq l}^{\infty} \frac{\alpha_{ji}\gamma_{lj}(\tau)}{\lambda_j(\tau) - \lambda_l(\tau)} e^{T_j(t)} \\ &+ \delta \sum_{j \neq l}^{\infty} \left[\alpha_{li} \int_0^{\tau} \frac{\gamma_{lj}(s)\gamma_{jl}(s)}{\lambda_l(s) - \lambda_j(s)} \,\mathrm{d}s - \frac{\alpha_{ji}\gamma_{lj}(0)}{\lambda_j(0) - \lambda_l(0)} \right] e^{T_l(t)} + O(\delta^2),\end{aligned} \tag{2.60}$$

where the T_l represent additional fast and slow times defined as

$$T_l(t) = \delta^{-1} \int_0^{\delta t} [\lambda_l(s) + \delta\gamma_{ll}(s)] \,\mathrm{d}s, \quad l = 1, 2, \ldots. \tag{2.61}$$

Furthermore, α_{li} denotes the initial value of α_l, defined as $\alpha_{li} = \langle v_l^\dagger, \tilde{U}_i \rangle^*(0)$, and the γ_{jl} are related to the slow-time derivatives of the eigenfunctions,

$$\gamma_{jl}(\tau) = -\langle v_j^\dagger, \partial_\tau v_l \rangle^*(\tau). \tag{2.62}$$

Here, the star denotes complex conjugation, $v_j^\dagger$ is the j-th adjoint eigenfunction, and $\langle \cdot, \cdot \rangle$ is the τ-dependent inner product which is defined for two functions $\hat{U}_j = [\hat{c}_j(z), \hat{h}_j]^T$, $j = 1, 2$, as

$$\langle \hat{U}_1, \hat{U}_2 \rangle(\tau) = \int_0^{\bar{h}(\tau)} \hat{c}_1(z)\hat{c}_2^*(z)\,\mathrm{d}z + F^2(\tau)\bar{h}^3(\tau)\hat{h}_1\hat{h}_2^*. \tag{2.63}$$

This unusual choice of inner product is made because it allows the rescaled frozen-time eigenfunctions in (2.52) to be used in the calculation of inner products instead of the original eigenfunctions in (2.50). This can be seen by transforming the functions $\hat{U}_1$ and $\hat{U}_2$ in (2.63) into two new functions, $\check{U}_j = [\check{c}_j(\zeta), \check{h}_j]^T$, $j = 1, 2$, using the rescaling in (2.51). The inner product in (2.63) can then be written as

$$\langle \hat{U}_1, \hat{U}_2 \rangle(\tau) = \bar{h}(\tau) \left[\int_0^1 \check{c}_1(\zeta)\check{c}_2^*(\zeta)\,d\zeta + \check{h}_1\check{h}_2^* \right]. \tag{2.64}$$

The rationale behind this approach is that it is computationally advantageous to use the rescaled eigenfunctions instead of the original ones.

With the inner product defined we can state the normalisation conditions for the eigenfunctions and their adjoints. These are given by

$$\langle v_l, v_l \rangle(\tau) \equiv 1, \quad \langle v_k^\dagger, v_l \rangle(\tau) \equiv \delta_{kl}, \tag{2.65}$$

where δ_{kl} denotes the Kronecker delta.

The expansion given in (2.58) and the approximation in (2.60) constitute an asymptotic solution to the linear problem given in (2.57). This solution is expected to be valid so long as the eigenvalues remain well separated. Merging or crossing of the eigenvalues requires a separate asymptotic treatment and we do not consider this case here.

2.3.3 Chapter outlook

We now have all of the machinery that is required to study the dynamics of the evaporating fluid layer. The proceeding discussion will be separated into two cases depending on whether the fluid surface is taken to be deformable or not. More specifically, we first explore the case when the surface is non-deformable, using this as a test problem to understand how a slowly varying base state can influence the stability of the system and to explore the properties of the asymptotic solution. Having established this, we then analyse the more realistic and complicated scenario involving a deformable fluid surface.

2.4 Dynamics with a non-deformable fluid surface

The example parameter values taken from the experiments of Bassou and Rharbi [8] indicate that the capillary number is small and the Galileo number is large. An examination of the normal-stress boundary condition written in (2.52f) shows that when this is the case, the perturbation to the film thickness $\check{h}$ is expected to be very small provided the wavenumbers a are sufficiently large. Thus, we assume the film is non-deformable and set $\check{h} = 0$. Strictly speaking, the subsequent analysis is only valid for wavenumbers that are $O(1)$ in size or larger. However, as we are considering this as a test problem, we ignore this fact and allow a to be unrestricted in the values it can take. A proper treatment of the small-wavenumber limit is given in the next section.

The analysis of this problem is split into two main parts. First, the frozen-time method is used to explore the instantaneous stability of the problem as the slow time τ changes parametrically. Then, the stability of the base state over long periods of time will be examined using the asymptotic solution presented in Section 2.3.2.2. The results from both of these methods will then be compared and connected.

2.4.1 Frozen-time analysis

When the surface is non-deformable, the eigenvalue problem presented in (2.52) can be simplified slightly. By taking $\check{h} = 0$, the corresponding problem for the fluid velocity $\check{w}$ can be written as

$$(\partial_\zeta^2 - a^2)^2 \check{w} = 0, \tag{2.66a}$$

subject to the conditions

$$\check{w} = 0, \qquad \zeta = 0, 1, \tag{2.66b}$$

$$\partial_\zeta \check{w} = 0, \qquad \zeta = 0, \tag{2.66c}$$

$$\partial_\zeta^2 \check{w} = -a^2 M \check{c}, \quad \zeta = 1. \tag{2.66d}$$

The solution to this problem can be written as $\check{w}(\zeta) = W_c(\zeta; a)\check{c}(1)$, where

$$W_c(\zeta; a) = B_1 \zeta \cosh(a\zeta) + (B_2 \zeta - B_1/a) \sinh(a\zeta), \tag{2.67a}$$

and the coefficients B_1 and B_2 are given by

$$B_1 = -a^2 M \left(\frac{\sinh(a)}{\sinh(2a) - 2a} \right), \quad B_2 = aM \left(\frac{a\cosh(a) - \sinh(a)}{\sinh(2a) - 2a} \right). \tag{2.67b}$$

In the case of non-deformable surface, the expression for the eigenvalues in (2.56) reduces to

$$\int_0^1 \zeta W_c(\zeta;a)\cosh(\sqrt{a^2+\sigma}\zeta)\,\mathrm{d}\zeta = \sqrt{a^2+\sigma}\sinh(\sqrt{a^2+\sigma}), \tag{2.68}$$

with W_c given in (2.67).

To gain some insight into the structure of the eigenvalues, we first examine their behaviour when the wavenumber a is small. From (2.67), it follows that

$$W_c(\zeta;a) = \frac{1}{4}a^2 M\zeta^2(1-\zeta) + O(a^4) \tag{2.69}$$

for $a \ll 1$. If we assume that $\sigma = O(1)$, then naively taking $a \to 0$ in (2.68) yields the leading-order problem given by $\sinh(\sqrt{\sigma}) = 0$. The solutions of this equation are $\sigma = -n^2\pi^2$ where n is an integer. These eigenvalues correspond to linearly stable modes. However, a distinguished limit emerges by taking $\sigma = O(a^2)$ as $a \to 0$ in the characteristic equation (2.68). Thus, by scaling σ with a^2 and carrying out the appropriate expansions and integration, it is straightforward to show that

$$\sigma = a^2\left(\frac{M}{80} - 1\right) + O(a^4). \tag{2.70}$$

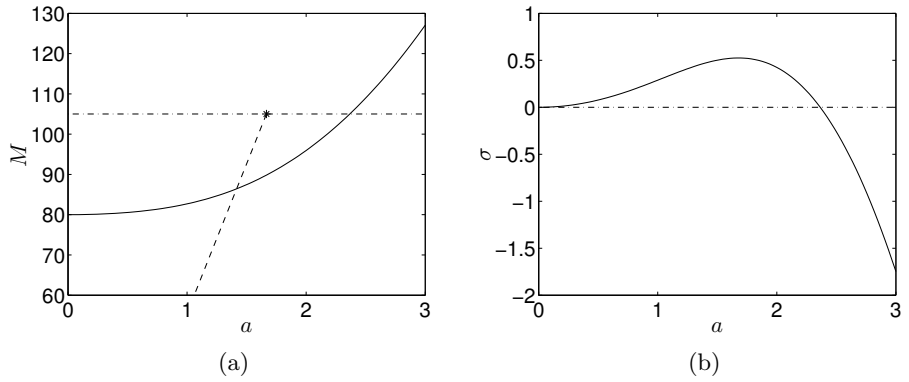
We will refer to the eigenvalue in (2.70) as the top eigenvalue because it has the largest real part. This will be a terminology that is used throughout the remainder of the chapter. We can conclude from this analysis that the long-wave eigenvalues are real when the surface is non-deformable. Furthermore, the top eigenvalue becomes positive as the Marangoni number is increased beyond 80 which indicates the onset of a stationary mode of instability.

To investigate the onset of the stationary instability over larger wavenumbers, we compute curves in parameter space for which the real part of the top eigenvalue is equal to zero. In time-independent stability problems, these curves are referred to as neutral stability curves and we adopt the same terminology in this chapter. The neutral stability curves separate parameter space into regions where the real part of the top eigenvalue is either positive or negative. In the context of the frozen-time analysis, they can be used to identify regions of parameter space where the base state is instantaneously stable or unstable.

The neutral stability curves are written as $M = M(a)$. In this form, they describe the Marangoni number that must be exceeded for a perturbation to the base state with wavenumber a to grow. Alternatively, for a given value of M, these curves enable one to determine the wavenumbers of any growing perturbations.

The stationary neutral stability curves associated with a top eigenvalue that is equal to zero can be computed by setting $\sigma = 0$ in (2.68) and carrying out the integration to yield

$$M = \frac{12a^3(\sinh 2a - 2a)}{3a\cosh a\sinh a - (2a^2+3)a^2 - 3\sinh^2 a + 3a^3\coth a}. \tag{2.71}$$



(a) (b)

Figure 2.4: Left (a): The neutral stability curve (solid) traces out a path in parameter space where the top frozen-time eigenvalue is equal to zero. The top eigenvalue is positive and negative above and below this curve, respectively. Therefore, the neutral stability curve defines the boundary between stable and unstable regions of parameter space. Here, M and a denote the rescaled Marangoni number and wavenumber, respectively; see (2.51) and (2.53). The dashed line gives an example of how these effective parameters change from their initial values (denoted by the star) as the slow time τ increases. Right (b): The top frozen-time eigenvalue σ as a function of the rescaled wavenumber a when $\tau = 0$ and $M = 105$. These parameters correspond to the dashed-dot line shown in panel (a).

For $a \ll 1$, this curve can be approximated by

$$M = 80 + \frac{128}{63}\, a^2 + O(a^4); \tag{2.72}$$

thus, it is a locally increasing function of a. To examine the behaviour over larger values of the wavenumber, we plot this function as shown in Figure 2.4 (a). The curve monotonically increases from its minimum value of $M_s = 80$ when $a = 0$. This minimum defines a critical value of the Marangoni number that separates unstable from stable regions of parameter space. For Marangoni numbers that are larger than M_s, there is a band of wavenumbers given by $0 < a < a_1(M)$ such that the top eigenvalue is positive and the base state is unstable. For Marangoni numbers that satisfy $M < M_s$, the top eigenvalue is negative and the system is always linearly stable.

An example of the top eigenvalue as a function of the wavenumber is shown in Figure 2.4 (b) when $M = 105 > M_s$. The eigenvalue is real and it has a maximum when $a \simeq 1.67$. In traditional stability problems with stationary base states, the fastest-growing perturbation generally corresponds to the dominant mode, *i.e.*, the Fourier mode with the largest amplitude. This mode often has physical manifestations, as it corresponds to the one that is usually observed in reality. Furthermore, the wavenumber of the dominant mode is responsible for setting the geometrical aspects of the instability before nonlinear effects become important. In time-dependent stability problems, however, this is not necessarily the case. The slow evolution of the eigenvalues means that the wavenumber of the dominant mode at a time τ does not have to be equal to the wavenumber of fastest-growing perturbation

at that instance. Dziwnik *et al.* [59] discuss this further in the context of dewetting films, where they are able to explicitly track the evolution of the dominant wavenumber.

The stability of the base state is ultimately related to the physically meaningful variables, which in this problem are Ma and k. When $\tau = 0$, the relations $\mathrm{Ma} = M$ and $k = a$ hold true from (2.51) and (2.53); thus, the neutral stability curve shown in Figure 2.4 (a) provides a good indication of the initial stability of the system. To examine temporal changes in the stability, we consider the original neutral stability curves, which are of the form $\mathrm{Ma} = \mathrm{Ma}(k)$. Using (2.51) and (2.53), we see that these curves can be parameterised by τ and written as

$$\mathrm{Ma}(k;\tau) = \left(\frac{\beta}{\bar{h}(\tau) - 1 + \beta}\right) M(\bar{h}(\tau)k), \tag{2.73}$$

where M is given by (2.71). Therefore, the τ-dependent neutral stability curves are just stretched and scaled versions of the "master" curve $M = M(a)$. For a given τ, the unstable region will be that which lies above the curve defined in (2.73). Since $\bar{h} \searrow 1 - \beta$ as $\tau \to \infty$, the neutral stability curve moves upwards in the (k, Ma) plane indefinitely. Regardless of the Marangoni number, there will always be a time τ at which the value of Ma lies below the neutral stability curve. After this point, the system is expected to stabilise.

There is an alternative approach for assessing how the stability changes in time using the neutral stability curve shown in Figure 2.4 (a). This entails choosing a fixed value of Ma and k, corresponding to a point in this figure, and then plotting the paths that are traced out as the effective parameters M and a vary with τ. These paths turn out to be straight lines given by

$$M(a) = \left(\frac{\mathrm{Ma}}{\beta k}\right) a - \left(\frac{1-\beta}{\beta}\right) \mathrm{Ma}, \tag{2.74}$$

where $a(\tau = 0) = k$ and $a(\tau \to \infty) = (1 - \beta)k$ can be used to define the start and end of the curve. An example path for $\mathrm{Ma} = 105$ and $k = 1.67$ is shown as a dashed line in Figure 2.4 (a). This point starts in the unstable region but, as τ increases, the path crosses the neutral stability curve to enter the stable regime. The precise time when this happens is $\tau \simeq 0.18$, after which the perturbation is expected to start decaying.

2.4.2 Asymptotic analysis

The benefit of the frozen-time method is that it facilitates the identification of regions in parameter space where an instability occurs, at least locally in time. This corresponds to perturbations that exhibit a transient period of growth. The shortcoming of this method, however, is that it cannot be used to directly infer how large these perturbations grow before

the system begins to stabilise. This is important information to have when attempting to assess how relevant an instability may be.

We now use refined methods to study the evolution of perturbations in more detail. More specifically, we track the long-term changes that occur in the perturbation amplification using the asymptotic solution from Section 2.3.2.2 and by numerically solving (2.57) as an initial value problem. The numerical scheme is similar to the one used for approximating solutions to the base state; space is discretised using second-order finite differences and the resulting problem is treated as a system of ordinary differential equations. We use the large-time asymptotic solution for the base state (2.44) in the numerical solution of the linearised problem to be consistent with our previous analysis. The effects of using the full base state with fast transient dynamics will be briefly discussed further below. The amplification of a perturbation, A, is defined according to

$$A(t) = \frac{\|\tilde{U}(z,t)\|}{\|\tilde{U}_i(z)\|}, \tag{2.75}$$

where $\|\cdot\|^2 = \langle\cdot,\cdot\rangle$ defines a norm using the inner product in (2.63), $\tilde{U}$ is the solution to the linearised problem that is computed numerically or asymptotically using (2.58) and (2.60), and $\tilde{U}_i$ is the initial condition. We will use the notation A_{asy} and A_{num} to describe amplifications that have been computed using the asymptotic and numerical solutions for $\tilde{U}$, respectively.

We first consider the case when the initial condition is in the form of the top eigenfunction, that is, the eigenfunction associated with the top eigenvalue. This choice is expected to produce near-maximal amplifications by minimising contributions from sub-dominant modes. Numerical experimentation has given evidence to suggest that the eigenvalues are real when the surface is non-deformable. Thus, we consider only the top mode associated with the largest eigenvalue in the asymptotic solution for $\tilde{U}$. Under these assumptions, this solution simplifies to

$$\tilde{U}(z,t) = v_1(z;\delta t)\exp\left\{\delta^{-1}\int_0^{\delta t}\left[\lambda_1(s) + \delta\gamma_{11}(s)\right]\,\mathrm{d}s\right\}. \tag{2.76}$$

By making use of the normalisation condition for the eigenfunctions in (2.65) and using the assumption that the eigenvalues are real, the associated amplification can be written as

$$A_{\text{asy}}(t) = \exp\left\{\delta^{-1}\int_0^{\delta t}\left[\lambda_1(s) + \delta\gamma_{11}(s)\right]\,\mathrm{d}s\right\}. \tag{2.77}$$

We also explore the amplifications produced by an asymptotic solution that does not consider the self-coupling term γ_{11}. Such a solution takes the intuitive form given by

$$\tilde{U}^{(0)}(z,t) = v_1(z;\delta t)\exp\left[\delta^{-1}\int_0^{\delta t}\lambda_1(s)\,\mathrm{d}s\right], \tag{2.78}$$

and we write its corresponding amplification as $A^{(0)}_{\text{asy}}(t)$, where

$$A^{(0)}_{\text{asy}}(t) = \exp\left[\delta^{-1}\int_0^{\delta t}\lambda_1(s)\,\mathrm{d}s\right]. \tag{2.79}$$

By differentiating this expression with respect to time, we see that the maximum amplification is obtained when the top eigenvalue is equal to zero. This establishes a "leading-order" connection between the frozen-time eigenvalues and the stability of slowly evolving systems: positive and negative eigenvalues correspond to growing and decaying perturbations, respectively. Thus, the conventional relationship between eigenvalues and stability is recovered, at least when the small contribution from the γ_{11} term is neglected.

We first explore the dynamics that occur when the perturbation wavenumber is small. In this case, the eigenvalue λ_1 can be written using the asymptotic expression in (2.72) to yield

$$\lambda_1(\tau) = k^2\left(\frac{\bar{h}(\tau)-1+\beta}{\beta}\frac{\mathrm{Ma}}{80}-1\right)+O(k^4), \tag{2.80}$$

for $k \ll 1$. The quadratic leading-order dependence of the eigenvalue on the wavenumber means that perturbations are expected to grow slowly in this regime. Thus, there is a limit on how small the wavenumber can be in order for the separation of time scales between the base state and the perturbations to be maintained; in particular, we require $\delta^{1/2} \ll k \ll 1$.

Is it relatively straightforward to show that the leading-order top eigenfunction and its adjoint can be written, after suitable normalisation, as

$$v_1(z;\tau) = v_1^\dagger(z;\tau) \equiv \frac{1}{\bar{h}^{1/2}(\tau)}. \tag{2.81}$$

Using these, the self-coupling γ_{11} term can be computed. We find that

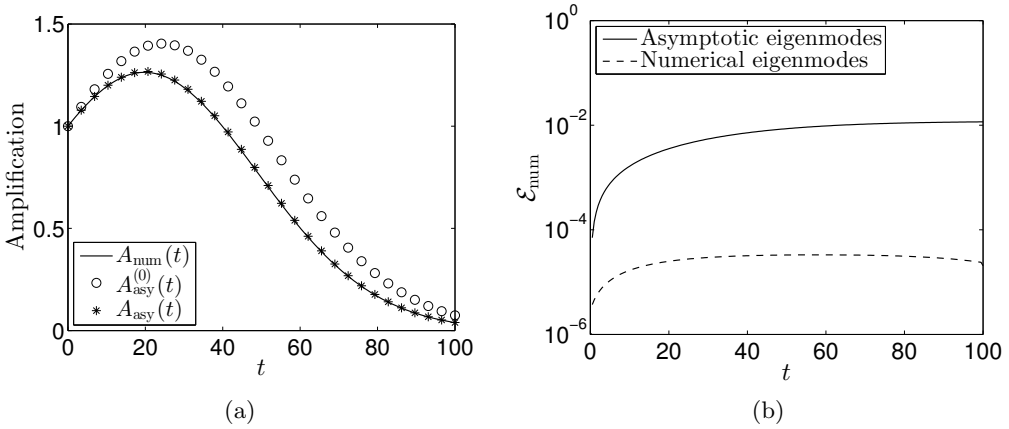
$$\gamma_{11}(\tau) = \frac{1}{2\bar{h}(\tau)}\frac{\mathrm{d}\bar{h}}{\mathrm{d}\tau} = -\frac{\bar{h}(\tau)-1+\beta}{2\bar{h}^2(\tau)}. \tag{2.82}$$

The integrals in the exponentials of (2.77) and (2.79) can be evaluated explicitly by making the change of variable $\eta = \bar{h}(s)$. The corresponding amplifications are given by

$$A_{\text{asy}}(t) = \bar{h}^{1/2}(\delta t)\exp\left\{-k^2 t + \frac{1}{160}\frac{k^2\mathrm{Ma}}{\delta\beta}\left[1-\bar{h}^2(\delta t)\right]\right\}, \tag{2.83a}$$

$$A^{(0)}_{\text{asy}}(t) = \exp\left\{-k^2 t + \frac{1}{160}\frac{k^2\mathrm{Ma}}{\delta\beta}\left[1-\bar{h}^2(\delta t)\right]\right\}. \tag{2.83b}$$

Examples of these functions for the parameter values of $\beta = 0.85$, $k = 0.3$, $\mathrm{Ma} = 105$, and $\delta = 0.01$ are shown in Figure 2.5 (a). All of the amplifications show an initial period of growth, followed by an indefinite period of decay. The two asymptotic amplifications are in good qualitative agreement with each other and with the numerical amplification. The



(a) (b)

Figure 2.5: Left (a): Amplification of a long-wavelength perturbation by the stationary Marangoni instability. The asymptotic amplifications, $A_{\rm asy}$ and $A^{(0)}_{\rm asy}$, are defined in (2.83a) and (2.83b), respectively. The numerical amplification is computed from time-stepping the linearised problem. Right (b): The relative error between the numerical and asymptotic solution defined according to (2.87). The initial condition was taken to be the top eigenfunction and the parameters are Ma = 105, $k = 0.3$, $\beta = 0.85$, and $\delta = 0.01$.

quantitative match between the asymptotic amplification given by (2.83a) and the numerical amplification is remarkable, considering the former is based on approximate expressions for the top eigenvalue and eigenfunctions.

The relative error between the asymptotic amplifications in (2.83), written in terms of the slow time τ, is given by

$$\mathcal{E}(\tau) = \frac{1 - \bar{h}^{1/2}(\tau)}{\bar{h}^{1/2}(\tau)}. \tag{2.84}$$

This error grows monotonically with time, corresponding to the cumulative effects of neglecting the γ_{11} term, and has a limiting value given by

$$\mathcal{E}(\tau \to \infty) = \frac{1 - (1-\beta)^{1/2}}{(1-\beta)^{1/2}}, \tag{2.85}$$

which can become $O(1)$ and larger if β is close to one. Moreover, for a fixed value of τ, the accuracy of the amplification approximation given by (2.79) cannot be improved by simply reducing δ, assuming that the base-state thickness $\bar{h}$ is exact. This is true even in the general sense, as the relative error between (2.77) and (2.79) is given by

$$\mathcal{E}(\tau) = \left| 1 - \exp\left[- \int_0^\tau \gamma_{11}(s)\, \mathrm{d}s \right] \right|. \tag{2.86}$$

Thus, the self-coupling term γ_{11} is particularly important when using the asymptotic solutions to obtain quantitatively accurate estimates of the amplification of perturbations.

The relative error between the numerical and asymptotic amplification is defined as

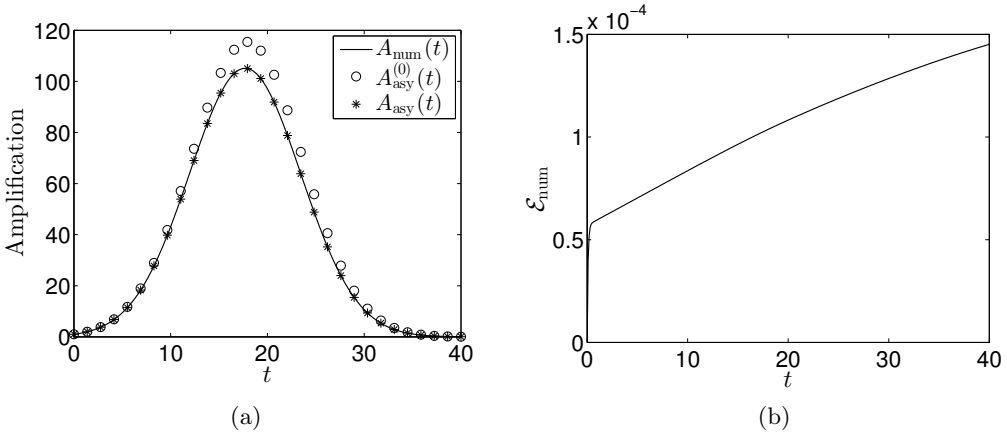
$$\mathcal{E}_{\text{num}}(t) = \frac{|A_{\text{num}}(t) - A_{\text{asy}}|}{A_{\text{num}}}. \tag{2.87}$$

For long-wavelength perturbations, we examine this error using two forms of A_{asy}. The first is constructed using the asymptotic expressions for the eigenvalues and eigenfunctions, and is given by (2.83a). The second uses (2.77) with eigenvalues and eigenvectors that have been computed numerically. The corresponding errors are plotted in Figure 2.5 (b) using the same parameter values as above. This figure shows that the asymptotic amplification constructed from the approximate solution of the eigenvalue problem provides an accurate quantitative description of the fully numerical amplification. The error remains of size $O(\delta)$, which would be expected if the eigenvalue and the self-coupling term were exact. However, the approximation of the eigensolution introduces additional errors into the asymptotic amplification (2.83a). When $\delta^{1/2} \ll k$, the majority of this error comes from approximating the top eigenvalue λ_1. We can estimate the errors introduced by this approximation by calculating the quantity $|1 - \exp(-I)|$, where

$$I = \delta^{-1} \int_0^{\delta t} [\lambda_{\text{num}}(s) - \lambda_{\text{asy}}(s)] \, \mathrm{d}s. \tag{2.88}$$

This estimate is based on the relative error between asymptotic amplifications that use numerical and asymptotic top eigenvalues, λ_{num} and λ_{asy}, respectively, and which neglect contributions from the γ_{11} terms. When calculating I, we take λ_{asy} to be the leading-order part of (2.80). We find that the error due to approximating the top eigenvalue grows monotonically from roughly 10^{-3} to 10^{-2}. This is close to the $O(\delta)$ amount of error that is expected from using a simplified form of the asymptotic solution given in (2.76). Thus, to determine whether the main source of error in the amplification given by (2.83a) is from the long-wave approximation of the eigenvalue or the asymptotic approximation of the solution $\tilde{U}$, we examine the relative error $\mathcal{E}_{\text{num}}$ using an asymptotic amplification A_{asy} based on numerical eigensolutions. This error is shown as a dashed line in Figure 2.5 (b). From this, it can be seen that using a numerical eigensolution reduces the relative error by nearly three orders of magnitude. Thus, the accuracy in the fully asymptotic amplification (2.83a) is limited by the long-wavelength approximation rather than the form of the approximate solution to the linearised problem.

We now consider the dynamics for larger wavenumbers, keeping the other parameter values the same. In this case, the eigenvalues, the eigenfunctions, and their adjoints must be computed numerically for each value of the slow time τ. The initial condition is still chosen to be the top eigenfunction when $\tau = 0$ and only the dynamics of the top mode are considered. We choose $\mathrm{Ma} = 105$ and $k = 1.67$ so that the evolution of the system follows



(a) (b)

Figure 2.6: Amplification of a short-wavelength perturbation by the stationary Marangoni instability. Left (a): Comparison of the asymptotic and numerical amplifications. The asymptotic curves are based on the single-mode expressions in (2.77) and (2.79) with eigenvalues and eigenfunctions that have been computed numerically for each value of the slow time τ. Right (b): The relative error between the numerical and asymptotic solution defined according to (2.87). The initial condition was taken to be the top eigenfunction and the parameters are Ma = 105, $k = 1.67$, $\beta = 0.85$, and $\delta = 0.01$. For these parameter values, the system evolves according to the dashed line show in Figure 2.4 (a).

the path traced out in Figure 2.4 (a). This value of the wavenumber maximises the top eigenvalue when $\tau = 0$ so we expect to obtain near-maximal amplification of perturbations for this particular Marangoni number. Figure 2.6 (a) shows the amplifications as functions of time. Like before, there is an initial period of perturbation growth followed by decay. In this case, however, the perturbation is amplified by two orders of magnitude before the system stabilises, which may be large enough for the instability to be detectable in an experimental setting.

We find there is exceptional quantitative agreement between the full asymptotic approximation, $A_{\rm asy}$, and the numerical amplification. The relative error between these solutions, $\mathcal{E}_{\rm num}$, is shown in Figure 2.6 (b). After a rapid transient caused by neglecting sub-dominant modes in the asymptotic solution, the error increases at nearly a constant rate. Remarkably, the error is $O(\delta^2)$ in size, which is better than the $O(\delta)$ values that are expected.

The simplified asymptotic amplification $A^{(0)}_{\rm asy}$ shows good qualitative agreement with the other two, but there are minor quantitative discrepancies. The maximum amplifications of the asymptotic solutions occur at roughly the same time, $\tau_m \simeq 0.18$, with $\max\{A_{\rm asy}\} \simeq 105$, whereas $\max\{A^{(0)}_{\rm asy}\} \simeq 115$. The relative error between these maximum amplifications is about 9.86%. By numerically evaluating the relative error between the asymptotic amplifications in (2.86), we find that $\mathcal{E}(\tau_m) \simeq 9.88\%$, a near-perfect agreement, as should be expected. The time at which the maxima are obtained matches the value of τ at which the path in Figure 2.4 (a) crosses the neutral stability curve, highlighting the connection

between the frozen-mode analysis and the dynamics that are seen by solving the linearised problem directly.

To explore the $O(\delta)$ contributions to the asymptotic solution, we now consider a two-mode solution constructed from the largest and second-largest eigenmodes. To minimise the effects of mode-mixing, which would mask these small contributions, the initial condition is taken to be an eigenfunction. In particular, the top eigenfunction is chosen. In this case, the coefficients α_1 and α_2 in (2.58) can be written as

$$\alpha_1(t) = \left[1 + \delta \int_0^{\delta t} \frac{\gamma_{12}(s)\gamma_{21}(s)}{\lambda_1(s) - \lambda_2(s)}\,\mathrm{d}s\right] e^{T_1(t)} + O(\delta^2), \tag{2.89a}$$

$$\alpha_2(t) = \delta\left[\frac{\gamma_{21}(\delta t)}{\lambda_1(\delta t) - \lambda_2(\delta t)}\, e^{T_1(t)} - \frac{\gamma_{21}(0)}{\lambda_1(0) - \lambda_2(0)}\, e^{T_2(t)}\right] + O(\delta^2), \tag{2.89b}$$

where the fast times T_i are given by

$$T_i(t) = \delta^{-1} \int_0^{\delta t} \left[\lambda_i(s) + \delta\gamma_{ii}(s)\right]\,\mathrm{d}s, \quad i = 1, 2. \tag{2.89c}$$

Note that if we had not chosen an eigenfunction as the initial condition, there would be $O(1)$ contributions to both α_1 and α_2. Examples of these functions are shown in Figure 2.7 (a)–(b) for $k = 1.67$ and the same parameter values as above. Also shown are numerical approximations of α_1 and α_2. These are obtained by evaluating $\alpha_i = \langle v_i^\dagger, \tilde{U}\rangle$, $i = 1, 2$, at each time step, where $\tilde{U}$ in this case is a numerical solution to (2.57). The asymptotic approximations perfectly capture the qualitative and quantitative properties of the numerical solutions. The smallness of the contributions from the second mode, which at times are roughly four orders of magnitude smaller than those from the top mode, partly explains why the single-mode results presented above are so accurate.

To further explore the accuracy of the asymptotic expressions for α_1 and α_2 given in (2.89), we compute the relative errors based on comparisons with numerical solutions. These errors are shown 2.7 (c)–(d). Recalling that a value of $\delta = 10^{-2}$ was used in the simulation, we see that both errors are within their expected limits. In particular, relative error in the first coefficient, α_1, is $O(\delta^2)$. Since the second coefficient, α_2, is of $O(\delta)$ in size, the relative error is only expected to be of $O(\delta)$, which it is indeed.

We now explore the case when the initial perturbation is not in the form of a single eigenfunction. Accordingly, we use the functions

$$\tilde{c}_i(z) = 3\sqrt{70}\, z^2(1 - z)^2, \quad \tilde{h}_i = 0, \tag{2.90}$$

in the initial condition $\tilde{U}_i(z) = [\tilde{c}_i(z), \tilde{h}]^T$ for the linearised problem. The unusual multiplicative factor is merely a normalisation constant that is chosen in order for $\|\tilde{U}_i\| = 1$ to be true. This initial condition has components that lie along all of the eigenfunctions, the sizes

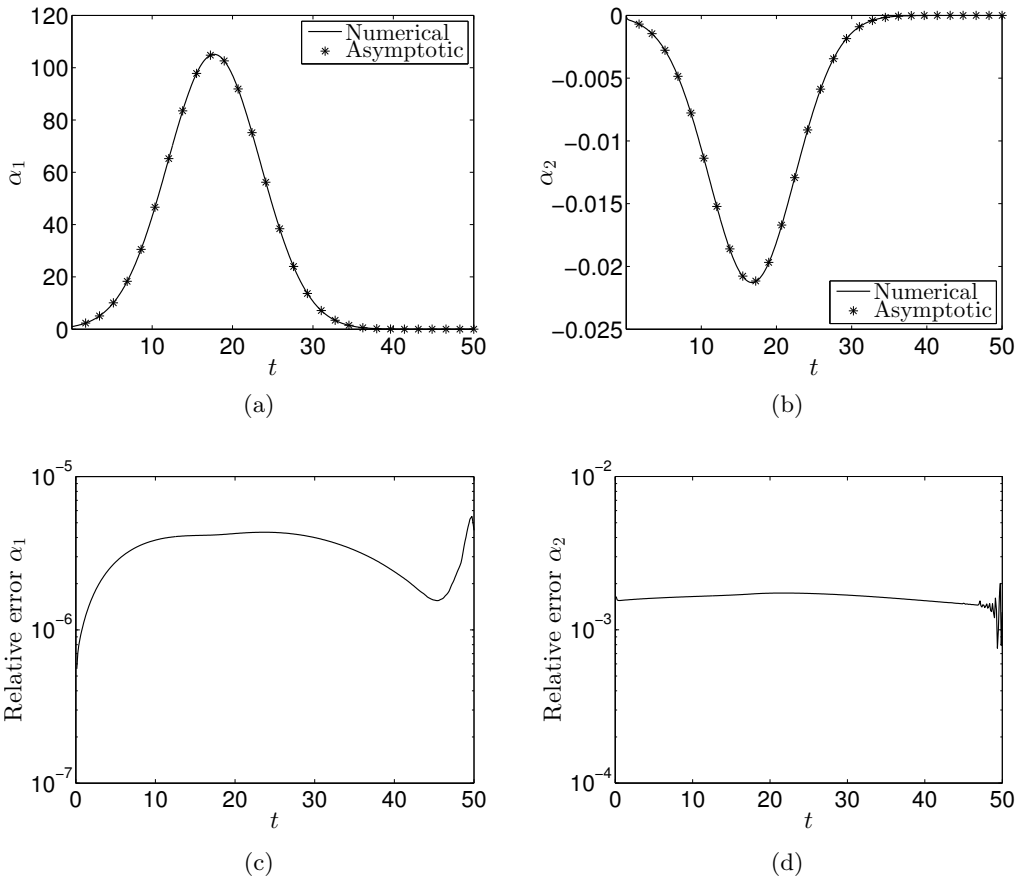


Figure 2.7: Top (a)–(b): Eigenfunction coefficients in a two-mode asymptotic approximation of the solution to the linearised problem. The initial condition was taken to be the top eigenfunction. Despite the solution not having any component along the second eigenfunction at time $t = 0$, this mode does become active, although its contributions to the asymptotic solution remain small. The exact expressions for α_1 and α_2 are given in (2.89). Bottom (c)–(d): Relative error between numerical and asymptotic approximations to the functions α_1 and α_2. Parameter values are $k = 1.67$, $\mathrm{Ma} = 105$, $\beta = 0.85$, and $\delta = 0.01$.

of which can be determined by evaluating $\alpha_{li} = \langle v_l^\dagger, \tilde{U}_i \rangle$, $l = 1, 2, \ldots$, numerically. We find that these coefficients rapidly decrease with l, which indicates the asymptotic approximation can be truncated after a few modes without much loss of accuracy. When building the asymptotic approximation using (2.58) and (2.60), we consider one-, two-, and four-mode solutions that only include the leading-order contributions. More specifically, we write the asymptotic solutions as

$$\tilde{U}_N(z,t) = \sum_{l=1}^{N} \alpha_{li} v_l(z;\delta t) \exp\left\{ \delta^{-1} \int_0^{\delta t} \left[\lambda_l(s) + \delta \gamma_{ll}(s) \right] \mathrm{d}s \right\}, \tag{2.91}$$

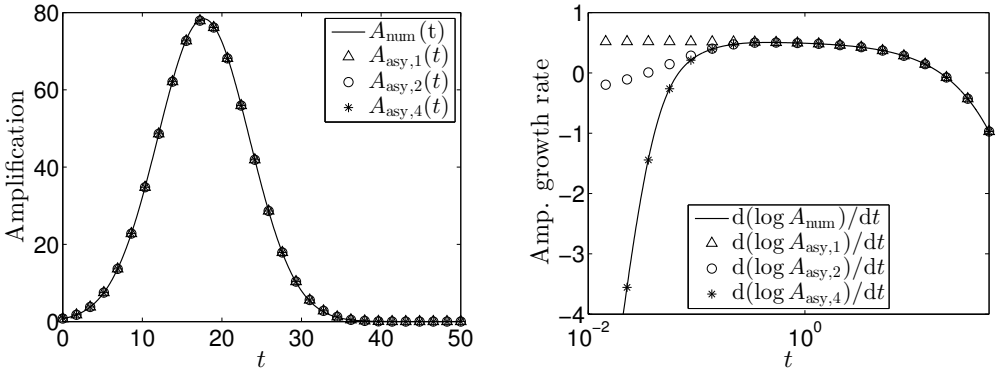
where $N = 1$, 2, or 4. The corresponding amplifications are written as

$$A_{\mathrm{asy},N} = \|\tilde{U}_N(z,t)\|. \tag{2.92}$$

The three asymptotic approximations to the perturbation amplification are shown in Figure 2.8 for the example parameter values of $k = 1.67$, $\mathrm{Ma} = 105$, $\beta = 0.85$, and $\delta = 0.01$. Also plotted is the numerical amplification for comparison purposes. All of the asymptotic approximations, and notably the one constructed using only the top mode, coincide perfectly with the numerical solution. Since there is no noticeable increase in accuracy when more modes are used, we can conclude that the truncated asymptotic solution has, for all practical purposes, converged to the true asymptotic solution that would be constructed using all of the modes.

The parameter values used in Figure 2.8 (a) are exactly the same as those in Figure 2.6. Thus, perturbations that are initially composed of several eigenfunctions rather than only the top mode experience a reduced amplification from the instability. The difference in the maximum amplification that is observed in these two figures can be understood quantitatively. We can characterise the reduction in amplification by taking the ratio of the maxima. This is roughly $78.4/105 \simeq 0.748$. The asymptotic solution $A_{\mathrm{asy},1}$ in Figure 2.8 (a) is the same as A_{asy} in Figure 2.6 except the former has a prefactor of $|\alpha_{1i}| < 1$ that accounts for the initial condition having components along non-top eigenfunctions. We find that $|\alpha_{1i}| \simeq 0.745$, which almost perfectly captures the decay in amplification. Therefore, the reduction in amplification seems exclusively due to the decreased component of the initial perturbation along the top eigenfunction. This further suggests that the reduction does not depend on how this perturbation is distributed amongst the lower modes.

To examine the accuracy of the different asymptotic approximations in more detail, the time derivative of the logarithm of the amplifications (one-mode, two-mode, four-mode, and numerical) have been computed. This quantity represents, in some sense, growth rate of the amplification. Figure 2.8 (b) shows the evolution of the growth rates and it clearly highlights



(a) (b)

Figure 2.8: Left (a): Amplifications of a perturbation that initially composed of many eigenfunctions. The exact form of the initial condition is given by (2.90). The amplifications given by $A_{\text{asy,N}}$ are computed asymptotically using the top N modes; see (2.92). The numerical solution is captured remarkably well by even the single-mode asymptotic approximation. Right (b): Effective growth rates of the amplifications. These are computed by taking the time derivative of the logarithm of the amplification. Parameter values are the same as in Figure 2.6; in particular, $k = 1.67$, $\text{Ma} = 105$, $\beta = 0.85$, and $\delta = 0.01$.

the differences between the solutions. In particular, the asymptotic approximation captures the initial period where the growth rate is negative, $t \lesssim 10^{-1}$, with a higher degree of accuracy as more modes are included. When four modes are used, this initially negative growth rate is almost captured perfectly. The single-mode solution, which has a growth rate that is approximately equal to the top eigenvalue, predicts positive growth at the start. In the long-term, all of the asymptotic solutions coincide with each other. This is expected because the higher modes have negative eigenvalues, hence their contributions eventually decay.

The impact of using the full base state with fast transients instead of its quasi-steady approximation is described in Hennessy & Münch [74]. The main effect is a slight reduction in the amplification of perturbations. This is because the strength of the instability is weakened during the transient phase where the vertical concentration gradient is first developing.

2.5 Dynamics with a deformable fluid surface

Having established the connection between the frozen-time and asymptotic analysis as well as verified that the asymptotic solution accurately captures the evolution of perturbations, we now explore the realistic case of a fluid layer with a deformable surface. The approach we take mirrors the previous analysis; we first perform a small-wavenumber expansion of the frozen-time eigenvalues, then we investigate the neutral stability curves, and finally,

we examine the amplification of perturbations directly via the asymptotic solution and numerical simulations.

2.5.1 Long-wave expansion

It turns out that the most enlightening way to perform the long-wavelength expansion of the frozen-time eigenvalues is to start from the linearised problem (2.52) as opposed to only using the characteristic equation written in (2.56). The reason is that the corresponding eigenfunctions give much insight into the long-wave instability in this case. For convenience, we write the frozen-time problem here; it is given by

$$(\partial_\zeta^2 - a^2)^2 \check{w} = 0, \tag{2.93a}$$

$$\sigma \check{c} - \zeta \check{w} = -a^2 \check{c} + \partial_\zeta^2 \check{c}, \tag{2.93b}$$

subject to the boundary conditions

$$\check{w} = \partial_\zeta \check{w} = \partial_\zeta \check{c} = 0, \quad \zeta = 0, \tag{2.93c}$$

and

$$\check{w} - \sigma \check{h} = 0, \qquad \zeta = 1, \tag{2.93d}$$

$$-\check{h} + \partial_\zeta \check{c} = 0, \qquad \zeta = 1, \tag{2.93e}$$

$$-\partial_\zeta^3 \check{w} + 3a^2 \partial_\zeta \check{w} = -a^2(a^2 C^{-1} + G)\check{h}, \quad \zeta = 1, \tag{2.93f}$$

$$\partial_\zeta^2 \check{w} + a^2 \check{w} = -a^2 M(\check{c} - \check{h}), \qquad \zeta = 1. \tag{2.93g}$$

We now seek an asymptotic solution to this problem of the form

$$\check{c}(\zeta) = \check{c}_0(\zeta) + a\check{c}_1(\zeta) + O(a^2), \tag{2.94a}$$

$$\check{w}(\zeta) = a^2 \check{w}_2(\zeta) + a^3 \check{w}_3(\zeta) + O(a^4), \tag{2.94b}$$

$$\check{h} = a\check{h}_1 + a^2 \check{h}_2 + O(a^3), \tag{2.94c}$$

$$\sigma = a\sigma_1 + a^2\sigma_2 + a^3\sigma_3 + a^4\sigma_4 + O(a^5). \tag{2.94d}$$

Using these expansions, we first compute the vertical velocities in terms of the thickness and the solvent concentration. The $O(a^2)$ problem is given by

$$\partial_\zeta^4 \check{w}_2 = 0, \tag{2.95a}$$

subject to the conditions

$$\check{w}_2 = 0, \qquad \zeta = 0, \tag{2.95b}$$

$$\partial_\zeta \check{w}_2 = 0, \qquad \zeta = 0, \tag{2.95c}$$

$$\partial_\zeta^3 \check{w}_2 = 0, \qquad \zeta = 1, \tag{2.95d}$$

$$\partial_\zeta^2 \check{w}_2 = -M\check{c}_0, \quad \zeta = 1. \tag{2.95e}$$

The solution to this is straightforward to obtain and is given by

$$\check{w}_2(\zeta) = -\frac{1}{2}\, M\check{c}_0(1)\zeta^2. \tag{2.96}$$

The $O(a^3)$ problem for the velocity has a similar form and it reads

$$\partial_\zeta^4 \check{w}_3 = 0, \tag{2.97a}$$

subject to the boundary conditions

$$\check{w}_3 = 0, \qquad \zeta = 0, \tag{2.97b}$$

$$\partial_\zeta \check{w}_3 = 0, \qquad \zeta = 0, \tag{2.97c}$$

$$\partial_\zeta^3 \check{w}_3 = G\check{h}_1, \qquad \zeta = 1, \tag{2.97d}$$

$$\partial_\zeta^2 \check{w}_3 = -M(\check{c}_1 - \check{h}_1), \quad \zeta = 1. \tag{2.97e}$$

This can be easily solved to find

$$\check{w}_3(\zeta) = \frac{1}{6}\, G\check{h}_1\zeta^3 - \frac{1}{2}\left[G\check{h}_1 + M(\check{c}_1(1) - \check{h}_1)\right]\zeta^2. \tag{2.98}$$

By expanding (2.93d) and collecting powers of a, two identities emerge. At $O(a^2)$ we find that

$$\sigma_1\check{h}_1 = -\frac{1}{2}\, M\check{c}_0(1), \tag{2.99a}$$

and at $O(a^3)$ we have

$$\sigma_2\check{h}_1 + \sigma_2\check{h}_2 = \frac{1}{6}\, G\check{h}_1 - \frac{1}{2}\left[G\check{h}_1 + M(\check{c}_1(1) - \check{h}_1)\right]. \tag{2.99b}$$

We now solve for the concentration fields and the eigenvalues using (2.93b), (2.93c), and (2.93e) in combination with the previous results. The $O(1)$ problem is given by

$$\partial_\zeta^2 \check{c}_0 = 0, \tag{2.100}$$

subject to $\partial_\zeta \check{c}_0 = 0$ at $\zeta = 0, 1$. The leading-order solvent concentration is, therefore, independent of ζ so we write $\check{c}_0(\zeta) \equiv \check{c}_0$.

Proceeding to the $O(a)$ problem, we find that this can be written as

$$\partial_\zeta^2 \check{c}_1 = \sigma_1\check{c}_0, \tag{2.101a}$$

which is supplemented with the boundary conditions

$$\partial_\zeta \check{c}_1 = 0, \quad \zeta = 0, \tag{2.101b}$$

$$\partial_\zeta \check{c}_1 = \check{h}_1, \quad \zeta = 1. \tag{2.101c}$$

By integrating the differential equation (2.101a) once and applying the above boundary conditions, we obtain a solvability condition that can be used with (2.99a) to show that the leading-order eigenvalues are complex conjugates given by

$$\sigma_1 = \pm i\,(M/2)^{1/2}\,. \tag{2.102}$$

The corresponding concentration profile can be written as

$$\check{c}_1(\zeta) = \pm i \left(\frac{M}{8}\right)^{1/2} \check{c}_0\zeta^2 + \check{c}_1(0). \tag{2.103}$$

It suffices to leave $\check{c}_1(0)$ undetermined, as this will later be absorbed into a normalisation constant.

To determine the growth rate of the associated modes and hence assess whether an instability can occur, we must consider the $O(a^2)$ problem. This is given by

$$\partial_\zeta \check{c}_2 = \sigma_1\check{c}_1(\zeta) + \sigma_2\check{c}_0 - \zeta\check{w}_2(\zeta) + \check{c}_0 \tag{2.104a}$$

subject to

$$\partial_\zeta \check{c}_2 = 0, \quad \zeta = 0, \tag{2.104b}$$

$$\partial_\zeta \check{c}_2 = \check{h}_2, \quad \zeta = 1. \tag{2.104c}$$

We follow the same steps as before to determine the eigenvalues σ_2. In particular, the differential equation (2.104a) is integrated and the boundary conditions are applied to produce a solvability condition that is used with (2.99b). We find that the $O(a^2)$ contribution to the eigenvalue is real and given by

$$\sigma_2 = \frac{5}{48}\,M - \frac{1}{6}\,G - \frac{1}{2}. \tag{2.105}$$

From this expression, it follows that the leading-order real part of the top eigenvalue is positive for $M > (24 + 8G)/5$, thus indicating the presence of a long-wavelength oscillatory instability in the system. Further corrections to the eigenvalues can be obtained by continuing this process or by expanding the characteristic equation (2.56). The intermediate calculations are not very enlightening so they will be omitted. We find that the higher-order contributions to the eigenvalue σ are given by

$$\sigma_3 = \frac{\pm i}{23040}\left(\frac{2}{M}\right)^{1/2}\left(1920G - 14160M + 352MG - 181M^2 - 320G^2 - 2880\right), \tag{2.106a}$$

$$\sigma_4 = \frac{3}{10}\,G - \frac{593}{483840}\,M^2 - \frac{281}{1440}\,M + \frac{107}{60480}\,MG - \frac{1}{6}\,C. \tag{2.106b}$$

Thus, σ_3 provides a correction to the oscillation frequency, whereas σ_4 gives a better estimate of the growth rate.

To gain some insight into the physical mechanisms behind the oscillations, we examine the spatiotemporal evolution of the perturbations associated with the solvent concentration at the surface and the film thickness. The eigenfunctions are normalised so that the concentration on the substrate is equal to one, $\check{c}(0) = 1$. This yields $\check{c}_0 = 1$. Thus, we can write

$$\check{c}(1) = 1 \pm ia\left(\frac{M}{8}\right)^{1/2} + O(a^2), \tag{2.107a}$$

$$\check{h} = \pm ia\left(\frac{M}{2}\right)^{1/2} + O(a^2). \tag{2.107b}$$

The corresponding eigenvalues are written as

$$\sigma = \pm i\omega + O(a^2), \tag{2.108}$$

where $\omega = a(M/2)^{1/2}$.

In the context of the frozen-time analysis, the temporal behaviour associated with these perturbations can be determined by multiplying the eigenfunctions in (2.107) with their normal-mode factors $\exp(\sigma t)$ and then using the principle of superposition to yield

$$\check{C}(t) = \left[1 + ia\left(\frac{M}{8}\right)^{1/2}\right] e^{i\omega t} + c.c. + O(a^2), \tag{2.109a}$$

$$\check{H}(t) = ia\left(\frac{M}{2}\right)^{1/2} e^{i\omega t} + c.c. + O(a^2), \tag{2.109b}$$

where *c.c.* denotes the complex conjugate. These expressions can be written as

$$\check{C}(t) = \left(4 + a^2M/2\right)^{1/2}\cos(\omega t + \varphi) + O(a^2), \tag{2.110a}$$

$$\check{H}(t) = -a(2M)^{1/2}\sin(\omega t) + O(a^2), \tag{2.110b}$$

where the phase shift φ satisfies

$$\tan\varphi = a(M/8)^{1/2}. \tag{2.110c}$$

Finally, to obtain the full spatiotemporal behaviour of the perturbation to the surface concentration and film thickness, we multiply these modes by $\exp(iax)$ and take the real part to obtain

$$\tilde{C}(x,t) = \mathrm{Re}\{\check{C}(t)e^{iax}\} = \left(4 + a^2M/2\right)^{1/2}\cos(\omega t + \varphi)\cos(ax) + O(a^2), \tag{2.111a}$$

$$\tilde{H}(x,t) = \mathrm{Re}\{\check{H}(t)e^{iax}\} = -a(2M)^{1/2}\sin(\omega t)\cos(ax) + O(a^2). \tag{2.111b}$$

These perturbations are shown at four various times in Figure 2.9. Initially, the film profile is flat (panel (a)) but concentration gradients along the surface generate Marangoni stresses

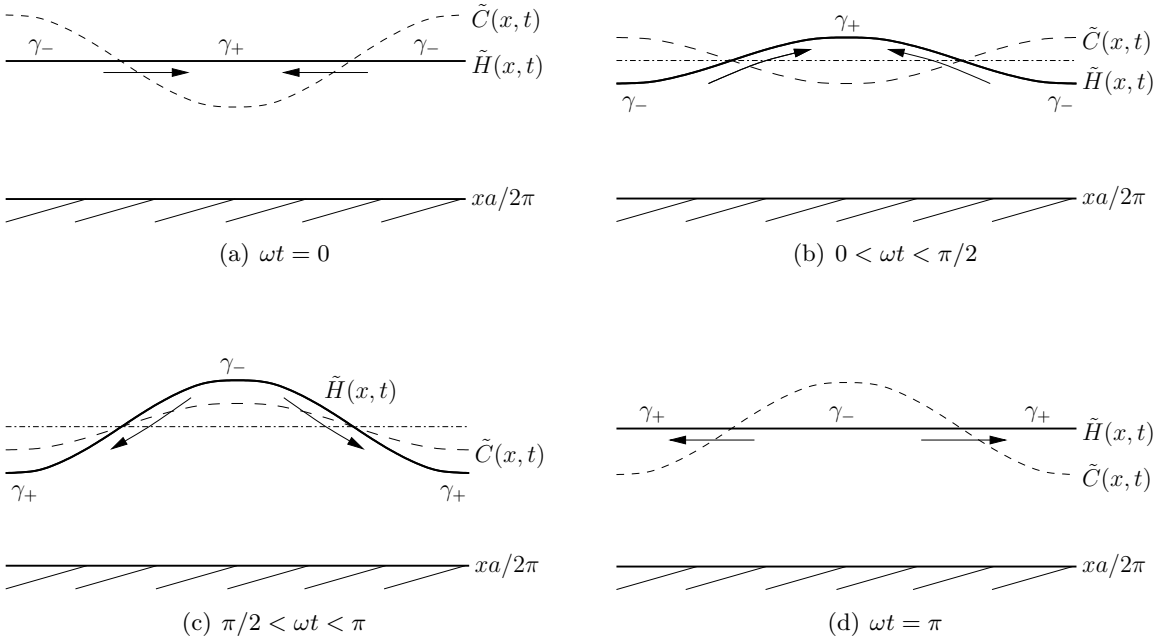


Figure 2.9: Progression of the oscillatory instability. Shown are the perturbations to the surface solvent concentration (dashed), $\tilde{C}$, and the film thickness (solid), $\tilde{H}$, both of which are defined in (2.111). The arrows indicate the instantaneous direction of flow and γ_+ and γ_- denote regions of high and low surface tension, respectively. Furthermore, $\omega = (M/2)^{1/2}$ represents the frequency of oscillation. See text for a detailed explanation of the dynamics.

which drive a flow. The build up of solvent-rich fluid due to this flow deforms the layer (panel (b)) and reduces the concentration gradients. As the deformations grow larger, the surface concentration eventually reverses so that regions which were initially solvent rich become solvent depleted and vice versa. This changes the direction of the Marangoni stresses so that when the surface deformation is maximal (when $\omega t = \pi/2$; not shown), the film begins to level (panel (c)). During the levelling process, the concentration increases under the crests and decreases under the troughs. This magnifies the Marangoni stresses and accelerates the levelling. Furthermore, these Marangoni stresses are still present when the surface returns to a flat state (panel (d)), thus causing the entire process to repeat.

2.5.2 Initial neutral stability curves

The initial stability of the system is investigated over a wider range of wavenumbers by setting $\tau = 0$ and plotting the neutral stability curves. When the interface is deformable, there are two types of neutral stability curves that must be considered. The first of these corresponds to a top eigenvalue that is equal to zero, whereas the second type is associated with top eigenvalues that are a complex conjugate pair with zero real part. We refer to these as stationary and oscillatory neutral stability curves, respectively, to reflect the type

of instability that occurs as they are crossed. As before, we write the neutral stability curves as functions of the rescaled wavenumber a. However, these curves now depend on the effective capillary and Galileo numbers, C and G, respectively. Therefore, they are written as $M = M(a; C, G)$.

The stationary neutral stability curves can be computed analytically by setting $\sigma = 0$ in (2.56) and carrying out the integration to find

$$\begin{aligned} M =& 12a^3(\sinh 2a - 2a)(a^2C^{-1} + G)\big/\big\{[3a\cosh a \sinh a - (2a^2+3)a^2 \\ & - 3\sinh^2 a + 3a^3 \coth a](a^2C^{-1} + G) + 24a^5(a - \coth a)\big\}. \end{aligned} \tag{2.112}$$

In the limit $C \to 0$ or $G \to \infty$, corresponding to infinitely strong surface tension or strong gravity, respectively, (2.112) reduces to

$$M_\infty = \frac{12a^3(\sinh 2a - 2a)}{3a\cosh a \sinh a - (2a^2+3)a^2 - 3\sinh^2 a + 3a^3 \coth a}, \tag{2.113}$$

which recovers the neutral stability curve (2.71) for the case of a non-deformable fluid surface. This limit will be discussed in more detail below. For finite G and $C > 0$ we also have $M \simeq M_\infty$ for $a \gg 1$. Thus, for large wavenumbers, the dynamics of this system are expected to be similar to those when the free surface is non-deformable.

The stationary neutral stability curve (2.112) is shown as the dashed line in Figure 2.10 for the example parameter values of $G = 100$ and $C = 0.01$. Also shown is the limiting curve given by (2.113). For large wavenumbers the two curves coincide with one another. However, their behaviour at small wavenumbers differs significantly. As a is decreased from a sufficiently large value, the stationary neutral stability curve given by (2.112) diverges at some critical value of a denoted by a_s, which is found to be $a_s \simeq 0.7$ when $G = 100$ and $C = 0.01$. On the other hand, the limiting curve M_∞ monotonically decreases to its minimum value of 80 when $a = 0$. The key properties of the singularity in the (deformable) neutral stability curve are defined by the limits

$$\lim_{a \to a_s^{\pm}} M(a; G, C) = \pm\infty. \tag{2.114}$$

This singularity divides the neutral stability curve into two sections. The first of these lies to the right of the singularity and it exists only in the upper-quarter plane. This is the section shown in Figure 2.10 that resembles the shape of a 'u', where the left branch is constrained by the vertical asymptote at a_s and the right branch tends towards (2.113) for large a. The shape of this section of curve implies the existence of a band of unstable wavenumbers with positive top eigenvalues given by $a_s < a_2(M) < a < a_3(M)$. Moreover, there is a critical value of $M = M_s$, where $M_s \simeq 82$ for $G = 100$ and $C = 0.01$, such that

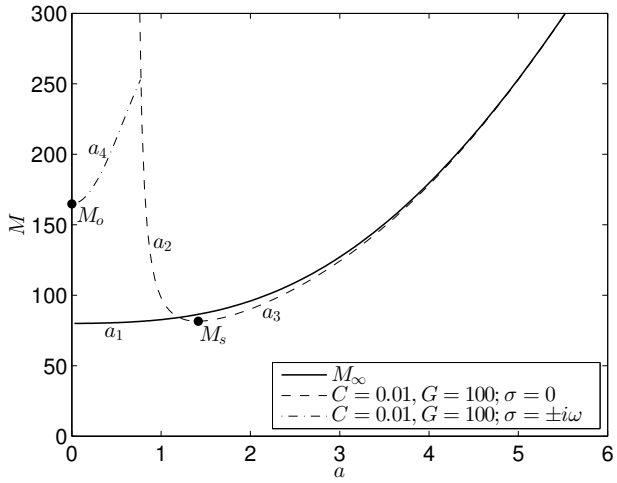
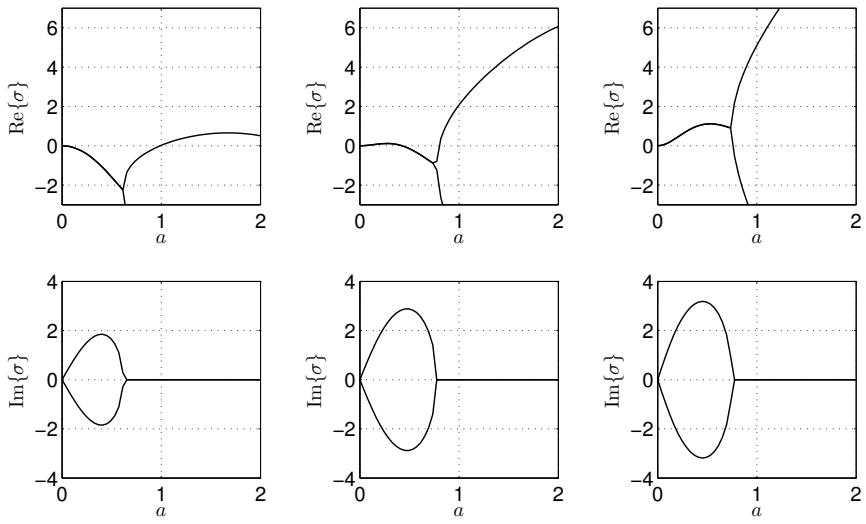


Figure 2.10: Neutral stability curves for non-deformable systems (solid black) and deformable systems (dashed and dashed-dot). The solid and dashed curves correspond to locations in parameter space where the top eigenvalue is zero. The dashed-dot line corresponds to where the top eigenvalue is purely imaginary. See text for definitions of M_s, M_o, and the a_i.



(a) $M = 100 \in R_{u,1}$ (b) $M = 200 \in R_{u,2}$ (c) $M = 300 \in R_{u,3}$

Figure 2.11: The dependence of the top two eigenvalues on the disturbance wavenumber for various effective Marangoni numbers. The values of C and G are chosen to coincide with the neutral stability diagram in Figure 2.10, thus $C = 0.01$ and $G = 100$. Each value of M illustrates a qualitatively distinct behaviour of the eigenvalues and each behaviour characterises a subregion of the neutral stability diagram. See text for full details. The definitions of the $R_{u,i}$ are given in (2.115).

$a_2(M_s) = a_3(M_s)$. This critical value of M corresponds to the minimum of the stationary neutral stability curve in the upper-quarter plane.

The second section of the stationary neutral stability curve lies to the left of the singularity and it corresponds to negative values of the Marangoni number. Although this indicates the presence of a stationary instability when $M < 0$, we do not investigate this situation here.

A long-wave approximation to the oscillatory neutral stability curve can be obtained using the leading- and next-order contributions to the real part of the top eigenvalue given by (2.105) and (2.106b), respectively. In particular, we find that $\sigma_2(M)+a^2\sigma_4(M) = 0$ gives an implicit representation of the oscillatory neutral stability curve in the limit $a \ll 1$. This curve monotonically increases with a from its local minimum of $M = (24 + 8G)/5$ at the point $a = 0$. For larger wavenumbers, the oscillatory neutral stability curve can, in principle, be determined by setting $\sigma = i\omega$ in the characteristic equation (2.56) and performing the integration, where ω is a real and positive number corresponding to the frequency of oscillation. The real and imaginary parts of the resulting equation provide two expressions that can be used to determine the neutral stability curve and the oscillation frequency ω. In practice, however, this curve is computed numerically using a basic continuation scheme.

The oscillatory neutral stability curve is shown as the dashed-dot line in Figure 2.10. This curve increases monotonically with a from its value of $M_o = 165$ when $a = 0$ until it collides with the left-most branch of the 'u'-shaped stationary neutral stability curve when $M = 253$. Thus, for $M > 165$, we expect there to be a band of wavenumbers with complex conjugate eigenvalues with positive real part, thus indicating the locations in parameter space where the oscillatory instability is present.

The stationary and oscillatory neutral stability curves in Figure 2.10 divide the parameter space into four regions, each of which corresponds to a distinct behaviour of the top eigenvalue as the wavenumber a is varied. These regions are characterised by the effective Marangoni number M and are given by

$$R_s = \{M : 0 < M < M_s\}, \tag{2.115a}$$

$$R_{u,1} = \{M : M_s < M < M_o\}, \tag{2.115b}$$

$$R_{u,2} = \{M : M_o < M < 253\}, \tag{2.115c}$$

$$R_{u,3} = \{M : 253 < M\}, \tag{2.115d}$$

where $M_s \simeq 82$ and $M_o \simeq 165$ denote the critical Marangoni numbers associated with the onset of the stationary and oscillatory instability when $G = 100$ and $C = 0.01$, respectively. In R_s, the real part of the top eigenvalue is always negative; hence, the base state is stable for these values of the effective Marangoni number. In the three other regions, $R_{u,i}$, $i = 1, 2, 3$,

the real part of the top eigenvalue is positive for some wavenumbers so the base state is linearly unstable. The top eigenvalue exhibits markedly different behaviour within each of these regions. This is demonstrated in Figure 2.11, where the dependence of the top two eigenvalues on the wavenumber is displayed for three exemplary values of the Marangoni number, each of which characterises one of the three unstable regions. From this figure, we see that the top eigenvalues are always a complex conjugate pair for sufficiently small wavenumbers, but as the wavenumber increases, the imaginary parts eventually vanish, causing a transition where the complex conjugate pair splits into two real and distinct eigenvalues. The sign of the real parts for small wavenumbers and the sign of the real part when the transition happens distinguishes the three regions.

In the region $R_{u,1}$ (Figure 2.11 (a)), the complex eigenvalues always have negative real parts including when they undergo the transition to real eigenvalues. After this transition happens, the largest of the two eigenvalues grows to become positive, giving rise to the stationary instability that occurs for wavenumbers in the range $a_2(M) < a < a_3(M)$.

The behaviour of the top eigenvalue in $R_{u,2}$ (Figure 2.11 (b)) is very similar to in $R_{u,1}$, except there is now a small band of wavenumbers given by $0 < a < a_4(M)$ where the real parts of the complex eigenvalues are positive. For $a > a_4(M)$, the behaviour of the top eigenvalue is qualitatively identical to in $R_{u,1}$.

The region $R_{u,3}$ (Figure 2.11 (c)) is defined by the fact that the complex eigenvalues always have positive real parts. Thus, when the transition to real eigenvalues occurs, the largest grows to become even more positive, whereas the smaller of the two decreases, eventually becoming negative when a is increased beyond $a_2(M)$.

From the analysis of the eigenvalues in these regions, we can conclude that only the stationary instability occurs in $R_{u,1}$, whereas both modes of instability occur in $R_{u,2}$ and $R_{u,3}$.

We now revisit the non-deformable limit by studying how the neutral stability curves collapse onto the M_∞ curve when surface tension or gravity is strong, *i.e.*, when $C \to 0$ or $G \to \infty$, respectively. It can be shown that the location of the singularity in the stationary neutral stability curve is given approximately by $a_s^2 \simeq (-GC + \sqrt{G^2C^2 + 480C})/2$ when $C \ll 1$ or $G \gg 1$ or when both of these are true. Furthermore, the wavenumber that marks the minimum of the stationary neutral stability curve is given by $a_c \simeq (4725/G)^{1/4}$ when $G \gg 1$, and $a_c \simeq (9450C)^{1/6}$ when $C \ll 1$. Therefore, when $C \to 0$ or $G \to \infty$, both the singularity and the minimum of the stationary neutral stability curve tend towards $a = 0$. The implication is that the entire left branch of this curve, *i.e.*, the branch defined by a_2, effectively vanishes in this limit. Moreover, because the oscillatory neutral stability curve exists in the region to the left of the a_2 branch, it is eliminated in this limit as well. Thus,

as $C \searrow 0$ or $G \nearrow \infty$, the region of complex eigenvalues with positive real parts gradually shrinks until it is completely eliminated.

2.5.3 Competing modes of instability

The neutral stability curves shown in Figure 2.10 indicate that it is possible for the short-wave stationary and long-wave oscillatory instabilities to occur simultaneously for certain parameter values. The dominant mode of instability, if there is one, is determined by the eigenvalue that has the largest real part over all of the disturbance wavenumbers and the corresponding eigenfunction. An examination of Figure 2.11 reveals that, at least initially and for those parameter values, the oscillatory instability is unlikely to be of any physical relevance because the real parts of the complex eigenvalues are always much less than the purely real eigenvalues. That is, the oscillatory modes are dominated by the faster-growing stationary ones, thus reducing their chances of being detectable or observable. To reverse the situation so that the oscillatory instability is dominant, the complex eigenvalues need to have the largest real part over all perturbation wavenumbers. This is not easy to achieve if both instabilities occur simultaneously because the real parts of the complex eigenvalues grow much slower with the effective Marangoni number, M, than the purely real eigenvalues; see Figure 2.11. However, it may be possible to make the oscillatory mode dominant by isolating it in the sense that it is the only instability to occur for a given set of parameter values. This will be the case if the onset of the oscillatory instability occurs at lower values of the Marangoni number than the stationary mode. We now investigate whether such situations actually arise.

The effective Marangoni numbers that are associated with the onset of the instabilities are characterised by the minima of the stationary and oscillatory neutral stability curves. The locations of these two minima depend on the other parameter of the system, namely the effective Galileo and capillary numbers G and C, respectively. Thus, by tuning these parameters, it may be possible to induce the oscillatory instability before the stationary one. We denote by M_o and M_s the Marangoni numbers that correspond to the minima of the oscillatory and stationary neutral stability curves, respectively. An analysis of the long-wave approximation to the oscillatory neutral stability curve shows that it has a local minimum at $a = 0$. Numerical calculations of this curve show that this point is, in fact, the global minimum. Therefore, we have

$$M_o = \frac{24 + 8G}{5}. \tag{2.116}$$

The minima of the stationary neutral stability curves can, in theory, be found directly from (2.112). However, the wavenumbers that minimise this curve satisfy a cumbersome transcendental equation and hence they must be found numerically.

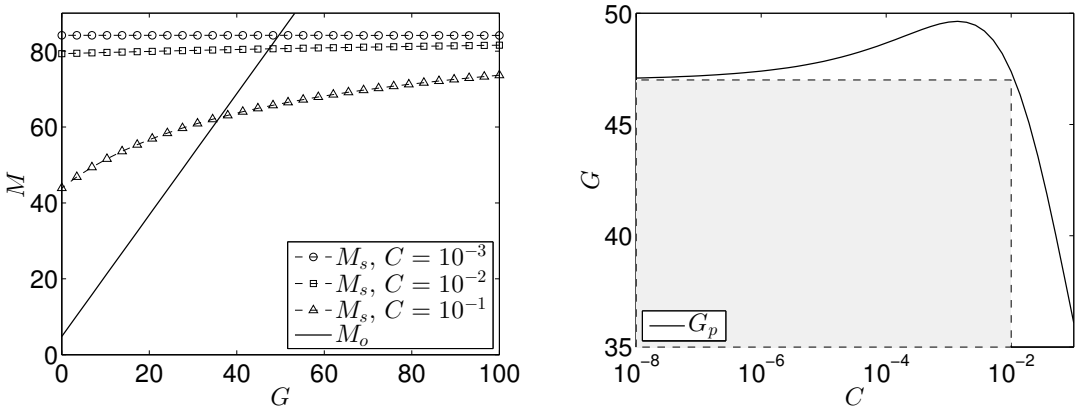
The parameter dependence of these two minima is shown in Figure 2.12 (a). Both of these minima are plotted as functions of the effective Galileo number G and several plots of M_s are shown for different values of the effective capillary number C. Thus, for a given value of C and G, this figure shows the two critical Marangoni numbers that correspond to the onset of the two types of instability. Parameter regimes where only the oscillatory mode of instability occurs can be identified as those which satisfy $M_o(G) < M < M_s(C, G)$. An examination of Figure 2.12 (a) shows that for each value of C, the curves $M_o = M_o(G)$ and $M_s = M_s(G)$ always intersect at one particular value of G, denoted by G_p. Moreover, for $G < G_p(C)$, the condition $M_o < M_s$ holds. The dependence of G_p on C is shown in Figure 2.12 (b) and the region under this curve corresponds to the parameter regime where the oscillatory instability can potentially be isolated. The non-monotonicity of G_p arises because the growth of M_s with decreasing C (for fixed G) is not monotonic either. As can be seen from Figure 2.12 (a), decreasing C from 10^{-1} to 10^{-3} increases M_s to approximately 84 for all G. However, as the non-deformable limit must be recovered as surface tension gets arbitrarily strong, we have that $M_s \to 80$ as $C \to 0$, *i.e.*, M_s eventually begins to decrease. The limiting value of G_p that is approached as $C \searrow 0$ (see Figure 2.12 (b)) can be computed by setting $M_o = M_s = 80$ and solving for G. We find that $G_p \simeq 47$ as $C \searrow 0$. For effective capillary numbers in the range $C < 10^{-2}$, we have that G_p is always greater than 47 and the onset of the stationary instability occurs for $M > 80$. Thus, the following rule of thumb can be established: the stationary instability can be suppressed and the oscillatory instability can be induced if C, G, and M are chosen such that

$$C < 10^{-2}, \quad G < 47, \quad M_o < M < 80. \tag{2.117}$$

This region of parameter space is shown as the grey area in Figure 2.12 (b); clearly it lies below the curve defined by G_p. For small but moderate values of C, *i.e.*, for $10^{-2} < C \ll 1$, the value of G_p will be less than 47 and the upper bound on M will have to be replaced by its corresponding value of M_s. If $G > G_p$, or if $M > M_s$, the stationary instability is expected to dominate, if it occurs at all.

2.5.4 Evolution of the neutral stability curves

Having identified the regions of parameter space where the oscillatory instability is initially dominant, we now seek to understand how these regions evolve with changes in the slow time variable τ. Of particular interest is determining the persistence of the region where



(a) (b)

Figure 2.12: Left (a): Critical Marangoni numbers as a functions of the effective Galileo number G and the effective capillary number C. The solid black line denotes the Marangoni numbers associated with the onset of an oscillatory instability and is given analytically by (2.116). The dashed lines with symbols denote Marangoni numbers associated with the onset of stationary instabilities. For each value of C these curves intersect at one particular value of G denoted by G_p. Right (b): The dependence of the function G_p on the capillary number C. For $G < G_p$, the inequality $M_o < M_s$ is satisfied. Thus, the region below this curve corresponds to parameter regimes where it is possible to only induce the oscillatory mode of instability. The grey area is defined by the parameters $C < 10^{-2}$ and $G < 47$. The grey area denotes the parameter regime where it is possible to isolate the oscillatory instability if $M < 80$; see text for further details.

the oscillatory instability dominates, as this will be important for assessing how likely it is for this instability to be observed experimentally.

When the surface is deformable, the slow evolution of the stability regions is most conveniently monitored through the τ dependence of the neutral stability curves rather than tracing out paths in the (a, M) plane. The τ dependence can be introduced in a physically intuitive manner by replacing the effective non-dimensional numbers M, C, and G with their original, time-independent counterparts given in (2.53). In this case, the neutral stability curves can be written in terms of the original parameters as

$$\mathrm{Ma}(k;\tau) = \left(\frac{\beta}{\bar{h}(\tau) - 1 + \beta}\right) M\left(\bar{h}(\tau)k; \bar{h}(\tau)^{-1}\,\mathrm{Ca}, \bar{h}^3(\tau)\,\mathrm{Ga}\right). \tag{2.118}$$

For stationary neutral stability curves, the M in the above equation is given by (2.112), whereas the oscillatory neutral stability curves are computed numerically. In the discussion that follows, it is convenient to parameterise the slow evolution of the neutral stability curves according to $\bar{h}$ instead of τ. The two parameterisations are equivalent owing to the monotonicity of the function $\bar{h}(\tau)$.

An example of how the neutral stability curves evolve with the base state film thickness is shown in Figure 2.13. The parameter values are $\mathrm{Ca} = 0.01$, $\mathrm{Ga} = 30$, and $\beta = 0.85$. These are chosen so that when $\tau = 0$, there is a band of Marangoni numbers given by

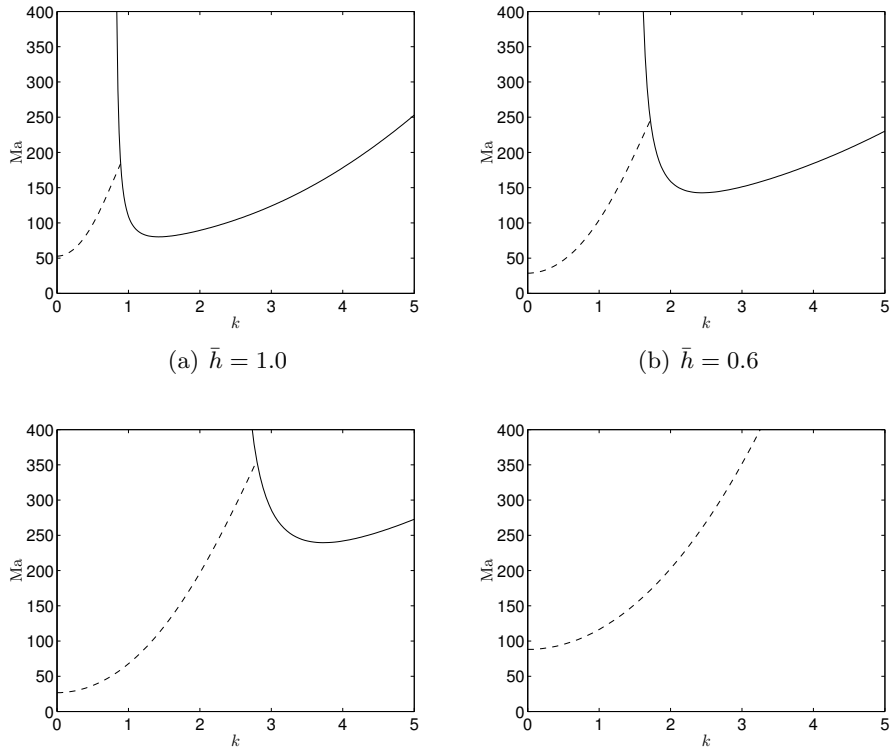
$53 < \mathrm{Ma} < 80$ where only the oscillatory instability occurs. The figure shows that as $\bar{h}$ decreases (corresponding to increasing τ), the stationary neutral stability curve moves upward. This suggests that for these values of Ca and Ga, the stationary instability is weakened as time progresses. This can be understood by fixing a value of Ma that lies above the minimum of the initial stationary neutral stability curve. As τ increases, the stationary curve moves upwards and eventually its minimum will grow beyond the fixed value of Ma, implying that the stationary instability no longer occurs for this value of the Marangoni number. Interestingly, the situation for the oscillatory neutral stability curve is the opposite, at least initially. That is, Figure 2.13 shows that as $\bar{h}$ decreases, the oscillatory curve moves downwards, thus suggesting an amplification of this instability. This amplification can be verified by transforming the long-wave eigenvalues given in (2.94d) into the original frozen-time eigenvalues via the rescaling in (2.51) and (2.53), which shows that the real part temporarily increases as τ is increased from zero. The downwards motion of the oscillatory curve also means that some Marangoni numbers that are initially in the stable regime, *i.e.*, those below the value of 53, can enter the unstable regime. The decrease in the oscillatory curve is only temporary, however, and eventually it begins to increase. As $\bar{h}$ tends towards its steady state value of $1-\beta$, both neutral stability curves tend to infinity.

The key behaviour of the neutral stability curves can be captured by plotting how their minima evolve with $\bar{h}$. Figure 2.14 (a) shows this for the case described above when $\mathrm{Ca} = 0.01$, $\mathrm{Ga} = 30$, and $\beta = 0.85$. In the figure, $\mathrm{Ma_s}$ and $\mathrm{Ma_o}$ denote the critical Marangoni numbers associated with the stationary and oscillatory neutral stability curve, respectively. The curve for $\mathrm{Ma_o}$ can be obtained analytically by rescaling (2.116) to yield

$$\mathrm{Ma_o} = \frac{\beta}{\bar{h}-1+\beta}\left(\frac{24+8\bar{h}^3\mathrm{Ga}}{5}\right), \tag{2.119}$$

and $\mathrm{Ma_s}$ is found numerically. From the figure, it is easy to see that $\mathrm{Ma_s}$ increases monotonically as $\bar{h}$ decreases (corresponding to increasing τ). In contrast, $\mathrm{Ma_o}$ decreases with $\bar{h}$ until $\bar{h} \simeq 0.46$, after which it begins to increase rapidly. This behaviour has important physical consequences as it implies that the band of Marangoni numbers where the oscillatory instability is initially isolated is preserved throughout much of the evolution. Thus, if an experiment is performed that has a Marangoni number within this band, the oscillatory instability will not become dominated by the stationary instability, nor is it expected to quickly stabilise. In contrast, the monotonic increase of $\mathrm{Ma_s}$ with time indicates that the stationary instability will quickly stabilise unless the Marangoni number is much larger than $\mathrm{Ma_s}$.

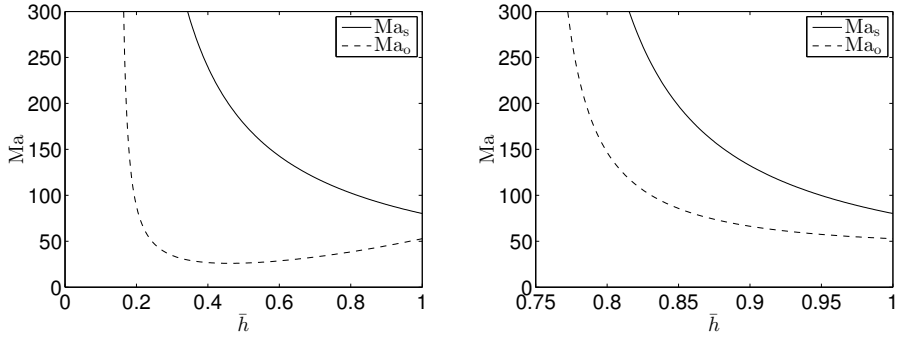
An analysis of the analytical expression for $\mathrm{Ma_o}$ given in (2.119) reveals that the oscillatory neutral stability curves do not always have to decrease initially and in some cases it



(a) $\bar{h} = 1.0$ (b) $\bar{h} = 0.6$

(c) $\bar{h} = 0.4$ (d) $\bar{h} = 0.2$

Figure 2.13: Evolution of the neutral stability curves in the upper-quarter plane in terms of the base state film thickness $\bar{h}$. Stationary neutral stability curves are shown as solid black lines and oscillatory ones as dashed lines. Parameter values are Ca = 0.01, Ga = 30, and $\beta = 0.85$. As $\bar{h} \to 1 - \beta = 0.15$ the curves tend to infinity.



(a) (b)

Figure 2.14: The evolution of the minima of the stationary (solid) and oscillatory (dashed) neutral stability curves. The parameter values are (a): Ca = 0.01, Ga = 30, $\beta = 0.85$; (b): Ca = 0.01, Ga = 30, $\beta = 0.25$. Note the difference in scales in panel (b).

increases. There is a relationship between β and Ga that determines the initial behaviour of this curve. If we think of Ga as being fixed for a given set of experiments, then it is possible to define a critical value of the initial solvent volume fraction β that separates the two behaviours. This is value is given by

$$\beta_c = \frac{1}{3}\frac{3 + \mathrm{Ga}}{\mathrm{Ga}}. \tag{2.120}$$

If $\mathrm{Ga} > 3/2$, then values of β such that $\beta_c < \beta < 1$ will yield an initially decreasing oscillatory neutral stability curve. In the case when $\mathrm{Ga} < 3/2$, the curve always increases. When $\mathrm{Ga} \gg 1$, as in the case of the experiments by Bassou & Rharbi [8], we have $\beta_c \simeq 1/3$. Figure 2.14 (b) shows an example of $\mathrm{Ma_o}$ increasing with time for the example parameter values of $\mathrm{Ca} = 0.01$, $\mathrm{Ga} = 30$, and $\beta = 0.25$. The value of β_c in this case is $\beta_c \simeq 0.37$.

These results indicate that regions of parameter space where the oscillatory instability is isolated will persist during the drying process provided that $\beta > \beta_c$ and $\mathrm{Ma_s}$ increases with τ. It is not easy to formulate analytical conditions which guarantee the increase of $\mathrm{Ma_s}$; however, numerical experiments in the regime $\mathrm{Ca} \ll 1$ suggest this is always the case.

2.5.5 Asymptotic analysis

Using the frozen-time method, it was possible to identify regions of parameter space where the oscillatory mode of instability is isolated. We now use the asymptotic solution presented in Section 2.3.2.2 to determine the maximum amplification of perturbations caused by this instability. This will give additional insight into its physical relevance. Furthermore, the asymptotic solution is used to better understand the competition that exists between the two modes of instability.

The perturbation amplification is defined in the same manner as before, namely,

$$A(t) = \frac{\|\tilde{U}(z,t)\|}{\|\tilde{U}_i(z)\|}, \tag{2.121}$$

where $\|\cdot\|$ is the norm associated with the inner product in (2.63). We consider amplifications that are based on asymptotic and numerical solutions to the linearised problem; these are denoted as A_{asy} and A_{num}, respectively. Based on the rapid convergence of the asymptotic solution with increasing number of modes that was observed when the fluid surface was non-deformable, the amplifications A_{asy} are constructed using a two-mode approximation. This allows us to deal with the case when the top eigenvalues are a complex conjugate pair and both corresponding modes need to be included in the asymptotic solution. Furthermore, the initial condition is always chosen to be the top eigenfunction.

We first investigate the disturbance amplifications that result from the oscillatory instability. We set $\mathrm{Ma} = 70$, and take the other parameters to be

$$\mathrm{Ca} = 0.01, \quad \mathrm{Ga} = 30, \quad \beta = 0.85, \quad \delta = 0.01. \tag{2.122}$$

These parameters correspond to the situation shown in Figure 2.13, where disturbances with wavenumbers that satisfy $k < 0.31$ are expected to grow in an oscillatory fashion until the system begins to stabilise.

Figure 2.15 shows the evolution of the top two eigenvalues, the real part of disturbance to the film thickness measured relative to its initial value, and the disturbance amplification when the wavenumber is set to $k = 0.21$. This particular wavenumber is chosen because it corresponds to the eigenvalue with the largest real part when $\tau = 0$. For these parameters values, the disturbance is amplified by more than three orders of magnitude before the system begins to stabilise, which may be large enough for this instability to be observed experimentally.

An examination of the top eigenvalues in Figure 2.15 shows that the imaginary parts tend toward zero after an initial period of growth, causing the complex conjugate pair to split into two distinct, real eigenvalues. The slow change in the imaginary parts of the eigenvalues causes a modulation in the frequency of oscillation. This can be observed in the middle panel of Figure 2.15; as the imaginary parts increase so does the oscillation frequency. However, the eventual decay of the imaginary part to zero leads to the frequency decreasing until the oscillations are completely suppressed.

As the imaginary parts of the top eigenvalues tend toward zero, the distance between the two eigenvalues decreases. At the point where the imaginary part vanishes, the two eigenvalues are identical; thus, the asymptotic solution in Section 2.3.2.2 breaks down. This can be clearly seen in Figure 2.15; in particular, the asymptotic solutions diverge as the critical value of $\tau \simeq 2.64$ is approached. Before this breakdown occurs, however, the asymptotic solution matches the numerical simulation with a very high degree of accuracy. The stabilisation of the system and the long-term dynamics are accurately captured, and the relative error in the maximum amplification is less than 0.1%.

By increasing Ma while maintaining the inequality $\mathrm{Ma} < \mathrm{Ma_s}$, it is possible to strengthen the oscillatory instability while preventing the onset of the stationary mode. However, the fast stabilisation of the stationary instability that is predicted by the frozen-time analysis may suggest that the oscillatory mode can remain dominant if Ma is slightly above $\mathrm{Ma_s}$. Indeed, when $\mathrm{Ma} = 90$, keeping the other parameters as in (2.122), the oscillatory mode with wavenumber $k = 0.3$ is amplified by more than four orders of magnitude before it begins to stabilise, whereas the maximum amplification of a stationary mode with $k = 1.54$

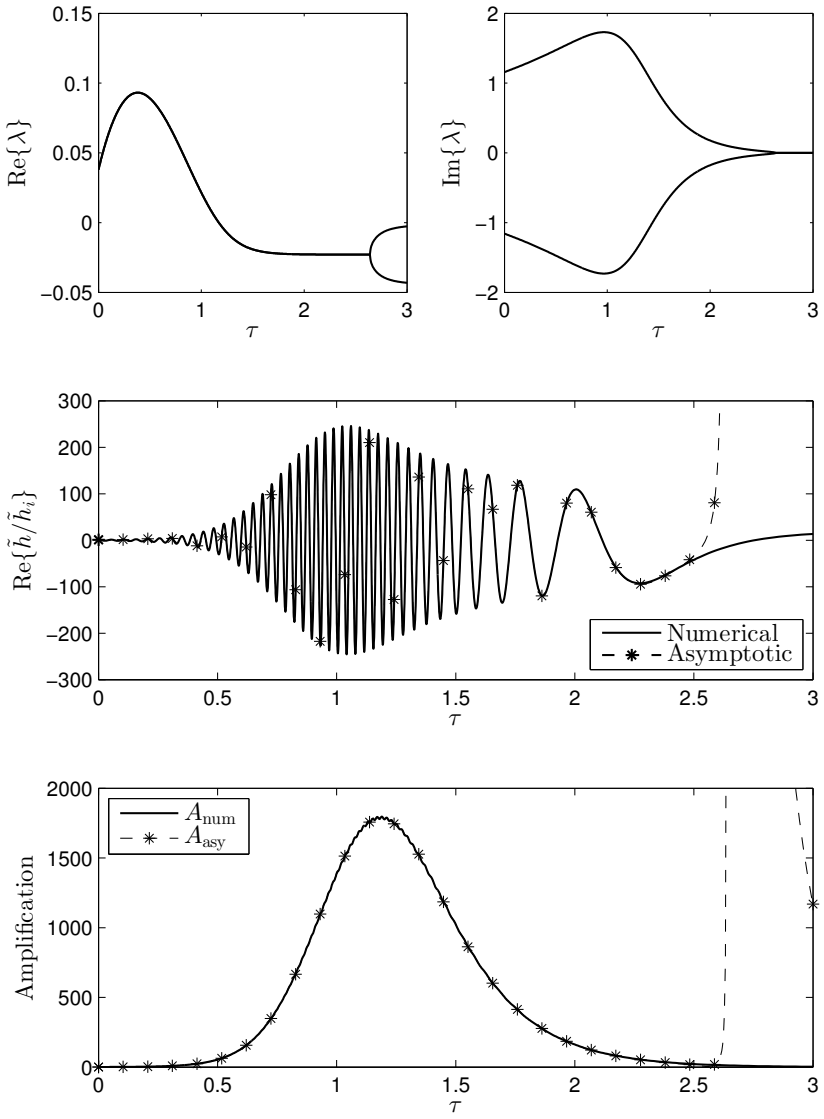


Figure 2.15: The oscillatory instability. Top (a): The evolution of the real and imaginary parts of the top two eigenvalues. Middle (b): Evolution of the real part of the disturbance to the film thickness relative to its initial value. Bottom (c): Disturbance amplification as a function of time. The asymptotic solution in Section 2.3.2.2 breaks down and diverges as the imaginary parts of the eigenvalues tend toward zero. Parameter values are Ma = 70, Ca = 0.01, Ga = 30, $\beta = 0.85$, $\delta = 0.01$, and $k = 0.21$. The top eigenfunction at $\tau = 0$ is used as the initial condition.

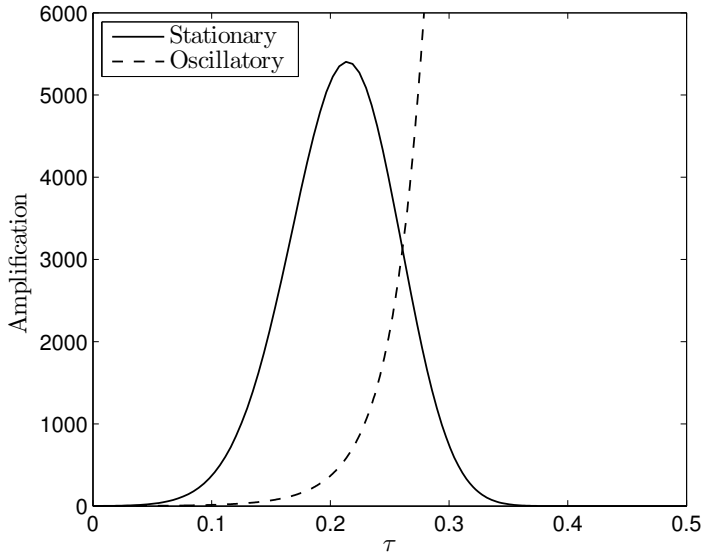


Figure 2.16: Numerically computed amplifications of stationary (solid) and oscillatory (dashed) modes when Ma = 100, Ga = 30, Ca = 0.01, $\beta = 0.85$, and $\delta = 0.01$. The stationary mode has wavenumber $k = 1.65$ whereas the oscillatory mode has $k = 0.33$ and the initial condition is taken to be the top eigenfunction at time $\tau = 0$. While the oscillatory mode obtains a larger overall amplification, the rapid growth of the stationary mode means that it can obtain much larger initial amplifications.

is less than eight times its initial value. The wavenumber $k = 0.3$ maximises the real part of the complex eigenvalues when $\tau = 0$, and $k = 1.54$ maximises the purely real eigenvalues.

As the Marangoni number is increased further, the oscillatory modes still obtain larger overall amplifications. However, the rapid initial growth of the stationary modes means they obtain larger amplifications in a shorter amount of time. For example, when Ma = 100, a stationary mode with wavenumber $k = 1.65$ obtains a maximum amplification of roughly 5500, whereas an oscillatory mode with wavenumber $k = 0.33$ has only been amplified by a factor of about 550 in the same duration. Figure 2.16 shows this situation in more detail. Again, these wavenumbers are chosen to maximise the real parts of the eigenvalues when $\tau = 0$. For $\mathrm{Ma} \gg \mathrm{Ma_s}$, we can conclude that the switch in dominance occurs not necessarily because the stationary modes obtain larger overall amplifications before the stabilisation occurs, but because they are amplified much more rapidly than the oscillatory modes.

The frozen-time analysis predicted that when Ga = 30, Ca = 0.01, and $\beta = 0.85$, it was possible for the oscillatory instability to occur for Marangoni numbers that are less than the initial critical value of $\mathrm{Ma_o} \simeq 53$. This raises the question of whether there is a smaller critical Marangoni that could be used to denote the onset of the instability. In the case when Ma = 53 and $\delta = 0.01$, we find that disturbances only obtain moderate amplifications with the largest being approximately 58. Moreover, the maximum amplification rapidly

decreases with Ma; for example, when $\mathrm{Ma} = 45$, we have $\max_{k,t} A(t;k) \simeq 5$. Therefore, the instabilities that occur for $\mathrm{Ma} < \mathrm{Ma_o}$ are unlikely to have any significant physical relevance and the critical Marangoni number is not expected to be below its initial value of $\mathrm{Ma_o} \simeq 53$.

We can compare the initial critical value of the Marangoni number associated with the onset of any instability when the fluid surface is and is not deformable. The linear stability analysis in Section 2.4 indicates that the critical Marangoni number in the non-deformable limit is 80. This is considerably larger than the value of 53 found above using the parameter values in (2.122). Furthermore, Figure 2.12 shows that the critical Marangoni number can be made even smaller by further decreasing Ga. Thus, films with deformable upper surfaces are much more susceptible to Marangoni instabilities, particularly when gravity is weak and surface tension is strong.

2.6 Application to experiments

We now apply the results from the linear stability analysis to several experimental studies of evaporating binary mixtures. First, we focus on the polystyrene-toluene mixtures of Bassou & Rharbi [8]. Later, we discuss experiments of drying paint layers. In addition, the linear stability results are used to determine conditions that may enable the oscillatory instability to be observed experimentally.

2.6.1 Interpreting the experimental results of Bassou & Rharbi

The results of the linear stability analysis can be compared with the experimental observations of Bassou & Rharbi [8], who studied convection in polystyrene-toluene mixtures. These mixtures were deposited onto a glass substrate and spread into a thin film using a doctor blade to control the initial thickness. The substrate-film system was stored inside a chamber that was held at 22.5°C. The exact lateral dimensions of their films were not reported; however, their data indicates that the films span at least 1 cm in both horizontal directions. The thickest fluid layers had an initial height of 1.4 mm so taking the films to be of infinite horizontal dimension in our mathematical model is at least somewhat justified. To control the evaporation rate, the roof of the chamber had several metallic covers, each with a different number of uniformly distributed holes. The rate of evaporation was determined by placing the system on a microbalance, measuring the mass loss as a function of time, and then dividing by the surface area of the film. The evaporation rate was found to vary during the experiments, so the values that Bassou and Rharbi report are those that were measured during the first 30 seconds of the experiment. The convection cells were visualised indirectly using particle tracking and the borders of these cells could be directly observed using a microscope.

The first set of data that is presented by Bassou and Rharbi is the final profile of a film that was initially composed of $\beta = 85\%$ solvent (by volume) with a mean thickness of $h_m = 1.4$ mm. Upon drying, the layer obtained an average thickness of 95 μm. This can be compared to the (dimensional) steady-state base-state film thickness, which is $(1 - \beta)h_m$. This limit corresponds to the situation when all of the solvent evaporates from the fluid layer; therefore, it represents a theoretical minimum of the film thickness. By inserting the relevant parameter values, we find that $(1 - \beta)h_m = 210$ μm, which is more than twice the experimental value. This is a slightly puzzling result, although the reduction in volume may be a result of conformational changes that occur in the polymer phase, enabling them to pack more tightly together.

Another interesting aspect of the film profile is that it clearly shows the layer has a non-uniform thickness. The height of the film varies from 70 μm to 120 μm, giving the surface a corrugated appearance. These corrugations have a well-ordered periodic structure with a wavelength of roughly two millimetres. This is about one order of magnitude larger than the mean thickness of the film; thus, the corrugations can be considered to be long relative to the height of the layer. The capillary and Galileo numbers for this film can be estimated using the parameter values in Table 2.1. For a film that is initially 1.4 mm thick, we find that $\mathrm{Ca} \simeq 5 \cdot 10^{-6}$ and $\mathrm{Ga} \simeq 10^5$. Based on these, one may expect the film to remain flat because of strong surface tension and gravity. However, the strengths of these effects slowly decrease with the film thickness so the effective non-dimensional numbers given in (2.53) provide a better characterisation of their physical relevance. From the inverse relationship between the effective capillary number and the film thickness, we find that C decreases by only one order of magnitude to $C \simeq 7 \cdot 10^{-5}$ as the film thins to an average thickness of 95 μm. This seems to indicate that surface tension is likely to remain strong throughout the drying process, thus inhibiting the formation of short-wave corrugations. The cubic dependence of the Galileo number on the film thickness, however, means that the stabilising effects of gravity are substantially weakened as the film dries. Indeed, we find that $G \simeq 41$ at the end of the drying; a reduction by roughly four orders of magnitude. This may account for the appearance of long-wave surface deformations, which gravity is known to stabilise.

The next set of data that is relevant for this analysis concerns the onset of convection. Bassou and Rharbi only document the appearance of stationary convection cells in their experiments; they make no mention of oscillatory behaviour. Reasons for this will be discussed further below. The conditions for stationary convection in mixtures that were initially composed of 85% solvent by volume were studied. For convection to be consistently observed, the films were required to have a thickness of at least 100 μm. This film height defines an experimental critical Marangoni number of approximately 14.5. The associated

Galileo and capillary numbers are Ga $\simeq$ 48 and Ca $\simeq 7 \cdot 10^{-5}$. The frozen-time analysis predicts that for these values of Ga and Ca the onset of both modes of instability, stationary and oscillatory, occurs when Ma $\simeq$ 80; see Figure 2.12 (a). The corresponding critical film thickness is 235 μm, which is considerably larger than the experimental value of 100 μm. Thus, the frozen-time approach seems to predict that films are stable when experimentally they are found to be unstable.

To explore this in more detail, we look at the maximum perturbation amplifications that result from the instability. If the initial height of the film is taken to be 294 μm, which is 25% larger than the theoretical value of the critical thickness, then the corresponding non-dimensional numbers are $\delta \simeq 0.075$, Ma $\simeq$ 125, Ca $\simeq 2 \cdot 10^{-5}$, Ga $\simeq 10^3$, and $\beta = 0.85$. The maximum amplification in time and over a range of wavenumbers is computed when the initial condition is taken to be the top eigenfunction. We find that such perturbations can only be amplified by a factor of about 18. This is likely to be too small for convection patterns to be observed in an experimental setting; hence, the system can still be considered stable.

Many of the results presented by Bassou and Rharbi are for films that have an initial thickness of 1.4 mm. In this case, the Marangoni number is roughly $3 \cdot 10^3$, which greatly exceeds the theoretical critical value of approximately 80. Consequently, the top eigenvalues are real and large; we find that $\max_k\{\lambda(k)\} \simeq 221$ when $\tau = 0$. The rapid amplification of perturbations in this parameter regime suggests that the instability will quickly develop and possibly enter the nonlinear regime before the base state settles into its quasi-stationary profile. Thus, the application of our linear stability analysis to this system is questionable. Nevertheless, these results give a strong indication that a Marangoni instability occurs in such films. This would explain the appearance of surface deflections discussed previously and the observation of convection in films that are initially 1.4 mm thick.

The additional stability that the mathematical model exhibits may be the result of assuming the system is isothermal. In reality, the evaporation of solvent will cool the fluid near the gas-liquid interface because some thermal energy is required to overcome the latent heat of vaporisation. The vertical temperature gradient that subsequently develops across the fluid layer can support buoyancy-driven and/or thermocapillary-driven convection. Bassou and Rharbi argue that these physical mechanisms, individually, are not strong enough to induce convection in their experiments. The relevance of thermally induced gradients in the density and surface tension can be assessed by calculating the thermal Rayleigh and Marangoni numbers, Ra_T and Ma_T, respectively. These are defined as

$$\mathrm{Ra}_T = \frac{\rho g \alpha \Delta T h_m^3}{\mu \kappa}, \quad \mathrm{Ma}_T = \frac{\gamma_T \Delta T h_m}{\mu \kappa}, \tag{2.123}$$

where α is the coefficient of thermal expansion, ΔT is the vertical temperature gradient across the film, $\gamma_T = -\partial\gamma/\partial T$ describes how the surface tension changes with respect to temperature, and κ is the thermal diffusivity. Bassou and Rharbi measured both the temperature difference across the layer and the variation of surface tension with temperature to find that $\Delta T = 5$ K and $\gamma_T = 1.5 \times 10^{-4}$ N·m^{-1}·K^{-1}. Furthermore, they report that for pure toluene, $\alpha = 1.07 \times 10^{-3}$ K^{-1} and $\kappa = 1.04 \times 10^{-7}$ m^2·s^{-1}. For the thickest films with $h_m = 1.4$ mm, the thermal Rayleigh number is $\mathrm{Ra}_T \simeq 9$. This is less than two orders of magnitude smaller than the critical value needed to induce convection [97]. Thus, thermal buoyancy effects are, indeed, likely to be negligible. For films that range from 100 μm to 1.4 mm, the thermal Marangoni numbers lie between 4.8 and 67. Although these are smaller than the critical value of 80 found by Pearson [121], thermal-Marangoni effects are appreciable in thicker films and they could act in conjunction with their solutal counterparts to induce and reinforce an instability.

To determine whether thermal and solutal Marangoni effects can act in tandem, we explore the time that is required to establish the associated gradients in temperature and composition. The Lewis number, Le, characterises the relative rates of mass diffusion and thermal diffusion. It is defined as the ratio of the time scale of mass diffusion, $\tau_{\mathrm{mass}} = h_m^2/D$, to the time scale of thermal diffusion, $\tau_{\mathrm{heat}} = h_m^2/\kappa$. Thus, the Lewis number is given by

$$\mathrm{Le} = \frac{\kappa}{D}. \tag{2.124}$$

Using the aforementioned parameter values along with those in Table 2.1, the Lewis number is found to be approximately 75. The large size of this number implies that heat diffuses much more rapidly than solvent. Therefore, by the time the solutal boundary layer begins to propagate through the film, the temperature profile and, in particular, the thermal gradient have fully developed. Thus, thermal contributions to surface-tension gradients may, indeed, act simultaneously with their solutal counterparts to reinforce the Marangoni instability. There could be experimental evidence to support such a claim. Bassou and Rharbi report that convection cells appear as early as 24 seconds in a film which is initially 1.4 mm thick. The corresponding time scales of thermal and mass diffusion are approximately 20 and 1,420 seconds, respectively. This calculation indicates that the thermal gradient would have been close to fully developed by the time convection cells were observed in this experiment, whereas the composition gradient would have still been forming and relatively weak. On one hand, this gives evidence to suggest that these convection cells are unlikely to be the sole result of a solutal Marangoni instability. On the other, the large solutal Marangoni number associated with such a film ($\mathrm{Ma} \sim 10^3$) does suggest the solutal instability will amplify disturbances at very large rates.

One destabilising mechanism that has yet to be discussed is compositional buoyancy. This may be relevant because polystyrene has a density that is roughly 21% greater than toluene; see Section 2.2.1. Thus, the evaporation of solvent from the surface will result in a layer of dense fluid above less dense fluid and this could trigger the onset of buoyancy-driven convection. The relevance of compositional buoyancy can be estimated by calculating the solutal Rayleigh number, Ra_S, given by

$$\mathrm{Ra}_S = \frac{(\rho_p - \rho_s) g h_m^3}{\mu D}, \tag{2.125}$$

where ρ_s and ρ_p correspond to the densities of solvent and polymer, respectively. Bassou and Rharbi state that $\rho_s = 867$ kg·m^{-3} and $\rho_p = 1050$ kg·m^{-3}. For films in the 100 μm to 1.4 mm range, we find that the solutal Rayleigh number lies roughly between $10 < \mathrm{Ra}_S < 10^4$. Thus, compositional buoyancy may, indeed, play a significant role in the onset of convection, particularly in the thicker films.

2.6.2 Observing the oscillatory instability

The parameter regime where the oscillatory instability is most likely to be observed corresponds to the physical situation when surface tension is strong and gravity is weak. The ideal way to achieve such conditions would be to run an experiment in a microgravity environment; however, using thin, low-density mixtures can also offset the stabilising effects of gravity.

There are practical limits to how strong the effects of surface tension can be. This is partly due to the fact that the range of wavenumbers which are in the unstable, oscillatory regime tends to decrease with the capillary number. In the extreme case when the capillary number tends towards zero, this range of wavenumbers vanishes and the oscillatory instability is completely suppressed. Thus, if surface tension is too strong, the wavelength of the unstable oscillatory modes could be larger than the dimensions of the vessel containing the mixture. Another aspect to consider is that strong surface tension will tend to reduce the amplitude of surface deflections, perhaps increasing the difficulty of detecting the presence of the oscillatory instability.

From the definition of the capillary and Galileo numbers (see (2.16) and (2.19)), it is clear that a simple way to vary the effective strength of surface tension and gravity is by changing the initial thickness of the fluid layer. Furthermore, the linear stability analysis indicates that the oscillatory instability can initially be isolated whenever $\mathrm{Ca} < 10^{-2}$ and $\mathrm{Ga} < 47$. Thus, by imposing these conditions, a range of film thicknesses can be determined that allow the oscillatory instability to be dominant provided the Marangoni number is not

too large. This range is given explicitly by

$$\frac{100\mu D}{\gamma_r} < h_m < \left(\frac{47\mu D}{\rho g}\right)^{1/3}. \tag{2.126}$$

For films that lie outside of this region because they are too thick, gravity causes the onset of the oscillatory instability to occur at larger Marangoni numbers than the stationary mode. This makes it unlikely for the oscillatory modes to grow larger than the stationary ones. If h_m is below the lower bound in (2.126), then both modes of instability can dominate in theory. The dominance is determined mainly by whether the Galileo number is above or below the particular value Ga_p defined in Section 2.5.3.

The final conditions that ensure the oscillatory instability is isolated are on the Marangoni number. In particular, the Marangoni number must exceed the threshold required to activate the oscillatory mode of instability, but it must remain small enough to prevent the onset of the stationary mode. If h_m is chosen in such a way that the inequality in (2.126) is satisfied, then the strength of the Marangoni effects can be controlled through the evaporation rate k_m. For the oscillatory instability to occur at least initially, the Marangoni number must be greater than $\mathrm{Ma}_\mathrm{o} = (24 + 8\,\mathrm{Ga})/5$. To prevent the onset of the stationary instability it must also satisfy $\mathrm{Ma} \lesssim 80$. These restrictions limit the evaporation rate to lie between the values

$$\left(\frac{24 + 8\,\mathrm{Ga}}{5}\right)\frac{\mu D^2}{\beta(1-\beta)\rho\gamma_c h_m^2} < k_m < \frac{80\mu D^2}{\beta(1-\beta)\rho\gamma_c h_m^2} \ll \frac{D}{h_m}, \tag{2.127}$$

where the last inequality arises due to our primary assumption that $\delta \ll 1$.

To further aid in the observation of the oscillatory instability, the initial solvent volume fraction β can be chosen to be larger than the critical value of β_c given in (2.120), which requires that $\mathrm{Ga} > 3/2$. Under these conditions, the critical Marangoni number associated with the onset of the oscillatory instability, Ma_o, decreases initially, thus prolonging the duration of this instability.

These results can be discussed in the context Bassou and Rharbi's experiments by evaluating the inequality in (2.126) using the parameter values listed in Table 2.1. For the oscillatory instability to occur at lower Marangoni numbers than the stationary instability, the films should have an initial thickness between 690 nm and 100 μm. This range lies slightly outside the thinnest films that were studied in any detail by Bassou and Rharbi, which were 150 μm initially. In such films the oscillatory instability would be subdominant, which likely explains why only the stationary instability was observed in their experiments.

We can also apply the linear stability results to investigate the dynamics of drying paint films; see, for example, Howison *et al.* [79] or Wilson [156]. Although no instabilities are found in these studies, several observations, namely the crest-to-trough reversal that is

described in the introduction and decaying oscillations in numerical simulations, indicate that the parameters associated with paint films might be close to the regime where the oscillatory instability occurs. If we insert the parameter values from Howison *et al.* [79] into (2.126), we find that the oscillatory instability should be observed in paint films with an initial thickness between 20 μm and 298 μm, provided the Marangoni number is above the critical value of $\mathrm{Ma_o}$. The paint films studied in the aforementioned references do fall within this range; for example, $h_m = 60$ μm is often used as a characteristic value of the initial thickness of the layer. According to our theory, however, these films are linearly stable because of small Marangoni numbers; we find that $\mathrm{Ma} \simeq 1.3 \times 10^{-3}$ whereas the critical value is $\mathrm{Ma_o} \simeq 5.4$. Although the films have the correct initial thickness for the oscillatory instability to occur, they are ultimately stable which could explain the presence of decaying oscillations and a finite number of reversals.

It would be interesting to perform experiments with evaporating layers of paint with greater initial thicknesses and larger evaporation rates. The latter could be made possible by, for example, prescribing an airflow above the layer, although one would have to be certain that the air does not influence the dynamics of the film. Both of these factors will lead to larger Marangoni numbers and it might be possible to surpass the value that is needed to induce the oscillatory instability in the system.

2.7 Discussion and conclusion

In this chapter we address two main questions. Firstly, we investigate the role of solutal Marangoni instabilities in evaporating mixtures. Secondly, we explore methods for systematically assessing the linear stability of a slowly evolving base state.

In this context, the solutal Marangoni instability is a result of evaporation-induced concentration gradients and variations in the surface tension. When the surface tension depends on the local composition of the mixture, surface-tension gradients caused by non-uniformities in the concentration can trigger the onset of convection cells and lead to surface deformations if they are strong enough to overcome the stabilising effects of viscosity, mean surface tension, and gravity.

The onset of instability was investigated mathematically within the framework of linear stability theory. Unlike traditional linear stability problems, the base state is time dependent as a result of evaporative mass loss. By assuming that evaporation occurs on a much longer time scale than diffusion, we find that the quasi-stationary evolution of the base state is much slower than the evolution of perturbations to it. This separation of time scales is exploited to study the stability of the base state using frozen-time and asymptotic methods.

The frozen-time method treats the slow time that appears in the base state as a parameter rather than a time variable, thus allowing traditional techniques from linear stability theory to be applied. One benefit of this approach is that it is possible to deduce the instantaneous stability of the system over a wide range of parameter values as the system slowly evolves. Moreover, it is relatively easy to identify regions of parameter space where an instability of a particular type is likely to occur. The main shortcoming of this method is that it does not give any direct insight into how large perturbations to the base state are amplified before the system stablises.

Overcoming this issue led to the derivation of an asymptotic solution to the linear stability problem that is uniformly valid over the long periods of time on which the base state evolves. The asymptotic solution is derived in two different ways. One approach is based on the method of multiple scales, whereas the other starts from the WKB anstaz. This asymptotic solution generalises the one presented by Hennessy & Münch [74] by considering an arbitrary number of eigenmodes. It also extends the results of Lick [103] and Doumenc *et al.* [55] by considering the next-order corrections. A comparison of the asymptotic approximations to numerical solutions of the linearised problem shows that the former is exceptionally accurate, provided that the eigenvalues of the linear operator remain well separated. Extending the asymptotic solution to the case of repeating or crossing eigenvalues would be a useful area of future work, as these cases do arise in practice; see Figure 2.15, for instance. The asymptotic solution was also used to establish a connection between the frozen-time eigenvalues and the temporal evolution of the system. In particular, we found that the conventional notions of stability can be applied to slowly varying problems; positive and negative eigenvalues correspond to growing and decaying perturbations, respectively, and a zero eigenvalue corresponds to a transition from growth to decay or vice-versa. Our analysis shows that the frozen-time and asymptotic approaches complement each other well, with each method providing crucial insight into the dynamics that occur within the system.

A key result of the linear stability analysis is that it indicates the presence of two modes of instability in the system. One of these corresponds to the classical Bénard–Marangoni instability first investigated by Pearson [121]. This mode is typically associated with short-wavelength convection cells and small surface deformations; see Figure 2.1 (a). The second mode of instability is oscillatory and is related to the crest-to-trough reversals that are seen in drying paint layers and waterborne coatings. This mode is due to the combined action of gravity, surface tension, and surface-tension gradients. When a deformed film levels under the action of gravity and surface tension, the concentration of solvent is higher under the crests compared to the troughs. This leads to surface-tension gradients that enhance the levelling process. Moreover, these gradients are still present when the film becomes flat, and

thus fluid is pulled from regions that used to be crests to regions that used to be troughs. The accumulation and depletion of fluid causes crests to become troughs and vice-versa, and the process then repeats itself.

The two modes of instability are found to compete with each other, with the stationary mode typically being dominant when both occur for the same parameter values. This dominance arises because short-wave cellular modes are amplified more rapidly than long-wave deformational modes. However, in films with strong surface tension, which we characterise by the capillary number condition $\mathrm{Ca} < 10^{-2}$, the dominance can be reversed if the Marangoni number is not too large. This is due to the fact that when $\mathrm{Ca} < 10^{-2}$, regions of parameter space exist where only the oscillatory mode of instability occurs. A defining feature of these regions is that the onset of the oscillatory mode occurs at lower values of the Marangoni number compared to the stationary mode. The existence and size of these regions depend sensitively on the effective strength of gravity, as measured by the Galileo number, Ga. This is because gravity plays a major role in determining the critical Marangoni number associated with the onset of the oscillatory instability. Physically, this strong dependence corresponds to the fact that surface-tension gradients have to pull harder to cause a reversal in heavier fluids; thus, the critical Marangoni number increases with Ga. The exact relation is $\mathrm{Ma_o} = (24 + 8\,\mathrm{Ga})/5$. On the other hand, gravity does not play a large role in determining the critical Marangoni number associated with the onset of the stationary instability, $\mathrm{Ma_s}$, when surface tension is strong. This is due to the fact that, in the absence of buoyancy, gravity will only play a role if the fluid surface is deformed. Strong surface tension, however, prevents the short-wave cellular patterns from deforming the surface. For $\mathrm{Ca} < 10^{-2}$, our analysis indicates that $\mathrm{Ma_s} \geq 80$. Therefore, the regions where the oscillatory instability is isolated and consequently dominant can be identified as $\mathrm{Ca} < 10^{-2}$, $\mathrm{Ga} < 47$, and $(24 + 8\,\mathrm{Ga})/5 < \mathrm{Ma} < 80$. Using these parameter bounds, we have determined experimental conditions, such as film thicknesses and evaporation rates, that might be useful when attempting to locate or observe the oscillatory instability.

A comparison of our theoretical results with the experimental observations of Bassou & Rharbi [8] led to several interesting findings. Firstly, their films developed long-wavelength corrugations with amplitudes that are comparable to the mean thickness of the layer. This is remarkable because the small capillary and large Galileo numbers associated with the system suggest that the films should remain relatively flat. From a modelling perspective, this makes it tempting to only consider the case when the fluid surface is non-deformable. However, these two stabilising mechanisms weaken during the drying process, as characterised by effective non-dimensional numbers that arise from an additional rescaling of the linearised problem. Gravitational effects, in particular, are expected to decrease by four

orders of magnitude, possibly explaining the occurrence of long-wave surface deformations. This problem shows that some care needs to be taken when studying the stability of slowly varying base states because it is possible for simplifying assumptions to become invalid as the system evolves over long time scales.

This comparison also showed that our theoretical films are much more stable compared to Bassou and Rharbi's experimental films. Our analysis predicts that, in the regime of strong surface tension and gravity, the minimum film thickness needed to observe convection is 235 μm. This is roughly two times larger than the critical experimental thickness of 100 μm. Two destabilising mechanisms were discussed that could account for this disparity. The first of these is related to thermally induced gradients in the surface tension. A comparison of diffusive time scales reveals that thermal gradients develop much more rapidly than their solutal counterparts. Thus, it seems likely that thermal Marangoni effects, while not strong enough to cause an instability on their own, can act in conjunction with solutal Marangoni effects to enhance the instability. The second potential mechanism that could lead to additional destabilisation is compositional buoyancy. This results from density differences between the two components, particularly when the volatile solvent is less dense than the non-volatile solute. For the polystyrene-toluene mixtures considered by Bassou and Rharbi, compositional buoyancy is only expected to play a role in thicker films. The topic of compositional buoyancy will be further discussed in Chapter 3.

An insightful topic of future work would be the investigation of the combined action of solutal and thermal Marangoni effects in evaporating binary mixtures. Of particular interest would be a study that determines whether including both effects can reconcile the differences between our theory and Bassou and Rharbi's experiment. Obtaining knowledge about the relevance of thermal effects will be invaluable for future studies that aim to model complex scenarios involving multiple polymers blended in a solvent or spin-cast mixtures.

The onset of both modes of instability and their persistence over long times is likely to be strongly influenced by the rheology of the fluid. In this chapter, we have assumed the mixture remains Newtonian with a constant viscosity. However, this is generally not true for polymer solutions because they exhibit shear-thinning behaviour after a critical shear rate is exceeded. Below this critical value, the Newtonian regime is recovered [44, 116]. As shown by Kulicke & Kniewske [100] for polystyrene (PS) and toluene mixtures, the critical value of the shear rate can decrease by several orders of magnitude as the molecular weight and concentration of polymer increases. Using their data, we can roughly estimate the relevance of shear-thinning behaviour in this work, which is based on the PS-toluene solutions used by Bassou & Rharbi [8]. The critical shear rate, $\dot{\gamma}_{\text{crit}}$, in a 3% mixture by weight using PS with a (relative) molecular weight of 3.3×10^5 is approximately 10^4 s^{-1}.

The PS used by Bassou and Rharbi had a slightly smaller molecular weight of 1.5×10^5, but the initial concentration of polymer was often 15% by volume (17.6% by weight). If we assume that these two mixtures can still be compared, then a typical shear stress can be estimated using (2.18h) to obtain

$$\dot{\gamma} \simeq \frac{D}{h_m^2}\,\mathrm{Ma} = \frac{k_m \beta(1-\beta)\rho\gamma_c}{\mu D}. \tag{2.128}$$

The order of magnitude of these parameters can be determined from Table 2.1. Using these to calculate the shear rate, we find that $\dot{\gamma} \simeq 1\ \mathrm{s}^{-1} \ll \dot{\gamma}_{\mathrm{crit}}$. This comparison gives some indication that shear-thinning effects are not important during the early stages of drying when the instability is developing and it provides some justification for the Newtonian rheology used in the mathematical model.

In the absence of non-Newtonian effects, the viscosity of a binary mixture will still depend on the solute concentration. Previous theoretical works have modelled the viscosity as an exponentially increasing function of the polymer concentration; see Münch *et al.* [112] or Eres *et al.* [63]. Including this dependence in the current model is expected to stabilise the system because Marangoni effects are effectively weakened as the mixture viscosity increases due to the depletion of solvent. Indeed, the main stabilising mechanism in the paint drying simulations of Eres *et al.* [63] seems to be due to a composition-dependent viscosity. Thus, a more comprehensive linear stability analysis that includes realistic fluid rheologies would also aid in determining whether the oscillatory instability found here is physically relevant. The asymptotic solution that was derived in Appendix A.1 would be a helpful tool to carry out such an analysis because it can capture the slow rheological changes that occur during drying process. This serves to further highlight the usefulness and wide range of applicability of such a solution.

Chapter 3

Multiphase models of solvent-polymer mixtures

3.1 Introduction

Fluids that are composed of two or more components are ubiquitous in nature, biology, and industry. Examples of such fluids include magma, which is a mixture of molten rock and volatile compounds, and clouds, which are suspensions of liquid droplets that travel in a gas. Blood is a suspension of cells in a plasma and also falls into this category. Much of our industry revolves around multiphase and multicomponent fluids. For instance, many cooling systems operate by transferring heat to a moving liquid. This can cause the liquid coolant to boil, resulting in a two-phase flow composed of liquid and gas. The ability and capacity for such fluids to effectively transfer heat will depend crucially on the fraction of gas to liquid as well as the spatial distribution of these phases, thus demonstrating the importance of having models to predict the motion and thermal properties of two-phase fluids. A further example of the industrial use of multicomponent fluids is in the fabrication of thin polymer films. This is often done using a coating process, whereby one or many polymers are blended in a volatile solvent and the mixture is deposited onto a substrate where it is left to dry. Several complex physicochemical processes occur during the drying process, leading to interesting and non-trivial spatial distributions of polymer. The arrangement of polymers within the film and its surface morphology are generally linked in some way to its performance. This makes it tempting to try to optimise the performance of the film over different morphologies and arrangements of polymer. While this is a nice theoretical concept, carrying this out in practice requires an extensive understanding of how the various components of mixture interact and evolve as the solvent is removed from the system.

The wide-spread appearance of multicomponent flows in many areas of the applied sciences has led to a broad literature where mathematical models of such fluids are used to study a diverse set of problems. In the realm of mathematical biology, Breward *et al.* [29]

have studied avascular tumour growth using a two-phase model for the tumour cells and the extracellular water. Two-phase models were also used by Bohun & Breward [25] to examine the dynamics of egg yolk in amphibian embryos and by Kimpton *et al.* [92, 93] to study cell motility. King & Oliver [95] investigate the motion of a poroviscous drop over a substrate with a multiphase model in the context of cell movement. Recent work by Winstanely *et al.* [157] focuses on developing and analysing a solvent-polymer model for the growth of biofilms. Multiphase models have also been applied to the geosciences by Takei & Katz [147] and Katz & Takei [90], who study the effects of viscous anisotropy in a deforming, two-phase aggregate that is supposed to represent magma and rock. Further applications of multiphase fluids extend as far as the food and beverage industry. Howell & Muldoon [78] discuss how ice cream can be modelled as a two-phase mixture consisting of gas bubbles that are trapped in a deformable matrix. Fowler [67] briefly mentions how a two-phase model can be used to study wave flow in a freshly poured pint of Guinness.

A unifying theme that relates these studies is their formulation of the problem and approach to modelling the mixture. Rather than considering the microscopic motion of the individual phases, macroscopic equations that describe the average motion and composition of each phase are used. One benefit of this approach is that it enables the phases to be treated as overlapping and continuous, which removes the need to track the geometry and boundaries of single-phase microscopic domains. An important point is that the individual phases of the mixture remain distinguishable in the macroscopic model; thus, they can be treated separately, which allows their unique physical properties, such as density and rheology, to still be captured. In addition, chemical reactions and bulk phase transformations can also be incorporated into such models.

Macroscopic models provide a flexible framework for studying a wide variety of mixtures. Despite this fact, there seems to be relatively little work on formulating multicomponent models of evaporating solvent-polymer blends. Many of the models that are found in the literature focus on the case of binary mixtures consisting of a non-volatile solute and a volatile solvent. It is often assumed that the mixture has a constant density and that the mass flux of each component can be decomposed into a advective flux associated with the mixture velocity, and a diffusive flux given by Fick's law[1] [63, 79, 156]. Using these two assumptions, the model can be reduced to what is essentially a single-phase hydrodynamic system governing the mixture velocity and pressure, and an advection-diffusion equation describing the transport of solvent or solute. In fact, this procedure was used to derive the model in Chapter 2. The advantage of such a model is that it is relatively simple; however,

[1]Here we mean the traditional form of Fick's law for ideal mixtures, which states the diffusive flux is proportional to the concentration gradient.

it is not without its criticisms. For one, the polymer (or solute) is generally much denser than the solvent. Furthermore, the assumption that Fick's law holds throughout the entire drying process and, in particular, when the solvent and solute have equal concentrations, is questionable.

Density differences between the solvent and polymer phases and the associated effects of compositional buoyancy can generate flows that may play an important role during the drying process. For example, the depletion of solvent from the free surface due to evaporation will tend to produce a polymer-rich skin. This can inhibit further evaporation, thus terminating the drying process before all of the solvent has been removed from the layer. However, if the density of the polymer is greater than that of the solvent, gravity may inhibit the formation of this skin by causing the polymer to settle on the substrate before it can accumulate below the free surface. The formation of a dense layer of polymer-rich fluid on top of a less-dense layer of solvent-rich fluid naturally leads to the question of whether an instability can arise in the system. Bergantz & Ni [15] use numerical simulations of a macroscopic two-phase model to study the evolution of a mixture that begins with a thin layer of the denser fluid on top of the less-dense fluid. They show that a Rayleigh–Taylor instability leads to the formation of dense plumes that fall towards the bottom surface. Depending on the viscosity ratio of the two components, the plumes either merge or remain relatively well separated. The onset of convection in an evaporating binary mixture has been studied by Machrafi *et al.* [104]. The mixture velocity and pressure were assumed to satisfy the incompressible Navier–Stokes equations in the Boussinesq approximation and advection-diffusion equations were used to model the evolution of the concentration and temperature fields. Effects due to compositional buoyancy were considered in their study, but they were not found to play a significant role in the onset of convection.

3.1.1 Aims and outline

The goal of this chapter is to derive a macroscopic model for an evaporating solvent-polymer mixture based on a rigorous averaging of a microscopic model. We will not assume that the polymer and solvent have the same density, nor will we prescribe how these phases flow relative to each other. Rather, we will let this be determined by the physics of the model. Two main scenarios will be explored using the macroscopic model. First, we will consider a two-component mixture consisting of a polymer phase and a less-dense solvent phase in a gravitational field. Using this model, the interplay between gravity, evaporation, and skin formation will be explored. The second situation we consider is that of three-phase flow in the absence of gravitational effects. The three phases correspond to a volatile solvent, dispersed or partially dissolved polymers, and polymers that have completely demixed from

the solvent. By considering two separate polymer phases, we can explore how phase separation may be captured, at least qualitatively, in a multiphase fluid model. An interesting consequence is that such a model will also provide a framework for exploring the coupling and interaction between phase separation and the hydrodynamics of the mixture. This is particularly relevant for industrial applications involving evaporating solvent-polymer mixtures because hydrodynamic effects, such as instabilities, are believed to initiate the process of phase separation, which is responsible for the formation of polymer-rich structures throughout the dried film [60].

The outline of the chapter is as follows. In Section 3.2, we formulate a microscopic model of an evaporating solvent-polymer model and average it to obtain a macroscopic model. We then examine the behaviour of an evaporating two-phase fluid in a gravitational field in Section 3.3. In Section 3.4, we focus on three-phase flow without gravitational effects. A discussion of the results and a conclusion is given in Section 3.5.

3.2 Mathematical modelling

The development of a mathematical model of a multiphase fluid generally requires three major steps. The first is the formulation of a microscopic model that details both the bulk and interfacial behaviour of all of the phases. Once this is established, a macroscopic set of equations is derived from the microscopic model using a suitable averaging procedure. The final step involves closing the model by postulating that certain macroscopic quantities satisfy some prescribed constitutive laws. Occasionally, these laws can be motivated from what happens on the microscale.

We now build our model of a solvent-polymer mixture using this three-step procedure. Our derivation will closely follow that found in the paper by Drew [56] and the textbook by Drew & Passman [57], both of which have become standard sources of literature on the subject. However, similar treatments are also given in Fowler [67] and Ishii & Hibiki [80].

3.2.1 Microscopic model

The problems we are interested in studying involve a thin layer of fluid that consists of a polymer that has been blended in a solvent. We think of the fluid as being a three-component mixture that is composed of a solvent, partially dissolved polymers that are mixed with the solvent, and polymers that have demixed or separated from the solvent; see Figure 3.1 (a). Our consideration of two polymeric phases enables the model to capture the process of phase separation by allowing the polymer to go from a mixed phase to a demixed phase. The dispersed polymer phase is thought to overlap with the solvent phase, whereas the separated polymer phase forms its own domains that are embedded within the mixture.

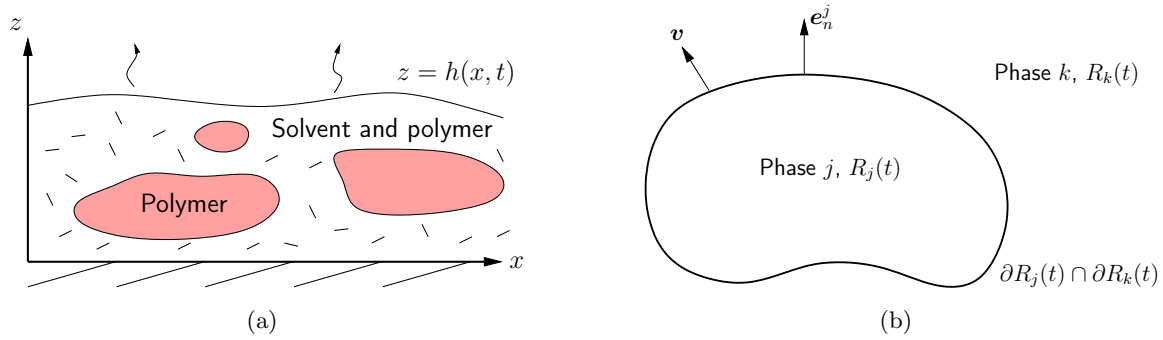


Figure 3.1: Left (a): We consider a three-component mixture consisting of a volatile solvent, a dispersed or partially dissolved polymer phase (short lines), and demixed polymers that have separated from the solvent (pink). This fluid is assumed to form a long layer of height $h(x,t)$ on a flat substrate. Right (b): The microscopic geometry between two phases. Regions of phase j and k are denoted as $R_j(t)$ and $R_k(t)$, respectively. The interface between these domains is given by $\partial R_j(t) \cap \partial R_k(t)$. The unit vector $\boldsymbol{e}_n^j$ points out of phase j and $\boldsymbol{v}$ describes the velocity of the j-k interface.

The fluid is assumed to lie on top of a non-permeable substrate and the upper surface of the layer is exposed to an open and unsaturated atmosphere. The solvent is assumed to be the only volatile component and hence it evaporates. For simplicity, the fluid is assumed to be isothermal. As in Chapter 2, we neglect the dynamics of the gas above the fluid layer.

The fluid layer is modelled as two dimensional and described by the unbounded horizontal coordinate $x \in \mathbb{R}$ and the bounded vertical coordinate z, where $0 \leq z \leq h(x,t)$. Here, the free surface is given by $z = h(x,t)$, where t denotes time. We let $\boldsymbol{x} = x\boldsymbol{e}_x + z\boldsymbol{e}_z$ denote the position vector, where $\boldsymbol{e}_x$ and $\boldsymbol{e}_z$ are Cartesian basis vectors along the horizontal and vertical directions, respectively. We denote the regions occupied by the three phases as $R_s(t)$, $R_d(t)$, and $R_p(t)$, where the subscripts s, d, and p represent quantities associated with the solvent, dispersed polymer that is mixed with the solvent, and pure polymer that has separated from the solvent. The boundaries of these domains are given by $\partial R_j(t)$ and hence $\partial R_j(t) \cap \partial R_k(t)$; $j = s,d,p$; $k \neq j$ are the interfaces that form between different phases. We let $\boldsymbol{e}_n^j$ be the outward-pointing unit vector that is normal to the surface of phase j; see Figure 3.1 (b). The direction of tangent vectors to the interfaces do not matter so we denote these by simply $\boldsymbol{e}_t$. Similarly, when the direction of the normal vector does not matter, we write $\boldsymbol{e}_n$.

We now have the topological framework that is required to apply the laws of conservation of mass and momentum within each phase and on their boundaries. At this point, we make no assumptions about the compressibility or rheology of the phases. However, we do assume that the flow is sufficiently slow that inertial terms can be neglected in the momentum

balance. Thus, in each region, conservation of mass and momentum can be written as

$$\partial_t \rho_j + \nabla \cdot (\rho_j \boldsymbol{u}_j) = 0, \quad \boldsymbol{x} \in R_j(t), \quad j = s, d, p, \tag{3.1a}$$

$$\nabla \cdot \mathbf{T}_j - \rho_j g \boldsymbol{e}_z = 0, \quad \boldsymbol{x} \in R_j(t), \quad j = s, d, p, \tag{3.1b}$$

where ρ_j, $\boldsymbol{u}_j$, and $\mathbf{T}_j$ denote the corresponding density, velocity, and stress tensor of phase j, respectively, and g is the acceleration due to gravity. Initial conditions for the densities are given by $\rho_j(x, z, 0) = \rho_{ji}(x, z)$, where $j = s, d, p$.

Along the substrate we impose the usual no-flux and no-slip boundary conditions; thus,

$$\boldsymbol{u}_j = 0, \quad \text{on } \{z = 0\} \cap \partial R_j, \quad j = s, d, p. \tag{3.1c}$$

The solvent is assumed to evaporate from the free surface with a mass flux given by q_{evap}. This function will generally depend on the composition at the surface; in particular, it is expected to decrese as the concentration of the dispersed polymer phase increases. Conservation of solvent at the upper surface gives

$$\rho_s \left(\boldsymbol{u}_s - \boldsymbol{v}\right) \cdot \boldsymbol{e}_n^g = q_{\text{evap}}, \quad \text{on } \{z = h(x, t)\} \cap \partial R_s(t), \tag{3.1d}$$

where $\boldsymbol{v}$ denotes the velocity of the interface and $\boldsymbol{e}_n^g$ is the unit normal vector pointing into the gas. For this surface in particular, we may write

$$\boldsymbol{e}_n^g = \frac{-(\partial_x h)\boldsymbol{e}_x + \boldsymbol{e}_z}{\sqrt{1 + (\partial_x h)^2}}, \quad \boldsymbol{v} \cdot \boldsymbol{e}_n^g = \frac{\partial_t h}{\sqrt{1 + (\partial_x h)^2}}. \tag{3.1e}$$

Although the dispersed polymeric phase is mixed with the solvent, it cannot evaporate. This means that the net mass flux of the dispersed phase must be zero at the free surface. The same is true for the demixed polymer phase, as it cannot evaporate either. Thus, we have that

$$\rho_j \left(\boldsymbol{u}_j - \boldsymbol{v}\right) \cdot \boldsymbol{e}_n^g = 0, \quad \text{on } \{z = h(x, t)\} \cap \partial R_j(t), \quad j = d, p. \tag{3.1f}$$

The final set of boundary conditions at the free surface correspond to a stress balance across the interface. Shear stresses due to surface-tension gradients, *i.e.*, Marangoni stresses, are not considered here. In this case, the stress conditions become

$$\mathbf{T}_j \cdot \boldsymbol{e}_n^g = \sigma_{jg} \kappa \boldsymbol{e}_n^g, \quad \text{on } \{z = h(x, t)\} \cap \partial R_j(t), \quad j = s, d, p, \tag{3.1g}$$

where σ_{jg} corresponds to the surface tension between phase j and the gas and $\kappa = -\nabla \cdot \boldsymbol{e}_n^g$ is the curvature. The unit tangent vector at the free surface and the curvature can be written as

$$\boldsymbol{e}_t = \frac{\boldsymbol{e}_x + (\partial_x h)\boldsymbol{e}_z}{\sqrt{1 + (\partial_x h)^2}}, \quad \kappa = \frac{\partial_x^2 h}{\left[1 + (\partial_x h)^2\right]^{3/2}}. \tag{3.1h}$$

We remark that additional conditions would be required at the common interfaces that could potentially form between two of the mixture phases and the gas layer. Such interfaces are referred to as trijunctions because they form when three phases are simultaneously in contact with each other. The extra boundary conditions would likely take the form of stress and mass balances. However, such conditions will not be required in our derivation of a macroscopic model and hence we will not discuss them any further.

Additional boundary conditions are needed at the internal interfaces formed between adjacent phases. We assume that the polymer phases, on a microscopic level, are impermeable and, therefore, no solvent can flow into these regions. Thus, at the solvent-polymer interfaces, we have

$$(\boldsymbol{u}_s - \boldsymbol{v}) \cdot \boldsymbol{e}_n^s = 0, \quad \text{on} \quad \partial R_s(t) \cap \partial R_j(t), \quad j = d, p, \tag{3.1i}$$

Similarly, conservation of polymer across solvent-polymer interfaces requires

$$(\boldsymbol{u}_j - \boldsymbol{v}) \cdot \boldsymbol{e}_n^j = 0, \quad \text{on} \quad \partial R_s(t) \cap \partial R_j(t), \quad j = d, p. \tag{3.1j}$$

Polymers can partially dissolve into and separate from the solvent. This is modelled through interfacial mass transfer between the two polymer phases. We let q_r denote a reactive mass flux that leads to mixing or demixing of polymers. We associate $q_r > 0$ with demixing and the generation of polymer-rich domains. Thus, at polymer-polymer interfaces, we have the conditions

$$\rho_p \, (\boldsymbol{u}_p - \boldsymbol{v}) \cdot \boldsymbol{e}_n^p = -q_r(\rho_s, \rho_d, \rho_p), \quad \text{on} \quad \partial R_p(t) \cap \partial R_d(t), \tag{3.1k}$$

$$\rho_d \, (\boldsymbol{u}_d - \boldsymbol{v}) \cdot \boldsymbol{e}_n^d = q_r(\rho_s, \rho_d, \rho_p), \quad \text{on} \quad \partial R_p(t) \cap \partial R_d(t), \tag{3.1l}$$

where we note that $\boldsymbol{e}_n^p = -\boldsymbol{e}_n^d$ on these boundaries. From (3.1i)–(3.1l), we see that the usual jump conditions for mass are recovered; in particular,

$$[\rho_i \, (\boldsymbol{u}_i - \boldsymbol{v}) \cdot \boldsymbol{e}_n]_j^k = 0, \quad \text{on} \quad \partial R_j(t) \cap \partial R_k(t), \quad j = s, d, p, \quad k \neq j. \tag{3.1m}$$

The lack of a superscript on the normal vector means it can be either $\boldsymbol{e}_n^j$ or $\boldsymbol{e}_n^k$, as long as the same one used in the jump condition.

It is assumed that the tangential components of the velocities are equal across interfaces. Thus, we have the following no-slip conditions on all internal interfaces:

$$[\boldsymbol{u} \cdot \boldsymbol{e}_t]_j^k = 0, \quad \text{on} \quad \partial R_j(t) \cap \partial R_k(t), \quad j = s, d, p, \quad k \neq j. \tag{3.1n}$$

The last set of boundary conditions for the microscopic model represent normal and tangential stress balances across the internal interfaces. As before, Marangoni stresses due

to surface-tension gradients are not considered. The jump conditions for the stresses can be written as

$$-\left[\mathbf{T}\cdot\boldsymbol{e}_n\right]_j^k = \sigma_{jk}\kappa\boldsymbol{e}_n, \quad \text{on} \quad \partial R_j(t)\cap\partial R_k(t), \quad j=s,d,p, \quad k\neq j, \tag{3.1o}$$

where the curvature is given by $\kappa = -\nabla\cdot\boldsymbol{e}_n^j$.

Closing the microscopic model requires the prescription of constitutive laws for the stress tensors $\mathbf{T}_j$, $j=s,d,p$; the reactive mass flux q_r; and the evaporative mass flux q_{evap}. Once these are given, this model can, in principle, be solved to obtain a microscopic view of the dynamics. This is not expected to be straightforward due to the complex and time-dependent geometries of the domains. Thus, we focus on averaging these equations to obtain a macroscopic view of the dynamics. A detailed discussion of the microscopic constitutive laws, along with their relation to macroscopic quantities, will be given in Section 3.2.3.

3.2.1.1 Caveats of the microscopic model

The microscopic model presented here does have its limitations. For example, describing the demixing of polymers by an interfacial growth process prohibits the model from capturing the nucleation of domains. However, this shortcoming of the microscopic model can be avoided in the macroscopic model by a suitable choice of constitutive relations describing the conversion of one phase into the other. Additional details will be given below.

3.2.2 Averaging and the macroscopic model

A main difficulty with using the microscopic model is the need to track the constantly changing domains in which the bulk equations of the model hold. A macroscopic model, on the other hand, looks at the broader picture and does not consider individual domains of any particular phase. Instead, it takes an average of the microscopic model to obtain macroscopic equations that hold throughout the entire spatial domain. There are many different types of averages that can be used. Time and volume averages are commonly used in practice, as well as ensemble averages which consider many different realisations of the system [56, 57, 80]. Although the time and volume averages are perhaps the most intuitive and familiar, they can be mathematically cumbersome. Ensemble averages, which are slightly more abstract, have an elegant mathematical framework that draws upon the theory of generalised functions and distributions. To facilitate the derivation of the macroscopic equations, we will focus on ensemble averaging. Similar results can be obtained from the other averages, however.

The ensemble average of a scalar function $f(\boldsymbol{x},t)$ is defined as

$$\langle f\rangle(\boldsymbol{x},t) = \int_{\mathcal{E}} f(\boldsymbol{x},t;\nu)\,\mathrm{d}m(\nu), \tag{3.2}$$

where ν is a single realisation of the system; $\mathcal{E}$ is the ensemble, or set, of all possible realisations; and $\mathrm{d}m$ is the probability density of the states contained within the ensemble $\mathcal{E}$. The averaging operator inherits many of the linearity properties that are possessed by the integration operator [57]. Furthermore, when f is sufficiently smooth, the averaging operator commutes with differentiation operators:

$$\partial_t \langle f \rangle = \langle \partial_t f \rangle, \tag{3.3a}$$

$$\nabla \langle f \rangle = \langle \nabla f \rangle. \tag{3.3b}$$

The averages of vector and tensorial quantities are defined analogously to (3.2) and are assumed to satisfy the same linearity and differentiability properties.

3.2.2.1 The indicator function

Ideally, we would like to apply the averaging operator directly to the bulk equations of motion. In doing so, some difficulty is encountered because it becomes unclear whether a given equation will hold at a point $\boldsymbol{x}$ and time t in any given realisation. Thus, we introduce an indicator function that picks out the regions of the various phases at each time t in the realisation ν. More specifically, the indicator function for phase k, denoted by X_k, is defined as

$$X_k(\boldsymbol{x}, t; \nu) = \begin{cases} 1, & \boldsymbol{x} \in R_k(t; \nu), \\ 0, & \text{otherwise.} \end{cases} \tag{3.4}$$

By pre-multiplying the bulk equations with their corresponding indicator function, the ensemble averaging process becomes well defined. Before carrying this out, we first state several important properties of X_k. Details and proofs of these properties can be found in Appendix B.1.

To deal with the discontinuous nature of the indicator function, it is treated as a generalised function. This enables us to formally define its space and time derivatives within the framework of distributions. With this in mind, we can write the gradient of the indicator function as

$$\nabla X_k = -\delta_{\partial R_k}(\boldsymbol{x} - \boldsymbol{x}')\boldsymbol{e}_n^k, \tag{3.5}$$

where $\delta_{\partial R_k}(\boldsymbol{x})$ is the interfacial delta function, which is defined through the expression

$$\int_R \phi(\boldsymbol{x}')\delta_{\partial R_k}(\boldsymbol{x}' - \boldsymbol{x})\,\mathrm{d}V' = \int_{\partial R_k} \phi(\boldsymbol{x})\,\mathrm{d}s. \tag{3.6}$$

Here, R is a sufficiently large spatial domain that fully contains a region of phase k. From (3.5) and (3.6), we see that ∇X_k acts to pick out surface quantities related to the k-th phase.

The indicator function also satisfies the so-called topological equation,

$$\partial_t X_k + \boldsymbol{v} \cdot \nabla X_k = 0, \tag{3.7}$$

where $\boldsymbol{v}$ is a smooth extension of the interface velocity $\boldsymbol{v}$ into the domain R_k. This expression implies that the indicator function is transported with the interface.

It can also be shown that the indicator function satisfies several product rules. For example, when f is a scalar field, we have

$$\nabla(X_k f) = X_k \nabla f + f \nabla X_k. \tag{3.8a}$$

Due to the delta-function behaviour of ∇X_k (see (3.5)), the last term effectively picks out values of f on the interface of phase k. Analogous identities can be obtained if f is replaced with a vector quantity $\boldsymbol{w}$, or a tensor quantity $\mathbf{Q}$:

$$\nabla \cdot (X_k \boldsymbol{w}) = X_k \nabla \cdot \boldsymbol{w} + \boldsymbol{w} \cdot \nabla X_k, \tag{3.8b}$$

$$\nabla \cdot (X_k \mathbf{Q}) = X_k \nabla \cdot \mathbf{Q} + \mathbf{Q} \cdot \nabla X_k. \tag{3.8c}$$

Similarly, for time derivatives we find

$$\partial_t(X_k f) = X_k \partial_t f + f \partial_t X_k. \tag{3.9}$$

By interpreting (3.8) and (3.9) in a distributional sense, we can apply the averaging operator to them and use linearity and commutativity to obtain, in the case of the scalar function f, the identities

$$\langle \nabla(X_k f) \rangle = \nabla \langle X_f f \rangle = \langle X_k \nabla f \rangle + \langle f \nabla X_k \rangle, \tag{3.10a}$$

$$\langle \partial_t(X_k f) \rangle = \partial_t \langle X_k f \rangle = \langle X_k \partial_t f \rangle + \langle f \partial_t X_k \rangle. \tag{3.10b}$$

Furthermore, for vector and tensor quantities we have

$$\langle \nabla \cdot (X_k \boldsymbol{w}) \rangle = \nabla \cdot \langle X_f \boldsymbol{w} \rangle = \langle X_k \nabla \cdot \boldsymbol{w} \rangle + \langle \boldsymbol{w} \cdot \nabla X_k \rangle, \tag{3.10c}$$

$$\langle \nabla \cdot (X_k \mathbf{Q}) \rangle = \nabla \cdot \langle X_f \mathbf{Q} \rangle = \langle X_k \nabla \cdot \mathbf{Q} \rangle + \langle \mathbf{Q} \cdot \nabla X_k \rangle. \tag{3.10d}$$

The last terms in these expressions correspond to interfacial averages of the various quantities. Using these identities, the microscopic bulk equations can now be averaged to obtain a macroscopic model.

3.2.2.2 Averaged equations

Multiplying the continuity equations (3.1a) with X_j and making use of (3.8) and (3.9) yields

$$\partial_t(X_j\rho_j) + \nabla\cdot(X_j\rho_j\boldsymbol{u}_j) = \rho_j\left(\partial_t X_j + \boldsymbol{u}_j\cdot\nabla X_j\right), \quad j = s,d,p. \tag{3.11}$$

The right-hand side can be simplified using the topological equation (3.7). Taking the average of this equation and using the identities in (3.10) gives

$$\partial_t\langle X_j\rho_j\rangle + \nabla\cdot\langle X_j\rho_j\boldsymbol{u}_j\rangle = \langle\rho_j\left(\boldsymbol{u}_j - \boldsymbol{v}\right)\cdot\nabla X_j\rangle, \quad j = s,d,p. \tag{3.12}$$

Carrying out the same process for the momentum balance in (3.1b) results in the equations given by

$$\nabla\cdot\langle X_j\mathbf{T}_j\rangle - \langle X_j\rho_j g\boldsymbol{e}_z\rangle - \langle\mathbf{T}_j\cdot\nabla X_j\rangle = 0, \quad j = s,d,p. \tag{3.13}$$

The incorporation of the indicator function in the averaged equations (3.12) and (3.13) enables them to be applied throughout the entire domain of the problem, which, in this case, is given by $x\in\mathbb{R}$ and $0 < z < h(x,t)$.

The term on the right-hand side of (3.12) and the third term in (3.13) represent average interfacial mass and momentum sources, respectively. For convenience, we write

$$\Gamma_j = \langle\rho_j\left(\boldsymbol{u}_j - \boldsymbol{v}\right)\cdot\nabla X_j\rangle, \quad j = s,d,p \tag{3.14a}$$

$$\boldsymbol{m}_j = -\langle\mathbf{T}_j\cdot\nabla X_j\rangle, \qquad j = s,d,p. \tag{3.14b}$$

Without these terms, there would be no bulk interactions between the various phases as the internal interfaces have been averaged out. Thus, these terms will act as a strong source of dynamics and some care must be taken when constructing expressions for them.

Due to the mixture having three components, each phase can share an interface with two other phases. Thus, there can be two separate contributions to the interfacial source terms. This motivates decomposing them as

$$\Gamma_j = \Gamma_{jk} + \Gamma_{jl}, \tag{3.15a}$$

$$\boldsymbol{m}_j = \boldsymbol{m}_{jk} + \boldsymbol{m}_{jl}, \tag{3.15b}$$

where j, k, and l denote different phases. Before defining what these terms are, we introduce some additional notation that is required to distinguish the same quantity but at different interfaces. We denote the quantity f associated with phase j at the interface formed with phase k as f^I_{jk}. The interfacial source terms can then be written as

$$\Gamma_{jk} = \langle\rho^I_{jk}\left(\boldsymbol{u}^I_{jk} - \boldsymbol{v}\right)\cdot\nabla X_j\rangle, \tag{3.16}$$

$$\boldsymbol{m}_{jk} = -\langle\mathbf{T}^I_{jk}\cdot\nabla X_j\rangle. \tag{3.17}$$

These expressions enable the microscopic boundary conditions to be used in evaluating the macroscopic interfacial source terms.

We begin with the mass transfer across interfaces. The solvent does not react with any of the polymer phases nor does it undergo any phase change in the bulk. By substituting (3.1i) into (3.16), we find that $\Gamma_{sd} = \Gamma_{sp} = \Gamma_{ds} = \Gamma_{ps} = 0$. From these relations, it immediately follows from (3.15a) with $j = s$ that

$$\Gamma_s = 0. \tag{3.18}$$

The dispersed polymer phase can separate from the mixture, leading to the interfacial growth of concentrated polymer domains. It is also conceivable for some of the polymers to partially dissolve into the solvent. Using the local kinematic boundary conditions at the polymer-polymer interfaces, (3.1k) and (3.1i), it follows from (3.16) that

$$\Gamma_{dp} = -\langle q_r \delta(\boldsymbol{x} - \boldsymbol{x}_{dp}(t))\rangle, \tag{3.19a}$$

$$\Gamma_{pd} = \langle q_r \delta(\boldsymbol{x} - \boldsymbol{x}_{dp}(t))\rangle, \tag{3.19b}$$

where $\boldsymbol{x}_{dp}(t) = \{\boldsymbol{x} : \boldsymbol{x} \in \partial R_d(t) \cap \partial R_p(t)\}$. By recalling that these expressions are to be interpreted in a distributional sense, it becomes clear the delta function has the effect of converting volume integrals into surface integrals over *d-p* interfaces.

By adding these expressions we see that

$$\Gamma_{dp} + \Gamma_{pd} = 0 \tag{3.20}$$

in a distributional sense. This is a macroscopic manifestation of the microscopic jump conditions given in (3.1m). From (3.18) and (3.20) it follows that

$$\Gamma_s + \Gamma_d + \Gamma_p = 0, \tag{3.21}$$

which means no net mass is created, as expected.

We now consider the interfacial momentum transfer terms. We first write the microscopic stress tensor for each phase in terms of a pressure, p_j, and a deviatoric stress tensor, $\boldsymbol{\tau}_j$, so that

$$\mathbf{T}_j = -p_j \mathbf{I} + \boldsymbol{\tau}_j, \tag{3.22}$$

where $\mathbf{I}$ is the identity operator. The term $\boldsymbol{m}_{jk}$ can then be written as

$$\boldsymbol{m}_{jk} = \langle p^I_{jk} \nabla X_j\rangle - \langle \boldsymbol{\tau}^I_{jk} \cdot \nabla X_j\rangle, \tag{3.23}$$

Without loss of generality, we may decompose the interfacial deviatoric stresses into components that are normal and tangential to the interface:

$$\boldsymbol{\tau}^I_{jk} \cdot \nabla X_j = \tau^I_{jk} \nabla X_j + \boldsymbol{t}^I_{jk}. \tag{3.24}$$

Here, τ^I_{jk} is a scalar that corresponds to the normal component of interfacial stress in phase j, whereas $\boldsymbol{t}^I_{jk}$ is a vector that describes the tangential component of the interfacial stress which satisfies $\boldsymbol{t}^I_{jk} \cdot \nabla X_j = 0$. Thus, the interfacial momentum source can be written as

$$\boldsymbol{m}_j = \langle (p^I_{jk} + p^I_{jl}) \nabla X_j \rangle - \langle (\tau^I_{jk} + \tau^I_{jl}) \nabla X_j \rangle - \langle \boldsymbol{t}^I_{jk} \rangle - \langle \boldsymbol{t}^I_{jl} \rangle. \tag{3.25}$$

Further relationships between the interfacial pressures and stresses can be obtained from the microscopic interfacial stress balances (3.1g). At an interface formed between phase j and phase k, we have

$$-p^I_{jk} \nabla X_j + p^I_{kj} \nabla X_j + \tau^I_{jk} \nabla X_j - \tau^I_{kj} \nabla X_j + \boldsymbol{t}^I_{jk} - \boldsymbol{t}^I_{kj} = -\sigma_{jk} \kappa_{jk} \nabla X_j. \tag{3.26}$$

Taking the inner product of this equation with $\boldsymbol{e}^j_n$ yields

$$-p^I_{jk} + p^I_{kj} + \tau^I_{jk} - \tau^I_{kj} = -\sigma_{jk} \kappa_{jk}, \tag{3.27}$$

By multiplying this expression by ∇X_j and averaging, we obtain

$$-\langle p^I_{jk} \nabla X_j \rangle + \langle p^I_{kj} \nabla X_j \rangle + \langle \tau^I_{jk} \nabla X_j \rangle - \langle \tau^I_{kj} \nabla X_j \rangle = -\langle \sigma_{jk} \kappa_{jk} \nabla X_j \rangle. \tag{3.28a}$$

We then apply the averaging operator to (3.26) and use this result to find that the average of the tangential components of the interfacial stresses must balance:

$$\langle \boldsymbol{t}^I_{jk} \rangle + \langle \boldsymbol{t}^I_{kj} \rangle = 0. \tag{3.28b}$$

3.2.2.3 Averaged variables

We now introduce several averaged variables that represent macroscopic quantities of the system. The ensemble average of the indicator function,

$$\alpha_k(\boldsymbol{x}, t) = \langle X_k \rangle (\boldsymbol{x}, t), \tag{3.29}$$

represents the mean fraction of occurrences where phase k occupies the point $\boldsymbol{x}$ at time t. As mentioned by Drew [57], this variable is often referred to as the volume fraction of phase k. That is, α_k is thought to be the ratio of the volume occupied by phase k in some sample of mixture to the total volume of that sample. In the context of ensemble averaging,

this interpretation is only appropriate in the limit as the control volume tends to zero. By interpreting X_k within the framework of generalised functions, it follows that

$$\partial_t \alpha_k = \langle \partial_t X_k \rangle, \tag{3.30a}$$

$$\nabla \alpha_k = \langle \nabla X_k \rangle. \tag{3.30b}$$

We assume that every point is always occupied by one of the three phases so that

$$\alpha_s + \alpha_d + \alpha_p = 1. \tag{3.31}$$

The macroscopic densities, $\bar{\rho}_k$, are defined in terms of component-weighted averages of the form

$$\bar{\rho}_k = \frac{\langle X_k \rho_k \rangle}{\alpha_k}. \tag{3.32}$$

The same holds true for the macroscopic stress tensors, which are defined as

$$\overline{\mathbf{T}}_k = \frac{\langle X_k \mathbf{T}_k \rangle}{\alpha_k}. \tag{3.33}$$

From the decomposition of the average stress tensor given in (3.22), we can define the component-averaged pressure and deviatoric stress as

$$\bar{p}_k = \frac{\langle X_k p_k \rangle}{\alpha_k}, \tag{3.34a}$$

$$\bar{\boldsymbol{\tau}}_k = \frac{\langle X_k \boldsymbol{\tau}_k \rangle}{\alpha_k}. \tag{3.34b}$$

Thus, the average stress tensor is given by

$$\overline{\mathbf{T}}_k = -\bar{p}_k \mathbf{I} + \bar{\boldsymbol{\tau}}_k, \tag{3.35}$$

The form of $\bar{\boldsymbol{\tau}}_k$ will be discussed below. The most convenient way to define the average fluid velocities are in terms of mass-weighted averages:

$$\bar{\boldsymbol{u}}_k = \frac{\langle X_k \rho_k \boldsymbol{u}_k \rangle}{\bar{\rho}_k \alpha_k}. \tag{3.36}$$

The average interfacial pressures and normal components of the deviatoric stress are defined as

$$\bar{p}^I_{jk} \nabla \alpha_j = \langle p^{ik}_j \nabla X_j \rangle, \tag{3.37a}$$

$$\bar{\tau}^I_{jk} \nabla \alpha_j = \langle \tau^{ik}_{jn} \nabla X_j \rangle, \tag{3.37b}$$

respectively. The average of the tangential components of the deviatoric stress are given by

$$\bar{\boldsymbol{t}}^I_{jk} = \langle \boldsymbol{t}^I_{jk} \rangle. \tag{3.38}$$

By neglecting Marangoni stresses, we have implicitly assumed the surface tension is a constant. Therefore, the average of the interfacial terms due to surface-tension effects is defined as

$$\sigma_{jk}\bar{\kappa}_{jk}\nabla\alpha_j = \langle\sigma_{jk}\kappa_{jk}\nabla X_j\rangle, \tag{3.39}$$

where $\bar{\kappa}_{jk}$ is the mean curvature of an interface formed between phase j and k. In general, the curvature $\bar{\kappa}_{ij}$ may be a function of the volume fractions and mean densities.

Using these averaged quantities, we can state the macroscopic equations which hold throughout the fluid layer:

$$\alpha_s + \alpha_d + \alpha_p = 1, \tag{3.40a}$$

$$\partial_t\left(\alpha_j\bar{\rho}_j\right) + \nabla\cdot\left(\alpha_j\bar{\rho}_j\bar{\boldsymbol{u}}_j\right) = \Gamma_j, \quad j = s,d,p, \tag{3.40b}$$

$$-\nabla(\alpha_j\bar{p}_j) + \nabla\cdot(\alpha_j\bar{\tau}_j) - \alpha_j\bar{\rho}_j g\boldsymbol{e}_z + \boldsymbol{m}_j = 0, \quad j = s,d,p, \tag{3.40c}$$

The interfacial source terms are given by

$$\Gamma_s = 0, \tag{3.40d}$$

$$\Gamma_d = \Gamma_{dp}, \tag{3.40e}$$

$$\Gamma_p = \Gamma_{pd}, \tag{3.40f}$$

$$\boldsymbol{m}_j = \left(\bar{p}^I_{jk} + \bar{p}^I_{jl}\right)\nabla\alpha_j - \left(\bar{\tau}^I_{jk} + \bar{\tau}^I_{jl}\right)\nabla\alpha_j - \bar{\boldsymbol{t}}^I_{jk} - \bar{\boldsymbol{t}}^I_{jl}, \tag{3.40g}$$

and the following macroscopic jump conditions must be satisfied:

$$\Gamma_{dp} + \Gamma_{pd} = 0, \tag{3.40h}$$

$$-\bar{p}^I_{jk} + \bar{p}^I_{kj} + \bar{\tau}^I_{jk} - \bar{\tau}^I_{kj} = -\sigma_{jk}\bar{\kappa}_{jk}, \tag{3.40i}$$

$$\bar{\boldsymbol{t}}^I_{jk} + \bar{\boldsymbol{t}}^I_{kj} = 0. \tag{3.40j}$$

Each phase k is described by a volume fraction α_k; an average density, velocity vector, pressure, and deviatoric stress tensor, $\bar{\rho}_k$, $\bar{\boldsymbol{u}}_k$, $\bar{p}_k$, and $\bar{\boldsymbol{\tau}}_k$, respectively; and has several interfacial variables that appear in the source terms Γ_k and $\boldsymbol{m}_k$. The number of dependent variables greatly exceeds the number of equations. Thus, closing the macroscopic model will require further relationships between these variables.

3.2.2.4 Caveats of the macroscopic model

The benefit of the macroscopic model is that the phases are treated as overlapping and continuous. As a result, there is no longer a need to solve bulk equations on constantly changing domains which need to be found as part of the solution. That being said, one

immediate consequence of this simplification is that the geometrical details of the internal interfaces are lost. These can be important if interfacial processes drive the flow. It is tempting to assume there is a link between the volume fraction and the average curvature of the interfaces, which motivates deriving appropriate constitutive laws linking the two quantities. This is the approach taken by Howell & Muldoon [78] when modelling ice cream. However, it is not difficult to imagine situations that have the same local volume fraction but vastly different interfacial geometries. For instance, if one considers the case of an array of body-centred cubic-packed solid spheres surrounded by fluid, then a short calculation shows that the volume fraction of solid is always $\pi/6$, regardless of the size of the spheres. One can also imagine a rectangular control volume filled with two components of equal volume fractions. These components could be distributed in the form of two layers, or one phase could be dispersed within other. Problems can arise in the modelling process if the volume fraction does not encode enough information about the interfacial geometry. Drew and Passman [57] discuss this issue in detail and derive extended models that include transport equations for the average interfacial area per unit volume, mean curvature, and Gaussian curvature. As discussed below, the curvature will not enter our model so these issues do not arise. However, addressing them in the context of solvent-polymer mixtures may be an interesting avenue of future work.

3.2.3 Constitutive laws and model closure

The constitutive laws that we use to close the mathematical model are motivated by our aim to keep the model as simple as possible while retaining the essential physics. Although our model will lack realism in certain areas, it will benefit from additional mathematical tractability. Starting our analysis with an idealised set of equations will enable us to gain valuable first insights into how multicomponent models can be used to study the dynamics of evaporating solvent-polymer mixtures.

We begin by treating the individual phases of the mixture as incompressible. Thus, the mean densities are assumed to be constant in both space and time; that is, $\bar{\rho}_j(\boldsymbol{x}, t) \equiv \bar{\rho}_j$. From this point onwards, we treat the mean densities $\bar{\rho}_j$ as the densities of the pure components. We also let the mean polymer densities be equal, which implies that $\bar{\rho}_d = \bar{\rho}_p$. In addition, the mean reactive mass fluxes, Γ_{pd} and Γ_{dp}, are written as

$$\Gamma_{dp} = -\bar{\rho}_p \gamma, \tag{3.41a}$$

$$\Gamma_{pd} = \bar{\rho}_p \gamma, \tag{3.41b}$$

where γ corresponds to an average mixing/demixing rate with units of time^{-1}. It immediately follows that $\Gamma_{dp} + \Gamma_{pd} = 0$, thus satisfying the macroscopic jump condition in (3.40h). The precise form of γ will be discussed in Section 3.4.

The next set of assumptions deals with the rheology of the phases. Each component of the mixture is assumed to behave as a Newtonian fluid. This motivates writing the deviatoric stress tensor as

$$\bar{\boldsymbol{\tau}}_j = 2\bar{\mu}_j \overline{\mathbf{D}}_j, \quad \overline{\mathbf{D}}_j = \frac{1}{2}\left[\nabla \bar{\boldsymbol{u}}_j + (\nabla \bar{\boldsymbol{u}}_j)^T\right], \quad j = s, d, p, \tag{3.42}$$

where $\bar{\mu}_j$ are the mean kinematic viscosities of the components. We assume the two polymeric phases have the same average viscosity so that $\bar{\mu}_d = \bar{\mu}_p$. Later, we will also make the assumption that the solvent is much less viscous than the polymer, $\bar{\mu}_s \ll \bar{\mu}_p$. It is well known that the Newtonian rheology of the mixture will break down during the drying process. When the polymer concentration becomes sufficiently high, the fluid is likely to exhibit shear-thinning and viscoelastic behaviour. We will not consider such effects for the time being. The viscosity of the solvent is expected to depend strongly on the concentration of polymer. When the concentration is low, the viscosity can be modelled using Einstein's relation for dilute suspensions [61],

$$\bar{\mu}_s = \mu_s \left(1 + \frac{5}{2}\alpha_d\right), \tag{3.43}$$

where μ_s corresponds to the viscosity of pure solvent. Alternative viscosity models, including those which diverge at a critical solute concentration corresponding to the maximum packing fraction, can be used for non-dilute suspensions; see, for example, Bergantz & Ni [15], Drew & Passman [57], or Ahnert *et al.* [3]. However, for simplicity, all of the viscosities are assumed to be constant in this model.

The final set of assumptions deals with the numerous variables that appear in the interfacial momentum transfer terms. For simplicity, we will neglect surface-tension effects in the bulk of the fluid layer by setting $\sigma_{jk} = 0$. Similarly, the normal component of the interfacial deviatoric stresses are also set equal to zero, $\bar{\tau}^I_{jk} = 0$. The average pressures of phase j at interfaces formed between regions of phase k and l are written in terms of an overall interfacial pressure: $\bar{p}^I_{jk} = \bar{p}^I_{jl} = \bar{p}^I_j/2$, which implies that $\bar{p}^I_{jk} + \bar{p}^I_{jl} = \bar{p}^I_j$. The average interfacial pressures are assumed to be equal to the bulk pressures, $\bar{p}^I_j = \bar{p}_j$. Due to the previous assumptions and from the macroscopic jump conditions in (3.40i), this implies that all of the pressures are, in fact, equal. Thus, the system can be described by a single macroscopic pressure $\bar{p}$. Due to our treatment of the phases as liquids, we do not consider contact pressures that could occur within the solid polymer phases; see, for example, Drew [56]. In the case of solvent-polymer mixtures, an osmotic pressure can be introduced into

the model to account for the tendency of the solvent to percolate through polymer-rich domains [157], although we do not consider this here.

The no-slip boundary conditions (3.1n) of the microscopic model imply that tangential velocities along the boundary of one phase will be transmitted into the adjacent phase. This leads to adjacent phases dragging each other which, on the macroscale, is captured through the mean tangential stresses at the interface, $\bar{\boldsymbol{t}}^I_{jk}$. In particular, these are treated as drag terms between phases j and k. There is a wide literature on the different forms of drag laws that can be used depending on the flow regime and the physical characteristics of the mixture [56, 67]. Often, these take the form

$$\bar{\boldsymbol{t}}^I_{jk} = \bar{C}_{jk}(\alpha_j, \alpha_k)(\bar{\boldsymbol{u}}_k - \bar{\boldsymbol{u}}_j), \tag{3.44}$$

where $\bar{C}_{jk}$ is an average drag "coefficient" that may depend on other physical parameters such as viscosities. Note that this form of drag law automatically satisfies the macroscopic jump conditions for the tangential stress at the interface (3.40j). For the purposes of this chapter, we take the drag coefficients to be $\bar{C}_{ij}(\alpha_j, \alpha_k) = \bar{c}_{ij}\alpha_j\alpha_k$.

3.2.4 Summary of model

The above approximations and constitutive relations complete the mathematical model. In total, the model consists of three equations for mass, six equations for the momentum, plus an extra condition that can be interpreted as volume conservation. These ten equations hold throughout the region corresponding to the fluid layer given by $x \in \mathbb{R}$ and $0 < z < h(x,t)$. From this point forward, we drop all of the bars on the averaged variables. The equations representing mass conservation are given by

$$\partial_t \alpha_s + \nabla \cdot (\alpha_s \boldsymbol{u}_s) = 0, \tag{3.45a}$$

$$\partial_t \alpha_d + \nabla \cdot (\alpha_d \boldsymbol{u}_d) = -\gamma, \tag{3.45b}$$

$$\partial_t \alpha_p + \nabla \cdot (\alpha_p \boldsymbol{u}_p) = \gamma, \tag{3.45c}$$

$$\alpha_s + \alpha_d + \alpha_p = 1. \tag{3.45d}$$

The averaged form of the momentum equations are given by

$$-\alpha_s \nabla p + 2\mu_s \nabla \cdot (\alpha_s \mathbf{D}_s) - \alpha_s \rho_s g \boldsymbol{e}_z - c_{sd}\alpha_s\alpha_d(\boldsymbol{u}_s - \boldsymbol{u}_d) - c_{sp}\alpha_s\alpha_p(\boldsymbol{u}_s - \boldsymbol{u}_p) = 0, \tag{3.45e}$$

$$-\alpha_d \nabla p + 2\mu_p \nabla \cdot (\alpha_d \mathbf{D}_d) - \alpha_d \rho_p g \boldsymbol{e}_z + c_{sd}\alpha_s\alpha_d(\boldsymbol{u}_s - \boldsymbol{u}_d) - c_{dp}\alpha_d\alpha_p(\boldsymbol{u}_d - \boldsymbol{u}_p) = 0, \tag{3.45f}$$

$$-\alpha_p \nabla p + 2\mu_p \nabla \cdot (\alpha_p \mathbf{D}_p) - \alpha_p \rho_p g \boldsymbol{e}_z + c_{sp}\alpha_s\alpha_p(\boldsymbol{u}_s - \boldsymbol{u}_p) + c_{dp}\alpha_d\alpha_p(\boldsymbol{u}_d - \boldsymbol{u}_p) = 0, \tag{3.45g}$$

where the rate of deformation tensors, $\mathbf{D}_j$, are given by

$$\mathbf{D}_j = \frac{1}{2}\left[\nabla \boldsymbol{u}_j + (\nabla \boldsymbol{u}_j)^T\right], \quad j = s, d, p. \tag{3.46}$$

Upon summing the three equations for mass conservation (3.45a)–(3.45b) and using (3.45d), we find that

$$\nabla \cdot (\alpha_s \boldsymbol{u}_s + \alpha_d \boldsymbol{u}_d + \alpha_p \boldsymbol{u}_p) = 0. \tag{3.47}$$

Similarly, adding the three momentum equations (3.45e)–(3.45g) gives a net momentum balance for the mixture:

$$-\nabla p + 2\,\nabla \cdot (\mu_s \alpha_s \mathbf{D}_s + \mu_p \alpha_d \mathbf{D}_d + \mu_p \alpha_p \mathbf{D}_p) - (\alpha_s \rho_s + \alpha_d \rho_p + \alpha_p \rho_p)\, g \boldsymbol{e}_z = 0. \tag{3.48}$$

Typically, we will eliminate one of the volume fractions using (3.45d). The corresponding equation representing mass conservation for that species is then replaced with (3.47). Furthermore, we replace one of the three momentum equations (3.45e)–(3.45g) with that for the mixture (3.48).

We introduce the phase-averaged mixture density ρ_m, velocity $\boldsymbol{u}_m$, and deviatoric stress tensor $\boldsymbol{\tau}_m$, which are defined according to

$$\rho_m = \alpha_s \rho_s + \alpha_d \rho_p + \alpha_p \rho_p, \tag{3.49a}$$

$$\boldsymbol{u}_m = \alpha_s \boldsymbol{u}_s + \alpha_d \boldsymbol{u}_d + \alpha_p \boldsymbol{u}_p, \tag{3.49b}$$

$$\boldsymbol{\tau}_m = 2\,(\mu_s \alpha_s \mathbf{D}_s + \mu_p \alpha_d \mathbf{D}_d + \mu_p \alpha_p \mathbf{D}_p)\,. \tag{3.49c}$$

With these definitions, the mass and momentum balance for the mixture, (3.47) and (3.48), can be written as

$$-\nabla p + \nabla \cdot \boldsymbol{\tau}_m - \rho_m g \boldsymbol{e}_z = 0, \tag{3.50a}$$

$$\nabla \cdot \boldsymbol{u}_m = 0, \tag{3.50b}$$

which bears a marked resemblance to the hydrodynamic model used in Chapter 2.

3.2.4.1 Initial and boundary conditions

The initial conditions for the three volume fractions are written as

$$\alpha_j(x, z, 0) = \alpha_{ji}(x, z), \quad j = s, d, p. \tag{3.51}$$

Only two of these three need to be specified due to the requirement that $\alpha_{si} + \alpha_{di} + \alpha_{pi} = 1$.

We assume that the boundary conditions on the substrate and at the free surface for the averaged quantities are analogous to those posed in Section 3.2.1 for the microscopic quantities. Therefore, along the substrate, the usual no-slip and no-flux conditions are imposed on the average velocities,

$$\boldsymbol{u}_j = 0, \quad z = 0, \quad j = s, d, p. \tag{3.52}$$

The average mass flux of solvent due to evaporation is written as

$$q_{\text{evap}} = \rho_s E \alpha_s^2, \tag{3.53}$$

where E is a mass transfer coefficient with units of length·time^{-1}. The kinematic boundary conditions at the free surface, which represent conservation of mass across this interface, can be written as

$$\rho_s \alpha_s (\boldsymbol{u}_s - \boldsymbol{v}) \cdot \boldsymbol{e}_n^g = q_{\text{evap}}, \quad z = h(x,t), \tag{3.54a}$$

$$(\boldsymbol{u}_d - \boldsymbol{v}) \cdot \boldsymbol{e}_n^g = 0, \qquad z = h(x,t), \tag{3.54b}$$

$$(\boldsymbol{u}_p - \boldsymbol{v}) \cdot \boldsymbol{e}_n^g = 0, \qquad z = h(x,t), \tag{3.54c}$$

where the normal vector $\boldsymbol{e}_n^g$ and the normal component of the interface velocity, $\boldsymbol{v} \cdot \boldsymbol{e}_n^g$, are given by

$$\boldsymbol{e}_n^g = \frac{-(\partial_x h)\boldsymbol{e}_x + \boldsymbol{e}_z}{\sqrt{1 + (\partial_x h)^2}}, \quad \boldsymbol{v} \cdot \boldsymbol{e}_n^g = \frac{\partial_t h}{\sqrt{1 + (\partial_x h)^2}}. \tag{3.55}$$

By integrating (3.47) over the depth of the fluid layer and using (3.52) and (3.54), an evolution equation for the film thickness $h(x,t)$ can be obtained:

$$\frac{\partial h}{\partial t} + \frac{\partial}{\partial x} \int_0^{h(x,t)} (\alpha_s u_s + \alpha_d u_d + \alpha_p u_p) \, \mathrm{d}z = -E \alpha_s^2(x, h(x,t), t) \left[1 + \left(\frac{\partial h}{\partial x} \right)^2 \right]^{1/2}. \tag{3.56}$$

This equation is supplemented with the initial condition given by $h(x,0) = h_i(x)$.

The last set of boundary conditions are those related to the tangential and normal components of the stresses. In these, it is tempting to use a surface tension for the mixture, σ_m, that is a phase average of the solvent and polymer surface tensions. However, this will lead to Marangoni stresses which are beyond the scope of the current study. Therefore, we take the surface tension of the mixture to be a constant. Consequently, the tangential component of the stress must vanish in each of the phases at the surface, implying that

$$\boldsymbol{e}_t^g \cdot \mathbf{D}_j \cdot \boldsymbol{e}_n^g = 0, \quad z = h(x,t), \quad j = s, d, p, \tag{3.57}$$

where the unit tangent vector to the fluid surface is given by

$$\boldsymbol{e}_t^g = \frac{\boldsymbol{e}_x + (\partial_x h)\boldsymbol{e}_z}{\sqrt{1 + (\partial_x h)^2}}. \tag{3.58}$$

By summing the three relations given in (3.57), it is easy to deduce that the tangential component of the mixture stress also vanishes at the surface, $\boldsymbol{e}_t^g \cdot \boldsymbol{\tau}_m \cdot \boldsymbol{e}_n^g = 0$. Due to the fact that our model contains only one pressure corresponding to that of the mixture, we choose to balance the normal component of the mixture stress with surface tension so that

$$\boldsymbol{e}_n^g \cdot \boldsymbol{\tau}_m \cdot \boldsymbol{e}_n^g = -\sigma_m \nabla \cdot \boldsymbol{e}_n^g, \quad z = h(x,t). \tag{3.59}$$

Had our model contained distinct pressures for the phases, we would have replaced (3.59) with analogous conditions for each component.

3.3 Two-phase flow in a gravitational field

We first investigate the dynamics of an evaporating two-phase mixture under the action of gravity. The mixture consists of a volatile solvent and a non-volatile polymer. We assume there is no mass transfer between the two phases nor any phase change within the bulk of the fluid layer. The corresponding set of equations for this situation can be written as

$$\partial_t \alpha_p + \nabla \cdot (\alpha_p \boldsymbol{u}_p) = 0, \tag{3.60a}$$

$$\nabla \cdot ((1-\alpha_p)\boldsymbol{u}_s + \alpha_p \boldsymbol{u}_p) = 0, \tag{3.60b}$$

$$-\alpha_p \nabla p + 2\mu_p \nabla \cdot (\alpha_p \mathbf{D}_p) - \alpha_p \rho_p g \boldsymbol{e}_z + c_{sp}\alpha_p(1-\alpha_p)(\boldsymbol{u}_s - \boldsymbol{u}_p) = 0, \tag{3.60c}$$

$$-\nabla p + 2\,\nabla \cdot (\mu_s(1-\alpha_p)\mathbf{D}_s + \mu_p \alpha_p \mathbf{D}_p) - ((1-\alpha_p)\rho_s + \alpha_p \rho_p) g \boldsymbol{e}_z = 0, \tag{3.60d}$$

with $\mathbf{D}_j$ as in (3.46). The boundary conditions along the substrate are

$$\boldsymbol{u}_j = 0, \quad z = 0, \quad j = s, p. \tag{3.60e}$$

At the free surface, we impose kinematic and stress conditions given by

$$(\boldsymbol{u}_s - \boldsymbol{v}) \cdot \boldsymbol{e}_n^g = E(1-\alpha_p), \quad z = h(x,t), \tag{3.60f}$$

$$(\boldsymbol{u}_d - \boldsymbol{v}) \cdot \boldsymbol{e}_n^g = 0, \quad z = h(x,t), \tag{3.60g}$$

$$\boldsymbol{e}_t^g \cdot \mathbf{D}_s \cdot \boldsymbol{e}_n^g = 0, \quad z = h(x,t), \tag{3.60h}$$

$$\boldsymbol{e}_t^g \cdot \mathbf{D}_p \cdot \boldsymbol{e}_n^g = 0, \quad z = h(x,t), \tag{3.60i}$$

$$-p + 2\,\boldsymbol{e}_n^g \cdot (\mu_s(1-\alpha_p)\mathbf{D}_s + \mu_p \alpha_p \mathbf{D}_p) \cdot \boldsymbol{e}_n^g = -\sigma_m \nabla \cdot \boldsymbol{e}_n^g, \quad z = h(x,t). \tag{3.60j}$$

Finally, the free surface evolves according to

$$\frac{\partial h}{\partial t} + \frac{\partial}{\partial x}\int_0^{h(x,t)} [(1-\alpha_p)u_s + \alpha_p u_p]\,\mathrm{d}z = -E[1-\alpha_p(x,h(x,t),t)]^2\left[1 + \left(\frac{\partial h}{\partial x}\right)^2\right]^{1/2}. \tag{3.60k}$$

Initial conditions for this problem are given by

$$\alpha_p(x,z,0) = \alpha_{pi}(x,z), \tag{3.60l}$$

$$h(x,0) = h_i(x). \tag{3.60m}$$

We let A and H denote the mean initial values of the polymer volume fraction and the film thickness,

$$A = \lim_{L\to\infty} \frac{1}{2L}\int_{-L}^{L} \frac{1}{h_i(x)} \int_0^{h_i(x)} \alpha_{pi}(x,z)\,\mathrm{d}z\mathrm{d}x, \quad H = \lim_{L\to\infty} \frac{1}{2L}\int_{-L}^{L} h_i(x)\,\mathrm{d}x. \tag{3.61}$$

3.3.1 Non-dimensionalisation

The two-phase model presented in (3.60) is scaled in a manner that makes the role of compositional buoyancy most apparent. This is achieved by writing the pressure p as $p = p' - \rho_p g z$. We then scale the lengths with the initial average height of the film H, the velocity with the mass transfer coefficient E, and time with H/E. For the moment, we balance the pressure with the viscous stress in the polymer so that $p' \sim \mu_p E/H$. The polymer volume fraction is scaled with A since we will be interested in the dilute limit where $A \to 0$. The resulting non-dimensional equations in the bulk are (upon dropping the prime for the pressure)

$$\partial_t \alpha_p + \nabla \cdot (\alpha_p \boldsymbol{u}_p) = 0, \tag{3.62a}$$

$$\nabla \cdot ((1 - A\alpha_p)\boldsymbol{u}_s + A\alpha_p \boldsymbol{u}_p) = 0, \tag{3.62b}$$

$$-\alpha_p \nabla p + 2\,\nabla \cdot (\alpha_p \mathbf{D}_p) + D\alpha_p(1 - A\alpha_p)(\boldsymbol{u}_s - \boldsymbol{u}_p) = 0, \tag{3.62c}$$

$$-\nabla p + 2\,\nabla \cdot (\mu(1 - A\alpha_p)\mathbf{D}_s + A\alpha_p \mathbf{D}_p) + R(1 - A\alpha_p)\boldsymbol{e}_z = 0, \tag{3.62d}$$

where

$$R = \frac{(\rho_p - \rho_s)gH^2}{\mu_p E}, \quad D = \frac{c_{sp}H^2}{\mu_p}, \quad \mu = \frac{\mu_s}{\mu_p} \tag{3.63}$$

define a compositional Rayleigh number, the effective drag coefficient, and the relative kinematic viscosity. Thus, we can vary the relative importance of compositional buoyancy in the model through changes in the Rayleigh number. In the proceeding analysis, we shall assume that $R > 0$ so that the polymer is denser than the solvent.

The boundary conditions on the substrate remain unchanged,

$$\boldsymbol{u}_j = 0, \quad z = 0, \quad j = s, p. \tag{3.64}$$

Before writing all of the boundary conditions at the free surface, we first examine that which is associated with the normal component of the mixture stress. In non-dimensional form, this equation reads

$$-p + 2\,\boldsymbol{e}_n^g \cdot (\mu(1 - A\alpha_p)\mathbf{D}_s + A\alpha_p \mathbf{D}_p) \cdot \boldsymbol{e}_n^g = -Gh - C^{-1}\nabla \cdot \boldsymbol{e}_n^g, \tag{3.65}$$

where the Galileo number G and the capillary number C are defined as

$$G = \frac{\rho_p g H^2}{\mu_p E}, \quad C = \frac{\mu_p E}{\sigma_m}. \tag{3.66}$$

Although it is not easy to determine a viscosity of the polymer phase, we suspect that $C \ll 1$ in most cases. This is partly motivated by the polystyrene-toluene mixtures used

by Bassou & Rharbi. Here, the polymer viscosity would have to be approximately 10^5 Pa·s for $C = 1$; see Table 2.1 for the relevant parameter values. The regime $C \ll 1$ corresponds to surface tension being sufficiently strong to maintain a relatively flat interface. Thus, as a first approximation, we treat the fluid surface as flat and given by $h(x,t) \equiv h(t)$.

The boundary conditions at a flat free surface are given by

$$w_s - \partial_t h = (1 - A\alpha_p), \quad z = h(t), \tag{3.67a}$$

$$w_p - \partial_t h = 0, \quad z = h(t), \tag{3.67b}$$

$$\partial_z u_s + \partial_x w_s = 0, \quad z = h(t), \tag{3.67c}$$

$$\partial_z u_p + \partial_x w_p = 0, \quad z = h(t), \tag{3.67d}$$

$$-p + 2\left[\mu(1 - A\alpha_p)\partial_z w_s + A\alpha_p \partial_z w_p\right] = -Gh, \quad z = h(t), \tag{3.67e}$$

The initial conditions are given by $\alpha_p(x,z,0) = \alpha_{pi}(x,z)$, where α_{pi} now has a mean value of one, and $h(0) = 1$.

3.3.2 The dilute polymer approximation

It is often the case in experiments that the initial concentration of polymer is low. Typical polymer volume fractions range from a few percent up to 15–20% initially. In our two-phase model, this corresponds to the parameter A, defined in (3.61), being small. Thus, it is reasonable to consider a dilute-polymer limit by taking $A \searrow 0$ in (3.62) and (3.67). The problem for the solvent reduces to

$$-\nabla p + \mu \nabla^2 \boldsymbol{u}_s + Re\boldsymbol{e}_z = 0, \tag{3.68a}$$

$$\nabla \cdot \boldsymbol{u}_s = 0. \tag{3.68b}$$

The corresponding boundary conditions are given by

$$\boldsymbol{u}_s = 0, \quad z = 0, \tag{3.69a}$$

$$w_s - \partial_t h = 1, \quad z = h(t), \tag{3.69b}$$

$$\partial_z u_s = 0, \quad z = h(t), \tag{3.69c}$$

$$-p + 2\mu\, \partial_z w_s = -Gh, \quad z = h(t). \tag{3.69d}$$

We remark that the term $\partial_x w_s$ that would normally appear in (3.69c) is equal to zero. This can be seen by differentiating (3.69b) with respect to x and recalling that h is only a function of time t.

The problem for the polymer is given by

$$\partial_t \alpha_p + \nabla \cdot (\alpha_p \boldsymbol{u}_p) = 0, \tag{3.70a}$$

$$-\alpha_p \nabla p + 2\,\nabla \cdot (\alpha_p \mathbf{D}_p) + D\alpha_p(\boldsymbol{u}_s - \boldsymbol{u}_p) = 0. \tag{3.70b}$$

The boundary conditions for this problem are

$$\boldsymbol{u}_p = 0, \quad z = 0, \tag{3.71a}$$

$$w_p - \partial_t h = 0, \quad z = h(t), \tag{3.71b}$$

$$\partial_z u_p = 0, \quad z = h(t). \tag{3.71c}$$

There is nothing to drive the flow of solvent in this problem and hence we can set $\boldsymbol{u}_s \equiv 0$ and $\nabla p = R\boldsymbol{e}_z$. From the boundary condition (3.69b), the film thickness can be found analytically and it is given by $h(t) = 1 - t$. Thus, the model will break down when $t = 1$; however, it may do so well before this time if the scaled polymer volume fraction α_p becomes of size $O(A^{-1})$. Assuming this is not the case, the problem for the polymer can then be written in a self-contained form given by

$$\partial_t \alpha_p + \nabla \cdot (\alpha_p \boldsymbol{u}_p) = 0, \tag{3.72a}$$

$$2\nabla \cdot (\alpha_p \mathbf{D}_p) - D\alpha_p \boldsymbol{u}_p - R\alpha_p \boldsymbol{e}_z = 0, \tag{3.72b}$$

with boundary and initial conditions

$$\boldsymbol{u}_p = 0, \qquad z = 0, \tag{3.73a}$$

$$w_p = -1, \quad z = 1 - t, \tag{3.73b}$$

$$\partial_z u_p = 0, \qquad z = 1 - t, \tag{3.73c}$$

$$\alpha_p = \alpha_{pi}, \quad t = 0. \tag{3.73d}$$

3.3.2.1 Solution in one dimension

We first consider the dilute problem for the polymer given by (3.72) and (3.73) in one space dimension. Accordingly, we let $\alpha_p = \alpha_p(z,t)$, $u_p \equiv 0$, and $w_p = w_p(z,t)$. The problem then becomes

$$\frac{\partial \alpha_p}{\partial t} + \frac{\partial}{\partial z}(\alpha_p w_p) = 0, \tag{3.74a}$$

$$2\frac{\partial}{\partial z}\left(\alpha_p \frac{\partial w_p}{\partial z}\right) - D\alpha_p w_p - R\alpha_p = 0, \tag{3.74b}$$

with $w_p = 0$ at $z = 0$ and $w_p = -1$ at $z = 1 - t$. The initial condition $\alpha_{pi}(z) \equiv 1$ is taken, which corresponds to a homogeneous distribution of polymer.

To simplify this problem, we introduce Lagrangian variables $\tau > 0$ and $s \in [0,1]$, and we write

$$\frac{\partial t}{\partial \tau} = 1, \tag{3.75a}$$

$$\frac{\partial z}{\partial \tau} = w_p, \tag{3.75b}$$

$$\frac{\partial \alpha_p}{\partial \tau} = -\alpha_p \frac{\partial w_p}{\partial z}, \tag{3.75c}$$

which have initial conditions $t(0,s) = 0$, $z(0,s) = s$, and $\alpha_p(0,s) = 1$. We must also have $z(\tau,0) = 0$ and $z(\tau,1) = 1-\tau$. From (3.75a), we have that $t = \tau$ and from the chain rule, $\partial/\partial z = (\partial z/\partial s)^{-1}(\partial/\partial s)$. Thus, we can write $\partial w_p/\partial z = (\partial w_p/\partial s)/(\partial z/\partial s)$ and, by using (3.75b) in this expression, we have

$$\frac{\partial w_p}{\partial z} = \frac{\partial^2 z/(\partial s \partial \tau)}{\partial z/\partial s}. \tag{3.76}$$

Inserting this into (3.75c) yields

$$\frac{\partial}{\partial \tau}\left(\alpha_p \frac{\partial z}{\partial s}\right) = 0, \tag{3.77}$$

which can be integrated to give

$$\alpha_p \frac{\partial z}{\partial s} = 1. \tag{3.78}$$

This expression provides a means of transforming z derivatives via

$$\frac{\partial}{\partial z} = \frac{1}{\alpha_p}\frac{\partial}{\partial s}. \tag{3.79}$$

Using this along with (3.75b) and (3.75c) in the momentum equation (3.74b) leads to significant simplifications:

$$2\frac{\partial}{\partial \tau}\left(\frac{\partial \alpha_p}{\partial s}\right) + D\frac{\partial z}{\partial \tau} + R = 0. \tag{3.80}$$

Integrating this with respect to τ yields

$$2\frac{\partial \alpha_p}{\partial s} = D(s-z) - R\tau. \tag{3.81}$$

Differentiating (3.78) with respect to s and using the above results yields a second-order, nonlinear boundary value problem for z:

$$2\frac{\partial^2 z}{\partial s^2} + [D(s-z) - R\tau]\left(\frac{\partial z}{\partial s}\right)^2 = 0, \tag{3.82}$$

with $z(\tau,0) = 0$ and $z(\tau,1) = 1-\tau$. Therefore, the solution to the entire problem can be obtained by solving (3.82) for z and then inserting this into (3.78) to find the volume fraction α_p. This process gives a parametric solution to the problem in terms of the Lagrangian coordinate s. When $\partial z/\partial s \neq 0$, the mapping between z and s is one-to-one, *i.e.* no shocks occur. Moreover, this means that the solution, in principle, can be written in terms of the original Eulerian coordinate z.

The product $R\tau$ that appears in (3.82) is particularly interesting because it implies the existence of a second time scale in the problem. This time scale is given by $1/R$ and it corresponds to the time required for the denser phase to settle on the substrate. The cases $R \ll 1$ and $R \gg 1$ imply that the settling process is slow and fast compared to evaporation, respectively.

Solution in the absence of drag and gravity The effects of drag and gravity can be neglected by setting $D = 0$ and $R = 0$, respectively. In this case, the solution to (3.82) is simply $z = s(1 - \tau)$ and hence $\alpha_p = (1 - \tau)^{-1}$. The concentration of polymer, therefore, increases with time but it remains uniformly distributed. The formation of a polymer-rich skin is not possible in this parameter regime.

Solution in the absence of drag When $D = 0$, the problem for z reduces to

$$\frac{\partial^2 z}{\partial s^2} - \frac{R\tau}{2}\left(\frac{\partial z}{\partial s}\right)^2 = 0, \tag{3.83}$$

with $z(\tau, 0) = 0$ and $z(\tau, 1) = 1 - \tau$. Although this equation is nonlinear, it still admits an analytical solution. This is given by

$$z(\tau, s) = -\frac{2}{R\tau}\log\left(s\left[\exp\left\{-R\tau(1-\tau)/2\right\} - 1\right] + 1\right). \tag{3.84}$$

For $R\tau \ll 1$, this solution for z becomes $z = s(1 - \tau) + O((R\tau)^2)$, which matches with the case $R = 0$. This is understandable because, in this limit, gravity has not had enough time to pull the polymer to the substrate. The volume fraction of polymer, written in terms of the original variables, is given by

$$\alpha_p(z, t) = \frac{Rt}{2}\frac{\exp\left(-Rtz/2\right)}{1 - \exp\left[-Rt(1-t)/2\right]}. \tag{3.85}$$

For each time t, the volume fraction decays exponentially with the distance from the substrate. As expected, this corresponds to an accumulation of polymer near the bottom of the fluid layer. For large values of R and as $t \nearrow 1$, a compositional boundary layer forms near the substrate that is of width $O(2/(Rt))$.

Long-term behaviour We now consider the "long-term" behaviour of the solution as $\tau \nearrow 1$ when both gravity and drag are considered. This is done by letting $\delta = 1 - \tau \ll 1$ and writing $z(s) = \delta\eta(s)$, where the τ dependence of z and η, which now enters through δ, is omitted for brevity. The governing equation for η is given by

$$\frac{\mathrm{d}^2\eta}{\mathrm{d}s^2} + \frac{\delta}{2}\left[D(s - \delta\eta) - R(1 - \delta)\right]\left(\frac{\mathrm{d}\eta}{\mathrm{d}s}\right)^2 = 0. \tag{3.86}$$

The corresponding boundary conditions for this equation are given by $\eta(0) = 0$ and $\eta(1) = 1$. If $R, D = O(1)$, which implies the effects of gravity and drag are not too strong, then this problem can be solved using a regular asymptotic expansion. That is, we write $\eta(s) = \eta_0(s) + \delta\eta_1(s) + O(\delta^2)$. The first two terms in the solution are

$$\eta(s) = s + \frac{\delta}{4}\left[\frac{D}{3}(s+1) - R\right]s(1-s). \tag{3.87}$$

The appearance of R and D in the $O(\delta)$ terms implies that neither gravity nor drag significantly influence the composition of the mixture. To investigate this in more detail, we compute the polymer volume fraction, which can be written as

$$\alpha_p(s) = \delta^{-1} - \frac{1}{4}\left[D\left(\frac{1}{3} - s^2\right) + R(2s-1)\right]. \tag{3.88}$$

From this, we see that the distribution of polymer remains roughly uniform during the drying process, with small variations caused by the effects of gravity and drag. Recalling that the Lagrangian coordinate s is bounded between $0 < s < 1$, we find that the volume fraction is a monotonically decreasing function on this interval when $R/D > 1$. This corresponds to a slight build up of polymer near the substrate. In the case when $R/D < 1$, the volume fraction has an interior minimum at $s = R/D$. In Eulerian coordinates, this corresponds roughly to the point $z_c(t) \simeq (1-t)R/D$. In physical terms, the existence of an interior minimum implies that gravity and drag lead to an accumulation of polymer near the substrate and the free surface, respectively. To determine which of these effects is the most prominent, we treat R and D as free parameters and we compare the polymer concentration at the surface and at the substrate. When $R > D/2$, there is a greater build up of polymer near the substrate than at the surface. In this case, we say the system is gravity dominated. Similarly, when $R < D/2$, the greatest accumulation occurs underneath the surface, corresponding to a drag-dominated system.

We now consider the regime where both gravity and drag are strong. The case with strong gravity but weak drag can be thought of as a small perturbation of the $D = 0$ problem that was solved earlier in Section 3.3.2.1. We now let $D \gg 1$, $r = R/D = O(1)$, and define $a^{-1} = \delta D/2$. We treat a as an $O(1)$ parameter, in which case, the leading-order problem (in δ) for η can be written as

$$a\frac{\mathrm{d}^2\eta}{\mathrm{d}s^2} + (s-r)\left(\frac{\mathrm{d}\eta}{\mathrm{d}s}\right)^2 = 0, \tag{3.89}$$

with $\eta(0) = 0$ and $\eta(1) = 1$. This can be solved analytically to obtain

$$\eta(s) = \frac{2a}{c}\left[\arctan\left(\frac{s-r}{c}\right) + \arctan\left(\frac{r}{c}\right)\right], \tag{3.90}$$

where c solves the transcendental equation

$$\frac{c}{a} = 2\left[\arctan\left(\frac{1-r}{c}\right) + \arctan\left(\frac{r}{c}\right)\right]. \tag{3.91}$$

The solutions of this equation can be examined graphically by writing the left- and right-hand sides as functions $f_1(c)$ and $f_2(c)$, respectively. We only consider the case $c \geq 0$ because both of these functions are odd with respect to c and the solution for η given in

(3.90) is invariant under $c \to -c$. The function f_1 is linear with slope given by $1/a$. The function f_2 tends to zero as $c \to \infty$, but its behaviour for small c depends on the parameter r. In particular,

$$\lim_{c\to 0} f_2(c) = \begin{cases} 2\pi, & r < 1, \\ \pi, & r = 1, \\ 0, & r > 1. \end{cases} \tag{3.92}$$

A schematic diagram showing the behaviour of f_1 and f_2 is shown in Figure 3.2. When $r \leq 1$, the function f_2 monotonically decreases from $f_2(0) > 0$ to zero as c increases. Thus, the functions f_1 and f_2 are always guaranteed to intersect at one point and (3.91) has a unique solution. If $a \ll 1$, this solution is approximately given by

$$c \simeq \begin{cases} 2\pi a \left[1 - \dfrac{2a}{r(r-1)}\right]^{-1}, & r < 1, \\ \pi a (1+2a)^{-1}, & r = 1. \end{cases} \tag{3.93}$$

When $r > 1$, there is always a solution to (3.91) given by $c = 0$. However, in the limit $c \to 0$, the solution in (3.90) becomes

$$\eta(s) = \frac{2as}{r(r-s)}, \tag{3.94}$$

which does not satisfy the boundary condition $\eta = 1$ at $s = 1$. Thus, $c = 0$ is not a true solution of the problem. Another solution to (3.91) is possible if the slope of f_2 at $c = 0$ is greater than the slope of f_1; that is, if

$$\frac{1}{a} < \frac{1}{a_c} = \frac{2}{r(r-1)}. \tag{3.95}$$

When the opposite is true, *i.e.*, when $a < a_c$, the solution to (3.91) is complex. Thus, we let $c = ib$, where $b \in \mathbb{R}$. After some algebraic manipulation, one finds that b satisfies the equation

$$\frac{b}{a} = \log\left(\frac{(b-r)(b+r-1)}{(b+r)(b-r+1)}\right). \tag{3.96}$$

Using the same geometric arguments as above, it can be shown that this equation only has a solution when $a < a_c$ and this solution satisfies $b < r - 1$.

The leading-order solution for the volume fraction α_p in this parameter regime can be written as

$$\alpha_p(s) = \frac{D}{4}\left[c^2 + (s-r)^2\right]. \tag{3.97}$$

When $r < 1$, the constant c is always real and the volume fraction has an interior minimum at $s = r$. This point corresponds to the Eulerian coordinate $z_c(t) = 4/(Dc(t)) \arctan(r/c(t))$,

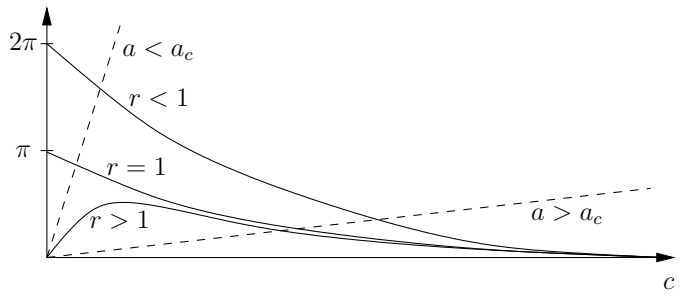


Figure 3.2: A schematic diagram of the functions f_1 (dashed) and f_2 (solid) that correspond to the left- and right-hand sides of (3.91), respectively. Solutions of this equation are given by the non-trivial intersections of these curves. When $r > 1$, the two curves only intersect if $a > a_c$, where a_c is defined in (3.95).

where the t dependence of c enters through δ via the parameter a. As in the $R, D = O(1)$ case considered previously, the presence of an interior minimum means that strong gravitational and drag effects lead to an accumulation of polymer near the substrate and below the evaporating surface, respectively. When $r > 1$, the constant c is complex and the function α_p does not have an interior minimum when written in terms of the Eulerian coordinate z. In this case, the volume fraction of polymer monotonically decreases as z increases. The physical situation corresponds to gravity being so strong relative to drag that there is no enrichment near the free surface at all. By writing $c = ib$ when $r > 1$, we find that the concentration of polymer at the surface is given by $\alpha_p(1) = (D/4)\left[(1-r)^2 - b^2\right]$. Since $b < r - 1$, the volume fraction of polymer at the surface remains positive. By comparing the concentration at the surface and substrate, we find that the system is gravity dominated when $R > D/2$ and drag dominated when $R < D/2$. Interestingly, the characterisation of the dominant regimes when $R, D \gg 1$ is the same as the case $R, D = O(1)$ analysed previously.

The corresponding parametric solution for the vertical velocity can be obtained through the expression $w = \partial_\tau z$. After a few calculations involving the chain rule and implicit differentiation, we find that

$$w_p(s,\tau) = \frac{4}{D(1-\tau)}\left[\frac{\partial f(s;c)}{\partial c} - \frac{f(s;c)}{c}\right]\left[1 - \frac{4}{D(1-\tau)}\frac{\partial f(1;c)}{\partial c}\right]^{-1}, \tag{3.98a}$$

where the function f is given by

$$f(s;c) = \arctan\left(\frac{s-r}{c}\right) + \arctan\left(\frac{r}{c}\right). \tag{3.98b}$$

A comparison of the asymptotic expressions for the volume fraction and the velocity with numerical solutions is shown in Figure 3.3. The numerical approximation is obtained by solving the nonlinear boundary value problem in (3.82) using a Chebyshev spectral method.

Three cases are shown in this figure: $R < D/2$, $D/2 < R < D$, and $R > D$, corresponding to the drag- and gravity-dominated behaviours discussed previously. The asymptotic and numerical approximations are found to be in good agreement with each other.

3.3.3 The full one-dimensional problem

The simplifications to the model that arise by considering the limit of a dilute polymer phase proved to be invaluable. The resulting equations could be studied analytically and this shed much insight into the dynamics that can occur as a mixture dries. However, the dilute model does have its shortcomings. In particular, it predicts that the film thins to zero thickness in a finite amount of time. As a direct consequence of this, the polymer volume fraction gets arbitrarily large, thus violating the key assumption underlying the dilute approximation. We now relax the assumption of a dilute polymer by treating the parameter A as an $O(1)$ quantity and considering the full one-dimensional problem. This will enable the validity of the previous results to be determined and allow new regimes to be explored, particularly those involving high polymer concentrations.

The full one-dimensional model consists of bulk equations given by

$$\frac{\partial \alpha_p}{\partial t} + \frac{\partial}{\partial z}\left(\alpha_p w_p\right) = 0, \tag{3.99a}$$

$$\frac{\partial}{\partial z}\left((1 - A\alpha_p)w_s + A\alpha_p w_p\right) = 0, \tag{3.99b}$$

$$-\alpha_p \frac{\partial p}{\partial z} + 2\,\frac{\partial}{\partial z}\left(\alpha_p \frac{\partial w_p}{\partial z}\right) + D\alpha_p(1-\alpha_p)(w_s - w_p) = 0, \tag{3.99c}$$

$$-\frac{\partial p}{\partial z} + 2\,\frac{\partial}{\partial z}\left(\mu(1 - A\alpha_p)\frac{\partial w_s}{\partial z} + A\alpha_p \frac{\partial w_p}{\partial z}\right) + R(1 - A\alpha_p) = 0. \tag{3.99d}$$

The corresponding boundary conditions at the fluid surface and at the substrate are

$$w_s = 0, \qquad z = 0, \tag{3.100a}$$

$$w_p = 0, \qquad z = 0, \tag{3.100b}$$

$$w_s - \frac{\mathrm{d}h}{\mathrm{d}t} = (1 - A\alpha_p), \quad z = h(t), \tag{3.100c}$$

$$w_p - \frac{\mathrm{d}h}{\mathrm{d}t} = 0, \qquad z = h(t), \tag{3.100d}$$

$$-p + 2\left[\mu(1 - A\alpha_p)\frac{\partial w_s}{\partial z} + A\alpha_p \frac{\partial w_p}{\partial z}\right] = -Gh, \qquad z = h(t). \tag{3.100e}$$

Furthermore, the evolution equation for the film height (3.56) reduces to

$$\frac{\mathrm{d}h}{\mathrm{d}t} = -\left[1 - A\alpha_p(h(t), t)\right]^2. \tag{3.101}$$

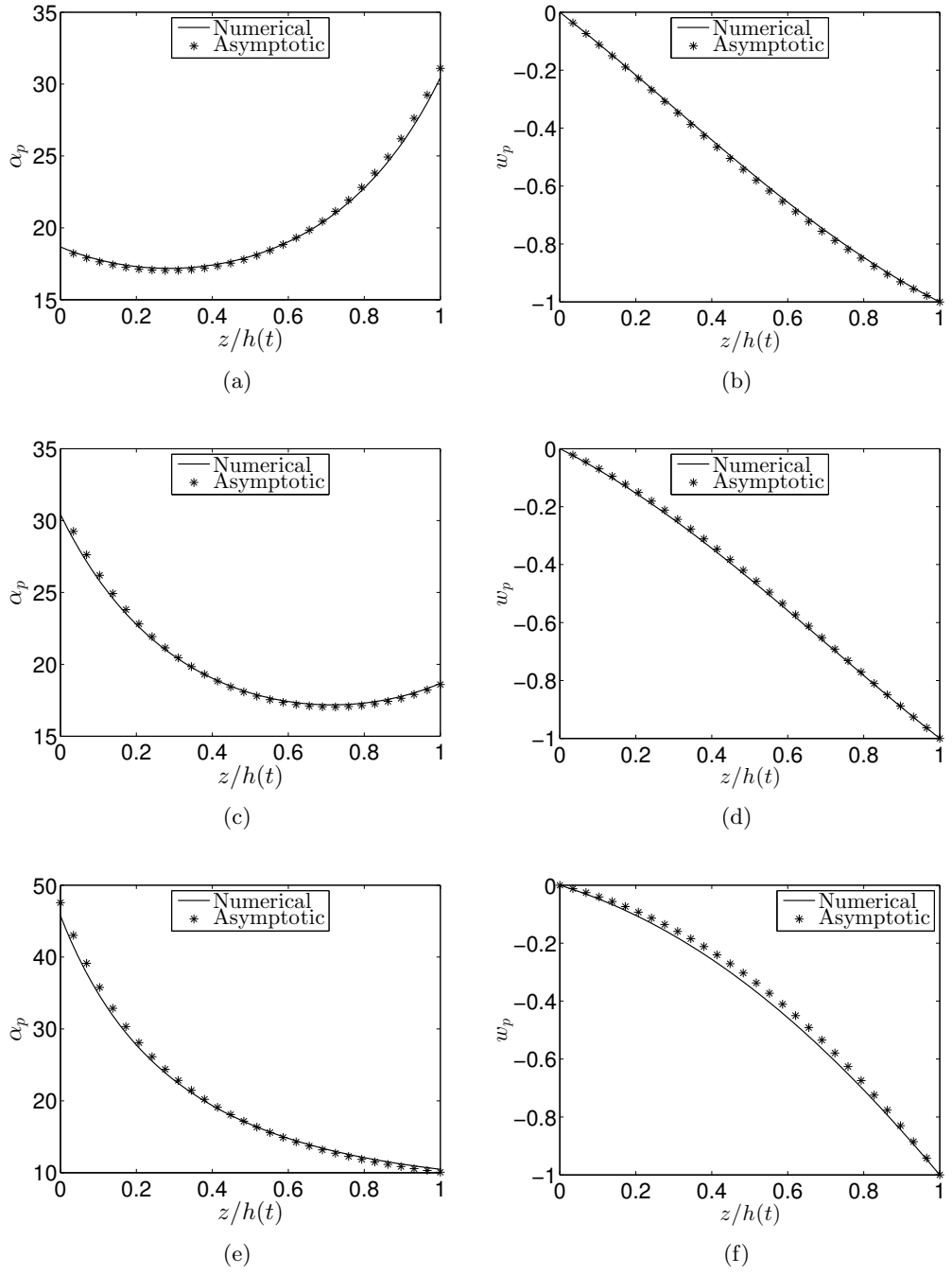


Figure 3.3: Comparison of the asymptotic solution as $t \to 1$ with numerical solutions to (3.82) when both R and D are large. The left column shows polymer volume fractions and the right column displays the corresponding vertical velocity. Parameter values are $t = 0.95$, $D = 100$, and $R = 25$, 75, and 125 for panels (a)–(b), (c)–(d), and (e)–(f), respectively. Panels (a)–(b) corresponds to the drag-dominated region of parameter space given by $R < D/2$. Panels (c)–(f) represent the gravity-dominated behaviour that occurs when $R > D/2$. This can be subdivided into two regimes. If $D/2 < R < D$, the volume fraction has an interior minimum and there is some accumulation of polymer near the surface (c). If $R > D$, gravity is so strong that the volume fraction decreases monotonically (e).

This can be inserted into (3.100c) and (3.100d) to obtain

$$w_s = A\alpha_p(1 - A\alpha_p), \quad z = h(t), \tag{3.102a}$$

$$w_p = -(1 - A\alpha_p)^2, \quad z = h(t), \tag{3.102b}$$

The incompressibility condition in (3.99b) can be integrated and, by applying the boundary conditions on the substrate, an expression for the solvent velocity can be obtained. In particular, we find that

$$w_s = -\frac{A\alpha_p}{1 - A\alpha_p}\, w_p, \tag{3.103}$$

which automatically satisfies the boundary conditions at the free surface. By combining (3.99c) and (3.99d) to eliminate the pressure gradient and by using (3.103) to remove the solvent velocity from the problem, a nonlinear differential equation for the polymer velocity emerges. Thus, the full one-dimensional problem can be written solely in terms of variables associated with the polymer. This is given by

$$\frac{\partial \alpha_p}{\partial t} + \frac{\partial}{\partial z}\left(\alpha_p w_p\right) = 0, \tag{3.104a}$$

$$2(1 - A\alpha_p)\frac{\partial}{\partial z}\left(\alpha_p \frac{\partial w_p}{\partial z}\right) + 2\mu A\alpha_p \frac{\partial}{\partial z}\left[(1 - A\alpha_p)\frac{\partial}{\partial z}\left(\frac{\alpha_p w_p}{1 - A\alpha_p}\right)\right] - D\alpha_p w_p - R\alpha_p(1 - A\alpha_p) = 0, \tag{3.104b}$$

subject to the conditions

$$w_p = 0, \quad z = 0, \tag{3.104c}$$

$$w_p = -(1 - A\alpha_p)^2, \quad z = h(t), \tag{3.104d}$$

$$\alpha_p = \alpha_{pi}(z), \quad t = 0, \tag{3.104e}$$

where the film height satisfies

$$\frac{\mathrm{d}h}{\mathrm{d}t} = -\left[1 - A\alpha_p(h(t), t)\right]^2, \tag{3.104f}$$

with $h(0) = 1$.

By taking the dilute polymer limit where $A \searrow 0$, we recover the simplified model that was studied in Section 3.3.2.1. Unlike in the dilute case, however, switching to a Lagrangian coordinate does not lead to simplifications in the full problem. This is rather intuitive and can be explained from the fact there are two Lagrangian coordinates in the full problem: one for each phase. Therefore, switching to one of these coordinates simplifies the equations for the corresponding phase, but this comes at a cost of increasing the complexity of the equations associated with the other phase. Thus, our analysis of the full problem is based

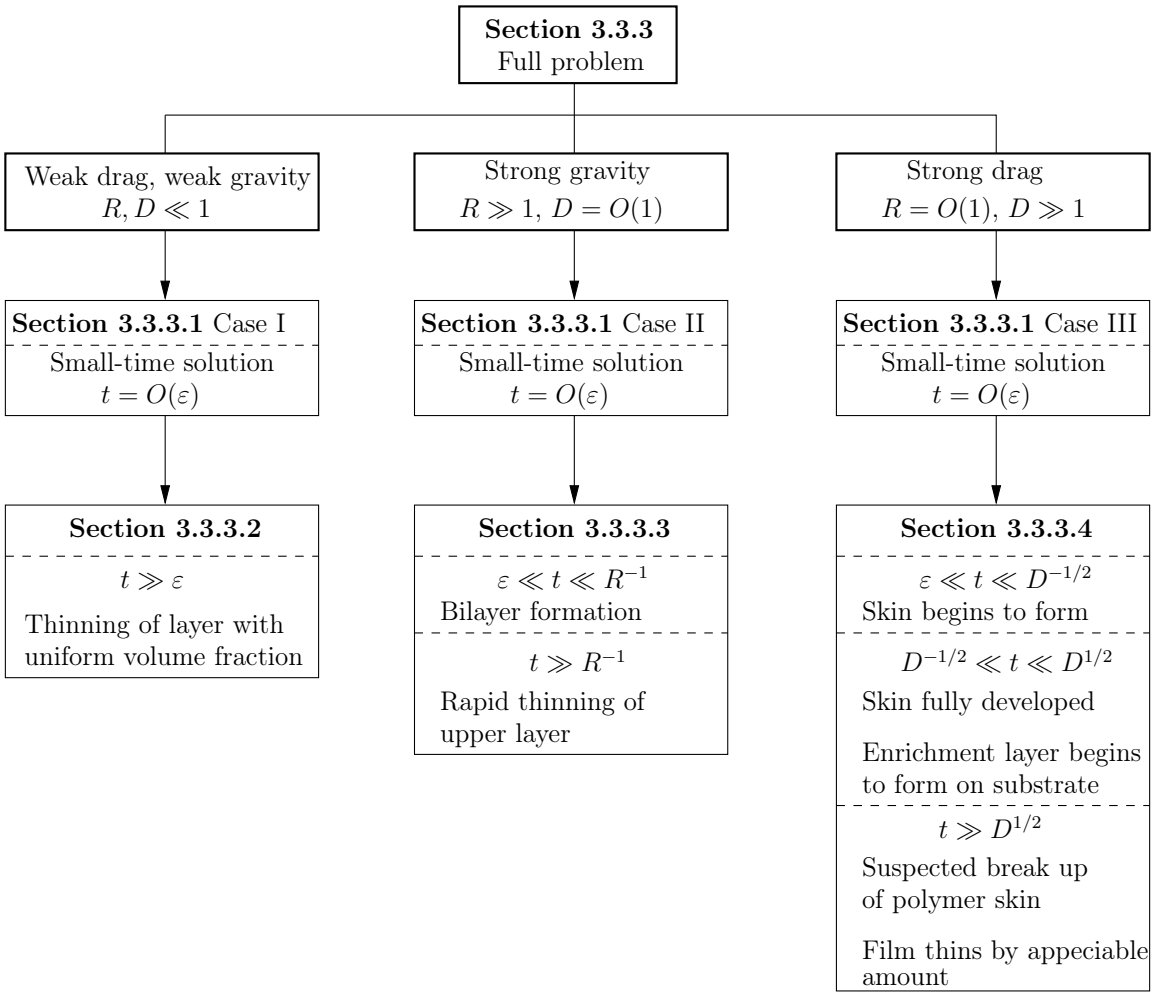


Figure 3.4: Flow chart showing the parameter and time regimes that are considered in the analysis of the one-dimensional two-phase problem given by (3.104). The key dynamics that occur in the various regimes are also summarised. The case with strong drag and strong gravity is briefly mentioned in Section 3.3.3.5 but is not shown in this diagram.

on Eulerian coordinates and to make analytical progress, we consider several limiting cases. A flow chart of the different cases that are studied in the subsequent sections can be found in Figure 3.4.

In general, the one-dimensional problem must be solved numerically. The scheme implemented here is based on implicit time stepping using Chebyshev spectral methods to accurately compute spatial derivatives. The computational domain is mapped to the unit interval via the transformation $\eta = z/h(t)$. This approach seems to work well provided that the volume fraction is neither too small nor too large. As the volume fraction tends to zero, the left-hand side of the momentum balance (3.104b) vanishes, corresponding to a row of zeros in the Jacobian matrix that appears in the numerical method. Such a matrix obviously cannot be inverted and so the method breaks down. If the volume fraction increases to A^{-1}, the second term on the left-hand side of (3.104b) becomes singular, which also causes the numerical method to struggle.

3.3.3.1 Small-time solution

We first explore the behaviour of solutions for sufficiently short times. Therefore, we write $t = \varepsilon\tau$, where $\varepsilon \ll 1$ and $\tau = O(1)$. The mixture is assumed to be initially homogeneous in composition so that $\alpha_p(z,0) \equiv 1$. The volume fraction, velocity, and film thickness are expanded as an asymptotic series of the form

$$\alpha_p(z,\tau) = \alpha_p^{(0)}(z,\tau) + \varepsilon\alpha_p^{(1)}(z,\tau) + O(\varepsilon^2), \tag{3.105a}$$

$$w_p(z,\tau) = w_p^{(0)}(z,\tau) + \varepsilon w_p^{(1)}(z,\tau) + O(\varepsilon^2), \tag{3.105b}$$

$$h(\tau) = h^{(0)}(\tau) + \varepsilon h^{(1)}(\tau) + O(\varepsilon^2), \tag{3.105c}$$

By inserting this into (3.104) and expanding about $\varepsilon \ll 1$, we obtain the following $O(1)$ equations for the volume fraction and the film thickness,

$$\frac{\partial \alpha_p^{(0)}}{\partial \tau} = 0, \tag{3.106a}$$

$$\frac{\mathrm{d}h^{(0)}}{\mathrm{d}\tau} = 0, \tag{3.106b}$$

which are subject to the initial conditions given by $\alpha_p^{(0)}(z,0) \equiv 1$ and $h^{(0)}(0) = 1$. The leading-order solution is easy to obtain and simply given by

$$\alpha_p^{(0)}(z,\tau) \equiv 1, \tag{3.107a}$$

$$h^{(0)}(\tau) \equiv 1. \tag{3.107b}$$

By using these expressions in the $O(1)$ problem for the vertical velocity, we find that it reduces to

$$\ell^2 \frac{\partial^2 w_p^{(0)}}{\partial z^2} - w_p^{(0)} = r(1-A), \tag{3.108a}$$

where $r = R/D$ and ℓ defines a length scale given by

$$\ell^2 = 2\left[1 + (\mu - 1)A\right] D^{-1}. \tag{3.108b}$$

When $D \gg 1$, this length corresponds to the width of the enrichment layer of polymer that forms beneath the free surface due to drag. The corresponding boundary conditions for this problem are

$$w_p^{(0)} = 0, \qquad z = 0, \tag{3.108c}$$

$$w_p^{(0)} = -(1-A)^2, \quad z = 1, \tag{3.108d}$$

An analytical solution for the vertical velocity is straightforward to obtain and can be written as

$$\begin{aligned} w_p^{(0)}(z) = {} & r(1-A)\left[\cosh(z/\ell) - 1\right] \\ & - (1-A)\left\{1 - A + r\left[\cosh(1/\ell) - 1\right]\right\} \frac{\sinh(z/\ell)}{\sinh(1/\ell)}. \end{aligned} \tag{3.109}$$

The $O(\varepsilon)$ problems for the volume fraction and film thickness read

$$\frac{\partial \alpha_p^{(1)}}{\partial \tau} + \frac{\mathrm{d}w_p^{(0)}}{\mathrm{d}z} = 0, \tag{3.110a}$$

$$\frac{\mathrm{d}h^{(1)}}{\mathrm{d}\tau} = -(1-A)^2, \tag{3.110b}$$

which initial conditions given by

$$\alpha_p^{(1)} = 0, \quad t = 0, \tag{3.110c}$$

$$h^{(1)} = 0, \quad t = 0. \tag{3.110d}$$

Since the leading-order velocity $w_p^{(0)}$ is independent of time, (3.110a) can be integrated directly to obtain

$$\alpha_p^{(1)}(z,\tau) = -\left(\frac{\mathrm{d}w_p^{(0)}}{\mathrm{d}z}\right)\tau. \tag{3.111}$$

Similarly, the correction to the film thickness is easy to find and this is simply

$$h^{(1)}(\tau) = -(1-A)^2\tau. \tag{3.112}$$

To determine the initial gravity- and drag-dominated regimes valid for small times, we compare the concentration of polymer at the substrate and the free surface. We find that the gravity- and drag-dominated regimes correspond to $R > (1-A)D/2$ and $R < (1-A)D/2$, respectively. Thus, for a fixed value of D, non-dilute polymer concentrations have the effect of reducing the size of the drag-dominated region. This means that the strength of gravity is enhanced, which leads to larger accumulations of polymer on the substrate. In order for this concentration to be matched at the free surface, stronger drag forces are required. Taking $A \searrow 0$ in these two inequalities recovers the results for the case of a dilute polymer phase.

We now investigate some additional properties of this solution in different parameter regimes. Such an analysis will provide further insights that can be used to tackle the full one-dimensional problem on longer time scales.

Case I: Weak drag and gravity We first consider the case when $D \ll 1$ with $R = o(D)$, corresponding to weak drag and gravity. When the non-dimensional drag coefficient is small, the length scale ℓ defined in (3.108b) is large; therefore, $\ell \to \infty$ as $D \to 0$. Furthermore, this restriction on the Rayleigh number implies that $r = R/D \to 0$ as $D \to 0$. Thus, by taking $D \to 0$ in the expression for the velocity (3.109), we obtain a linear profile given by

$$w_p^{(0)}(z) = -(1-A)^2 z + O(D) \tag{3.113}$$

as $D \to 0$. Inserting this into the correction for the volume fraction (3.111) shows that the corresponding composition remains homogeneous:

$$\alpha_p^{(1)}(z,\tau) = (1-A)^2\tau. \tag{3.114}$$

Case II: Weak drag and strong gravity When the effects of drag are weak but the Rayleigh number is of size $O(D)$ or larger, gravity begins to affect the velocity of the polymer and the composition of the mixture. In particular, the velocity now takes on a quadratic profile given by

$$w_p^{(0)}(z) = -(1-A)^2 z - \frac{R}{4}\left[\frac{1-A}{1+(\mu-1)A}\right](1-z)z + O(D) \tag{3.115}$$

as $D \to 0$. For large Rayleigh numbers, the first term in this expression can be neglected and the velocity profile obtains its minimum at $z = 1/2$. To characterise the magnitude of the velocity when gravity is strong, we introduce the reduced Rayleigh number, $\mathcal{R}$, defined as

$$\mathcal{R} = \frac{R}{16}\left[\frac{1-A}{1+(\mu-1)A}\right], \tag{3.116}$$

so that in the limit $\mathcal{R} \gg 1$, we obtain

$$w_p(z) \simeq -4\mathcal{R}(1-z)z. \tag{3.117}$$

We then have that $w_p \simeq -\mathcal{R}$ at its minimum, *i.e.*, when $z \simeq 1/2$.

Case III: Strong drag and weak gravity An interesting situation arises when the drag coefficient is large, as the the length scale in (3.108b) becomes very small. This corresponds to the formation of a boundary layer (see (3.108a)) below the free surface which, in turn, is caused by strong drag forces which act to prevent the motion of polymer. This boundary layer is most easily seen by first taking the limit of small gravity, $R \to 0$, followed by the limit of strong drag, $D \to \infty$, in (3.109). In this case, the polymer velocity reduces to

$$w_p^{(0)}(z) = -(1-A)^2 \exp\left[-(1-z)/\ell\right]. \tag{3.118}$$

The associated volume fraction of polymer is

$$\alpha_p^{(1)}(z,\tau) = \ell^{-1}(1-A)^2\,\tau \exp\left[-(1-z)/\ell\right]. \tag{3.119}$$

3.3.3.2 Solution with weak drag and gravity

The dynamics that occur for larger times are now investigated. We first consider the simple case when both gravity and drag are weak and the mixture is initially homogeneous. Under these assumptions, the governing equations (3.104) can be written as

$$\frac{\partial \alpha_p}{\partial t} + \frac{\partial}{\partial z}\left(\alpha_p w_p\right) = 0, \tag{3.120a}$$

$$2(1-A\alpha_p)\frac{\partial}{\partial z}\left(\alpha_p \frac{\partial w_p}{\partial z}\right) + 2\mu A \alpha_p \frac{\partial}{\partial z}\left[(1-A\alpha_p)\frac{\partial}{\partial z}\left(\frac{\alpha_p w_p}{1-A\alpha_p}\right)\right] = 0, \tag{3.120b}$$

$$\frac{\mathrm{d}h}{\mathrm{d}t} = -\left[1 - A\alpha_p(h(t),t)\right]^2, \tag{3.120c}$$

subject to the conditions

$$w_p = 0, \qquad z = 0, \tag{3.120d}$$

$$w_p = -(1-A\alpha_p)^2, \quad z = h(t), \tag{3.120e}$$

$$\alpha_p = 1, \qquad t = 0, \tag{3.120f}$$

$$h = 1, \qquad t = 0. \tag{3.120g}$$

The small-time analysis in Section 3.3.3.1 showed that in this parameter regime, the volume fraction remains constant in space and the velocity profile is linear. This motivates an ansatz given by $\alpha_p(z,t) = \alpha_p(t)$, which satisfies

$$\frac{\mathrm{d}\alpha_p}{\mathrm{d}t} + \alpha_p \frac{\partial w_p}{\partial z} = 0. \tag{3.121}$$

When the volume fraction is spatially uniform, the polymer velocity is linear and given by

$$w_p = \frac{\mathrm{d}h}{\mathrm{d}t}\frac{z}{h}. \tag{3.122}$$

By inserting this expression into (3.121) and integrating in time, we find that

$$\alpha_p(t) = \frac{1}{h(t)}. \tag{3.123}$$

This can be used in the evolution equation for the film thickness (3.120c) to obtain the nonlinear differential equation given by

$$\frac{\mathrm{d}h}{\mathrm{d}t} = -(1 - A/h)^2, \quad h(0) = 1. \tag{3.124}$$

An implicit solution to this problem can be found and written as

$$h(t) - 1 + A^2\left(\frac{1}{1-A} - \frac{1}{h(t)-A}\right) + 2A\log\left(\frac{A-h(t)}{A-1}\right) = -t. \tag{3.125}$$

As $t \to \infty$, the thickness $h \to A$, corresponding to a film that is composed of only polymer. No skin formation occurs because the concentration of polymer remains uniform as the film dries.

Comparisons of the implicit solution for the film thickness given in (3.125) with numerical solutions are displayed in Figure 3.5 for various combinations of A, R, and D, with $\mu = 1$. Also shown is the thickness evolution predicted from the small-time analysis of Section 3.3.3.1. When the initial volume fraction is small (panel (a)), the implicit solution shows a remarkable amount of agreement with the numerical solution despite R and D being $O(1)$ in size. For larger initial volume fractions (panel (b)), the implicit solution still gives a good approximation of the film thickness; however, this is only the case for smaller values of R and D.

3.3.3.3 Dynamics with strong gravity

We now consider the dynamics of a mixture subject to strong gravitational effects, but with moderate drag between phases. In particular, we suppose that the reduced Rayleigh number, defined in (3.116), is large so that $\mathcal{R} \gg 1$. We further assume that the drag coefficient D is at most $O(1)$ in size. To balance terms in the momentum equation (3.104b), we scale the velocity with $\mathcal{R}$ so that $w_p = \mathcal{R}W$. Consequently, we introduce a fast time T given by $T = \mathcal{R}t$ to balance terms in the continuity equation (3.104a). The physical interpretation of this scaling is that strong gravity leads to a large downwards acceleration of the denser phase, resulting in large velocities. The evaporative time scale used in the original scaling is too slow to capture this rapid flow, hence the need to introduce the

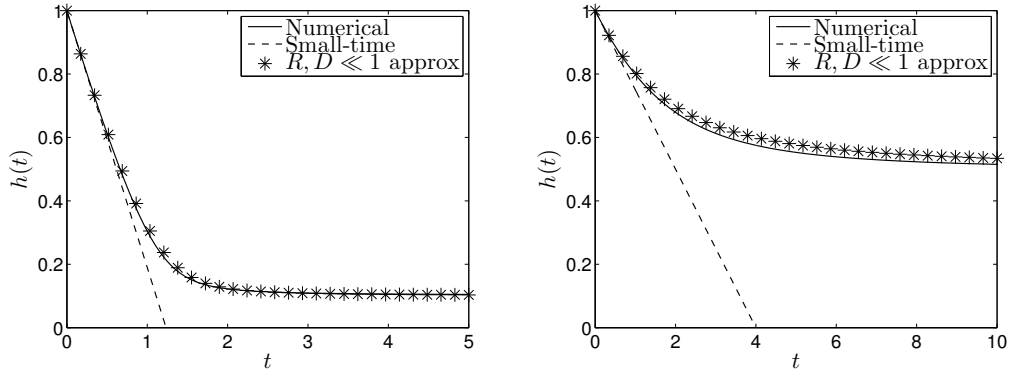


Figure 3.5: Comparison of approximate and numerical solutions for the film thickness when both drag and gravity are weak. The small-time approximation corresponds to the asymptotic solution for h given in Section 3.3.3.1. The $R, D \ll 1$ approximation corresponds to the implicit solution in (3.125). Parameter values are: (a) $A = 0.1$, $R = 2$, $D = 1$; (b) $A = 0.5$, $R = 0.6$, $D = 0.5$. In both cases, $\mu = 1$.

fast time. We write the film thickness and polymer volume fraction as $H(T)$ and $P(z, T)$, respectively, in this "inner" time region.

The rescaled equations can be written as

$$\frac{\partial P}{\partial T} + \frac{\partial}{\partial z}(PW) = 0, \tag{3.126a}$$

$$2(1-AP)\frac{\partial}{\partial z}\left(P\frac{\partial W}{\partial z}\right) + 2\mu AP\frac{\partial}{\partial z}\left[(1-AP)\frac{\partial}{\partial z}\left(\frac{PW}{1-AP}\right)\right] - DPW - \varsigma P(1-AP) = 0, \tag{3.126b}$$

where $\varsigma = R/\mathcal{R}$. These are subject to the conditions

$$W = 0, \qquad z = 0, \tag{3.126c}$$

$$W = -\mathcal{R}^{-1}(1-AP)^2, \quad z = H(T), \tag{3.126d}$$

$$P = P_i(z), \qquad T = 0. \tag{3.126e}$$

The film thickness satisfies

$$\frac{\mathrm{d}H}{\mathrm{d}T} = -\mathcal{R}^{-1}\left[1 - AP(H(T), T)\right]^2, \tag{3.126f}$$

with $H(0) = 1$. We now seek asymptotic expansions of the form

$$P(z,T) = P_0(z,T) + \mathcal{R}^{-1}P_1(z,T) + O(\mathcal{R}^{-2}), \tag{3.127}$$

$$W(z,T) = W_0(z,T) + \mathcal{R}^{-1}W_1(z,T) + O(\mathcal{R}^{-2}), \tag{3.128}$$

$$H(T) = H_0(z,T) + \mathcal{R}^{-1}H_1(T) + O(\mathcal{R}^{-2}), \tag{3.129}$$

as $\mathcal{R} \to \infty$. The $O(1)$ problem for the film thickness is simply

$$\frac{\mathrm{d}H_0}{\mathrm{d}T} = 0, \tag{3.130}$$

subject to $H_0(0) = 1$. Therefore, we have $H_0(T) \equiv 1$. The next-order correction satisfies

$$\frac{\mathrm{d}H_1}{\mathrm{d}T} = -\left[1 - AP_0(1,T)\right]^2, \tag{3.131}$$

subject to $H_1(0) = 0$, from which it follows that

$$H_1(T) = \int_0^T \left[1 - AP_0(1,\xi)\right]^2 \,\mathrm{d}\xi. \tag{3.132}$$

The leading-order solution for the volume fraction that is used in this expression can be determined by solving the $O(1)$ transport problem given by

$$\frac{\partial P_0}{\partial T} + \frac{\partial}{\partial z}\left(P_0 W_0\right) = 0, \tag{3.133}$$

$$2(1 - AP_0)\frac{\partial}{\partial z}\left(P_0 \frac{\partial W_0}{\partial z}\right) + 2\mu A P_0 \frac{\partial}{\partial z}\left[(1 - AP_0)\frac{\partial}{\partial z}\left(\frac{P_0 W_0}{1 - AP_0}\right)\right] - DP_0 W_0 - \varsigma P_0(1 - AP_0) = 0, \tag{3.134}$$

which has the following boundary and initial conditions:

$$W_0 = 0, \qquad z = 0, 1, \tag{3.135}$$

$$P_0 = P_i(z), \quad T = 0. \tag{3.136}$$

Aside from the simplified boundary conditions and a fixed domain, this problem is essentially as complicated as the original problem stated in (3.126). However, the form of the $O(1)$ equations does shed some insight into the dynamics. In particular, evaporation appears to be too slow to influence the behaviour of the mixture and the composition. Therefore, the leading-order solution describes the settling of the denser phase on the substrate. This process results in the creation of a bilayer, with the polymer on the bottom and the solvent on the top.

For large times given by $T = O(\mathcal{R})$, the evaporation of solvent leads to a significant thinning of the fluid layer. To capture these dynamics, we revert to the original time variable t by letting $T = \mathcal{R}t$. We use α_p and h to denote the outer solution for the volume fraction and film thickness, respectively. The scaling for the velocity is kept the same in order to match into the inner time region.

The equations representing the local conservation of mass and momentum are given by

$$\mathcal{R}^{-1}\frac{\partial \alpha_p}{\partial t} + \frac{\partial}{\partial z}\left(\alpha_p W\right) = 0, \tag{3.137a}$$

$$2(1 - A\alpha_p)\frac{\partial}{\partial z}\left(\alpha_p \frac{\partial W}{\partial z}\right) + 2\mu A \alpha_p \frac{\partial}{\partial z}\left[(1 - A\alpha_p)\frac{\partial}{\partial z}\left(\frac{\alpha_p W}{1 - A\alpha_p}\right)\right] - D\alpha_p W - \varsigma\alpha_p(1 - A\alpha_p) = 0, \tag{3.137b}$$

and these are subject to the boundary conditions

$$W = 0, \qquad z = 0, \tag{3.138a}$$

$$W = -\mathcal{R}^{-1}(1 - A\alpha_p)^2, \quad z = h(t). \tag{3.138b}$$

The film thickness satisfies

$$\frac{\mathrm{d}h}{\mathrm{d}t} = -\left[1 - A\alpha_p(h(t), t)\right]^2, \tag{3.139}$$

Initial conditions for α_p and h come from matching to the inner solution. For the film thickness, we have that $h \sim 1 + O(\mathcal{R}^{-1})$ as $t \searrow 0$.

We now seek an asymptotic expansion to this problem of the form

$$\alpha_p(z,t) = \alpha_p^{(0)}(z,t) + O(\mathcal{R}^{-1}), \tag{3.140}$$

$$W(z,t) = W^{(0)}(z,t) + O(\mathcal{R}^{-1}), \tag{3.141}$$

$$h(t) = h^{(0)}(t) + O(\mathcal{R}^{-1}), \tag{3.142}$$

as $\mathcal{R} \to \infty$. The leading-order part of (3.137a) shows that the mass flux $\alpha_p^{(0)} W^{(0)}$ is constant in space. Applying the boundary conditions in (3.138) gives $\alpha_p^{(0)} W^{(0)} \equiv 0$. Based on intuition and the dynamics that occur in the inner problem, we expect that $\alpha_p^{(0)} \equiv 0$ near the free surface $z = h(t)$. Similarly, the substrate is likely to be covered by the polymer and so $\alpha_p^{(0)} \neq 0$ near $z = 0$. In this case, we must have that $W^{(0)} \equiv 0$ near $z = 0$. This is sensible, as the small velocity means that the polymers are tightly packed and unable to move. There is a transition region that connects the layers near $z = 0$ and $z = h(t)$, although we will not discuss this further. The fact that $\alpha^{(0)} = 0$ near the free surface implies, from the leading-order part of (3.139) and the matching condition, that $h^{(0)}(t) = 1 - t$. Therefore, once the polymer has settled onto the substrate, the solvent layer freely evaporates until it is completely gone. The purity of the solvent layer implies that evaporation will take place at the highest rate, leading to the shortest drying times.

A numerical solution of the full one-dimensional model (3.104) in the regime of strong gravity is shown in Figure 3.6. Also shown are the asymptotic approximations to the film thickness in the two time regimes. Drag has been neglected so that $D = 0$, the viscosity ratio has been set to $\mu = 1$, and the mean polymer volume fraction was chosen to be $A = 1/2$ so the mixture is initially a 50:50 ratio of the two species. Furthermore, the initial distribution of the polymer is taken to be uniform; thus, $\alpha_{pi}(z) \equiv 1$. Panel (a) shows the formation of the bilayer, with polymer on the bottom and solvent on the top. Separating the two layers is a transition region. The formation of this bilayer is remarkably fast, even within the inner time regime. The polymer velocity is shown in panel (b). There appear to be three

distinct regions: one near the substrate, one near the free surface, and one in between these two. These roughly correspond to the two layers of the bilayer and the transition zone. The non-monotonicity of the velocity suggests that shocks may occur in the system; however, we do not investigate this any further. Panel (c) compares the numerical and asymptotic film thickness in the inner time regime. Evaluating the integral in the $O(\mathcal{R}^{-1})$ contribution to H is performed numerically. The solutions are found to be in near perfect agreement, and both show that thinning begins to become appreciable when $T = O(1)$. Panel (d) compares the numerical and asymptotic solutions for the film thickness in the outer time regime. There are clear discrepancies between the solutions. However, the rates of thinning, as given by the slopes of the curves, show excellent agreement after the fast transients have subsided, confirming the prediction that the film quickly forms a layer of pure solvent which evaporates at a constant rate until the mixture has completely dried.

3.3.3.4 Dynamics with strong drag

We now consider the opposite case whereby drag, rather than gravity, strongly influences the solution. Accordingly, we assume that $D \gg 1$ and $R = O(1)$. The small-time analysis of Section 3.3.3.1 indicated that in this parameter regime, strong drag forces induce the formation of a compositional boundary layer below the free surface. By examining the full momentum equation (3.104b) and balancing terms in it, we see that this boundary layer will occur in the full problem as well. Thus, we use a matched asymptotic expansion to construct solutions that are valid in outer and inner regions away from and close to the free surface, respectively.

The development of the boundary layer happens quickly so we introduce a fast time $\hat{t}$ defined as $\hat{t} = D^{1/2}t$. On this time scale, the problem becomes

$$\frac{\partial \alpha_p}{\partial \hat{t}} + D^{-1/2}\frac{\partial}{\partial z}\left(\alpha_p w_p\right) = 0, \tag{3.143a}$$

$$2(1-A\alpha_p)\frac{\partial}{\partial z}\left(\alpha_p \frac{\partial w_p}{\partial z}\right) + 2\mu A \alpha_p \frac{\partial}{\partial z}\left[(1-A\alpha_p)\frac{\partial}{\partial z}\left(\frac{\alpha_p w_p}{1-A\alpha_p}\right)\right] - D\alpha_p w_p - R\alpha_p(1-A\alpha_p) = 0, \tag{3.143b}$$

subject to the boundary conditions

$$w_p = 0, \qquad z = 0, \tag{3.143c}$$

$$w_p = -(1-A\alpha_p)^2, \quad z = h(\hat{t}). \tag{3.143d}$$

We suppose that the mixture is initially uniform in composition so that

$$\alpha_p(z,0) \equiv 1. \tag{3.143e}$$

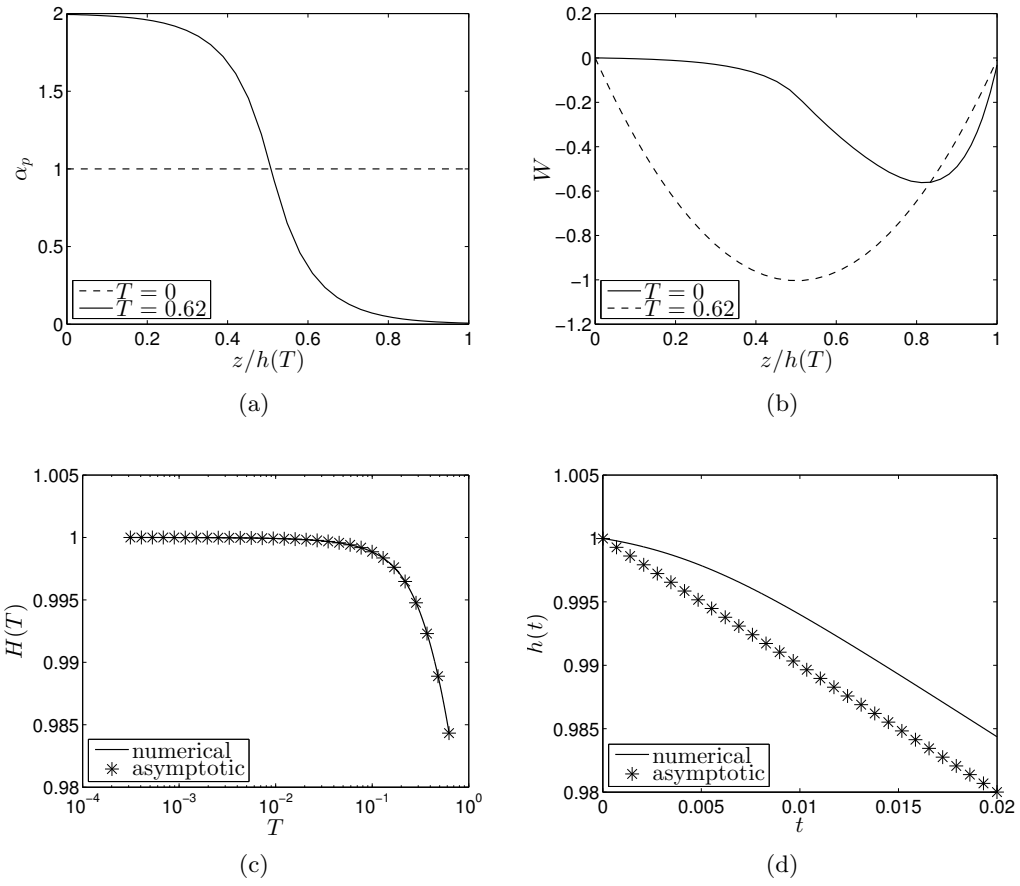


Figure 3.6: Dynamics when gravitational effects are strong. In this case, an initially homogeneous mixture rapidly evolves into a bilayer, with the denser polymer on the bottom and the solvent on the top (a). The velocity of polymers (b) is small near the substrate, where they are tightly packed. Little evaporation of solvent occurs during the rapid formation of the bilayer so the film thickness is approximately constant during this time interval (c). Once the bilayer has formed, the solvent-rich upper layer freely evaporates at a constant rate (d). The parameters used in the simulation are $A = 0.5$, $\mu = 1$, $D = 0$, $R = 1000$.

The film thickness evolves according to

$$\frac{\mathrm{d}h}{\mathrm{d}\hat{t}} = -D^{-1/2}\left[1 - A\alpha_p(h(\hat{t}),\hat{t})\right]^2, \tag{3.143f}$$

with $h(0) = 1$.

In the outer regime valid away from the free surface, the volume fraction and the velocity are written as $\hat{\alpha}$ and $\hat{w}$, respectively. By seeking an asymptotic expansion of the form

$$\hat{\alpha}(z,\hat{t}) = \hat{\alpha}_0 + O(D^{-1/2}), \tag{3.144}$$

$$\hat{w}(z,\hat{t}) = \hat{w}_0 + O(D^{-1/2}), \tag{3.145}$$

it is straightforward to deduce that

$$\hat{\alpha}_0(z,\hat{t}) \equiv 1, \quad \hat{w}_0(z,t) \equiv 0. \tag{3.146}$$

Therefore, the outer region is uninfluenced by the near-surface dynamics on this time scale.

In the inner region, the volume fraction, velocity, and film thickness are written as $\hat{P}$, $\hat{W}$, and $\hat{H}$, respectively. The inner problem is formulated by first introducing the change of variable given by

$$\hat{t} = \hat{t}', \quad \hat{\xi} = \frac{\hat{H}(\hat{t}) - z}{D^{-1/2}}, \tag{3.147}$$

The corresponding system of equations and their boundary conditions can be written as (upon dropping the primes)

$$\frac{\partial \hat{P}}{\partial \hat{t}} - \left[1 - A\hat{P}(\hat{H},\hat{t})\right]^2 \frac{\partial \hat{P}}{\partial \hat{\xi}} - \frac{\partial}{\partial \hat{\xi}}\left(\hat{P}\hat{W}\right) = 0, \tag{3.148a}$$

$$\begin{aligned} 2(1 - A\hat{P})\frac{\partial}{\partial \hat{\xi}}\left(\hat{P}\frac{\partial \hat{W}}{\partial \hat{\xi}}\right) + 2\mu A\hat{P}\frac{\partial}{\partial \hat{\xi}}\left[(1 - A\hat{P})\frac{\partial}{\partial \hat{\xi}}\left(\frac{\hat{P}\hat{W}}{1 - A\hat{P}}\right)\right] \\ -\hat{P}\hat{W} - D^{-1}R\hat{P}(1 - A\hat{P}) = 0, \end{aligned} \tag{3.148b}$$

subject to

$$\hat{P} = 1, \qquad \hat{t} = 0, \tag{3.148c}$$

$$\hat{W} = -(1 - A\hat{P})^2, \quad \hat{\xi} = 0, \tag{3.148d}$$

and a matching condition for $\hat{W}$ that will be specified below. The film thickness evolves according to

$$\frac{\mathrm{d}\hat{H}}{\mathrm{d}\hat{t}} = -D^{-1/2}\left[1 - A\hat{P}(\hat{H}(\hat{t}),\hat{t})\right]^2, \tag{3.148e}$$

with $\hat{H}(0) = 1$. As before, write the solution to this problem as an asymptotic expansion:

$$\hat{P}(\hat{\xi}, \hat{t}) = \hat{P}_0(\hat{\xi}, \hat{t}) + O(D^{-1/2}), \tag{3.149}$$

$$\hat{W}(\hat{\xi}, \hat{t}) = \hat{W}_0(\hat{\xi}, \hat{t}) + O(D^{-1/2}), \tag{3.150}$$

$$\hat{H}(\hat{t}) = \hat{H}_0(\hat{t}) + D^{-1/2}\hat{H}_1(\hat{t}) + O(D^{-1}). \tag{3.151}$$

By substituting these into (3.148e) and its initial condition, it immediately follows that

$$\hat{H}_0(\hat{t}) \equiv 1, \tag{3.152a}$$

$$\hat{H}_1(\hat{t}) = -\int_0^{\hat{t}} \left[1 - A\hat{P}_0(1, \zeta)\right]^2 \, \mathrm{d}\zeta. \tag{3.152b}$$

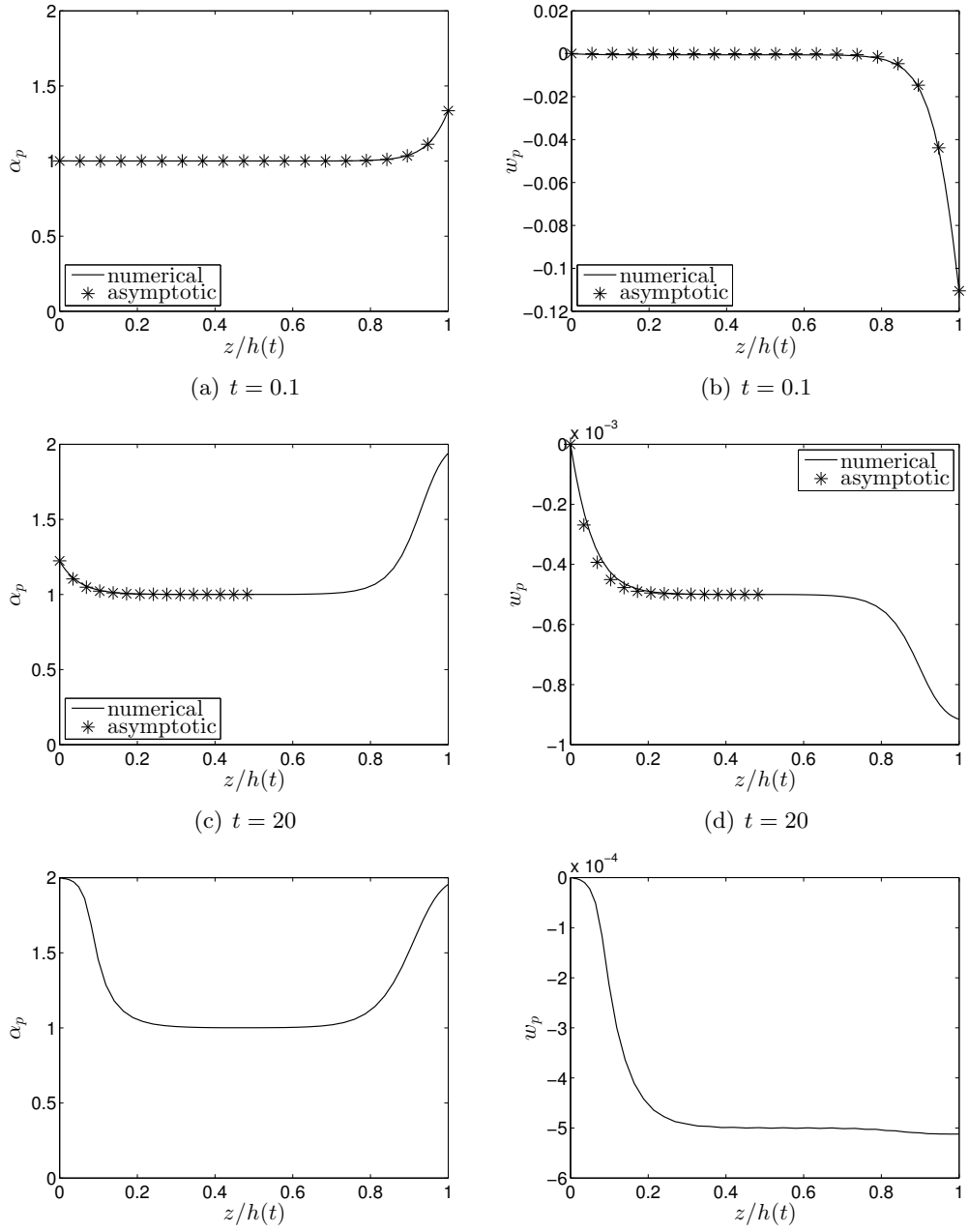
The $O(1)$ transport problem is nearly as complex as the full problem; the only simplification is that gravity no longer appears. However, this problem is relatively easy to solve numerically, particularly because the computational domain is now fixed, and this is the approach we take. In order to obtain a numerical solution for the leading-order inner problem, the matching condition $\hat{W}_0 \to 0$ as $\xi \to \infty$ must be imposed. When implemented in practice, the domain is truncated and the corresponding Dirichlet condition is imposed at the endpoint.

Figure 3.7 (a)–(b) shows the composite asymptotic solution in the $t = O(D^{-1/2})$ time regime and compares it with a numerical solution of the full equations (3.104). The parameter values were taken to be $A = 1/2$, $D = 1000$, $R = 1$, and $\mu = 1$. The match between the asymptotic and numerical solutions is found to be excellent. The solutions illustrate the growing boundary layer at the free surface that corresponds to a local build up of polymer caused by strong drag forces.

On longer time scales, the weak, but constant, downwards pull of gravity will begin to influence the dynamics of the system, leading to the slow development of enrichment layers near the substrate. To capture this behaviour, we recast the equations in terms of the original time variable by letting $\hat{t} = D^{1/2}t$ with $t = O(1)$. The analysis in the earlier $t = O(D^{-1/2})$ regime revealed that the velocity is small in an outer region away from the free surface. A new velocity scale can be obtained by balancing the drag and gravity terms in the momentum equation (3.104b), thus giving $w_p \sim D^{-1}$. Therefore, in regions away from the surface, we write $\alpha_p = \tilde{\alpha}$ and $w_p = D^{-1}\tilde{w}$, so that the corresponding problem becomes

$$\frac{\partial \tilde{\alpha}}{\partial t} + D^{-1}\frac{\partial}{\partial z}(\tilde{\alpha}\tilde{w}) = 0, \tag{3.153a}$$

$$2D^{-1}(1 - A\tilde{\alpha})\frac{\partial}{\partial z}\left(\tilde{\alpha}\frac{\partial \tilde{w}}{\partial z}\right) + 2D^{-1}\mu A\tilde{\alpha}\frac{\partial}{\partial z}\left[(1 - A\tilde{\alpha})\frac{\partial}{\partial z}\left(\frac{\tilde{\alpha}\tilde{w}}{1 - A\tilde{\alpha}}\right)\right] - \tilde{\alpha}\tilde{w} - R\tilde{\alpha}(1 - A\tilde{\alpha}) = 0, \tag{3.153b}$$



(a) $t = 0.1$ (b) $t = 0.1$

(c) $t = 20$ (d) $t = 20$

(e) $t = 175$ (f) $t = 175$

Figure 3.7: Dynamics in the limit of strong drag, $D \gg 1$, and moderate gravity, $R = O(1)$. An asymptotic analysis reveals three time regimes. The first is when $t = O(D^{-1/2})$, during which evaporation-induced drag leads to the rapid formation of a compositional boundary layer at the free surface. When $t = O(1)$, gravitational effects lead to the slow accumulation of polymers on the substrate and the development of a second boundary layer. For $t \gg 1$, layers that are nearly pure in polymer have developed at the surface and the substrate, leaving a two-phase core in the interior of the layer. Gravity is expected to slowly break up the polymer-rich skin at the free surface, after which the remaining solvent evaporates from the layer. Parameters values were taken to be $A = 1/2$, $D = 1000$, $R = 1$, $\mu = 1$. The initial condition was $\alpha_p(z, 0) \equiv 1$.

subject to

$$\tilde{w} = 0, \quad z = 0. \tag{3.153c}$$

The initial condition for $\tilde{\alpha}$ comes from matching into the previous time regime. We write the solution as

$$\tilde{\alpha}(z, \tilde{t}) = \tilde{\alpha}_0(z, \tilde{t}) + O(D^{-1/2}), \tag{3.154a}$$

$$\tilde{w}(z, \tilde{t}) = \tilde{w}_0(z, \tilde{t}) + O(D^{-1/2}). \tag{3.154b}$$

Using this expansion, we can match into the earlier time regime to deduce that $\tilde{\alpha}_0 \sim 1$ as $\tilde{t} \searrow 0$. By inserting (3.154) into (3.153), it follows that

$$\tilde{\alpha}_0(z, \tilde{t}) \equiv 1, \tag{3.155a}$$

$$\tilde{w}_0(z, \tilde{t}) = -R(1 - A). \tag{3.155b}$$

The solution for the vertical velocity does not satisfy the no-flux condition at the substrate; thus, there must be an additional boundary layer there. To resolve this, we introduce an inner region near the substrate and we write $z = D^{-1/2}\tilde{\eta}$. In this region, the volume fraction and velocity are denoted as $\tilde{P}$ and $\tilde{W}$, respectively. The associated problem for $\tilde{P}$ and $\tilde{W}$ is given by

$$\frac{\partial \tilde{P}}{\partial t} + D^{-1/2}\frac{\partial}{\partial \tilde{\eta}}\left(\tilde{P}\tilde{W}\right) = 0, \tag{3.156a}$$

$$2(1 - A\tilde{P})\frac{\partial}{\partial \tilde{\eta}}\left(\tilde{P}\frac{\partial \tilde{W}}{\partial \tilde{\eta}}\right) + 2\mu A\tilde{P}\frac{\partial}{\partial \tilde{\eta}}\left[(1 - A\tilde{P})\frac{\partial}{\partial \tilde{\eta}}\left(\frac{\tilde{P}\tilde{W}}{1 - A\tilde{P}}\right)\right] - \tilde{P}\tilde{W} - R\tilde{P}(1 - A\tilde{P}) = 0, \tag{3.156b}$$

subject to

$$\tilde{W} = 0, \quad \tilde{\eta} = 0. \tag{3.156c}$$

The solution to this problem is written in the form

$$\tilde{P}(z, \tilde{t}) = \tilde{P}_0(z, \tilde{t}) + O(D^{-1/2}), \tag{3.157}$$

$$\tilde{W}(z, \tilde{t}) = \tilde{W}_0(z, \tilde{t}) + O(D^{-1/2}). \tag{3.158}$$

The matching conditions for the $O(1)$ problem can be written as $P_0 \sim 1$ as $\tilde{t} \searrow 0$ and $\tilde{W}_0 \to -R(1 - A)$ as $\tilde{\eta} \to \infty$. An analytical solution to the $O(1)$ problem can be obtained

and combined with the inner solution near the substrate to form a leading-order composite solution given by

$$\alpha_p(z,t) = 1 + \frac{Rt}{\lambda D^{1/2}} \exp\left(D^{1/2} z/\lambda\right), \tag{3.159a}$$

$$w_p(z,t) = -D^{-1} R(1-A)\left[1 - \exp\left(-D^{1/2} z/\lambda\right)\right], \tag{3.159b}$$

where λ is a constant given by

$$\lambda = \left\{2\left[1 + (\mu - 1)A\right]\right\}^{1/2}. \tag{3.159c}$$

The composite solution for the volume fraction will first fail to be asymptotic when $t = \lambda D^{1/2}/R$. Roughly speaking, this corresponds to the time when the build up of polymer on the substrate has become significant.

In this $t = O(1)$ time regime, the enrichment layer below the free surface further develops, leading to the formation of a polymer-rich skin below the free surface. This slows the rate of evaporation and essentially freezes the composition below the surface. A mathematical analysis of this layer remains an area of future work.

Figures 3.7 (c)–(d) show the composite solution for the above parameter values given by $A = 1/2$, $D = 1000$, $R = \mu = 1$ at time $t = 20$ and compares it with a numerical solution. There is good agreement between the curves, and the development of an enrichment layer near the substrate can clearly be seen.

The evolution of the system for longer times has been investigated via numerical simulations of the full problem. A continuation of the previous solution until $t = 175$ is shown in Figures 3.7 (e)–(f). The growth of the boundary layer near the substrate corresponds to the appearance of a packed layer of polymer, similar to that observed in the situation with strong gravity. The qualitative and quantitative features of the skin near the surface remain mostly unchanged. Interestingly, this figure shows the appearance of a two-phase core in the interior of the layer that is composed of roughly equal concentrations of solvent and polymer. Numerical difficulties prevented the simulation from being continued even further; however, interesting dynamics are likely to arise on very long time scales. In particular, the formation of the skin will prevent solvent from evaporating, thus trapping it in the interior. Gravity will lead to the two-phase core separating into relatively pure layers of polymer and solvent. In the long term, gravity will also lead to the break up of the skin, enabling the layer to thin until all of the solvent is removed from the system.

The evolution of the film thickness is shown in Figure 3.8. For $O(1)$ times and, in particular, before the formation of a skin, the layer thins relatively rapidly. However, the rate of thinning decreases substantially once the skin has developed, which seems to occur on $O(D^{1/2})$ times. Once the skin has formed, the polymer concentration stays relatively

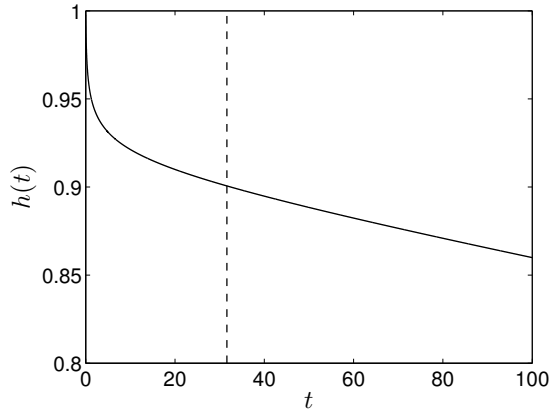


Figure 3.8: Evolution of the film thickness during the simulation shown in Figure 3.7. After a short period of rapid thinning, the development of a polymer-rich layer below the free surface decreases the evaporation rate. The near-surface composition changes slowly, leading to a film that decreases at a roughly uniform rate. The parameter used in the simulation were $A = 1/2$, $D = 1000$, $R = 1$, $\mu = 1$. The dashed line corresponds to when $t = D^{1/2}$.

constant at the surface, leading to a slow, linear decrease in the film thickness. The slow decrease in the film thickness, combined with the breakdown of the composite solution valid near the substrate (3.159), suggests that, in addition to the $t = O(D^{-1/2})$ and $t = O(1)$ regimes, there is a third time regime given by $t = O(D^{1/2})$ that can be considered. Further investigations of this will be the topic of future work.

3.3.3.5 Dynamics with strong drag and gravity

The qualitative features of the system in the case of strong drag and gravity are similar to those seen previously. In particular, strong gravity leads to the rapid development of an enrichment layer near the substrate, and strong drag quickly forms a polymer-rich skin. The dominant layer that emerges in the early stages of evolution can be deduced from the inequalities that were obtained from small-time analysis of Section 3.3.3.1, namely, $R > (1 - A)D/2$ and $R < (1 - A)D/2$, which characterise gravity- and drag-dominated regimes, respectively.

3.4 Three-phase flow in the absence of gravity

The analysis of the two-phase model showed that a rich variety of dynamics can emerge in the different parameter regimes. We now extend this model by considering a third phase, which can be interpreted as dispersed or partially dissolved polymers. An interesting feature of this model is that drag forces can now lead to the dispersed polymer phase being advected with the solvent. In the one-dimensional two-phase problem, conservation of mass always required the polymer and solvent phases to travel in opposite directions, as seen in (3.103).

A further attribute of this model is that it can now capture, in a qualitative sense, the process of phase separation, whereby the dissolved polymers demix from the solvent to form polymer-rich domains. Our investigation will focus mainly on exploring these two features in one space dimension without gravitational effects. The corresponding one-dimensional model, complete with boundary and initial conditions, can be written as

$$\frac{\partial \alpha_d}{\partial t} + \frac{\partial}{\partial z}\left(\alpha_d w_d\right) = -\gamma, \tag{3.160a}$$

$$\frac{\partial \alpha_p}{\partial t} + \frac{\partial}{\partial z}\left(\alpha_p w_p\right) = \gamma, \tag{3.160b}$$

$$\frac{\partial}{\partial z}\left((1-\alpha_d-\alpha_p)w_s + \alpha_d w_d + \alpha_p w_p\right) = 0, \tag{3.160c}$$

$$\begin{aligned} -\alpha_d \frac{\partial p}{\partial z} + 2\mu_p \left(\alpha_d \frac{\partial w_d}{\partial z}\right) + c_{sd}(1-\alpha_d-\alpha_p)\alpha_d(w_s - w_d) \\ -c_{dp}\alpha_d\alpha_p(w_d - w_p) = 0, \end{aligned} \tag{3.160d}$$

$$\begin{aligned} -\alpha_p \frac{\partial p}{\partial z} + 2\mu_p \left(\alpha_p \frac{\partial w_p}{\partial z}\right) + c_{sp}(1-\alpha_d-\alpha_p)\alpha_p(w_s - w_p) \\ +c_{dp}\alpha_d\alpha_p(w_d - w_p) = 0, \end{aligned} \tag{3.160e}$$

$$-\frac{\partial p}{\partial z} + 2\frac{\partial}{\partial z}\left(\mu_s(1-\alpha_d-\alpha_p)\frac{\partial w_s}{\partial z} + \mu_p\alpha_d\frac{\partial w_d}{\partial z} + \mu_p\alpha_p\frac{\partial w_p}{\partial z}\right) = 0, \tag{3.160f}$$

where the solvent volume fraction, α_s, has been eliminated from the problem through the use of (3.45d). The boundary conditions can be written as

$$w_s = 0, \qquad z = 0, \tag{3.161a}$$

$$w_d = 0, \qquad z = 0, \tag{3.161b}$$

$$w_p = 0, \qquad z = 0, \tag{3.161c}$$

$$w_s - \frac{\mathrm{d}h}{\mathrm{d}t} = E(1-\alpha_d-\alpha_p), \quad z = h(t), \tag{3.161d}$$

$$w_d - \frac{\mathrm{d}h}{\mathrm{d}t} = 0, \qquad z = h(t), \tag{3.161e}$$

$$w_p - \frac{\mathrm{d}h}{\mathrm{d}t} = 0, \qquad z = h(t). \tag{3.161f}$$

The film height evolves according to

$$\frac{\mathrm{d}h}{\mathrm{d}t} = -E\left[1-\alpha_d(h(t),t)-\alpha_p(h(t),t)\right]^2. \tag{3.162}$$

Initial conditions for the system are given by

$$\alpha_d = \alpha_{di}(z), \quad t = 0, \tag{3.163a}$$

$$\alpha_p = \alpha_{pi}(z), \quad t = 0, \tag{3.163b}$$

$$h = H, \qquad t = 0. \tag{3.163c}$$

The interfacial mass transfer term is written as

$$\gamma(\alpha_d, \alpha_p) = \Upsilon \alpha_d \alpha_p, \tag{3.164}$$

where Υ is a constant. This form is chosen so that reactions will only occur in regions where there are both polymeric phases. For simplicity, we have assumed that the demixing process is irreversible, *i.e.,* we do not allow polymers to redissolve into the solvent. More realistic forms for γ that account for the thermodynamics and kinetics of the reaction can be derived from the microscopic dynamics; however, this is not something is considered here. The form of this term indicates that the action of interfacial mass transfer on the microscale manifests itself as bulk mass transfer on the macroscale.

3.4.1 Non-dimensionalisation

To non-dimensionalise the system, we scale time with the inverse of the rate of interfacial mass transfer, $t \sim \Upsilon^{-1}$. In this problem, evaporation drives the flow, which suggests using the evaporative mass transfer coefficient as the velocity scale; thus, we let $w_j \sim E$ for $j = s, d, p$. Length is scaled according to the initial height of the layer, $z \sim H$. Finally, we choose the pressure scale so that pressure gradients balance the drag force between the solvent and polymer-rich phases. Thus, we have that $p \sim c_{sp} E H$. With these scalings, the governing system of equations becomes

$$\frac{\partial \alpha_d}{\partial t} + \beta \frac{\partial}{\partial z}\left(\alpha_d w_d\right) = -\alpha_d \alpha_p, \tag{3.165a}$$

$$\frac{\partial \alpha_p}{\partial t} + \beta \frac{\partial}{\partial z}\left(\alpha_p w_p\right) = \alpha_d \alpha_p, \tag{3.165b}$$

$$\frac{\partial}{\partial z}\left((1-\alpha_d-\alpha_p)w_s + \alpha_d w_d + \alpha_p w_p\right) = 0, \tag{3.165c}$$

$$\begin{aligned} -\alpha_d \frac{\partial p}{\partial z} + 2D^{-1}\left(\alpha_d \frac{\partial w_d}{\partial z}\right) + \varepsilon^{-1}(1-\alpha_d-\alpha_p)\alpha_d(w_s - w_d) \\ -\delta \alpha_d \alpha_p (w_d - w_p) = 0, \end{aligned} \tag{3.165d}$$

$$\begin{aligned} -\alpha_p \frac{\partial p}{\partial z} + 2D^{-1}\left(\alpha_p \frac{\partial w_p}{\partial z}\right) + (1-\alpha_d-\alpha_p)\alpha_p(w_s - w_p) \\ +\delta \alpha_d \alpha_p (w_d - w_p) = 0, \end{aligned} \tag{3.165e}$$

$$-\frac{\partial p}{\partial z} + 2D^{-1}\frac{\partial}{\partial z}\left(\mu(1-\alpha_d-\alpha_p)\frac{\partial w_s}{\partial z} + \alpha_d \frac{\partial w_d}{\partial z} + \alpha_p \frac{\partial w_p}{\partial z}\right) = 0, \tag{3.165f}$$

where the five non-dimensional numbers that appear are defined as

$$\beta = \frac{E}{\Upsilon H}, \quad D = \frac{c_{sp} H^2}{\mu_p}, \quad \mu = \frac{\mu_s}{\mu_p}, \quad \delta = \frac{c_{dp}}{c_{sp}}, \quad \varepsilon = \frac{c_{sp}}{c_{sd}}. \tag{3.166}$$

Of these, β measures the rate of bulk interfacial mass transfer to evaporative mass transfer. The parameters D and μ are the same drag coefficient and viscosity ratio that appeared in the two-phase problem. The two remaining numbers, δ and ε, correspond to drag ratios.

The non-dimensional boundary conditions read

$$w_s = 0, \qquad z = 0, \tag{3.167a}$$

$$w_d = 0, \qquad z = 0, \tag{3.167b}$$

$$w_p = 0, \qquad z = 0, \tag{3.167c}$$

$$\beta w_s - \frac{\mathrm{d}h}{\mathrm{d}t} = \beta(1 - \alpha_d - \alpha_p), \quad z = h(t), \tag{3.167d}$$

$$\beta w_d - \frac{\mathrm{d}h}{\mathrm{d}t} = 0, \qquad z = h(t), \tag{3.167e}$$

$$\beta w_p - \frac{\mathrm{d}h}{\mathrm{d}t} = 0, \qquad z = h(t). \tag{3.167f}$$

The film height evolves according to

$$\frac{\mathrm{d}h}{\mathrm{d}t} = -\beta \left[1 - \alpha_d(h(t), t) - \alpha_p(h(t), t)\right]^2. \tag{3.168}$$

This can be used to simplify the kinematic boundary conditions (3.167d)–(3.167f) so they become

$$w_s = (\alpha_d + \alpha_p)(1 - \alpha_d - \alpha_p), \quad z = h(t), \tag{3.169a}$$

$$w_d = -(1 - \alpha_d - \alpha_p)^2, \qquad z = h(t), \tag{3.169b}$$

$$w_p = -(1 - \alpha_d - \alpha_p)^2, \qquad z = h(t). \tag{3.169c}$$

Finally, the non-dimensional initial conditions for the problem are given by

$$\alpha_d = \alpha_{di}(z), \quad t = 0, \tag{3.170a}$$

$$\alpha_p = \alpha_{pi}(z), \quad t = 0, \tag{3.170b}$$

$$h = 1, \qquad t = 0. \tag{3.170c}$$

3.4.2 Reduction of the system

The non-dimensional system of equations can be simplified by making some assumptions about the size of the various non-dimensional numbers and by manipulating the equations. We suppose that the drag between the two polymer phases is much weaker than the drag between the solvent and the polymer-rich domains, which implies $\delta \ll 1$. On the other hand, the drag force between the solvent and the dispersed polymer phase is expected to be large so that the polymers are advected with the solvent. This is equivalent to saying that $\varepsilon \ll 1$. Furthermore, the solvent is assumed to be much less viscous than the polymer; thus, $\mu \ll 1$. Accordingly, we set $\delta = \mu = 0$ in the governing equations. The latter is potentially a singular limit; however, we show below that this will not be the case. Naively taking $\varepsilon \searrow 0$ yields $w_d = w_s$, which does not satisfy the kinematic boundary conditions (3.169).

Therefore, a boundary layer can be expected at the free surface. By balancing terms in (3.165d), we see this boundary layer will be of width $O(\varepsilon^{1/2})$. The singular nature of the $\varepsilon \searrow 0$ limit means some care needs to be taken when using it and thus we do not simply set $\varepsilon = 0$ in the governing equations. Rather, we deal with this limit on a case-by-case basis.

The simplified bulk equations can be written as

$$\frac{\partial \alpha_d}{\partial t} + \beta \frac{\partial}{\partial z}\left(\alpha_d w_d\right) = -\alpha_d \alpha_p, \tag{3.171a}$$

$$\frac{\partial \alpha_p}{\partial t} + \beta \frac{\partial}{\partial z}\left(\alpha_p w_p\right) = \alpha_d \alpha_p, \tag{3.171b}$$

$$\frac{\partial}{\partial z}\left((1-\alpha_d-\alpha_p)w_s + \alpha_d w_d + \alpha_p w_p\right) = 0, \tag{3.171c}$$

$$-\alpha_d \frac{\partial p}{\partial z} + 2D^{-1}\left(\alpha_d \frac{\partial w_d}{\partial z}\right) + \varepsilon^{-1}(1-\alpha_d-\alpha_p)\alpha_d(w_s - w_d) = 0, \tag{3.171d}$$

$$-\alpha_p \frac{\partial p}{\partial z} + 2D^{-1}\left(\alpha_p \frac{\partial w_p}{\partial z}\right) + (1-\alpha_d-\alpha_p)\alpha_p(w_s - w_p) = 0, \tag{3.171e}$$

$$-\frac{\partial p}{\partial z} + 2D^{-1}\frac{\partial}{\partial z}\left(\alpha_d \frac{\partial w_d}{\partial z} + \alpha_p \frac{\partial w_p}{\partial z}\right) = 0. \tag{3.171f}$$

By integrating (3.171c) and applying the boundary conditions on the substrate, we find that the solvent velocity can be written as

$$w_s = -\frac{\alpha_d w_d + \alpha_p w_p}{1-\alpha_d-\alpha_p}. \tag{3.172}$$

The kinematic boundary condition for the solvent (3.169a) is automatically satisfied by this expression, verifying that $\mu \searrow 0$ is not a singular limit. By using (3.172) and (3.171f) to eliminate w_s and $\partial_z p$ from the problem, respectively, the reduced system of equations describing the evolution of a three-phase mixture becomes

$$\frac{\partial \alpha_d}{\partial t} + \beta \frac{\partial}{\partial z}\left(\alpha_d w_d\right) = -\alpha_d \alpha_p, \tag{3.173a}$$

$$\frac{\partial \alpha_p}{\partial t} + \beta \frac{\partial}{\partial z}\left(\alpha_p w_p\right) = \alpha_d \alpha_p, \tag{3.173b}$$

$$\begin{aligned} 2\alpha_d \frac{\partial}{\partial z}\left(\alpha_p \frac{\partial w_p}{\partial z}\right) - 2(1-\alpha_d)\frac{\partial}{\partial z}\left(\alpha_d \frac{\partial w_d}{\partial z}\right) \\ +\varepsilon^{-1} D\alpha_d[\alpha_p w_p + (1-\alpha_p)w_d] = 0, \end{aligned} \tag{3.173c}$$

$$\begin{aligned} -2(1-\alpha_p)\frac{\partial}{\partial z}\left(\alpha_p \frac{\partial w_p}{\partial z}\right) + 2\alpha_p \frac{\partial}{\partial z}\left(\alpha_d \frac{\partial w_d}{\partial z}\right) \\ +D\alpha_p\left[(1-\alpha_d)w_p + \alpha_d w_d\right] = 0. \end{aligned} \tag{3.173d}$$

The film thickness evolves according to

$$\frac{\mathrm{d}h}{\mathrm{d}t} = \beta\left[1 - \alpha_d(h(t),t) - \alpha_p(h(t),t)\right]^2. \tag{3.174}$$

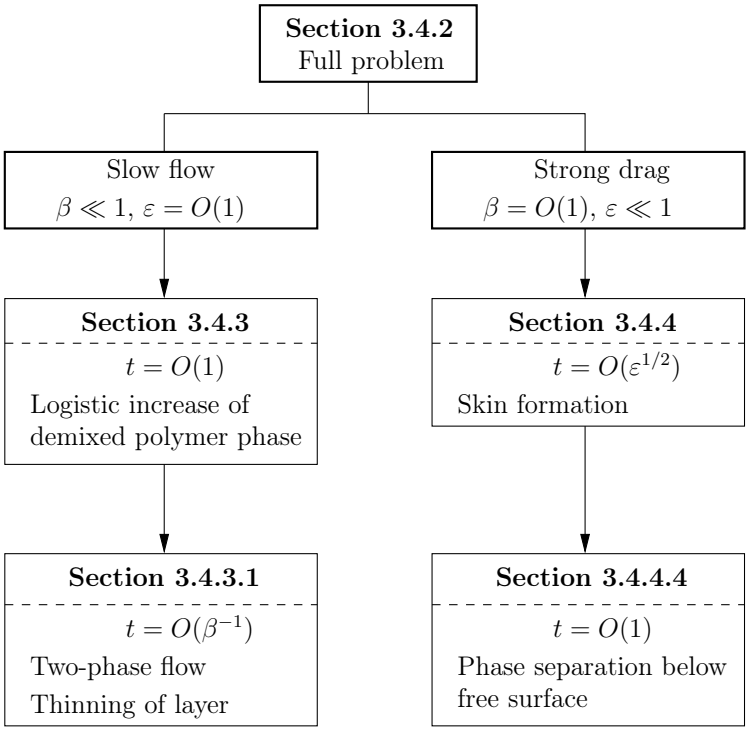


Figure 3.9: Flow chart showing the parameter and time regimes that are considered in the analysis of the one-dimensional three-phase problem given by (3.173)–(3.175). The key dynamics that occur in the various regimes are also summarised.

Finally, boundary and initial conditions for this problem are given by

$$w_d = 0, \qquad z = 0, \tag{3.175a}$$

$$w_p = 0, \qquad z = 0, \tag{3.175b}$$

$$w_d = -(1 - \alpha_d - \alpha_p)^2, \quad z = h(t), \tag{3.175c}$$

$$w_p = -(1 - \alpha_d - \alpha_p)^2, \quad z = h(t), \tag{3.175d}$$

$$\alpha_d \equiv \alpha_{di}, \qquad t = 0, \tag{3.175e}$$

$$\alpha_p \equiv \alpha_{pi}, \qquad t = 0, \tag{3.175f}$$

$$h = 1, \qquad t = 0, \tag{3.175g}$$

where we have assumed the volume fractions are spatially uniform at $t = 0$.

A flow chart that outlines the parameter regimes we analyse can be found in Figure 3.9.

3.4.3 The slow-flow limit

When the rate of evaporation is slow in comparison to the rate of interfacial mass transfer, the parameter β is small. Physically, this is equivalent to saying the phases appear motionless on the reactive time scale. The fact that $\beta \ll 1$ motivates seeking an asymptotic

expansion of the form

$$\alpha_d(z,t) = \alpha_d^{(0)}(z,t) + O(\beta), \tag{3.176a}$$

$$\alpha_p(z,t) = \alpha_p^{(0)}(z,t) + O(\beta), \tag{3.176b}$$

$$w_d(z,t) = w_d^{(0)}(z,t) + O(\beta), \tag{3.176c}$$

$$w_p(z,t) = w_p^{(0)}(z,t) + O(\beta), \tag{3.176d}$$

$$h(t) = h^{(0)}(t) + \beta h^{(1)}(t) + O(\beta^2). \tag{3.176e}$$

To facilitate the discussion, we suppose that $\varepsilon = O(1)$ so that there are no asymptotic contributions from boundary layers at the free surface. The $O(1)$ problem (in β) for the volume fractions is given by

$$\frac{\partial \alpha_d^{(0)}}{\partial t} = -\alpha_d^{(0)}\alpha_p^{(0)}, \tag{3.177a}$$

$$\frac{\partial \alpha_p^{(0)}}{\partial t} = \alpha_d^{(0)}\alpha_p^{(0)}, \tag{3.177b}$$

with $\alpha_d^{(0)}(0) = \alpha_{di}$ and $\alpha_p^{(0)}(0) = \alpha_{pi}$. From these initial conditions, we can deduce that the leading-order volume fractions remain spatially uniform for all time. Thus, the partial derivatives in (3.177) can be replaced by ordinary derivatives. We may add these two equations and integrate in time to obtain $\alpha_d^{(0)}(t) = \alpha_{di} + \alpha_{pi} - \alpha_p^{(0)}(t)$. This can be inserted in (3.177b) to obtain a logistic equation governing the evolution of the polymer-rich phase:

$$\frac{\mathrm{d}\alpha_p^{(0)}}{\mathrm{d}t} = \alpha_p^{(0)}\left(\alpha_{di} + \alpha_{pi} - \alpha_p^{(0)}\right). \tag{3.178}$$

Upon solving this equation, we find that the leading-order volume fractions are given by

$$\alpha_d^{(0)}(t) = \frac{(\alpha_{di}+\alpha_{pi})\alpha_{di}}{\alpha_{di} + \alpha_{pi}\exp\left[(\alpha_{di}+\alpha_{pi})t\right]}, \tag{3.179a}$$

$$\alpha_p^{(0)}(t) = \frac{(\alpha_{di}+\alpha_{pi})\alpha_{pi}}{\alpha_{pi} + \alpha_{di}\exp\left[-(\alpha_{di}+\alpha_{pi})t\right]}. \tag{3.179b}$$

The $O(1)$ and $O(\beta)$ problems for the film thickness read

$$\frac{\mathrm{d}h^{(0)}}{\mathrm{d}t} = 0, \tag{3.180}$$

$$\frac{\mathrm{d}h^{(1)}}{\mathrm{d}t} = -\left[1 - \alpha_d^{(0)}(t) - \alpha_p^{(0)}(t)\right]^2, \tag{3.181}$$

and these are subject to $h^{(0)}(0) = 1$ and $h^{(1)}(0) = 0$. The solutions are given by $h^{(0)}(t) \equiv 1$ and $h^{(1)}(t) = -(1-\alpha_{di}-\alpha_{pi})^2 t$. The linear decrease in the $O(\beta)$ correction to the thickness is due to the fact that, while the polymer concentrations vary at the surface, the solvent concentration remains the same, giving rise to a constant rate of evaporation.

The $O(1)$ problem for the velocities simplifies considerably due to the leading-order volume fractions being constant in space, and they satisfy:

$$2\alpha_p^{(0)}\frac{\partial^2 w_p^{(0)}}{\partial z^2} - 2\left(1-\alpha_d^{(0)}\right)\frac{\partial^2 w_d^{(0)}}{\partial z^2} + \varepsilon^{-1}D\left[\alpha_p^{(0)}w_p^{(0)} + \left(1-\alpha_p^{(0)}\right)w_d^{(0)}\right] = 0, \tag{3.182a}$$

$$-2\left(1-\alpha_p^{(0)}\right)\frac{\partial^2 w_p^{(0)}}{\partial z^2} + 2\alpha_p^{(0)}\frac{\partial^2 w_d^{(0)}}{\partial z^2} + D\left[\left(1-\alpha_d^{(0)}\right)w_p^{(0)} + \alpha_d^{(0)}w_d^{(0)}\right] = 0. \tag{3.182b}$$

These are supplemented with the boundary conditions

$$w_d^{(0)} = 0 \qquad z = 0, \tag{3.183a}$$

$$w_p^{(0)} = 0, \qquad z = 0, \tag{3.183b}$$

$$w_d^{(0)} = -(1-\alpha_{di}-\alpha_{pi})^2, \quad z = h(t), \tag{3.183c}$$

$$w_p^{(0)} = -(1-\alpha_{di}-\alpha_{pi})^2, \quad z = h(t). \tag{3.183d}$$

This problem consists of two linear ordinary differential equations with constant coefficients (in space), and in principle it can be solved analytically.

3.4.3.1 Large-time regime

The equation for the film thickness (3.174) suggests that when $\beta \ll 1$, there is a large-time regime given by $t \sim \beta^{-1}$. By introducing a slow time $\tau = \beta t$, the evolution problems for the volume fractions and film thickness become

$$\beta\frac{\partial \alpha_d}{\partial \tau} + \beta\frac{\partial}{\partial z}\left(\alpha_d w_d\right) = -\alpha_d\alpha_p, \tag{3.184a}$$

$$\beta\frac{\partial \alpha_p}{\partial \tau} + \beta\frac{\partial}{\partial z}\left(\alpha_p w_p\right) = \alpha_d\alpha_p. \tag{3.184b}$$

and

$$\frac{\mathrm{d}h}{\mathrm{d}\tau} = -\left[1-\alpha_d(h(t),t)-\alpha_p(h(t),t)\right]^2. \tag{3.184c}$$

By adding (3.184a) and (3.184b), we find that

$$\frac{\partial}{\partial \tau}\left(\alpha_d+\alpha_p\right) + \frac{\partial}{\partial z}\left(\alpha_d w_d + \alpha_p w_p\right) = 0. \tag{3.185}$$

This expression will be used to replace (3.184b).

The solution in this time regime is written as an asymptotic expansion of the form

$$\alpha_d(z,\tau) = \alpha_d^{(0)}(z,\tau) + O(\beta), \tag{3.186a}$$

$$\alpha_p(z,\tau) = \alpha_p^{(0)}(z,\tau) + O(\beta), \tag{3.186b}$$

$$w_d(z,\tau) = w_d^{(0)}(z,\tau) + O(\beta), \tag{3.186c}$$

$$w_p(z,\tau) = w_p^{(0)}(z,\tau) + O(\beta), \tag{3.186d}$$

$$h(\tau) = h^{(0)}(\tau) + O(\beta). \tag{3.186e}$$

By matching to the asymptotic solution in the $t = O(1)$ regime considered in Section 3.4.3, we find that $\alpha_d^{(0)} \sim 0$ and $\alpha_p^{(0)} \sim \alpha_{di} + \alpha_{pi}$ as $\tau \sim 0$.

The $O(1)$ part of (3.184a) reads $\alpha_d^{(0)}\alpha_p^{(0)} = 0$. From the initial conditions, we find that $\alpha_d^{(0)}(z,\tau) \equiv 0$. This means that, to leading order, all of the dispersed polymer remains demixed from the solvent. The $O(1)$ part of (3.185) simplifies to

$$\frac{\partial \alpha_p^{(0)}}{\partial \tau} + \frac{\partial}{\partial z}\left(\alpha_p^{(0)} w_p^{(0)}\right) = 0. \tag{3.187}$$

The associated hydrodynamic problem reads

$$2\left(1-\alpha_p^{(0)}\right)\frac{\partial}{\partial z}\left(\alpha_p^{(0)}\frac{\partial w_p^{(0)}}{\partial z}\right) - D\alpha_p^{(0)} w_p^{(0)} = 0, \tag{3.188}$$

subject to

$$w_p^{(0)} = 0, \qquad z = 0, \tag{3.189a}$$

$$w_p^{(0)} = -\left(1-\alpha_p^{(0)}\right)^2, \quad z = h^{(0)}(\tau). \tag{3.189b}$$

Finally, the leading-order problem for the film height is

$$\frac{\mathrm{d}h^{(0)}}{\mathrm{d}\tau} = -\left[1-\alpha_p^{(0)}(h^{(0)}(\tau),\tau)\right]^2. \tag{3.190}$$

By matching we find that $h^{(0)}(\tau) \sim 1 - (1-\alpha_{di}-\alpha_{pi})^2\tau$ as $\tau \sim 0$.

This system of equations is equivalent to those of the two-phase problem (3.104) in the limit $\mu \to 0$, $R \to 0$, and $A \to 1$. Therefore, in the limit of large time, the slow-flow problem reduces to a two-phase problem that is similar to the one previously considered. Physically, this means that the relatively fast rate of reaction completely eliminates one of the phases by the time evaporation begins to drive a flow.

3.4.4 The strong-drag limit

We now consider the case when $\beta = O(1)$ so that the solvent evaporates on an $O(1)$ time scale. However, we now exploit the fact that $\varepsilon \ll 1$. This corresponds to the situation where the transport of dispersed polymer is primarily through advection with the solvent. As the polymer is carried towards the free surface, its velocity must decrease because it cannot evaporate. This leads to a strong accumulation of the dispersed phase at the free boundary. This build up will, in turn, fuel the demixing of polymer.

The analysis proceeds by considering inner and outer regions that correspond to domains that are close to and away from the free surface. The solutions to these problems are then matched asymptotically.

3.4.4.1 The inner problem

As mentioned previously, the width of the boundary layer can be deduced by balancing the $O(\varepsilon^{-1})$ drag terms with the viscous terms. This leads to a boundary layer of width $O(\varepsilon^{1/2})$. For the inner problem, we introduce the variables

$$T = \beta\varepsilon^{-1/2}t, \quad \xi = \frac{h(t) - z}{\varepsilon^{1/2}}. \tag{3.191}$$

Note that T corresponds to a fast time, which signifies that the dynamics in the boundary layer (and hence those of the problem) evolve quite rapidly. We let P_j and W_j denote the volume fraction and velocity of phase j in the inner region, respectively, and let H describe the film height on this fast time scale.

Under this change of variable, the conservation of mass equations for the polymers (3.173a) and (3.173b) become

$$\frac{\partial P_d}{\partial T} + \frac{\partial}{\partial \xi}\left[\left(\varepsilon^{-1/2}\frac{\mathrm{d}H}{\mathrm{d}T} - W_d\right)P_d\right] = -\varepsilon^{1/2}\beta^{-1}P_dP_p, \tag{3.192a}$$

$$\frac{\partial P_p}{\partial T} + \frac{\partial}{\partial \xi}\left[\left(\varepsilon^{-1/2}\frac{\mathrm{d}H}{\mathrm{d}T} - W_p\right)P_p\right] = \varepsilon^{1/2}\beta^{-1}P_dP_p. \tag{3.192b}$$

We mention here that the term $\varepsilon^{-1/2}\partial_T H$ is, in fact, $O(1)$ in size because the equation for the film thickness reads

$$\frac{\mathrm{d}H}{\mathrm{d}T} = -\varepsilon^{1/2}\left[1 - P_d(H(T),T) - P_p(H(T),T)\right]^2. \tag{3.193}$$

The right-hand sides of (3.192) imply that little demixing occurs during the early stages of evolution when the boundary layer is first developing. The leading-order parts of the momentum equations (3.173c) and (3.173d) are given by

$$2P_d\frac{\partial}{\partial\xi}\left(P_p\frac{\partial W_p}{\partial\xi}\right) - 2(1-P_d)\frac{\partial}{\partial\xi}\left(P_d\frac{\partial W_d}{\partial\xi}\right) + DP_d[P_pW_p + (1-P_p)W_d] = 0, \tag{3.194a}$$

$$-(1-P_p)\frac{\partial}{\partial\xi}\left(P_p\frac{\partial W_p}{\partial\xi}\right) + P_p\frac{\partial}{\partial\xi}\left(P_d\frac{\partial W_d}{\partial\xi}\right) = 0, \tag{3.194b}$$

and these satisfy the boundary conditions

$$W_d = -(1-P_d-P_p)^2, \quad \xi = 0, \tag{3.195a}$$

$$W_p = -(1-P_d-P_p)^2, \quad \xi = 0. \tag{3.195b}$$

The two remaining boundary conditions for the velocities come from matching into the outer region. This will be discussed in detail below.

3.4.4.2 The outer problem

To formulate a compatible outer problem, we must use the same fast time as above, namely $T = \beta\varepsilon^{-1/2}t$. We also treat $h(t) - z = O(1)$. In this case, the bulk equations for the volume fraction can be written as

$$\frac{\partial \alpha_d}{\partial T} + \varepsilon^{1/2}\frac{\partial}{\partial z}\left(\alpha_d w_d\right) = -\varepsilon^{1/2}\beta^{-1}\alpha_d\alpha_p, \tag{3.196a}$$

$$\frac{\partial \alpha_p}{\partial T} + \varepsilon^{1/2}\frac{\partial}{\partial z}\left(\alpha_p w_p\right) = \varepsilon^{1/2}\beta^{-1}\alpha_d\alpha_p, \tag{3.196b}$$

Therefore, to leading order, the volume fractions maintain their initial values so that $\alpha_d(z,T) \equiv \alpha_{di}$ and $\alpha_p(z,T) \equiv \alpha_{pi}$.

In the outer region, we can take $\varepsilon \to 0$ in the momentum equation (3.173c) to obtain, at leading order,

$$w_d = -\frac{\alpha_{pi}}{1-\alpha_{pi}}\, w_p. \tag{3.197}$$

Using these results in the other momentum equation (3.173d) yields the following leading-order boundary value problem:

$$l^2\frac{\partial^2 w_p}{\partial z^2} - w_p = 0, \tag{3.198}$$

subject to $w_p(0,t) = 0$, where

$$l^2 = \frac{2\left[(1-\alpha_{pi})^2 + \alpha_{di}\alpha_{pi}\right]}{D(1-\alpha_{di}-\alpha_{pi})} \tag{3.199}$$

defines a length scale. The leading-order solutions for the velocities in the outer region are given by

$$w_d(z,T) = -\left(\frac{\alpha_{pi}}{1-\alpha_{pi}}\right)K(T)\sinh(z/l), \tag{3.200a}$$

$$w_p(z,T) = K(T)\sinh(z/l), \tag{3.200b}$$

where the time-dependent integration constant K is determined by matching to the inner region.

3.4.4.3 A comment on the matching

The fact that the leading-order outer solution is not fully determined leads to the question of whether the matching conditions provide enough information to determine all of the constants of integration in the inner and outer problem. If we define

$$W_d^{\infty}(T) = \lim_{\xi\to\infty} W_d(\xi,T), \quad W_p^{\infty}(T) = \lim_{\xi\to\infty} W_p(\xi,T), \tag{3.201}$$

then the leading-order matching conditions imply that

$$W_d^\infty(T) = -\left(\frac{\alpha_{pi}}{1-\alpha_{pi}}\right) K(T)\sinh(H(T)/l), \tag{3.202a}$$

$$W_p^\infty(T) = K(T)\sinh(H(T)/l). \tag{3.202b}$$

These are two equations for three unknowns; thus, it would appear that more information is required to fully determine the leading-order solution. It turns out this is not the case. To see why, we linearise the inner hydrodynamic problem (3.194) about its solution at infinity by writing

$$W_d(\xi,T) = W_d^\infty(T) + \widetilde{W}_d(\xi,T), \tag{3.203a}$$

$$W_p(\xi,T) = W_p^\infty(T) + \widetilde{W}_p(\xi,T), \tag{3.203b}$$

where $\widetilde{W}_d, \widetilde{W}_p \ll 1$. Using the fact that $P_d(\xi,T) \sim \alpha_{di}$ and $P_p(\xi,T) \sim \alpha_{pi}$ in the far field, the corresponding hydrodynamic problem becomes

$$2\alpha_{pi}\frac{\partial^2\widetilde{W}_p}{\partial\xi^2} - 2(1-\alpha_{pi})\frac{\partial^2\widetilde{W}_d}{\partial\xi^2} + D[\alpha_{pi}\widetilde{W}_p + (1-\alpha_{pi})\widetilde{W}_d] = 0, \tag{3.204a}$$

$$-(1-\alpha_{pi})\frac{\partial^2\widetilde{W}_p}{\partial\xi^2} + \alpha_{di}\frac{\partial^2\widetilde{W}_d}{\partial\xi^2} = 0. \tag{3.204b}$$

The general solution to this problem is given by

$$\widetilde{W}_d = -\left(\frac{\alpha_{pi}}{1-\alpha_{pi}}\right)(C_1 + C_2\xi) + \left(\frac{1-\alpha_{di}}{\alpha_{di}}\right)\left(C_3 e^{\xi/l} + C_4 e^{-\xi/l}\right), \tag{3.205a}$$

$$\widetilde{W}_p = C_1 + C_2\xi + C_3 e^{\xi/l} + C_4 e^{-\xi/l}, \tag{3.205b}$$

where l is defined in (3.199). In order for the matching conditions at infinity to be satisfied, we require $C_2 = C_3 = 0$. The remaining constants of integration, C_1 and C_4 can be determined from the two boundary conditions at $\xi = 0$. Thus, the inner solution is fully determined by imposing boundedness conditions in the far field and the boundary conditions at the free surface. This means the far-field values W_d^∞ and W_p^∞ are known, in principle. Either matching condition in (3.202) can then be used to determine the constant of integration K.

3.4.4.4 Numerical solutions

To further explore the dynamics of the system in the strong-drag limit, we solve the "full" three-phase problem given by (3.173)–(3.175) numerically using an implicit time stepping scheme with Chebyshev spectral methods. Figure 3.10 shows the evolution of the system when $\beta = 1$, corresponding to the situation where the evaporation and demixing rates are equal. The drag coefficient is set to $D = 1$ and the drag ratio is taken to be $\varepsilon = 10^{-3}$.

The initial conditions are given by $\alpha_{di} = \alpha_{pi} = 0.1$. The results from the simulation show there are two time regimes. As predicted from the asymptotic analysis, for small times the dispersed polymers are quickly transported to the free surface; see Figure 3.10 (c). The high polymer concentration prohibits the evaporation of solvent, which, in turn, results in a nearly motionless fluid layer. On $O(1)$ times, the dispersed polymer demixes from the solvent to form a thin, polymer-rich skin, as shown in Figure 3.10 (e).

Numerical solutions for the velocities are also compared with asymptotic solutions in Figure 3.10. The inner problem is solved numerically using a shooting method. Having found this, the matching conditions (3.202) are used to compute a value of K, after which the outer solution can be determined. Using these, the leading-order composite solution is then constructed. As the figure shows, the asymptotic solution agrees very well with the numerical solution.

The evolution of the film thickness is shown in Figure 3.11 for the above parameter values. For small times when the surface is solvent rich, the layer thins quite rapidly. However, evaporation ceases to occur after the skin has formed, which leads to a thick film where a large proportion of the solvent is trapped in the bulk.

3.4.5 Skin formation

To further explore the formation of a polymer skin, we run several simulations for different values of the parameters β and D and we compute the final (non-dimensional) mass of solvent that is left. This is defined as

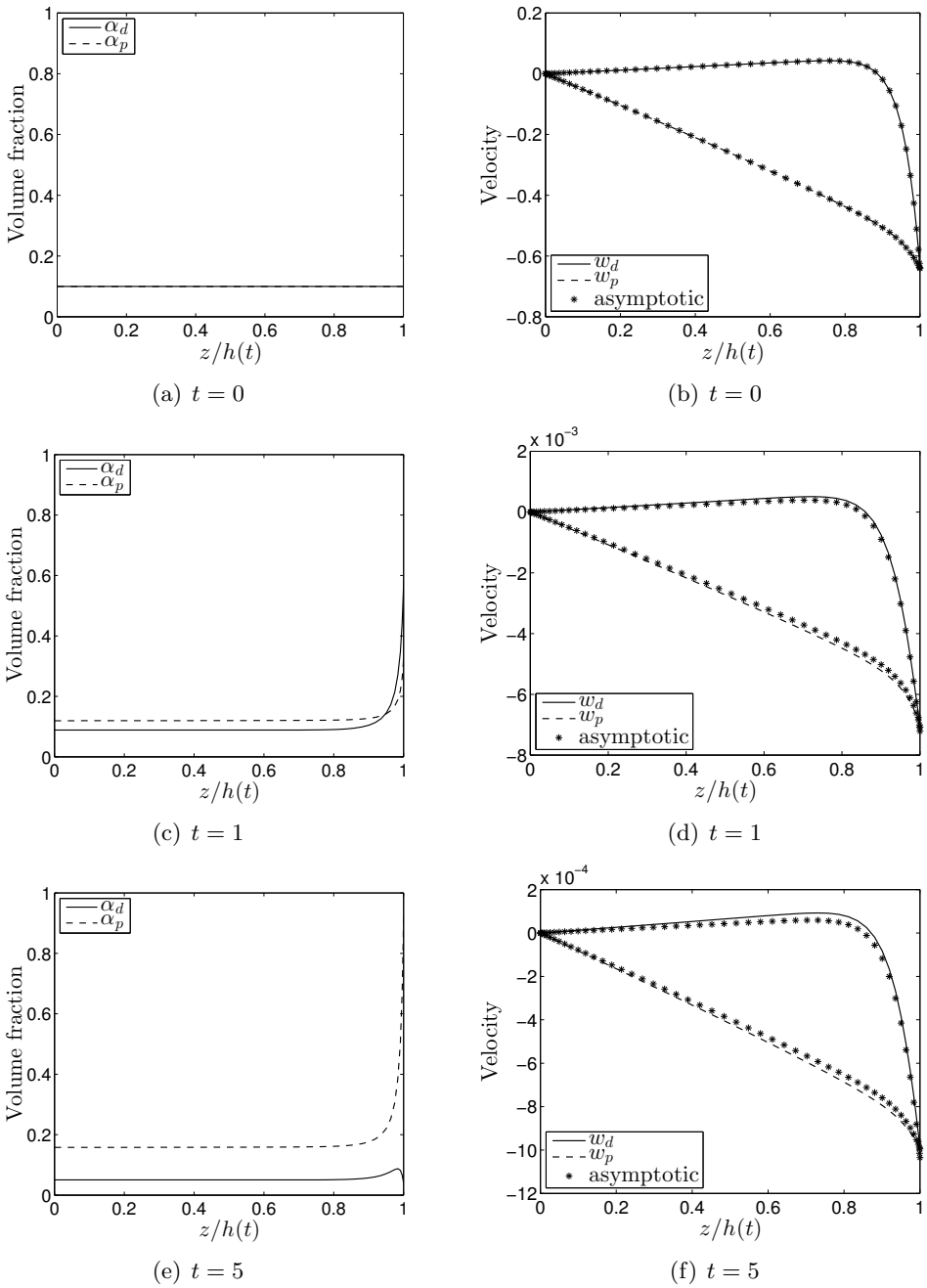
$$M_\infty = \int_0^{h_\infty} \alpha_{s,\infty}(z)\,\mathrm{d}z, \tag{3.206}$$

where h_∞ and $\alpha_{s,\infty}$ denote the steady-state film thickness and solvent volume fraction, respectively. Using the conservation equations, it is not difficult to show that

$$M_\infty = M_i + h_\infty - 1, \quad M_i = 1 - \alpha_{di} - \alpha_{pi}. \tag{3.207}$$

where M_i is the initial mass of solvent. From this expression, it can be seen that there is a direct relationship between the amount of solvent that is left in the bulk and the final thickness of the film. Dividing the final mass by the initial mass gives the fraction of solvent that has been retained within the bulk due to the formation of a skin. We will use $M_\infty/M_i > 1/2$ as a criterion for severe skin formation, as this means that more than half of the solvent is retained during the drying process.

Figure 3.12 illustrates how the solvent mass fraction M_∞/M_i varies with changes in D and β for two fixed values of ε. The black line in these figures is the contour given by $M_\infty/M_i = 1/2$. Thus, the region above this line corresponds to parameters that lead to



(a) $t = 0$ (b) $t = 0$

(c) $t = 1$ (d) $t = 1$

(e) $t = 5$ (f) $t = 5$

Figure 3.10: Dynamics of a three-phase mixture consisting of a solvent, dispersed polymers, and demixed polymers. The left column shows the volume fraction of the polymer phases and the right shows the corresponding velocities. Strong drag forces between the solvent and the dispersed polymers lead to the rapid formation of a compositional boundary layer (b) because the polymers, which are advected with the solvent, do not evaporate at the free surface. The accumulation of dispersed polymers enhances their demixing, leading to the formation of a polymer-rich layer at the top of the film (c). The simulation was computed using the following parameter values: $D = \beta = 1$, and $\varepsilon = 1/1000$. The initial conditions were $\alpha_{pi} = \alpha_{di} = 0.1$. The asymptotic approximations for the velocities are composite solutions formed from the inner and outer problems discussed in Sections 3.4.4.1–3.4.4.3.

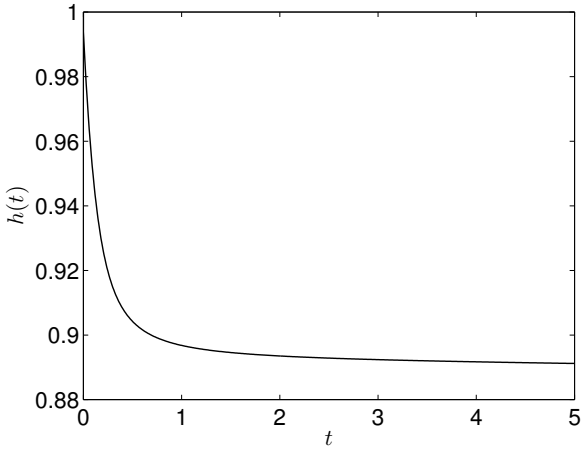
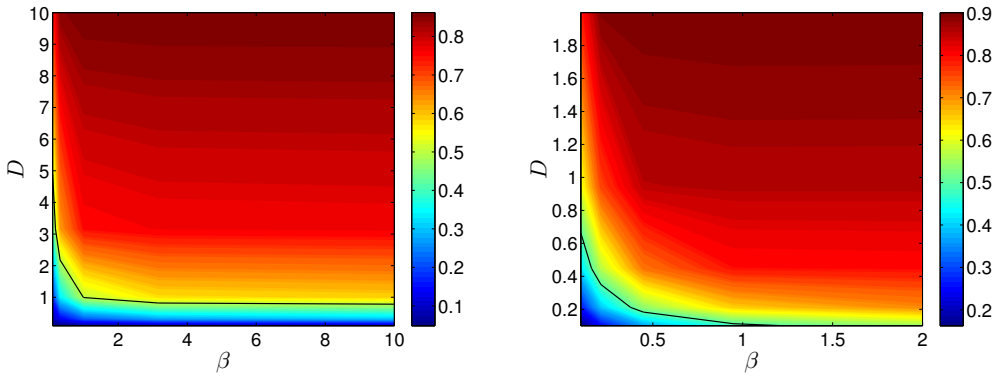


Figure 3.11: The corresponding film thickness for the simulation show in in Figure 3.10. The film rapidly thins for small times, but the build up of a polymer-rich skin at the surface significantly reduces the evaporation rate. In this case, amount 89% of the solvent remains trapped within the bulk. The parameter values were $D = \beta = 1$, and $\varepsilon = 1/1000$. The initial conditions were $\alpha_{pi} = \alpha_{di} = 0.1$.

the formation of a severe skin as judged by the 50% solvent retention criterion. The initial conditions for the volume fractions were taken to be $\alpha_{di} = \alpha_{pi} = 0.1$. The stopping condition used in the numerical simulations is when $|\partial_t h| < 10^{-3}$. In the case when $\varepsilon = 1/100$ (panel (a)), skin formation occurs mainly in the parameter range $\beta, D > 1$. In physical terms, this domain corresponds to fast evaporation and strong drag forces between the solvent and demixed polymers. An alternative interpretation of the $\beta \gg 1$ limit is that of slow demixing. This would imply the total concentration of dispersed polymer remains relatively constant during the drying process, thus maximising the amount of this phase that can be transported by the solvent to the interface. This is in contrast to the case when $\beta \ll 1$, corresponding to rapid demixing. Here, the fast generation of polymer-rich domains would consume most of the dispersed phase before it is dragged to the free surface. When $D < 1$, we find that the volume fractions are relatively uniform, enabling most of the solvent to be removed from the layer. When the drag ratio between the solvent and the dispersed polymer is decreased to $\varepsilon = 1/1000$, a significant amount of the solvent gets trapped within the bulk unless both D and β are small. Thus, we can conclude that skin formation is much more extreme for smaller values of ε, which is to be expected because this corresponds to stronger drag forces between the solvent and the dispersed phase.

3.5 Discussion and conclusion

In this chapter, we have explored how multiphase fluid models may be used to study the dynamics of evaporating solvent-polymer mixtures. A detailed microscopic model was de-



(a) $\varepsilon = 10^{-2}$ (b) $\varepsilon = 10^{-3}$

Figure 3.12: Steady-state solvent mass fractions as functions of the relative evaporation rate β and the drag coefficient D for two different values of the drag ratio ε. Parameters values that lie above the 0.5 contour (black) lead to more than half of the solvent remaining in the layer. The steady-state mass fraction is defined as the mass of solvent when $|\mathrm{d}h/\mathrm{d}t|$ first decreases to 10^{-3} divided by the initial solvent mass. Larger values of the mass fraction correspond to more solvent being trapped in the bulk. Decreasing ε leads to a significant increase in the formation of a skin. Note the change in scales between panels (a) and (b). The initial conditions in the simulations were $\alpha_{di} = \alpha_{pi} = 0.1$.

rived and then systematically averaged to obtain a macroscopic model. The benefit of this approach is that the macroscopic phases are treated as overlapping and there is no need to track the evolution of the microscopic interfaces that form between different domains. One drawback of this approach is that the bulk equations are generally very complicated, which prevents analytical solutions from being obtained in all but the simplest cases. Another shortcoming is that the averaging process gives rise to more dependent variables than equations; thus, several constitutive laws are required to close the macroscopic model. These laws can be motivated from the microscopic dynamics or approximated by simple phenomenological relations.

Two physical situations were examined using our multiphase model. The first of these was concerned with a two-phase fluid in a gravitational field. The second involved a three-phase mixture, but gravitational effects were not taken into account. Closed-form solutions were not possible to obtain in general, so a combination of asymptotic and numerical methods were used in our studies.

Solving the averaged equations numerically proved to be surprisingly challenging, particularly when the volume fraction of one of the phases was close to zero or one. These numerical difficulties usually led to the simulations terminating before the asymptotic regimes predicted by the analysis were entered. Thus, implementing improved numerical methods that are able to handle these regimes would be especially useful for examining the long-term dynamics of the system and for verifying the asymptotic analyses. The numerical scheme

proposed by Coquel *et al.* [47] could be a promising starting point, as it has been specifically designed to handle situations where only one phase is present. The idea behind this scheme is to decompose each time step into a hydrodynamic step and a correction step. The hydrodynamic step provides an update of the conserved quantities of each phase, for example, mass and momentum. The state variables that define these conserved quantities, such as the density and velocity, are then corrected to ensure that each phase, locally, has the same pressure. Using this scheme, Coquel *et al.* was able to robustly capture the formation and growth of single-phase regions in a two-phase mixture.

The analysis of the two-phase model showed an interesting interplay between gravity and drag. Gravitational effects lead to an accumulation of polymer near the substrate, whereas drag leads to the formation of a polymer-rich skin below the free surface. When the polymer phase was dilute or for sufficiently small times in the non-dilute case, it was possible to obtain analytical conditions that determine which of these accumulations is the most significant. When gravity is the dominant mechanism, the system quickly settles into a bilayer configuration and the solvent-rich upper layer rapidly evaporates. When drag is dominant, the skin inhibits the evaporation of solvent and a long-lasting two-phase core consisting of both solvent and polymer can form. However, the constant downwards pull of gravity is suspected to cause the eventual break up of the polymer skin, enabling the film to fully dry.

The density stratification that arises when a dense, polymer-rich skin forms on top of less-dense, solvent-rich fluid naturally leads to the question of whether an instability can occur in the system. Our two-phase model predicts that skin formation is only significant when $D \gg 1$. If $R = O(1)$, this skin might last enough for an instability to develop during the drying process; however, this regime is also associated with moderate gravitational effects. Hence, the threshold for instability might not be exceeded in the regime. When $R \gg 1$, the effects of gravity will be stronger, but this also means that the polymer will rapidly settle on top of the substrate. Once this happens, the polymer remains motionless and the likelihood of an instability developing is low. A useful future study would aim to verify these claims by carrying out a linear stability analysis or by performing two-dimensional numerical simulations. A stability analysis is expected to be non-trivial due to the time dependence of the one-dimensional solutions. However, if there are multiple time scales in the stability problem, then the methods developed in Chapter 2 might be of use. Further investigations into the stability of the system could shed additional insight into whether compositional buoyancy is the source of convection in Bassou & Rharbi's [8] experiments, which were discussed in the previous chapter. If compositional buoyancy

can be ruled out, then there would be further evidence to suggest that thermal effects are important in evaporating mixtures after all.

When a third phase, corresponding to dispersed polymer, is introduced into the model, the formation of a polymer-rich skin becomes much more severe. In this case, the skin arises primarily because the dispersed polymers are transported to the free surface by the solvent. However, they cannot evaporate and hence they accumulate. This is slightly different to skin formation in the two-phase model, where conservation of mass requires the polymer to travel towards the substrate whenever the solvent is moving towards the free surface. Strong drag forces between the two phases near the surface cause the polymer to experience an increased resistance to motion, thereby decreasing its velocity and increasing its local concentration. Gravitational effects eventually degrade the skin in the two-phase problem, but these are not considered in the case of a three-phase mixture. As a result, the continual accumulation of polymer gradually slows the rate of evaporation until, for all intents and purposes, it is completely extinguished. Generally, this occurs before before all of the solvent is removed from the system. In some cases, as much as 90% of the solvent could be retained in the layer.

In reality, there will be several physical mechanisms that mediate the formation and the effects of a skin. As mentioned already, gravity will play an important role. From an experimental standpoint, this fact implies that skin formation can be reduced by using a low-density solvent. In addition to gravity, diffusion of polymer and solvent may also mediate the effects of a skin. For example, if a polymer skin does form, diffusion of solvent through the skin may provide a mechanism by which evaporation can continue, albeit at a very slow rate. Moreover, diffusion of polymer in the solvent will inhibit the growth of a skin. Indeed, studies of spin-cast solvent-polymer mixtures by Münch *et al.* [112] show that there is a close link between evaporation, diffusion, and skin formation. In particular, they find that when evaporation is sufficiently slow, diffusion can flatten the concentration profile, thus enabling all of the solvent to be removed from the layer. Qualitatively similar dynamics are observed in the two-phase model when both gravity and drag are weak. In this case, a mixture that is initially homogeneous in composition remains approximately so for all time.

Diffusion may also play an important role in the bilayer formation that occurs in the $R \gg 1$, $D = O(1)$ regime that was considered in the two-phase problem; see Figure 3.6. In particular, diffusion is expected to select the width of the transition region that separates the two layers. In the current two-phase model, this width is theoretically equal to zero. This can be deduced by looking for steady-state solutions to (3.104) when evaporation is neglected; one finds that $\alpha_p = A^{-1}$ for $z < A$ and $\alpha_p = 0$ for $z > A$. Thus, including

diffusive transport in an extended model and looking at how it influences the dynamics might prove to be an interesting and fruitful area of research. As shown by Winstanley *et al.* [157], diffusion can be systematically included in a multiphase model of a solvent-polymer mixture by introducing an osmotic pressure which itself is related to the free energy of mixing.

Considering two polymer phases in our mathematical model provided a basic means of capturing the process of phase separation and coupling it to hydrodynamic effects. A particularly interesting result of our model is that the accumulation of polymer near the free surface leads to a local increase in the demixing of polymer from the solvent. This gives evidence to suggest that phase separation occurs from the surface down to the substrate in evaporating solvent-polymer mixtures, which is in agreement with the phase-field simulations by Buxton & Clarke [31] and the experimental studies of Ebbens *et al.* [60]. A more detailed and realistic theoretical investigation of the relationship between evaporation and phase separation could be obtained by extending the current model to incorporate a second species of polymer. The great flexibility of multiphase models would make such an extension a relatively straightforward task.

Chapter 4

Bilayer formation and topological transformations in a confined binary mixture

4.1 Introduction

The creation of high-quality, thin polymer films by spin coating a solvent-polymer mixture is an important industrial process with a number of modern applications. For example, it is a cheap and efficient method for creating the photoactive layers of polymeric organic solar cells [108]. The attractiveness of spin coating stems partly from the fact that it is a rapid one-step process for depositing a liquid film into a thin layer on top of a substrate. When two or more polymers are used, the resulting layer is often not uniformly thin nor homogeneous in composition. This is because the polymers spontaneously demix and self-assemble into microscale structures, which is an attractive feature in its own right. The morphology of the small-scale structures that emerge during spin coating can have an important impact on the performance of the polymer film or the subsequent role that it has to play. In the case of organic solar cells, the efficiency of the device is directly related to the shape of the interfaces between the polymer structures [124]. From a practical point of view, it is therefore highly desirable to understand and have control over how these structures form and subsequently evolve.

The scientific and industrial relevance of self-organising polymer films has motivated a number of recent experimental studies on the subject. Typically, these experiments involve spin coating a three-component mixture consisting of two polymers that have been blended in a common solvent. In addition, they focus on how the morphology of the final polymer film is influenced by the properties of the mixture and the environment. Dunbar *et al.* [58] and Wu *et al.* [159] investigate the relationship between the initial polymer concentration and the film morphology. Mokarian–Tabari *et al.* [107] use the evaporation rate as a system

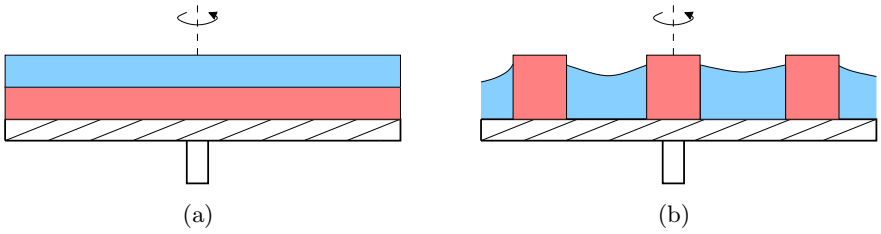


Figure 4.1: Typical cross sections of polymer films that are created by spin coating a mixture of two polymers, A and B, and a common solvent. The two colours represent A-rich and B-rich regions. As the solvent evaporates, the polymers undergo phase separation to either form a bilayer (a) or a laterally separated structure (b).

parameter that can be varied, whereas Jaczewska *et al.* [82] change the solubility parameters through the use of different solvents and polymers. The results from these experiments, along with those of Heriot & Jones [76] and Ebbens *et al.* [60], indicate that the polymer films often take one of two morphologies: either the constituent polymers demix and form a bilayer, where the interface of the bilayer runs parallel to the surface of the substrate (see Figure 4.1 (a)), or they demix to form laterally separated domains with polymer-polymer interfaces that are orthogonal to the substrate surface (see Figure 4.1 (b)). In the latter case, the cross sections of the film resemble sequences of columns or vertical stripes.

The formation of a polymer bilayer is thought to be the result of energetic interactions between the substrate and the polymers [76]. More specifically, the bilayer is a result of one of the polymers being preferentially attracted to the substrate, making it energetically favourable for that species to wet the substrate after the two polymers have demixed.

There are currently two main hypotheses for how the laterally separated or columnar topology shown in Figure 4.1 (b) is created. In the first of these, the columns are ultimately the result of an initial instability at the bilayer interface [58, 76, 82, 107]. This instability deforms the interface and causes it to become corrugated. These corrugations then grow in amplitude until they hit the substrate or reach the surface of the layer, at which point new contact lines are created. The contact lines then evolve to minimise the energy of the system, for example, by reducing the total area of the interfaces, and this forms the columns that are observed experimentally (see Figure 4.2 (a)–(c)).

The presence of a bilayer in this hypothesis suggests that it is energetically favourable for one of the polymers to be in contact with the substrate. If this is indeed the case, then the energy of the system will be increased whenever the other polymer covers the substrate. Thus, for the transformation from a bilayer to a laterally separated state to occur, the energy cost of creating domains of unpreferred polymer on the substrate must be offset by an energy reduction elsewhere. Such a reduction comes in the form of the large bilayer interface breaking up into much smaller vertical interfaces. The laterally separated

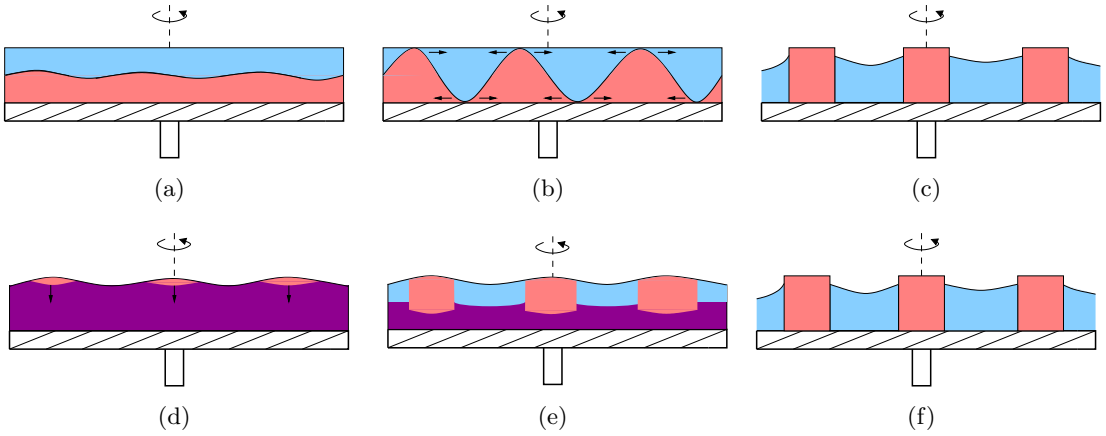


Figure 4.2: Two potential routes that lead to a laterally separated film morphology. Top (a)–(c): An instability develops at the bilayer interface, leading to corrugations that grow until they come in contact with the surface or substrate. The new contact lines move under the action of interface minimisation to form columnar structures. Bottom (d)–(f): An instability occurs at the top of the mixture while it is still homogeneous (the homogeneous regions are shown in purple). This leads to localised phase separation that proceeds from the surface down to the substrate.

state, with its significantly reduced interfacial area, is likely to correspond to the global energetic minimum of the system and be stable. The bilayer state, on the other hand, is only expected to be metastable. Thus, a perturbation of sufficient magnitude to the bilayer, such as one from an instability, will initiate the spontaneous transformation to a lower-energy configuration.

In the second hypothesis of how the laterally separated morphology arises, it is predicted that an initial instability occurs at the surface of the blend when it is still well mixed and homogeneous [60, 159]. This instability is thought to trigger localised phase separation that proceeds from the surface of the mixture down to the substrate (see Figure 4.2 (d)–(f)). Thus, the columns are essentially grown from the top down.

Both of the initial instabilities that occur in these hypotheses, namely the instability at the bilayer interface in the first hypothesis and the instability at the surface of the fluid layer in the second, are believed to be Marangoni-like in nature and driven by evaporation-induced gradients in the solvent concentration [76, 82, 107, 159].

4.1.1 Thermodynamics background

The tendency for polymers to separate in a solution is governed by the thermodynamic properties of the mixture. For the three-component systems considered in spin-coating experiments, these properties depend crucially on the solvent concentration. As the solvent evaporates at the free surface and is depleted from the bulk, the system is pushed into the

spinodal regime where small thermal fluctuations can spontaneously initiate demixing of polymers. This phase-separation process is known as spinodal decomposition.

It is well known that a similar scenario also occurs when a binary mixture or alloy is cooled below its critical temperature [33]. That is, the mixture remains homogeneous above the critical temperature, but spinodal decomposition can occur for temperatures below this value. The thermodynamics of the two systems are analogous when the solvent concentration and the temperature are spatially uniform [141]; therefore, we can use the extensive knowledge about binary mixtures to understand the thermodynamics of ternary systems by assuming the temperature plays the same role as the solvent.

The basic dynamics of unconfined, isotropic, isothermal binary mixtures are now relatively well understood. They can be intuitively described using the (homogeneous) Gibbs free energy of mixing, which we will denote by f. From thermodynamics, this free energy is defined as $f = H - TS$, where H and $S < 0$ are the enthalpy and entropy of mixing, respectively, and $T > 0$ is the absolute temperature [36]. The enthalpy and entropy, and hence the free energy f, all depend on the composition of the mixture. Precise forms of these functions are given in Section 4.2, but we mention here that enthalpy favours demixing whereas entropy promotes mixing.

As the system evolves to minimise its energy (for a fixed temperature), the composition of the mixture tends to the minima of the free energy f. For sufficiently high temperatures, the entropic contribution to the free energy dominates and gives rise to a convex f with only one minimum. Thus, the composition of the mixture tends to this one value, *i.e.*, the mixture becomes homogeneous. However, for sufficiently low temperatures, the enthalpic contribution dominates and the free energy obtains a double-well structure. Depending on the initial composition, the mixture either separates into two distinct co-existing phases or it tends to a homogeneous state. The homogeneous free energy is shown schematically in Figure 4.3 (a), where it is plotted as a function of the volume fraction φ of one of the constituent materials for two different temperatures. The temperature that separates the two behaviours is called the bulk critical temperature and this will be denoted by T_c.

The behaviour of the mixture for a given temperature and composition is conveniently described by the binary phase diagram, an example of which is shown in Figure 4.3 (b). The dashed line is called the spinodal and it denotes, for a given temperature, the compositions at which the homogeneous free energy has a vanishing second derivative (with respect to composition). We will refer to the region below the spinodal (for a fixed composition φ) as the spinodal region; this is shown as the blue area in Figure 4.3 (b). The solid line is referred to as the binodal or the co-existence curve and it describes the minima of the free energy for a given temperature. If the initial composition (assumed homogeneous) is below

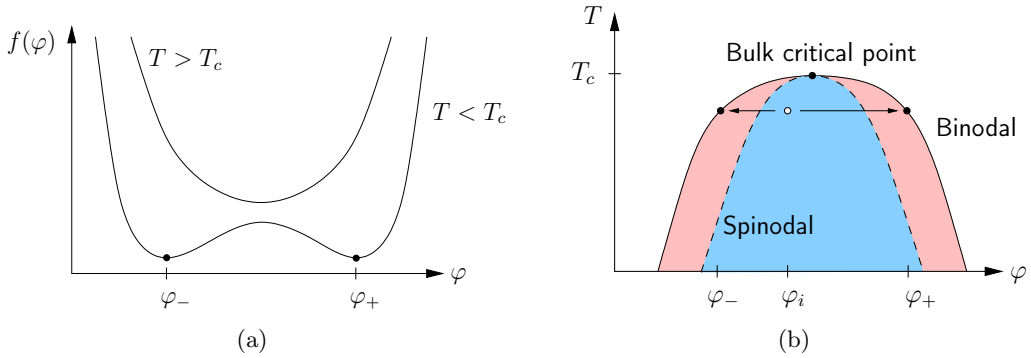


Figure 4.3: Left (a): The homogeneous free energy of mixing for binary mixture as a function of composition. If the temperature T is above the bulk critical temperature T_c, the free energy is convex. When $T < T_c$, the free energy has a double-well structure. Right (b): A typical binary phase diagram for an unconfined mixture. For a given temperature, the binodal and spinodal points correspond to compositions where f has a minimum and a vanishing second derivative, respectively. If the initial composition φ_i lies in the region above the binodal (the white region), which is always the case above the bulk critical point, the mixture will tend to a homogeneous state. However, if φ_i is below the spinodal (blue region), the mixture can separate into two co-existing phases with compositions given by $\varphi_\pm$ that lie on the binodal.

the spinodal, the amplification of small fluctuations can cause the solution to spontaneously demix into two phases with compositions that lie on the co-existence curve. However, if the initial composition lies in the region above the spinodal but below the binodal (shown as the pink area in Figure 4.3 (b)), the homogeneous state is metastable. Phase separation can occur, but via nucleation and growth instead of spinodal decomposition [118]. Domain nucleation requires an energy barrier to be overcome and hence phase separation does not occur spontaneously; thus, it is theoretically possible for homogeneous mixtures to exist in the metastable region between the spinodal and binodal [19, 20]. When the temperature is above the binodal, the homogeneous solution is stable and no phase separation occurs.

4.1.2 Phase separation in confined geometries

The presence of surfaces which act to confine a mixture can significantly influence the dynamics of phase separation and, as a consequence, the long-term morphology. In unconfined mixtures, spinodal decomposition leads to the rapid formation of small domains of roughly uniform size throughout the bulk. These domains slowly coarsen, with larger domains often absorbing smaller domains. For domain growth that is limited by diffusion rather than viscosity, convection, or other transport mechanisms, the Lifshitz–Slyozov law states that the size of a typical domain scales like $t^{1/3}$, where t is time [28]. The evolution of the system towards its lowest-energy state drives the growth and coalescence of domains until a minimal interfacial area is achieved. For the case of binary mixtures, this equilibrium

configuration will consist of a sphere of the minority phase embedded within the majority phase.

Introducing a confining surface into the system can lead to new interactions that occur between the components of the mixture and the molecules of the surface. In reality, these interactions manifest themselves through long- and short-range intermolecular forces. These can cause materials to be preferentially attracted to or repelled from the surface. Strong interactions between the surfaces and the components of the mixture can significantly alter the qualitative and quantitative properties of phase separation. Instead of small domains of uniform size forming throughout the bulk due to traditional spinodal decomposition, composition waves can propagate into the bulk with wavevectors that are normal to the surface, resulting in the formation of metastable layered structures. This mode of phase separation has been termed surface-directed spinodal decomposition and it was first observed experimentally by Jones *et al.* [86]. This discovery prompted intense research to understand how confining surfaces influence the dynamics of phase separation. Further experiments were conducted by Krausch *et al.* [99] in order to quantify the growth rate of the emerging layers. Their method involved measuring how a planar wavefront defined by a particular composition evolves with time. Remarkably, they found that the thickness of the layers scales like $t^{1/3}$, which is analogous to the diffusion-limited growth of bulk domains given by the Lifshitz–Slyozov law. The first successful theoretical study of surface-directed spinodal decomposition using a coarse-grained, continuous model is due to Puri & Binder [126]. They were able to capture the propagation of composition waves but their model predicted linear growth of the layers in time. Understanding the growth mechanisms of the layers remains a topic of current research, but it has become clear that the surface potential plays a primary role and hydrodynamic effects can eventually become important [85, 161]. Detailed summaries of the experimental aspects of phase separation in confined geometries can be found in the review papers by Geoghegan & Krausch [68] and Krausch [98]. The theoretical aspects of this topic are comprehensively reviewed by Puri [125] and Binder *et al.* [21].

The prospect of using surface-directed spinodal decomposition to generate small-scale layered structures in a controlled fashion has stimulated much research in this area. Das *et al.* [51] investigated the formation of layered structures in thin-film geometries by considering a binary mixture confined between two vertically separated walls. The interaction between the walls and the materials was modelled using a long-range potential. The layered morphologies that emerged in their simulations eventually broke up due to thermal fluctuations, resulting in a laterally separated morphology. A recent study by Coveney & Clarke [48] showed that the same dynamics can occur in a deterministic, polymer-based

model with short-range interactions between the walls and the materials. Jaiswal *et al.* [83] found that long-lasting layered morphologies can be induced when the initial composition has a gradient that is normal to unbiased walls. However, these layered structures decompose as well. Jaiswal *et al.* [84] and Ball & Essery [7] show that slowly cooling the mixture or imposing temperature gradients, respectively, can also lead to the formation of layers when there is no preferential attraction of the materials to the walls. Cahn [34] explored the relationship between temperature and the wetting properties of a wall, and found that complete wetting can occur above a critical wetting temperature but below the bulk critical point. Wodo & Ganapathysubramanian [158] perform three-dimensional simulations of an evaporating blend consisting of two polymers and a solvent that sits on a substrate. The energetic interactions between the substrate and the materials are neglected, but the formation of layered states is still possible.

4.1.3 Phase-field models

The dynamics of phase separation are driven by the thermodynamics of the mixture and the interactions between the walls and the constituent materials. Hence, any mathematical model that aims to describe the behaviour of a mixture and its compositional structure must incorporate these physics in an accurate manner.

Phase-field models have a long history of being used to describe the formation and evolution of microstructures in composite mixtures [43, 143]. This is due, in part, to the fact that a wide-range of physical processes can be captured by such models. Furthermore, they can also offer computational advantages because the interfaces between structures do not need to be explicitly tracked. Instead, phase-field models assume such interfaces are diffuse and spread over thin regions that naturally arise from the physics of the problem. The physical variables such as temperature and concentration are assumed to be continuous, but rapidly varying, across diffuse interfaces and hence multiple computational domains are not required.

The first theoretical investigation that made use of a diffuse interface between adjacent phases was by van der Waals [131]. Many of his results were independently reproduced by Cahn and Hilliard in their seminal paper on the free energy of isotropic binary mixtures [35]. Further developments by Cahn led to the derivation of the well-known Cahn–Hilliard equation, which describes the kinetics of spinodal decomposition in isotropic binary alloys [32]. The theory of Cahn and Hilliard has since been extended to anisotropic, multi-component mixtures [43], and to polymer-solvent systems by Flory, Huggins, and de Gennes [17, 141].

Alternative approaches to studying the dynamics of phase-separating mixtures involve simulating Ising and other lattice-based models using Monte Carlo algorithms [50, 125,

130]. Lattice models, in some sense, provide a more fundamental description of the physics by precisely taking into account the molecular interactions between the various materials. Furthermore, these models often serve as the starting point for derivations of phase-field models. The main advantage of lattice models is that they offer a greater range of validity compared to phase-field models. This is because phase-field models are often derived under the assumption of weak composition gradients which is only true near the critical point [17]. However, the tractability of phase-field models makes them particular appealing and they are often used in situations that are far from criticality, where they serve as useful phenomenological tools [21]. A comparison of lattice and continuum models in the context of phase separation in thin-film geometries is given by Das *et al.* [50] who found good agreement between the two models near the critical point.

4.1.4 Aims and assumptions

In this chapter, we use a highly simplified mathematical model to understand how the surface energy of the substrate can influence the dynamics of spinodal decomposition and lead to the formation of a bilayer. Furthermore, we investigate whether a local perturbation to such a bilayer can induce a transition to the columnar topology that is observed in experiments. However, we do not attempt to model the bilayer instability that is claimed to generate this perturbation. Instead, we examine the dynamics that would occur after the bilayer interface has been sufficiently deformed by the onset of an instability.

The mathematical model is based on a phase-field description of an isothermal binary mixture that is confined between two stationary (non-rotating) horizontal walls. Neglecting the rotation of the system is motivated by the experimental results of Mokarian–Tabari *et al.* [107], who find that the film morphology is essentially the same close to and far away from the axis of rotation. We suppose that the dynamics of interest do not depend on the polymeric nature of the mixture components. Therefore, we model the mixture as an isotropic, regular solution. The two components of the mixture correspond to the two species of polymer, and these are assumed to flow relative to each other via diffusion. To simulate the thermodynamic changes that occur as the solvent slowly evaporates, we allow the temperature of the system to slowly decrease.

The hydrodynamic aspects of the physical system are not considered here, despite the fact that these are likely to be important during the transformation from a bilayer to a laterally separated state. However, by first investigating the simpler case of diffusion-driven flow, we can develop the mathematical tools that are required to analyse more complex problems while gaining valuable insight into the basic features of the topological transformation.

The two walls in our mathematical model represent the fact that in reality, the mixture has a finite thickness and is essentially confined between the surface of the substrate and the overlying air. At this time we do not consider the possibility of deformations in the surface of the mixture. We also neglect evaporation, so the upper wall is held at a fixed position relative to the lower one and the height of the mixture remains constant. The substrate and the air are expected to interact with the components of the mixture, and this is taken into account by assigning a surface energy to the walls. This effectively biases each wall so that it has a preference for one particular species which, in turn, promotes compositional enrichment near the surfaces.

4.1.5 Summary of key results and outline of chapter

The phase-field model is analysed using a combination of asymptotic and numerical methods. If the temperature of the system is independent of time and below the bulk critical value when the walls are not strongly biased towards their preferred species, we find that the formation of a bilayer is not guaranteed. Instead, spinodal decomposition leads to the formation of small domains within the bulk and these subsequently coarsen into columns that resemble the laterally separated morphology shown in Figure 4.1 (b). When the walls are strongly biased, we find that surface-directed spinodal decomposition occurs, whereby the mixture separates into horizontal layers that appear to grow towards the bulk from the confining surfaces. Once these layers fully develop, they coarsen into a bilayer structure. If the temperature of the system is allowed to slowly vary with time and is decreased from the bulk critical value, the formation of small domains within the bulk can be suppressed and a bilayer can develop. This is shown to occur even when the walls are weakly biased. In this case, the bilayer is expected to be metastable due to its large interface and the weak attraction of the material to the walls. By manually perturbing a bilayer, we show that a cascade of topological transitions can be initiated that is driven by interface minimisation. Each transition creates new contact lines and the overall process leads to the film settling into a laterally separated state.

The chapter is organised as follows. In Section 4.2 the phase-field model is derived and a numerical scheme for approximating its solutions is presented. In Section 4.3, this model is used to explore the conditions under which a bilayer can form. In Section 4.4, we systematically reduce the phase-field model to a thin-film equation that describes the evolution of the bilayer interface. We then use both models to study how the bilayer responds to perturbations. The chapter concludes in Section 4.5. Additional details of the model and the asymptotics can be found in Appendix C.1, C.2, and C.3.

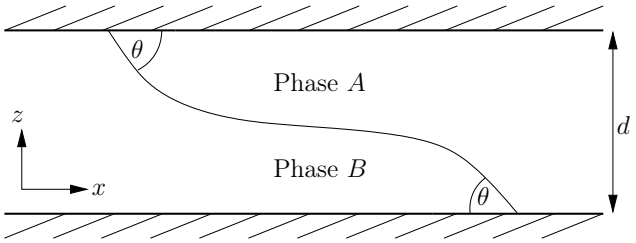


Figure 4.4: We consider a binary mixture consisting of material A and material B that is confined between two walls that are a distance d apart. If the temperature is below the critical point, a homogeneous mixture will separate into A-rich and B-rich phases, which are labelled as A and B, respectively. The walls interact with the mixture, causing each component to be preferentially attracted to one of the two surfaces. The strength of this attraction is measured through the equilibrium contact angle θ.

4.2 Mathematical formulation

We are interested in how a mixture of two materials, A and B, diffusively separates when it is confined between two walls of infinite horizontal extent. We assume these walls are vertically separated by a distance d. For the majority of this chapter it will be assumed that the walls are one dimensional so the mixture is confined within a two-dimensional channel. We will label compositionally distinct domains within the mixture as phase A and phase B according to the majority species in each domain; see Figure 4.4. A phase-field model will be used to describe the dynamics of phase separation and it will consist of a single evolution equation for the volume fraction φ of material A. The function φ is assumed to depend on the horizontal and vertical coordinates x and z, respectively, and time t. The formulation of the model will begin by defining the free energy of the system and this will be used, in turn, to derive an equation for φ describing the evolution towards an energy-minimising state. The derivation here will follow the traditional approach that was first presented by Cahn and Cahn & Hilliard [32, 35]; however, the same equations can be obtained through other means, for example, using entropy principles and dissipation inequalities from non-equilibrium thermodynamics [1] or with variational methods and gradient flows [37].

4.2.1 Free energy of the system

The total free energy of the system is assumed to have two contributions: one from the bulk free energy of the mixture and one from the surface energy of the walls. Therefore, the total free energy functional F is written as

$$F[\varphi] = F_b[\varphi] + F_s[\varphi], \tag{4.1}$$

where F_b and F_s denote the bulk and surface contributions, respectively. Following Cahn & Hilliard [35], the bulk free energy is further decomposed into two parts and is written as

$$F_b[\varphi] = N_v \int_\Omega \left[f(\varphi) + k_B T_c a^2 |\nabla \varphi|^2 \right] \mathrm{d}x\mathrm{d}z, \tag{4.2}$$

where $\Omega = \{(x, z) : x \in \mathbb{R},\, 0 < z < d\}$ is the spatial domain under consideration. The first term in (4.2) denotes the free energy of a spatially homogeneous mixture and the second term represents the energy cost of non-homogeneous states with composition gradients. The two-term form of (4.2) is derived from a more general Taylor-series expansion about small composition gradients, which has been simplified using symmetry arguments that are valid for an isotropic medium [35]. In the expression for F_b given by (4.2), f denotes the Gibbs free energy of mixing (per unit molecule), k_B is Boltzmann's constant, T_c is the bulk critical temperature, a represents an effective interaction length between molecules in the mixture, and N_v denotes the number density of molecules (assumed constant; implies the mixture is incompressible). The mixture is assumed to be regular, in which case the Gibbs free energy of mixing is given by [35]

$$f(\varphi) = 2k_B T_c \varphi(1-\varphi) + k_B T \left[\varphi \log \varphi + (1-\varphi) \log(1-\varphi) \right], \tag{4.3}$$

where T is the temperature. The first term is the enthalpy of mixing, which arises from nearest-neighbour interactions amongst the molecules. The second term represents the entropy of mixing. The enthalpic contribution is concave with its minima at $\varphi = 0$ and $\varphi = 1$; thus, it favours demixing into phases which are pure in each species. The entropic contribution is convex with its minima at $\varphi = 1/2$, thus favouring a homogeneous 50:50 blend. When these contributions are combined, the tendency to mix or demix is determined by the temperature of the system. For $T < T_c$, the free energy has a double-well structure with minima at $\varphi = \varphi_- < 1/2$ and $\varphi = \varphi_+ > 1/2$. This implies demixing is possible if the initial composition is in the spinodal region. For $T > T_c$, the entropic contribution to the free energy dominates and the system is driven towards a homogeneous 50:50 mixture.

The surface contribution to the free energy is given by

$$F_s[\varphi] = \int_{z=0} g_0(\varphi)\, \mathrm{d}x + \int_{z=d} g_d(\varphi)\, \mathrm{d}x, \tag{4.4}$$

where g_0 and g_d denote wall-material interaction potentials. These can be related to conventional surface energies using the results of Modica [106]; details of this are given in Appendix C.2. We assume that the walls are antisymmetric in the sense that they favour different materials but their affinity for their preferred species is the same. This yields the relation $g_0(\varphi) = g_d(1-\varphi)$, which allows g_d to be determined from g_0 and vice-versa. In the remainder of the chapter, we will always write g_d in terms of g_0. The precise form of g_0 will

be stated below. By adding explicit spatial dependencies to the functions g_0 and g_d, it is possible to account for chemical patterning of the substrates. This is not something that is explored here, however, and we refer the reader to Karim *et al.* [89] for more details.

4.2.2 Evolution equations

Given an initial condition for the volume fraction of material A, the system will evolve in such a way as to minimise its total free energy while conserving mass. The volume fraction φ, therefore, satisfies the standard conservation equation

$$\partial_t \varphi + \nabla \cdot \boldsymbol{q} = 0, \tag{4.5}$$

where $\boldsymbol{q}$ denotes the volume flux of material A. We assume that the flux satisfies a generalised form of Fick's law given by

$$\boldsymbol{q} = -m(\varphi)\nabla\mu, \tag{4.6}$$

where m is the composition-dependent mobility and μ is the chemical potential difference between the two materials. We follow Vladimirova *et al.* [152] and write the mobility as

$$m(\varphi) = D\varphi(1-\varphi), \tag{4.7}$$

where D is a diffusion coefficient (assumed constant). The chemical potential describes how the free energy of a system changes with composition; thus, it can be computed by taking the first variation of the free energy,

$$\mu = \frac{\delta}{\delta\varphi}\left(\frac{F}{N_v k_B T}\right) = \frac{1}{k_B T}\left[f'(\varphi) - 2k_B T_c a^2 \nabla^2 \varphi\right]. \tag{4.8}$$

Elimination of the boundary terms that arise in this variation yield boundary conditions for the order parameter describing the local influence of the walls:

$$2N_v k_B T_c a^2 \partial_z \varphi = g_0'(\varphi), \qquad z = 0, \tag{4.9a}$$

$$2N_v k_B T_c a^2 \partial_z \varphi = g_0'(1-\varphi), \quad z = d, \tag{4.9b}$$

where the prime denotes differentiation with respect to φ. Relating these boundary conditions to the equilibrium contact angle θ will be discussed in Section 4.2.5. We also impose no-flux conditions at the walls, which yield the two final boundary conditions:

$$\partial_z \mu = 0, \quad z = 0, \tag{4.10a}$$

$$\partial_z \mu = 0, \quad z = d. \tag{4.10b}$$

To close the problem an initial condition is prescribed and this is given by $\varphi(x, z, 0) = \varphi_i(x, z)$.

An interesting question arises when considering if the boundary conditions (4.9), which naturally appear when formulating the stationary version of the problem using variational calculus, are still suitable for the dynamic problem considered here. Our justification for using them stems from the fact that they guarantee the free energy of the system monotonically decreases with time (see Appendix C.1), which seems like a reasonable assumption given that no external energy is being put into the system.

From the form of (4.5) with the flux given by (4.6) and boundary conditions (4.10), a straightforward calculation shows that

$$\frac{\mathrm{d}}{\mathrm{d}t}\int_{\Omega}\varphi(x,z,t)\,\mathrm{d}x\mathrm{d}z = 0, \tag{4.11}$$

implying that mass is indeed conserved.

In summary, the dimensional model that we use to describe the evolution of a binary mixture is given by

$$\partial_t\varphi = D\nabla\cdot\left[\varphi(1-\varphi)\nabla\mu\right], \tag{4.12a}$$

$$\mu = \frac{1}{k_BT}\left[f'(\varphi) - 2k_BT_ca^2\nabla^2\varphi\right], \tag{4.12b}$$

$$f = 2k_BT_c\varphi(1-\varphi) + k_BT\left[\varphi\log\varphi + (1-\varphi)\log(1-\varphi)\right], \tag{4.12c}$$

subject to the boundary conditions

$$2N_vk_BT_ca^2\partial_z\varphi = g_0'(\varphi), \qquad z=0, \tag{4.12d}$$

$$\partial_z\mu = 0, \qquad z=0, \tag{4.12e}$$

$$2N_vk_BT_ca^2\partial_z\varphi = g_0'(1-\varphi), \qquad z=d, \tag{4.12f}$$

$$\partial_z\mu = 0, \qquad z=d, \tag{4.12g}$$

and the initial condition $\varphi(x,z,0) = \varphi_i(x,z)$.

4.2.3 Non-dimensionalisation

The evolution equations can be recast in a dimensionless form by writing the horizontal and vertical coordinates using the channel height d as a length scale; that is, we set $x = d\tilde{x}$ and $z = d\tilde{z}$. Furthermore, we assume the problem evolves on the diffusive time scale so we write $t = (2d^2/D)\tilde{t}$. The volume fraction is written in terms of a symmetric order parameter ϕ that takes the value of $+1$ in domains that are pure in material A and -1 in domains that are pure in material B. More specifically, we let $\varphi = (1+\phi)/2$, where ϕ satisfies $-1 < \phi < 1$. The Gibbs free energy of mixing and the wall-material interaction potential

are non-dimensionalised using

$$f(\varphi) = f((1+\phi)/2) = \frac{k_b T}{2}\left[\frac{T_c}{T} - 2\log 2 + \tilde{f}(\phi)\right], \tag{4.13a}$$

$$g_0(\varphi) = N_v k_B T_c a\, \tilde{g}_0((1+\phi)/2), \tag{4.13b}$$

respectively. After dropping the tildes, the non-dimensional evolution equations are given by

$$\partial_t \phi = \nabla \cdot ((1-\phi^2)\nabla\mu), \tag{4.13c}$$

$$\mu = f'(\phi) - \varepsilon^2 (T_c/T)\nabla^2\phi, \tag{4.13d}$$

$$f(\phi) = -(T_c/T)\phi^2 + (1+\phi)\log(1+\phi) + (1-\phi)\log(1-\phi), \tag{4.13e}$$

where $\varepsilon = a/d \ll 1$. The corresponding boundary conditions for the order parameter are

$$\varepsilon\partial_z\phi = g_0'((1+\phi)/2), \quad z = 0, \tag{4.13f}$$

$$\varepsilon\partial_z\phi = g_0'((1-\phi)/2), \quad z = 1, \tag{4.13g}$$

and for the chemical potential they are

$$\partial_z\mu = 0, \quad z = 0, 1. \tag{4.13h}$$

The initial condition is written as $\phi(x,z,0) = \phi_i(x,z) = 2\varphi_i(x,z) - 1$.

A non-dimensional free energy can be defined as

$$\tilde{F} = \frac{2}{N_v k_b T d^2} F, \tag{4.14}$$

and it is straightforward to show that $\tilde{F}$ is given by (upon dropping the tilde)

$$\begin{aligned} F = \int_\Omega \left[f(\phi) + \frac{\varepsilon^2}{2}\frac{T_c}{T}|\nabla\phi|^2\right] \mathrm{d}x\mathrm{d}z + 2\varepsilon\frac{T_c}{T}\int_{z=0} g_0((1+\phi)/2)\,\mathrm{d}x \\ + 2\varepsilon\frac{T_c}{T}\int_{z=1} g_0((1-\phi)/2)\,\mathrm{d}x. \end{aligned} \tag{4.15}$$

Furthermore, by differentiating F with respect to time, one can show that (see Appendix C.1)

$$\frac{\mathrm{d}F}{\mathrm{d}t} = -\int_\Omega (1-\phi^2)|\nabla\mu|^2\,\mathrm{d}x\mathrm{d}z \leq 0. \tag{4.16}$$

Therefore, the evolution that arises from the phase-field model (4.13) is such that it monotonically decreases the free energy of the system. This drives the system towards energetically favourable states that correspond to the local minimisers of F. Such states typically consist of domains with different, but roughly uniform, compositions that are given by the minima of the free energy of mixing. These domains are connected by transition regions that have widths which are dependent on the parameter ε and the temperature; see Pego [122] and Cahn & Hilliard [35] for more details.

4.2.4 The near-criticality approximation

When the temperature of the system is slightly below the bulk critical point, the rescaled free energy of mixing (4.13e) has two minima that are located close to zero. This can be verified by introducing the parameter $\chi = T_c/T - 1$, which gives a measure of how much the temperature deviates from the bulk critical value, and then seeking an asymptotic solution to the equation $f'(\phi) = 0$ for $0 < \chi \ll 1$. We find that the minima of f are given by $\phi = \pm(3\chi)^{1/2} + O(\chi^{3/2})$. The leading-order part of this solution suggests a scaling that can be used to simplify the governing equations. To account for the fact that the temperature will sometimes be a function of time, we write

$$\chi = \chi_0 \check{\chi}(t) = T_c/T(t) - 1, \tag{4.17}$$

where $\check{\chi}(t)$ satisfies $\check{\chi}(t) \leq 1$ for all time t and $0 < \chi_0 \ll 1$ denotes the characteristic or limiting value of $|\chi|$. According to these definitions, temperatures above and below the critical point are represented by negative and positive values of $\check{\chi}$, respectively. Although this seems slightly illogical, the majority of the chapter will be concerned with the dynamics that occur below the critical point, *i.e.*, when $\check{\chi} > 0$.

The variables are now scaled using χ_0 instead of χ. In particular, we let

$$\phi = (3\chi_0)^{1/2}\check{\phi}, \quad \mu = 3^{1/2}\chi_0^{3/2}\check{\mu}, \quad t = \chi_0^{-1}\check{t}, \tag{4.18}$$

and this yields the system

$$\partial_{\check{t}}\check{\phi} = \nabla \cdot \left((1 - 3\chi_0\check{\phi}^2)\nabla\check{\mu}\right), \tag{4.19a}$$

$$3^{1/2}\chi_0^{3/2}\check{\mu} = f'((3\chi_0)^{1/2}\check{\phi}) - (3\chi_0)^{1/2}\varepsilon^2(1 + \chi_0\check{\chi}(t))\nabla^2\check{\phi}. \tag{4.19b}$$

The derivative of the free energy of mixing can be expanded as

$$f'((3\chi_0)^{1/2}\check{\phi}) = 2 \cdot 3^{1/2}\chi_0^{3/2}(\check{\phi}^2 - \chi(t))\check{\phi} + O(\chi_0^{5/2}); \tag{4.20}$$

thus, by inserting this into the above, we have

$$\partial_{\check{t}}\check{\phi} = \nabla \cdot \left((1 - 3\chi_0\check{\phi}^2)\nabla\check{\mu}\right), \tag{4.21a}$$

$$\check{\mu} = 2(\check{\phi}^2 - \chi(t))\check{\phi} - \varepsilon^2(1 + 1/\chi_0)\gamma(t)\nabla^2\check{\phi} + O(\chi_0), \tag{4.21b}$$

where the function γ is defined as

$$\gamma(t) = \frac{1 + \chi_0\check{\chi}(t)}{1 + \chi_0}. \tag{4.22}$$

Taking $\chi_0 \searrow 0$ with $\delta^2 = \varepsilon^2(1 + 1/\chi_0) = O(1)$ yields the system[1]

$$\partial_{\check{t}}\check{\phi} = \nabla^2\check{\mu}, \tag{4.23a}$$

$$\check{\mu} = \check{f}'(\check{\phi}) - \delta^2\nabla^2\check{\phi}, \tag{4.23b}$$

$$\check{f}(\check{\phi}) = \frac{1}{2}(\check{\phi}^2 - \check{\chi}(t))^2, \tag{4.23c}$$

where a $\check{\phi}$-independent function of time has been added to $\check{f}$ for convenience. This additive function does not affect the dynamics of the system. By a suitable scaling of the interaction potential g_0 in (4.13f) and (4.13g), the boundary conditions for the order parameter may be written as

$$\delta\partial_z\check{\phi} = \check{g}_0'(\check{\phi}), \qquad z = 0, \tag{4.24a}$$

$$\delta\partial_z\check{\phi} = \check{g}_0'(-\check{\phi}), \quad z = 1. \tag{4.24b}$$

where now the prime denotes differentiation with respect to $\check{\phi}$.

We will often associate the case of a fixed, time-independent temperature with setting $\check{\chi} \equiv 1$. For a constant temperature this choice can always be made be redefining the value of χ_0. When $\check{\chi} = 1$, the minima of the scaled free energy $\check{f}$ lie at $\check{\phi} = \pm 1$.

For the remainder of the chapter we will work within the near-criticality limit and use variables that have been rescaled according to (4.18).

4.2.5 Surface interaction potentials and their relation to wetting properties

In order to close the model, a functional form for the surface-material interaction potential needs to be provided. In the literature, this function is generally written as power series in the order parameter and is truncated after the quadratic or cubic terms [18, 141, 160]. We consider cubic potentials of the form

$$\check{g}_0(\check{\phi}) = \check{\beta}\left(\check{\phi} - \check{\phi}^3/3\right) \tag{4.25}$$

and write the boundary conditions as

$$\delta\partial_z\check{\phi} = \check{\beta}\left(1 - \check{\phi}^2\right), \quad z = 0, 1. \tag{4.26}$$

In these expressions, $\check{\beta} \geq 0$ is a parameter that characterises the bias of each wall towards one of the two species. This specific form of $\check{g}_0$ is chosen for two related reasons. Firstly, it

[1]We could also consider the case $\delta \gg 1$ by further rescaling $\check{\mu} = \delta^2\check{\mu}$, $\check{\phi} = \check{\phi}$, and $\check{t} = \delta^{-2}\check{t}$ to yield $\partial_{\check{t}}\check{\phi} = \nabla^2\check{\mu}$ with $\check{\mu} = \delta^{-2}f'(\check{\phi}) - \nabla^2\check{\phi}$. In this case, the homogeneous free energy f, which drives phase separation, does not play a dominant role so solutions are expected to be relatively homogeneous in the bulk. Therefore, we focus on the case when $\delta = O(1)$ or smaller.

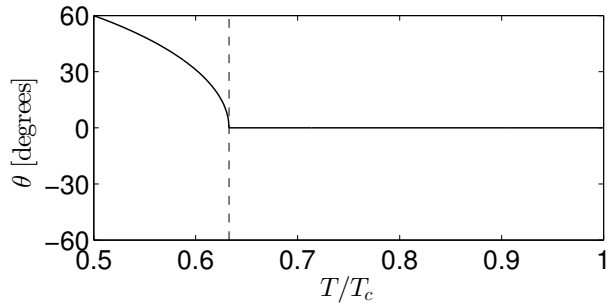


Figure 4.5: Characteristic temperature dependence of the equilibrium contact angle θ. For temperatures above a wetting temperature (dashed line), the walls are perfectly wetting. In this example, the bias of the walls is $\check{\beta} = 1/2$ and the wetting temperature corresponds to $T/T_c \simeq 0.63$. Details of the calculation used to determine θ are given in Appendix C.2.

eliminates the possibility of compositional boundary layers when the temperature is fixed at $\check{\chi} \equiv 1$. Secondly, it allows the parameter $\check{\beta}$ to be easily related to the equilibrium contact angle when $\check{\chi} \equiv 1$ [160]. By applying the results of Modica [106], we find that

$$\cos\theta = \begin{cases} \check{\beta} & \check{\beta} < 1, \\ 0 & \check{\beta} \geq 1, \end{cases} \tag{4.27}$$

when $\check{\chi} \equiv 1$. A derivation of this expression can be found in Appendix C.2. As expected, the wetting properties of the walls depend on how biased they are towards their preferred species. As $\check{\beta} \to 0$, the contact angle tends to ninety degrees and the bias vanishes. In this case, both materials equally favour both walls. However, as $\check{\beta}$ increases the contact angle decreases and when $\check{\beta} \geq 1$ it becomes zero, corresponding to a transition from partially wetting walls to perfectly wetting walls.

Early works by Cahn [34] have shown that the wetting properties of a substrate depend on the temperature of the system. As the temperature is raised towards the bulk critical point, a transition occurs whereby the substrate becomes perfectly wetting. The temperature at which this so-called wetting transition occurs is often referred to as the wetting temperature.

Evaluating the equilibrium contact angle for general values of $\check{\chi}$ with the surface energies given in (4.25) shows that a wetting transition occurs in this model. Details of this calculation can be found in Appendix C.2. For each value of $\check{\beta}$, there is a particular temperature above which the contact angle is equal to zero. Below this value, the contact angle is non-zero. An example of the temperature dependence of the contact angle when $\check{\beta} = 1/2$ is shown in Figure 4.5. Clearly illustrated is the general trend of θ decreasing as the temperature is increased until the wetting transition at $T/T_c \simeq 0.63$ occurs.

An alternative way of thinking about the wetting transition is that for a fixed temperature $\check{\chi}$, there is a critical value of $\check{\beta}$ above which the walls are perfectly wetting. When $\check{\chi}$

is small this value is approximately given by

$$\check{\beta}_c \simeq 0.68\check{\chi}, \quad \check{\chi} \ll 1. \tag{4.28}$$

Therefore, when the temperature is just below the critical value, even small values of $\check{\beta}$ correspond to strongly biased walls and small contact angles.

4.2.6 Model summary

In summary, the non-dimensional phase-field model in the near-criticality limit can be written, upon dropping the checks, as

$$\partial_t \phi = \nabla^2 \mu, \tag{4.29a}$$

$$\mu = f'(\phi) - \delta^2 \nabla^2 \phi, \tag{4.29b}$$

$$f(\phi) = \frac{1}{2}\left(\phi^2 - \chi(t)\right)^2, \tag{4.29c}$$

where $\delta = \varepsilon(1 + 1/\chi_0)^{1/2}$. Typically, we will assume that $\delta \ll 1$. The boundary conditions for these equations at $z = 0, 1$ are

$$\delta \partial_z \phi = \beta(1 - \phi^2), \tag{4.29d}$$

$$\partial_z \mu = 0, \tag{4.29e}$$

where $\beta = \cos\theta$ if $\beta \leq 1$ and $\chi \equiv 1$. To close the model, the initial condition $\phi(x, z, 0) = \phi_i(x, z)$ is prescribed. Despite the simplifications that have been made to obtain this model, it still conserves mass and leads to a monotonically decreasing free energy.

To simulate the unavoidable occurrence of thermal noise in any experimental setting, a source term can be added to the phase-field model that represents random fluctuations [46]. However, we choose to neglect such a term and assume that thermal noise only enters through the initial condition. The simulations by Jaiswal *et al.* [83] of a binary mixture that is confined between two walls (with similar boundary conditions to (4.29d)) with a temperature far below the bulk critical value show that a continuous source of noise only leads to small qualitative and quantitative changes in the solutions. Due to the close resemblance between their model and ours, we expect similar dynamics.

4.2.7 Numerical methods

We employ two different schemes for numerically simulating the governing equations (4.29). In the first, we use a hybrid spectral/finite-difference scheme where spectral methods are used to approximate spatial derivatives with a high degree of accuracy and finite difference methods are used to time step the resulting equations. The second method we use is a

implicit scheme based purely on finite differences. The advantages and shortcomings of each approach will be discussed below.

The derivation of the first scheme begins by taking the Fourier transform of the governing equations and their boundary/initial conditions to replace the x coordinate by a wavenumber k. The resulting problem in the bulk reads

$$\partial_t \hat{\phi} = (\partial_z^2 - k^2)\hat{\mu}, \tag{4.30a}$$

$$\hat{\mu} = \mathcal{F}\{f'(\phi)\} - \delta^2(\partial_z^2 - k^2)\hat{\phi}, \tag{4.30b}$$

where $\mathcal{F}$ denotes the Fourier transform in the x coordinate and

$$\hat{\phi}(z,t;k) = \mathcal{F}\{\phi(x,z,t)\}, \quad \hat{\mu}(z,t;k) = \mathcal{F}\{\mu(x,z,t)\}. \tag{4.30c}$$

The boundary conditions are given by

$$\delta\partial_z\hat{\phi} = \beta\mathcal{F}\{1-\phi^2\}, \tag{4.30d}$$

$$\partial_z\hat{\mu} = 0, \tag{4.30e}$$

at $z = 0, 1$, and the initial condition is $\hat{\phi}(z,0;k) = \hat{\phi}_i(z;k) = \mathcal{F}\{\phi_i(x,z)\}$. Although the wavenumber in the above set of equations is continuous, when this scheme is implemented in practice it takes on a discrete set of values.

The discretisation of the remaining spatial dimension is done using Chebyshev spectral methods. This entails replacing derivatives with respect to z in the bulk equations with the appropriate power of the Chebyshev differentiation matrix $\mathbf{D}$. Furthermore, evaluating derivatives on the boundary are equivalent to taking inner products with the first and last rows of $\mathbf{D}$. For additional details about this approach and the Chebyshev differentiation matrix, see Trefethen [150].

We discretise time into uniform units of length Δt and let

$$\hat{\phi}_j^{(n)}(k) \simeq \hat{\phi}(z_j, t_n; k), \quad \hat{\mu}_j^{(n)}(k) \simeq \hat{\mu}(z_j, t_n; k) \tag{4.31}$$

be the approximation to the solution at time $t_n = n\Delta t$ and at the j-th grid point. We will denote the vector of $\hat{\phi}_j^{(n)}$ and $\hat{\mu}_j^{(n)}$ values at the n-th time step as $\hat{\boldsymbol{\phi}}^{(n)}$ and $\hat{\boldsymbol{\mu}}^{(n)}$, respectively. The time derivative in (4.30a) is replaced by the standard first-order difference formula. To reduce the time-step restriction imposed by this fourth-order problem, we treat all linear terms implicitly, but we treat nonlinear terms explicitly to avoid the need for Newton–Raphson iterations at each time step.

Upon discretisation, the bulk equations (4.30) are reduced to a system of linear equations that must be solved at each time step and for every discrete value of the wavenumber k. Written explicitly, these equations are given by

$$\begin{bmatrix} \mathbf{I} & -\Delta t(\mathbf{D}^2 - k^2\mathbf{I}) \\ \delta^2(\mathbf{D}^2 - k^2\mathbf{I}) & \mathbf{I} \end{bmatrix} \begin{bmatrix} \hat{\boldsymbol{\phi}}^{(n+1)} \\ \hat{\boldsymbol{\mu}}^{(n+1)} \end{bmatrix} = \begin{bmatrix} \hat{\boldsymbol{\phi}}^{(n)} \\ \mathcal{F}\{f'(\boldsymbol{\phi}^{(n)})\} \end{bmatrix}, \tag{4.32}$$

where $\mathbf{I}$ denotes the identity matrix and $\boldsymbol{\phi}^{(n)}$ represents the vector of values $\phi_j^{(n)}(x) \simeq \phi(x, z_j, t_n)$. The bulk equations must be augmented with appropriate boundary conditions and these are given by

$$\delta \boldsymbol{d} \cdot \hat{\boldsymbol{\phi}}^{(n+1)} = \beta \mathcal{F}\left\{1 - \left[\phi_j^{(n)}\right]^2\right\}, \tag{4.33a}$$

$$\boldsymbol{d} \cdot \hat{\boldsymbol{\mu}}^{(n+1)} = 0, \tag{4.33b}$$

where $\boldsymbol{d}$ denotes the first or last row of the matrix $\mathbf{D}$ and j is chosen to correspond to the first or last grid point.

The advantage of the hybrid spectral/finite-difference scheme is that is it very straightforward to implement and spatial derivatives are computed with a high degree of accuracy. However, despite treating the fourth-order terms implicitly, in practice we find that the scheme is still unstable when sufficiently large time steps are used. Thus, we use this method for simulations that only require small time steps. In particular, this scheme was used to produce Figures 4.6–4.10 and Figure 4.12–4.14.

Our second approach is based on a fully implicit finite-difference scheme. Although a nonlinear problem must be solved at each time step in this method, when Δt is sufficiently large this is faster than solving many linear problems over smaller time steps using the hybrid scheme. Moreover, the implicit finite-difference scheme is implemented in the C programming language with the PETSc libraries [4, 5, 6], the latter of which offer a suite of parallelised routines for solving linear and nonlinear algebraic equations. This computational scheme was used to produce Figures 4.15–4.17.

4.3 Bilayer formation

The mathematical model will now be analysed using a combination of asymptotic and numerical methods. We first focus on how the bias of the walls affects the formation of bilayers when the system is held at a constant temperature by looking at two regimes that are determined by the size of the parameter β. Once this is established, we then explore the dynamics that occur as the system is slowly cooled.

4.3.1 Dynamics at constant temperature with weakly biased walls

If the bias of the walls is weak and the initial mixture composition is close to homogeneous, then it is possible to obtain an asymptotic solution to the governing equations when the temperature is constant in time. We take χ to be a constant and assume that the parameter $\alpha = \beta/\delta \ll 1$, where $\delta = O(1)$. The order parameter and the chemical potential are written as

$$\phi(x,z,t) = \phi_0(x,z,t) + \alpha\phi_1(x,z,t) + O(\alpha^2), \tag{4.34a}$$

$$\mu(x,z,t) = \mu_0(x,z,t) + \alpha\mu_1(x,z,t) + O(\alpha^2). \tag{4.34b}$$

We suppose the initial condition has the form $\phi_i(x,z) = \psi + \alpha\phi_{1i}(x,z) + O(\alpha^2)$ so that, to leading-order, the mixture is initially homogeneous. Any fluctuations in the initial composition are assumed to be a higher-order effect. We assume that ψ and ϕ_{1i} are prescribed.

Inserting these into the phase-field model (4.29) and expanding in powers of α yields the $O(1)$ problem given by

$$\partial_t\phi_0 = \nabla^2\mu_0, \tag{4.35a}$$

$$\mu_0 = f'(\phi_0) - \delta^2\nabla^2\phi_0, \tag{4.35b}$$

$$f(\phi_0) = \frac{1}{2}\left(\phi_0^2 - 1\right)^2, \tag{4.35c}$$

with boundary conditions

$$\partial_z\phi_0 = \partial_z\mu_0 = 0, \quad z = 0, 1, \tag{4.35d}$$

and the initial condition $\phi_0(x,z,0) = \psi$. The solution to the leading-order problem is a constant function in space and time; hence, we set $\phi_0(x,z,t) \equiv \psi$. We proceed to the $O(\alpha)$ problem, the bulk equations of which read

$$\partial_t\phi_1 = \nabla^2\mu_1, \tag{4.36a}$$

$$\mu_1 = f''(\psi)\phi_1 - \delta^2\nabla^2\phi_1, \tag{4.36b}$$

where $f''(\psi) = 6\psi^2 - 2\chi$. The corresponding boundary conditions are

$$\partial_z\phi_1 = 1 - \psi^2, \quad z = 0, 1, \tag{4.36c}$$

$$\partial_z\mu_1 = 0, \qquad z = 0, 1, \tag{4.36d}$$

and the initial condition is $\phi_1(x,z,0) = \phi_{1i}(x,z)$. The solution to this problem can be found in three steps: first, an appropriate linear function in z is added to ϕ_1 so that the boundary conditions become homogeneous; secondly, a Fourier transform is taken in the x

direction; and finally, the solution is sought in the form of a Fourier cosine expansion with time-dependent Fourier coefficients. The calculations are lengthy but straightforward so we present only the result here. The solution for ϕ_1 can be written as

$$\begin{aligned}\phi_1(x,z,t) = (1-\psi^2)(z-1/2) &+ \sum_{n=0}^{\infty} \mathcal{F}^{-1}\{\hat{a}_n(k)e^{\sigma_n(k)t}\}\cos(n\pi z) \\ &+ \frac{4(1-\psi^2)}{\pi^2}\sum_{n\text{ odd}}^{\infty}\left[\frac{e^{\sigma_n(0)t}}{n^2}\right]\cos(n\pi z) \\ &+ \frac{4(1-\psi^2)f''(\psi)}{\pi^2}\sum_{n\text{ odd}}^{\infty}\left[\frac{1-e^{\sigma_n(0)t}}{n^2(f''(\psi)+\delta^2 n^2\pi^2)}\right]\cos(n\pi z),\end{aligned} \tag{4.37a}$$

where k is a continuous horizontal wavenumber, σ_n denotes a growth rate given by

$$\sigma_n(k) = -(k^2+n^2\pi^2)\left[f''(\psi)+\delta^2(k^2+n^2\pi^2)\right], \tag{4.37b}$$

and $\hat{a}_n$ denotes the Fourier cosine components of the Fourier transform of the initial condition,

$$\hat{a}_n(k) = \frac{\int_0^1 \mathcal{F}\{\phi_{1i}(x,z)\}\cos(n\pi z)\,\mathrm{d}z}{\int_0^1 \cos^2(n\pi z)\,\mathrm{d}z}. \tag{4.37c}$$

This solution can be simplified by writing the first term as a Fourier cosine series and then combining the sums to yield

$$\begin{aligned}\phi_1(x,z,t) = &\sum_{n=0}^{\infty}\mathcal{F}^{-1}\{\hat{a}_n(k)e^{\sigma_n(k)t}\}\cos(n\pi z) \\ &- 4\delta^2(1-\psi^2)\sum_{n\text{ odd}}^{\infty}\left[\frac{1-e^{\sigma_n(0)t}}{f''(\psi)+\delta^2 n^2\pi^2}\right]\cos(n\pi z).\end{aligned} \tag{4.38}$$

The benefit of this expression is that the two processes which drive the evolution of the solution are clearly presented in the form of two different summations. The first sum describes how initial inhomogeneities in the composition evolve and it contains information about how the mixture may separate due to spinodal decomposition. The second sum describes how the bias of the walls influences the composition and, in particular, how it drives the formation of layered structures within the bulk.

We write the initial condition in (4.37c) as $\phi_{1i} = (\phi_i - \psi)/\alpha$ and replace α with β/δ in the resulting two-term asymptotic expansion for the solution $\phi_0 + \alpha\phi_1$ to yield

$$\begin{aligned}\phi(x,z,t) \simeq \psi &+ \sum_{n=0}^{\infty}\mathcal{F}^{-1}\{\hat{b}_n(k)e^{\sigma_n(k)t}\}\cos(n\pi z) \\ &- 4\delta\beta\left(1-\psi^2\right)\sum_{n\text{ odd}}^{\infty}\left[\frac{1-e^{\sigma_n(0)t}}{f''(\psi)+\delta^2 n^2\pi^2}\right]\cos(n\pi z),\end{aligned} \tag{4.39a}$$

where the $\hat{b}_n$ are given by

$$\hat{b}_n(k) = \frac{\int_0^1 \mathcal{F}\{\phi_i(x,z) - \psi\}\cos(n\pi z)\,\mathrm{d}z}{\int_0^1 \cos^2(n\pi z)\,\mathrm{d}z}. \tag{4.39b}$$

4.3.1.1 Morphology selection

The two processes mentioned above, namely spinodal decomposition and layer formation, can lead to substantially different morphologies. Spinodal decomposition has the tendency to create transient small-scale domains which slowly coarsen into large structures, with the smaller domains often merging with larger ones. The size of these transient domains can be estimated using the wavenumber that maximises the growth rate given in (4.37b). Similarly, the bias of the walls will induce a layered pattern and the number of layers can be also be estimated using this growth rate. Although these two processes often occur simultaneously, the growth rates of the associated modes are not equal and hence one process, or one morphology, might be far more pronounced than the other. We now analyse the growth rates and their dependence on the system parameters to determine the dominant morphologies.

The parameter space can be divided into two regimes that correspond to being above or below the spinodal in the binary phase diagram; see Figure 4.3 (b). Recalling that the spinodal is defined as the curve for which $f''(\psi) = 0$, our analysis implies that, for an initial mixture with a homogeneous composition ψ, the spinodal is given by $3\psi^2 - \chi = 0$, where $\chi\chi_0 = T_c/T - 1$. Keeping in mind the inverse relationship between χ and the temperature T, we shall refer to the region $\chi > 3\psi^2$ as being "below" the spinodal. When the initial composition corresponds to a 50:50 mixture ($\psi = 0$), being above or below the spinodal is equivalent to being above or below the critical temperature, respectively.

An examination of the growth rates in (4.37b) shows that all modes have negative growth rates except for the neutral $k = n = 0$ mode when the system lies above the spinodal ($\chi < 3\psi^2$). This implies that any inhomogeneities in the initial condition will decay exponentially fast. If the walls are neutral to both species, then the mixture will tend to a uniform composition. However, if the walls are biased, then enrichment layers of the preferred materials will form in their vicinity. To study these layers, we compute the steady-state solution, which can be found by taking the limit as $t \to \infty$ of the asymptotic solution (4.38) or by solving the stationary version of the governing equations (4.36) directly. When taking the latter approach, the problem must be augmented with an equation representing the conservation of mass,

$$\int_0^1 \int_{-\infty}^{\infty} [\phi_1(x,z) - \phi_{1i}(x,z)]\,\mathrm{d}x\mathrm{d}z = 0. \tag{4.40}$$

The steady state solution for ϕ_1 can be written explicitly as

$$\phi_1(z) = \lim_{L\to\infty} \frac{1}{2L} \int_0^1 \int_{-L}^{L} \phi_{1i}(x,z)\,\mathrm{d}x\mathrm{d}z + l\left(1-\psi^2\right) \frac{\sinh((z-1/2)/l)}{\cosh(1/(2l))}, \tag{4.41}$$

where l denotes the width of the enrichment layers and is given by $l = \delta/\sqrt{f''(\psi)}$. As the spinodal is approached, $\chi \nearrow 3\psi^2$, the widths of the layers increase and the steady state profile becomes increasingly linear. However, the presence of noise and the inclusion of nonlinear terms are likely to bound the growth of l as the spinodal is reached; thus, a truly linear profile would not be expected to occur in reality [83]. From this analysis, we can conclude that a bilayer is not expected to form when the system is above the spinodal.

The transient dynamics leading to the enrichment layers can be studied by numerical simulations of the full nonlinear system (4.29). Figure 4.6 (a)–(c) shows the evolution of a random perturbation to a 50:50 mixture when the temperature of the system is above the critical point. In particular, a value of $\chi = -1$ has been used along with $\delta = 0.06$ and $\beta = \delta/2$. The initial condition corresponds to $\psi = 0$ with ϕ_i being uniformly distributed random numbers between ± 0.2. As expected, the figure shows the perturbation decaying and the solution tending towards a mixture that is homogeneous except near the walls where there is an enrichment of the preferred species.

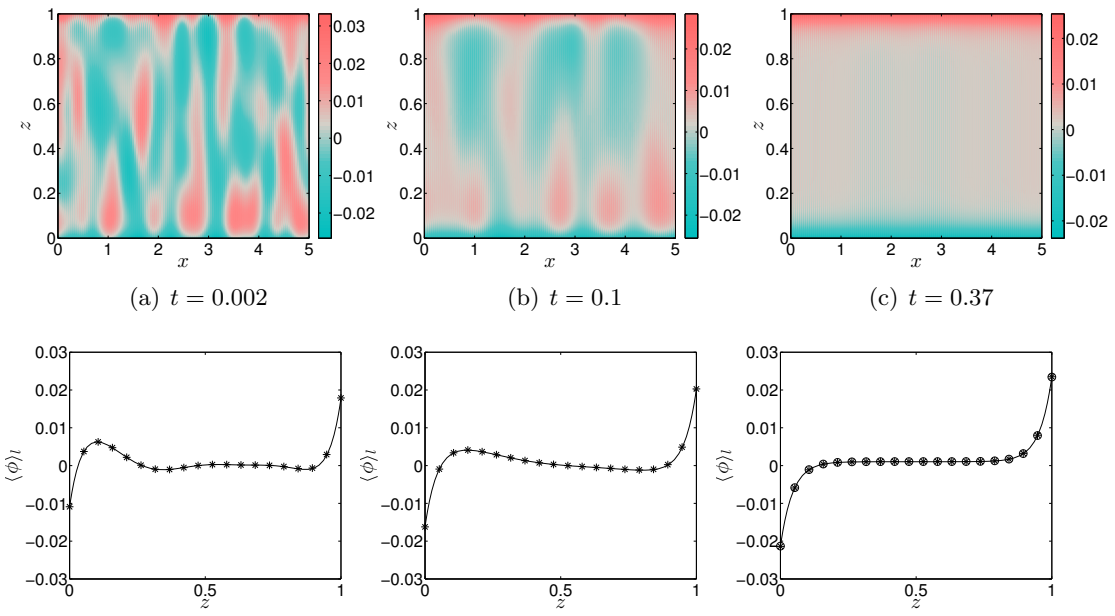
To assess the accuracy of the asymptotic solution, we define the laterally averaged order parameter,

$$\langle\phi\rangle_l(z,t) = \frac{1}{L}\int_0^L \phi(x,z,t)\,\mathrm{d}x, \tag{4.42}$$

and compare asymptotic and numerical approximations to it at various times. In the definition of $\langle\phi\rangle_l$, the parameter L denotes the horizontal length of the computational domain. Figure 4.6 (d)–(f) shows the laterally averaged profile at various times including the steady state for the previously mentioned parameter values. The numerical and asymptotic approximations of the laterally separated order parameter are in good agreement. Furthermore, the close agreement between the three profiles in panel (f), corresponding to $t = 0.37$, indicates that the evolution to the steady-state configuration is quite rapid when the system is above the spinodal.

For the remainder of the chapter we will focus on the dynamics that occur when the system is below the spinodal. In this case, the parameters satisfy $\chi > 3\psi^3$ and hence $f''(\psi) < 0$. There is now a range of modes that have positive growth rates, the wavenumbers of which satisfy

$$k^2 + n^2\pi^2 < -\frac{f''(\psi)}{\delta^2}. \tag{4.43}$$



(a) $t = 0.002$ (b) $t = 0.1$ (c) $t = 0.37$

(d) $t = 0.002$ (e) $t = 0.01$ (f) $t = 0.37$

Figure 4.6: Top (a)–(c): Numerical simulation showing the homogenisation of a perturbed 50:50 mixture and the formation of enrichment layers when the system lies above the spinodal and the temperature is constant. Bottom (d)–(f): Evolution of the laterally averaged order parameter (see (4.42) for a definition of $\langle\phi\rangle_l$). Solid lines and stars depict numerical and asymptotic solutions, respectively. The circles in panel (f) denote the asymptotic approximation to the steady-state solution computed using (4.41). Parameter values are $\psi = 0$, $\chi = -1$, $\delta = 0.06$, and $\beta = \delta/2$. The initial condition was uniformly distributed random numbers between ± 0.2.

There are three fundamental morphologies that can emerge due the temporary exponential growth of these modes. A laterally separated columnar morphology is possible due to the growth of modes with wavenumbers $k \neq 0$ and $n = 0$; a layered morphology that generalises the bilayer can emerge from the $k = 0$ and $n \neq 0$ modes; and finally, a mixed mode, cellular morphology can arise due to the growth of the $k \neq 0$ and $n \neq 0$ modes. Of these, only the modes associated with the laterally separated state are guaranteed to grow due to the restriction that the wavenumber n in (4.43) must take on integer values. In fact, there is a narrow band of temperatures given by $3\psi^2 < \chi < \chi_s$, where $\chi_s = 3\psi^2 + \delta^2\pi^2/2$, for which the laterally separated modes are the only ones that grow. If $\chi > \chi_s$, then all three types of modes can grow in theory. In this case, the dominant morphology will be determined by the fastest-growing mode. The wavenumbers of the fastest-growing columnar and cellular modes satisfy

$$\xi_m^2 = -\frac{f''(\psi)}{2\delta^2}, \tag{4.44}$$

where $\xi_m^2 = k_m^2 + n_m^2\pi^2$ is an average wavenumber, and the corresponding growth rate of these modes is

$$\sigma_m = \left[\frac{f''(\psi)}{2\delta}\right]^2. \tag{4.45}$$

Since this expression is independent of the wavenumber, we can conclude that the fastest-growing stripe and cellular modes will grow at the same rate. Determining the fastest-growing layered mode and its growth rate is not trivial. However, it is possible to show that $\sigma_n(0) < \sigma_m$ for all values of n; therefore, the layered modes are always subdominant. Thus, we expect that either a laterally separated or a cellular morphology will emerge during the early stages of evolution, with the specific choice being determined by the initial condition. The geometric properties of the associated domains can be determined from the fastest-growing wavenumber in (4.44). For example, the size of the emerging domains will be roughly equal to half of the wavelength λ_m given by

$$\lambda_m = \frac{2\pi}{\xi_m}, \tag{4.46}$$

where ξ_m is the wavenumber defined in (4.44).

The form of the asymptotic solution in (4.39) shows that unstable modes associated with positive growth rates, $\sigma_n(k) > 0$, where σ_n is given by (4.37b), grow exponentially in time. Eventually, this growth will be saturated by nonlinear effects and the subsequent morphology will be primarily driven by the minimisation of the A-B interface. Due to the assumption of a channel that is longer than it is high, we expect that cellular modes will eventually coarsen into columns instead of forming horizontal layers. Therefore, the

formation of a bilayer is not a generic phenomenon when the bias of the walls is weak and the temperature held constant below the critical value.

To verify the claims made from an analysis of the asymptotic solution, we simulate the full governing equations with parameters that lie in the spinodal region of the phase diagram. In particular, we consider a 50:50 mixture associated with $\psi = 0$ that is held at a temperature corresponding to $\chi = 1$. The initial condition is drawn from uniformly distributed random numbers of modulus 0.2. We set the bias of the walls equal to $\beta = \delta/2$ and in this particular case we take $\delta = 0.06$. The equivalent contact angle is $\theta = 88°$. The results from the simulation are presented in Figure 4.7 (a)–(d). The random fluctuations in the initial condition are quickly amplified by spinodal decomposition, resulting in the formation of small domains (panel (a)). The average size of these domains is in good agreement with the estimate of $\lambda_m/2 \simeq 0.2$ made from the asymptotic analysis, where λ_m is defined in (4.46). These small domains coarsen to into long filamentary structures (panel (b)). Further coarsening of these filaments (panel (c)) yields the expected laterally separated, columnar morphology (panel (d)).

The numerical solution at early times can be compared to the asymptotic solution using the laterally and vertically averaged order parameter, the latter of which is defined as

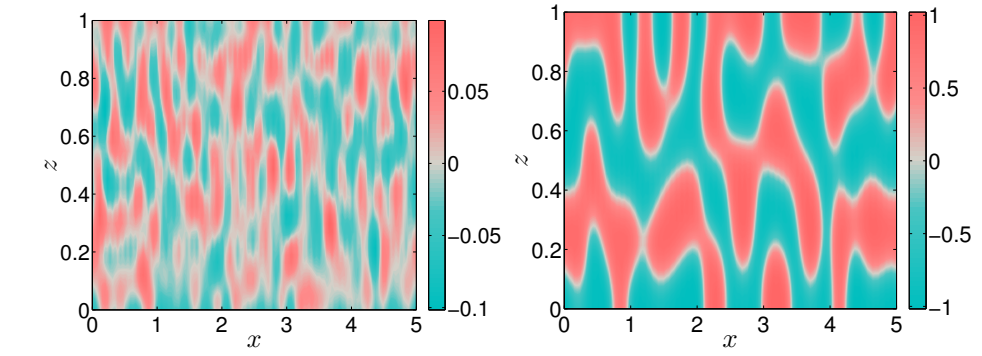
$$\langle \phi \rangle_v(x,t) = \int_0^1 \phi(x,z,t)\,\mathrm{d}z. \tag{4.47}$$

Numerical and asymptotic approximations to these functions at time $t = 5\times10^{-4}$ are shown in Figure 4.7 (e)–(f). The agreement between the two solutions is excellent, suggesting that the asymptotic solution does indeed capture the dynamics that occur before nonlinear effects become significant.

4.3.2 Dynamics at constant temperature with strongly biased walls

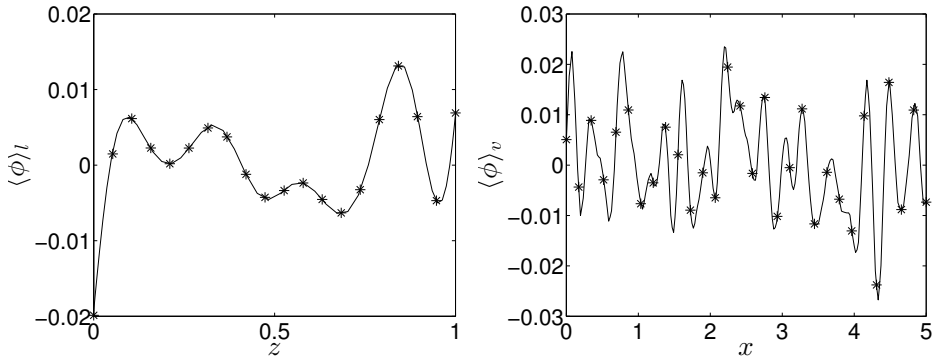
If the constituent materials are strongly attracted to their preferred walls, then one might expect the rapid formation of compositional boundary layers which represent near-surface enrichment. We have already seen that a similar situation can arise when the system lies above the spinodal in the phase diagram (see Figure 4.6) and we now explore this scenario for cooler temperatures. In particular, we set $\chi \equiv 1$ and assume the initial condition corresponds to a perfectly homogeneous 50:50 mixture so that $\phi(x,z,0) \equiv 0$. We further assume the bias of the walls is strong, which is equivalent to the equilibrium contact angle being small. From the relation $\beta = \cos\theta$ (see Section 4.2.5), we have that $\beta = O(1)$.

In the limit $\delta \to 0$, we find that the bulk equations for the order parameter and the chemical potential in (4.29) are satisfied by the uniform initial condition but the boundary conditions are not. Therefore, we expect thin compositional layers of width $O(\delta)$ to grow



(a) $t = 5 \times 10^{-4}$ (b) $t = 0.05$

(c) $t = 1$ (d) $t = 14.4$



(e) $t = 5 \times 10^{-4}$ (f) $t = 5 \times 10^{-4}$

Figure 4.7: (a)–(d): Dynamics of a 50:50 mixture in the spinodal regime of the phase diagram when the temperature is constant in time and the bias of the walls is weak. (a) Spinodal decomposition quickly amplifies fluctuations in the initial condition and leads to the formation of small domains within the bulk. (b)–(d): These domains coarsen until a laterally separated columnar morphology is obtained. (e)–(f): Comparison of the laterally averaged and vertically averaged order parameters that have been computed numerically (solid line) and asymptotically (stars). Parameter values are $\psi = 0$, $\chi = 1$, $\delta = 0.06$ and $\beta = \delta/2$. The initial condition is uniformly distributed random numbers between ± 0.2.

rapidly out of the initial condition. To capture this quick evolution, we consider a fast time $\check{\tau}$ given by $\check{\tau} = \delta^{-2}t$. Owing to the antisymmetry of this problem about $z = 1/2$, we only analyse the boundary layer that occurs at the bottom wall.

We begin with the outer problem that is posed away from the boundary layer at $z = 0$. The corresponding equations in the bulk are given by

$$\partial_{\check{\tau}}\phi = \delta^2\nabla^2\mu, \tag{4.48a}$$

$$\mu = 2(\phi^3 - \phi) - \delta^2\nabla^2\phi. \tag{4.48b}$$

These are combined with the initial condition $\phi \equiv 0$ at $\check{\tau} = 0$. The leading-order solution to this problem is given trivially by $\phi \equiv 0$ and $\mu \equiv 0$.

The inner problem is obtained by making the change of variable $z = \delta\eta$. We let $\Phi = \Phi(\eta, \check{\tau})$ and $M = M(\eta, \check{\tau})$ denote the inner solutions of the order parameter and the chemical potential in the boundary layer, respectively. The corresponding problem can then be written as

$$\partial_{\check{\tau}}\Phi = (\delta^2\partial_x^2 + \partial_\eta^2)M, \tag{4.49a}$$

$$M = 2(\Phi^3 - \Phi) - (\delta^2\partial_x^2 + \partial_\eta^2)\Phi, \tag{4.49b}$$

with boundary conditions

$$\partial_\eta\Phi = \beta(1 - \Phi^2), \tag{4.49c}$$

$$\partial_\eta M = 0, \tag{4.49d}$$

at $\eta = 0$. The two required far-field conditions come from matching Φ and M to the solution of the outer problem. The initial condition is $\Phi \equiv 0$ when $\check{\tau} = 0$.

We now consider only the leading-order part of (4.49) in the limit as $\delta \to 0$. The resulting equation in the bulk can be written as

$$\partial_{\check{\tau}}\Phi = \partial_\eta\left[(6\Phi^2 - 2)\partial_\eta\Phi\right] - \partial_\eta^4\Phi, \tag{4.50a}$$

which has boundary conditions given by

$$\partial_\eta\Phi = \beta(1 - \Phi^2), \tag{4.50b}$$

$$(6\Phi^2 - 2)\partial_\eta\Phi - \partial_\eta^3\Phi = 0, \tag{4.50c}$$

at $\eta = 0$. By matching to the leading-order outer solution, we find that the corresponding far-field conditions are

$$\Phi \to 0, \quad \partial_\eta^2\Phi \to 0 \tag{4.50d}$$

as $\eta \to \infty$. The initial condition remains unchanged and is given by $\Phi = 0$ when $\check{\tau} = 0$.

To proceed further, we look for a similarity solution. In general, the problem is not self-similar; however, it is for sufficiently small times. Thus, we let

$$\Phi(\eta, \check{\tau}) = \check{\tau}^{1/4} p(\xi), \quad \xi = \eta/\check{\tau}^{1/4}, \tag{4.51}$$

for $\check{\tau} \ll 1$. The full problem for p, which is not self-similar, can be written as

$$\frac{1}{4}\left(p - \xi p'\right) = -p'''' - 2\check{\tau}^{1/2} p'' + 6\check{\tau}\left(p^2 p'\right)', \tag{4.52a}$$

where the prime denotes differentiation with respect to ξ. The boundary conditions can be written as

$$p' = \beta\left(1 - \check{\tau}^{1/2} p^2\right), \tag{4.52b}$$

$$(6\check{\tau}p^2 - 2\check{\tau}^{1/2})p' - p''' = 0, \tag{4.52c}$$

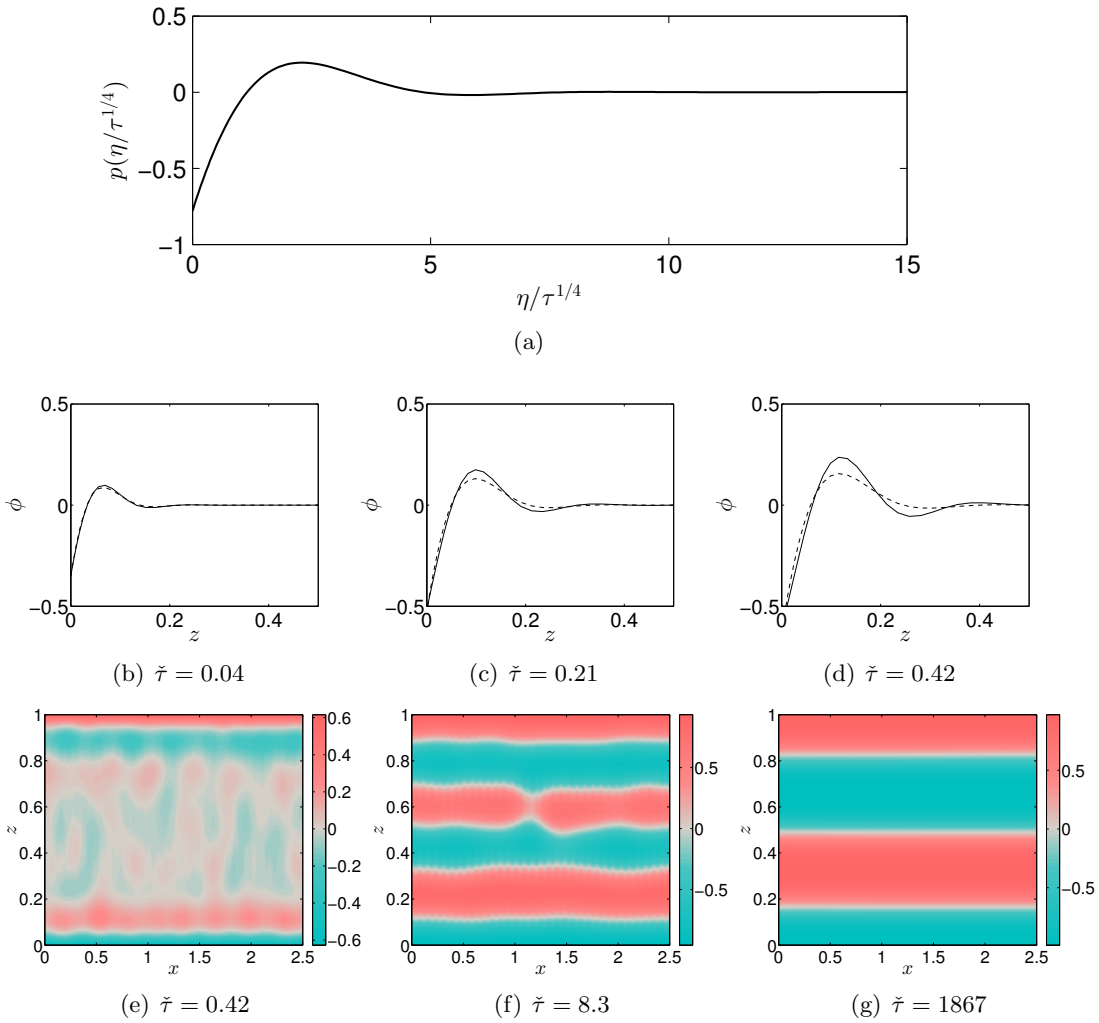
at $\xi = 0$ and $p \to 0$, $p'' \to 0$ as $\xi \to \infty$. The initial condition is automatically satisfied. Keeping with our assumption that this solution is only valid for short times, we can neglect terms of $O(\check{\tau}^{1/2})$ and higher to reduce the problem to one that is self-similar:

$$p - \xi p' = -4p'''' \tag{4.53}$$

with $p'(0) = \beta$, $p'''(0) = 0$, $p(\infty) = 0$, and $p''(\infty) = 0$. This problem can be simplified by noticing that $p(\xi) = \xi$ is a solution, which allows the order of the problem to be reduced by seeking a solution of the form $p(\xi) = \xi u(\xi)$. However, the solution to the reduced problem can only be written in terms of hypergeometric functions and is not especially insightful. A numerical approximation to the solution of (4.53) is shown in Figure 4.8 (a). The solution corresponds to a growing compositional boundary layer of the preferred species. The dip that occurs at $\xi \simeq 5$ corresponds to a depletion region where there is a local enrichment of unpreferred material.

Figure 4.8 (b)–(d) compares the similarity solution to a one-dimensional numerical simulation of the full model (4.29) when $\delta = 0.06$ and the walls are perfectly wetting, *i.e.*, when $\beta = 1$ ($\theta = 0$). For very small times, the similarity solution and the numerics are in excellent agreement, as shown in panel (b). However, neglecting the $O(\check{\tau}^{1/2})$ terms means that obvious qualitative and quantitative discrepancies do eventually appear; see panels (c)–(d).

The dynamics for larger times are studied using numerical simulations of the full two-dimensional problem. Figure 4.8 (e)–(g) shows the characteristic behaviour when the initial condition is a perturbation to a 50:50 blend consisting of uniformly distributed random



(a)

(b) $\check{\tau} = 0.04$ (c) $\check{\tau} = 0.21$ (d) $\check{\tau} = 0.42$

(e) $\check{\tau} = 0.42$ (f) $\check{\tau} = 8.3$ (g) $\check{\tau} = 1867$

Figure 4.8: Top (a): The early time similarity solution when the walls strongly interact with the materials. See text for definitions of $\check{\tau}$, η, and the function p. Middle (b)–(d): Comparison of the early time similarity solution (dashed line) to one-dimensional numerical solutions (solid line) when $\beta = 1$ ($\theta = 0$). Bottom (e)–(g): Two-dimensional simulations showing the formation of layered structures when the walls are perfectly wetting. The initial condition for panels (b)–(d) was taken to be a homogeneous 50:50 mixture corresponding to $\phi \equiv 0$, and for panels (e)–(g) it was a random perturbation of size 0.2 to the same state. In both cases a value of $\delta = 0.06$ was used.

numbers. In this case, the initial noise has amplitude 0.2 and the parameters are $\delta = 0.06$ with $\beta = 1$ ($\theta = 0$). The strong bias of the walls extinguishes the majority of the horizontal composition gradients. Furthermore, boundary layers of the preferred materials and depletion layers of unpreferred materials rapidly develop (panel (e)). The A-B interfaces between these layers propagate into the bulk from the boundaries, giving the layers a travelling-wave-like appearance. Different A-B interfaces travel at different speeds, thus causing the widths of the layers to increase. Eventually, an A-B layer forms in the middle of the channel, with an A-B interface at $z \simeq 0.5$ (panel (f)). This structure grows out of the small dip at $z = 0.25$ in panel (d) and the corresponding symmetric ridge that occurs at $z = 0.75$ but is not shown. The layers slowly coarsen until a bilayer is obtained (not shown, but it is identical to the bilayer in Figure 4.10 (c)).

The dynamics that are shown in Figure 4.8, where compositional layers appear to propagate as waves from the substrates into a relatively homogeneous bulk, are characteristic of surface-directed spinodal decomposition [18, 21]. Furthermore, the layer formation and coarsening dynamics shown in Figure 4.8 (e)–(g) bear a remarkable qualitative resemblance to the experimental figures of Jones *et al.* [86], where surface-directed spinodal decomposition is studied in a confined polymer blend.

To characterise the thickness of the layer that forms near the bottom wall, we follow previous theoretical and experimental studies (see Section 4.1.2) and use the first zero of the laterally averaged order parameter, which we denote by $\ell(t)$. According to our asymptotic analysis valid for $t \ll 1$ and, in particular, from the form of the similarity solution in (4.51), we must have that $\ell(t) \sim t^{1/4}$ for $t \ll 1$. In fact, we can write $\ell(t) = \delta^{1/2}\xi_1 t^{1/4}$, where $\xi_1 \simeq 1.146$ is the first root of the function p computed from (4.53). This growth law has been verified numerically by running 100 simulations with random initial conditions using fixed values of $\delta = 0.06$ and $\beta = 1$, and then averaging the results appropriately. Figure 4.9 compares the simulation-averaged thickness to the asymptotic growth law. The comparison is excellent for early times.

The qualitative dynamics of structure formation when the walls are strongly and weakly biased are markedly different. In the case of strongly biased walls, the small-scale structures are rapidly extinguished and the large-scale structures, which are layers with interfaces that are parallel to the walls, grow from the confining surfaces into the interior at a finite speed. As a result, layers form much sooner near the surface than in the bulk. This can be seen by comparing panels (e) and (f) in Figure 4.8; the pair of internal A-B layers appear after the boundary and depletion layers. When the bias of the wall is weak, however, the large-scale structures emerge from the coarsening of small domains that form within the bulk. This

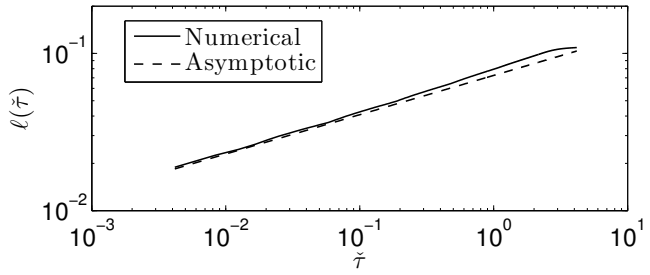


Figure 4.9: When the bias of the walls is strong, the layers satisfy a $\check{\tau}^{1/4}$ growth law for early times. The thickness of the bottom layer, ℓ, is measured using the first zero of the laterally averaged order parameter. The numerical values of ℓ have been averaged over several simulations using random initial conditions and fixed values of $\delta = 0.06$ and $\beta = 1$. See text for further details.

makes the large-scale structures appear at roughly at the same time, regardless of whether they are close to the walls or in the interior of the domain.

4.3.3 Dynamics of a slowly cooled mixture

The asymptotic analysis in the case of weakly biased walls and a constant temperature indicated that, in general, the onset of spinodal decomposition leads to the formation of small domains in the bulk which subsequently coarsen into laterally separated structures. We now examine how the system evolves when the temperature is slowly decreased from the critical point to determine whether this behaviour can be avoided. If this is indeed the case, then it may be possible to obtain layered morphologies when the walls are weakly biased. The motivation for this claim comes from the fact that, for fixed values of β, the bias of the walls is very strong at low temperatures; see Section 4.2.5. The results of Section 4.3.2 indicate that strongly biased walls lead to the formation of layered structures. Moreover, from (4.45) it is clear that fluctuations to homogeneous states develop slowly near the critical point, which will aid in suppressing the initial formation of cellular domains. Therefore, it is expected that layers will emerge at least initially during the cooling process; the main question is whether they are destroyed as the system is pushed further into the spinodal regime. To address this question, we first examine the linear stability of layered states for different values of χ but for fixed β.

The stability analysis proceeds by writing the solution to (4.29) as the sum of a layered state plus some small perturbation,

$$\phi(x,z,t) = \bar{\phi}(z) + \alpha\tilde{\phi}(z)e^{\lambda t + ikx}, \tag{4.54a}$$

$$\mu(x,z,t) = \bar{\mu}(z) + \alpha\tilde{\mu}(z)e^{\lambda t + ikx}, \tag{4.54b}$$

where $\alpha \ll 1$. Here, bars correspond to variables associated with the stationary layered state, also called the base state, and tildes are used to represent variables associated with

the perturbation. Moreover, λ and k denote the growth rate and wavenumber of the perturbation, respectively. We will restrict our attention to the case of 50:50 mixtures. The small parameter δ is treated as an $O(1)$ quantity, unless mentioned otherwise.

The solutions of the $O(1)$ problem (in α) define the stationary layered states. It is straightforward to show that the leading-order chemical potential is constant and hence we can write it as $\bar{\mu}(z) \equiv \bar{\mu}$. The associated problem for the order parameter is given by

$$\bar{\mu} = f'(\bar{\phi}) - \delta^2 \partial_z^2 \bar{\phi}, \tag{4.55a}$$

subject to the boundary conditions

$$\delta \partial_z \bar{\phi} = \beta \left(1 - \bar{\phi}^2\right), \quad z = 0, 1. \tag{4.55b}$$

The chemical potential now plays the role of a Lagrange multiplier and it ensures that the order parameter corresponds to a 50:50 mixture. To enforce this condition, the integral constraint

$$\int_0^1 \bar{\phi}(z)\, \mathrm{d}z = 0 \tag{4.55c}$$

is added to the problem.

The linear stability of these layered states can be determined from the $O(\alpha)$ problem, which has bulk equations given by

$$\lambda \tilde{\phi} = (-k^2 + \partial_z^2)\tilde{\phi}, \tag{4.56a}$$

$$\tilde{\mu} = f''(\bar{\phi}(z))\tilde{\phi} - \delta^2 \left(-k^2 + \partial_z^2\right) \tilde{\phi}, \tag{4.56b}$$

and the boundary conditions

$$\delta \tilde{\phi} = -2\beta \bar{\phi}\, \tilde{\phi}, \quad z = 0, 1. \tag{4.56c}$$

The nonlinearity of the $O(1)$ problem and the non-autonomous nature of the $O(\alpha)$ problem, the latter of which is inherited from the function $\bar{\phi} = \bar{\phi}(z)$, make finding useful closed form solutions to both of these particularly difficult. However, as noted by Souche & Clarke [141], the qualitative properties of the layered solutions can be deduced by studying the phase plane that is associated with (4.55). Trajectories in this phase plane are given by the contours of the function $E(u, v) = f(u) - \delta^2 v^2/2 - \mu u$, where $u = \bar{\phi}$ and $v = \partial_z \bar{\phi}$. Admissible trajectories will be those which satisfy the boundary conditions; therefore, they must begin from and end at the curve $v = (\beta/\delta)(1 - u^2)$ after a distance of $z = 1$ has been traversed. If $\bar{\phi}$ is a monotonic function of z, then this distance condition is equivalent to

$$1 = \int_0^1 \mathrm{d}z = \int_{\bar{\phi}(0)}^{\bar{\phi}(1)} \frac{\mathrm{d}z}{\mathrm{d}\bar{\phi}}\, \mathrm{d}\bar{\phi} = \int_{u(0)}^{u(1)} \frac{\mathrm{d}u}{v(u)}. \tag{4.57}$$

Although the phase plane can provide insightful information about the qualitative structure of the layers, it does not aid in the overall goal of determining their stability. Therefore, we do not proceed with it further. Instead, both the stationary problem for layered states and the linear stability problem are solved numerically.

Numerical solutions to the base state problem are shown as stars in Figure 4.10 (d)–(f) for temperatures corresponding to $\chi = 0.01$, 0.18, and 1, respectively, with $\delta = 0.06$ and $\beta = \delta/2$. At the highest temperature, the base state takes on an approximately linear profile which does not show a close resemblance to a layered state. However, as the temperature decreases, a clear bilayer morphology arises. When $\chi = 1$, the two layers are nearly uniform in composition and are separated by a very thin transition region. The corresponding growth rates of perturbations to these solutions are shown in Figure 4.10 (g)–(i). In all cases, the growth rates are negative, indicating the layered states are linearly stable.

The rapid transition in the base state that occurs at $z = 1/2$ when $\chi = 1$ (see Figure 4.10 (f)) motivates looking for an asymptotic approximation to this solution. In fact, both problems for the base state and its stability can be solved using a matched asymptotic expansion in this case. Details of these are given in Section 4.4.1.4 and Section 4.4.3. The leading-order solutions and the growth rate are given by

$$\bar{\phi}(z) = \tanh((z - 1/2)/\delta), \tag{4.58a}$$

$$\tilde{\phi}(z) = \operatorname{sech}^2((z - 1/2)/\delta), \tag{4.58b}$$

$$\lambda(k) = -(2/3)\delta k^3 \tanh(k/2). \tag{4.58c}$$

These solutions are shown as circles in Figures 4.10 (f) and (i), and they show good agreement with the numerical results.

If the temperature of the system is cooled sufficiently slowly so that the system evolves in a quasi-static sense, where at each moment in time the composition is approximately given by the corresponding steady state with a fixed value of $\chi(t)$, then the linear stability results suggest that the layers will persist as the system is pushed further into the spinodal regime. That is, small fluctuations to the layers, which in reality are expected to occur in the form of thermal noise, are unlikely to be amplified and drive the system to a lower-energy configuration.

To examine this in further detail, we now perform numerical solutions with a time-dependent χ. In particular, we will set $\chi(t) = 1 - \exp(-t/\tau_c)$, where $\tau_c \gg 1$ denotes the time scale of the cooling process. Notice that $t = 0$ corresponds to the critical temperature and $\chi \to 1$ as $t \to \infty$. The results of a such a simulation are shown in Figure 4.10 (a)–(c) when the parameters are set to $\delta = 0.06$, $\beta = \delta/2$, and $\tau_c = 100$. The initial condition was chosen to be uniformly distributed random numbers between ± 0.2. The order parameter is

shown at times $t = 1$, 20, and 500, corresponding to $\chi = 0.01$, 0.18, and 1. The strong bias of the walls at early times rapidly extinguishes any small-scale horizontal fluctuations and imprints a layered morphology. As the system is further cooled, the layers become more pronounced until a clear bilayer is formed.

The laterally averaged order parameter $\langle\phi\rangle_l$ has been computed at these three values of χ and is plotted together with corresponding steady states in Figure 4.10 (d)–(f). The system eventually settles into the steady-state profile, after which it evolves in a quasi-static manner until the final temperature of $\chi = 1$ is reached. We remark here that the parameters used in this simulation are the same as those of Figure 4.7, which shows that a laterally separated morphology arises when the temperature is fixed at $\chi = 1$. Thus, the cooling procedure is able to produce a bilayer morphology when a constant temperature would not.

4.4 Bilayer stability and topological transformations

Having established the conditions under which a bilayer can form, we now examine how it responds to both small and large perturbations when the temperature of the system is constant and held at $\chi = 1$. To aid our analysis, we first simplify the governing system of equations by exploiting the fact that the composition of the bilayer is approximately uniform except in a thin transition layer where it changes rapidly. Using this simplified model in combination with numerical simulations of the full system of equations, we then analyse how the system responds to a localised perturbation that brings the bilayer interface into contact with one of the walls.

4.4.1 Sharp-interface asymptotics

The simulations in the previous section showcase how a mixture has the tendency to separate into domains with compositions that are close to the minima of the free energy of mixing when the system is in the spinodal region of the phase diagram. If the non-dimensional parameter δ is small, these domains are separated by thin transition regions that slowly evolve as the domains coarsen. The disparity between length scales suggests that an asymptotic treatment of the large-time problem is possible by assuming the domains are separated by slowly evolving sharp interfaces. Such an analysis was first carried out by Pego [122], who showed that the large-time dynamics can be described by a quasi-steady Stefan problem similar to that seen in solidification problems [53]. In this section, we carry out a similar analysis to Pego and go one step further to derive a thin-film equation that can be used to describe the motion of the bilayer interface.

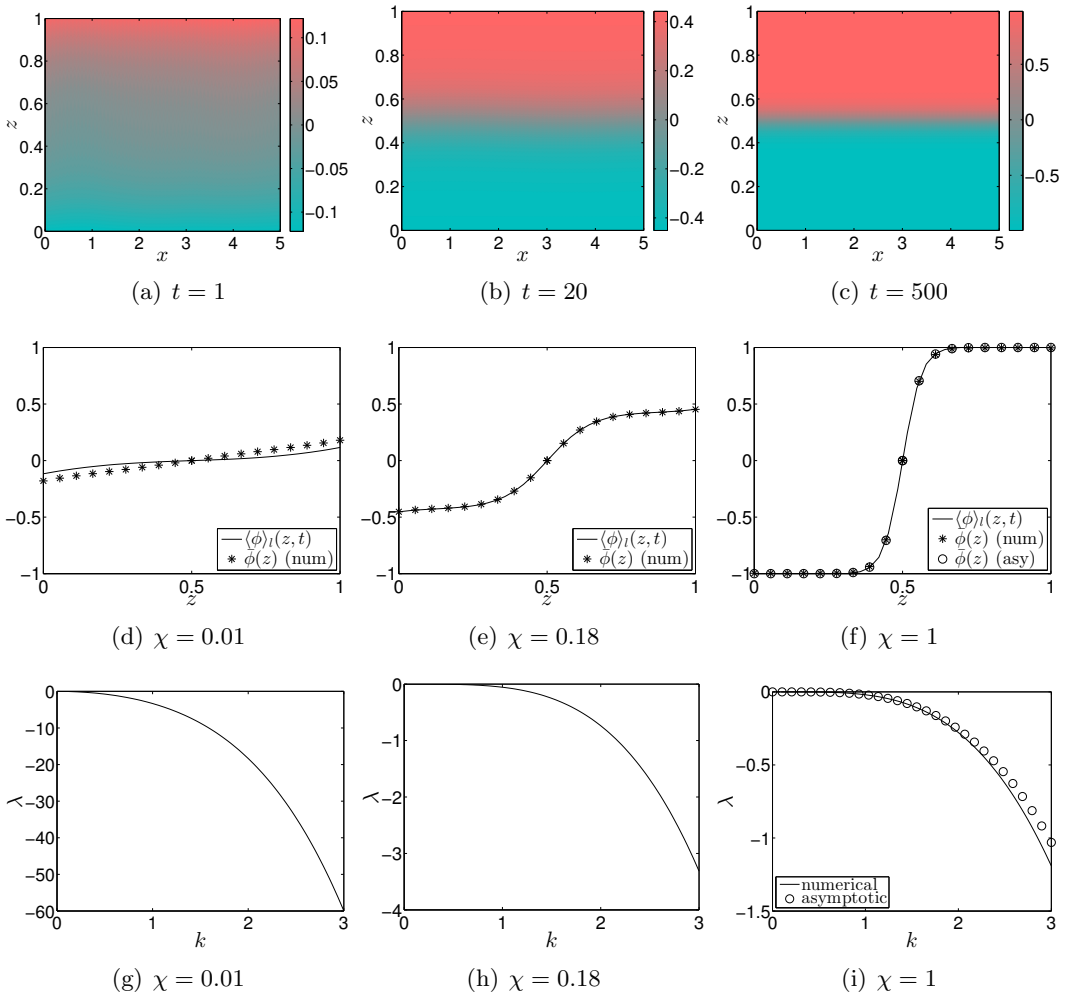


Figure 4.10: Top (a)–(c): A simulation of the phase-field model showing that a bilayer morphology can be induced by slowly cooling the system. In this case, the temperature evolves according to $\chi(t) = 1 - \exp(-t/\tau_c)$, where $\tau_c = 100$. The solution is shown at times $t = 1$, $t = 20$, and $t = 500$, corresponding to $\chi = 0.01$, 0.18, and 1, respectively. Middle (d)–(f): Comparison of the laterally averaged order parameter (line) computed from the numerical solutions shown in (a)–(c) with the instantaneous steady states (stars) associated with each value of χ. Bottom (g)–(i): Growth rate of perturbations to the steady -state profiles shown in (d)–(f). The parameters are $\delta = 0.06$ and $\beta = \delta/2$, which correspond to weakly biased walls.

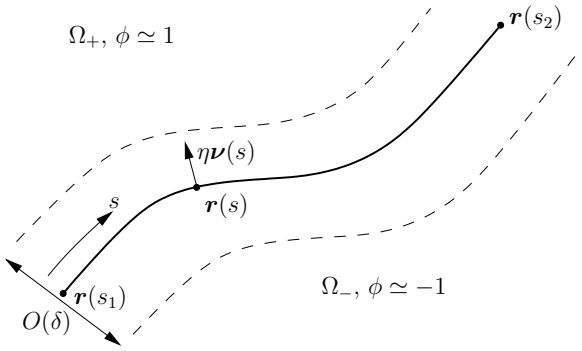


Figure 4.11: Schematic diagram of the sharp-interface model. The domains $\Omega_\pm$ correspond to the outer regions where the composition is approximately constant and given by $\phi \simeq \pm 1$, respectively. These domains are separated by a thin transition region of width $O(\delta)$. The transition region is described by the coordinates s and η, where s is the arclength along the centerline of this region $\boldsymbol{r}(s)$, and the coordinate η lies along the vector that is normal to the centerline, $\boldsymbol{\nu}(s)$. The centerline is precisely defined as the curve where $\phi(\boldsymbol{r}(s)) \equiv 0$.

We begin by assuming that a sufficient amount of time has passed for the mixture to separate into slowly evolving domains with roughly uniform compositions. Therefore, we write (4.29) in terms of the slow time variable $\tau = \delta t$ so that we obtain the system

$$\delta \partial_\tau \phi = \nabla^2 \mu, \tag{4.59a}$$

$$\mu = 2(\phi^3 - \phi) - \delta^2 \nabla^2 \phi, \tag{4.59b}$$

which has boundary conditions

$$\delta \partial_z \phi = \beta \left(1 - \phi^2\right), \tag{4.59c}$$

$$\partial_z \mu = 0, \tag{4.59d}$$

at $z = 0, 1$. The initial condition for ϕ comes from matching to the solution in the $t = O(1)$ time regime. Although we do not compute this solution analytically, numerical simulations indicate that its large-time limit corresponds to domains with compositions given by $\phi \simeq \pm 1$ which are separated by thin transition layers; see Figure 4.7 and Figure 4.8.

We now focus on the dynamics that occur between two adjacent domains with different compositions. These domains are denoted by $\Omega_\pm$ and we assume that they are separated by a thin transition region of width $O(\delta)$; see Figure 4.11. We are interested in approximating this transition region by a smooth curve that represents a sharp interface between the two domains. Asymptotic expansions in the limit $\delta \to 0$ will be used to compute inner and outer solutions that are valid within and away from the transition region, respectively. By matching these two solutions, effective boundary conditions can be derived for the outer problem which describe the evolution of the sharp interface.

4.4.1.1 The outer problem

The formulation of the outer problem begins by expanding the order parameter and the chemical potential as asymptotic series of the form

$$\phi(x,z,\tau) = \phi_0(x,z,\tau) + \delta\phi_1(x,z,\tau) + O(\delta^2), \tag{4.60a}$$

$$\mu(x,z,\tau) = \mu_0(x,z,\tau) + \delta\mu_1(x,z,\tau) + O(\delta^2). \tag{4.60b}$$

By matching to the solution in the previous time regime, we find that $\phi_0 \sim \pm 1$ as $\tau \sim 0$. The expansions in (4.60) are inserted into (4.59) and a sequence of subproblems are formed by collecting powers of δ. The bulk equations of the leading-order problem are given by

$$\nabla^2\mu_0 = 0, \tag{4.61a}$$

$$\mu_0 = 2(\phi_0^3 - \phi_0). \tag{4.61b}$$

If the outer region comes into contact with the wall, the boundary conditions $\phi_0^2 = 1$ and $\partial_z\mu_0 = 0$ are imposed there.

The solution to this problem is given by the initial condition so that $\phi_0(x,z,\tau) \equiv \pm 1$ together with $\mu_0 \equiv 0$. In physical terms, this solution corresponds to domains of constant composition. We assume that $\phi_0 = \pm 1$ in the domain $\Omega_\pm$.

The $O(\delta)$ problem for the chemical potential is given by

$$\nabla^2\mu_1 = 0, \tag{4.62}$$

which holds in both of the domains $\Omega_\pm$. If the outer region comes in contact with a wall, the boundary conditions there read $\partial_z\mu_1 = 0$. The two missing boundary conditions for μ_1, which hold at the sharp interface separating $\Omega_\pm$, come from matching to the inner solution.

4.4.1.2 The inner problem

In order to formulate the inner problem, we first need to establish a suitable coordinate system in the transition region. This is done by fitting a coordinate system to the centerline of this region, given by $\boldsymbol{r}(s,\tau)$, where $s_1 < s < s_2$ represents arclength. The centerline can be precisely defined as the curve for which $\phi(\boldsymbol{r}(s,\tau),\tau) \equiv 0$ and it can be written in component form as $\boldsymbol{r}(s,\tau) = r_1(s,\tau)\boldsymbol{e}_x + r_2(s,\tau)\boldsymbol{e}_z$, where $\boldsymbol{e}_x$ and $\boldsymbol{e}_z$ denote the Cartesian unit vectors. Furthermore, due to the use of an arclength parameterisation, the relation $(\partial_s r_1)^2 + (\partial_s r_2)^2 \equiv 1$ always holds. The vector that is normal to the centerline is written as $\boldsymbol{\nu}(s,\tau) = -\partial_s r_2(s,\tau)\boldsymbol{e}_x + \partial_s r_1(s,\tau)\boldsymbol{e}_z$. The quantity $\eta\boldsymbol{\nu}(s,\tau)$ represents taking a step of length η off the centerline in a direction normal to the curve. Using the variables s and

η, we can define a new curve-fitted coordinate system describing the inner region as small steps taken off the centerline in the normal direction. The associated change of variable is

$$\boldsymbol{x}(s,\tau') = \boldsymbol{r}(s,\tau') + \delta\eta\boldsymbol{\nu}(s,\tau'), \tag{4.63a}$$

$$\tau = \tau', \tag{4.63b}$$

where $\boldsymbol{x} = x\boldsymbol{e}_x + z\boldsymbol{e}_z$. We assume that $\eta \to \pm\infty$ corresponds to entering the domains $\Omega_\pm$ respectively, which is shown schematically in Figure 4.11. The additional details of this coordinate transformation, including the relationship between derivatives, can be found in Appendix C.3.

We drop the prime on τ' and write the order parameter and the chemical potential in the inner region as $\Phi = \Phi(s,\eta,\tau)$ and $M(s,\eta,\tau)$, respectively. The solution is written as an asymptotic expansion of the form

$$\Phi(s,\eta,\tau) = \Phi_0(s,\eta,\tau) + \delta\Phi_1(s,\eta,\eta) + \delta^2\Phi_2(s,\eta,\tau) + O(\delta^3), \tag{4.64a}$$

$$M(s,\eta,\tau) = M_0(s,\eta,\tau) + \delta M_1(s,\eta,\tau) + \delta^2 M_2(s,\eta,\tau) + O(\delta^3), \tag{4.64b}$$

and these expressions are inserted into the governing equations, which are then expanded in powers of δ. The $O(1)$ problem reads

$$\partial_\eta^2 M_0 = 0, \tag{4.65a}$$

$$M_0 = 2(\Phi_0^3 - \Phi_0) - \partial_\eta^2\Phi_0, \tag{4.65b}$$

and the leading-order matching conditions are $M_0 \to 0$ and $\Phi_0 \to \pm 1$ as $\eta \to \pm\infty$. The translational invariance of this problem is fixed by the condition defining the centerline, *i.e.*, $\Phi_0 = 0$ at $\eta = 0$. The solution to this problem is given by

$$\Phi_0(\eta) = \tanh\eta, \tag{4.66a}$$

$$M_0(\eta) \equiv 0, \tag{4.66b}$$

and it describes how the domains are connected through the transition region.

We now proceed to the higher-order inner problems in order to obtain boundary conditions for the $O(\delta)$ outer problem for the chemical potential. The $O(\delta)$ inner problem is given by

$$\partial_\eta^2 M_1 - \kappa\partial_\eta M_0 = 0, \tag{4.67a}$$

$$M_1 = (6\Phi_0^2 - 2)\Phi_1 - \partial_\eta^2\Phi_1 + \kappa\partial_\eta\Phi_0, \tag{4.67b}$$

where $\kappa = (\partial_s r_1)(\partial_s^2 r_2) - (\partial_s r_2)(\partial_s^2 r_1)$ denotes the curvature of the interface. The relevant matching condition for M_1 is

$$M_1(s,\eta,\tau) = \mu_1(\boldsymbol{r}(s,\tau),\tau) + \eta[\nabla\mu_0\cdot\boldsymbol{\nu}]_{\boldsymbol{x}=\boldsymbol{r}}. \tag{4.68}$$

as $\eta \to \pm\infty$. Since $\mu_0 \equiv 0$, we can conclude that the solution for M_1 does not depend on η; that is, $M_1 = M_1(s, \tau)$. By multiplying (4.67b) by $\partial_\eta \Phi_0$ and integrating over all η, we can fully specify the function M_1 in terms of the geometry of the interface; in particular,

$$2M_1 = \sigma\kappa, \tag{4.69}$$

where σ represents the surface energy and is given by

$$\sigma = \int_{-\infty}^{\infty} (\partial_\eta \Phi_0)^2 \, \mathrm{d}\eta = \frac{4}{3}. \tag{4.70}$$

By making use of the matching condition in (4.68), we obtain

$$2\mu_1 = \sigma\kappa \tag{4.71}$$

at $\boldsymbol{x} = \boldsymbol{r}$. Note that this condition also implies that the correction to the chemical potential is continuous across the interface.

The $O(\delta^2)$ part of (4.59a) is given by

$$-v_n \partial_\eta \Phi_0 = \partial_\eta^2 M_2 - \kappa \partial_\eta M_1 + (\partial_s^2 - \kappa^2 \eta \partial_\eta) M_0, \tag{4.72}$$

where $v_n = (\partial_\tau \boldsymbol{r}) \cdot \boldsymbol{\nu}$ denotes the normal component of the interface velocity. This equation can be integrated to obtain

$$-2v_n = [\partial_\eta M_2]_{-\infty}^{+\infty}. \tag{4.73}$$

The appropriate matching condition for the derivative is given by

$$\boldsymbol{\nu} \partial_\eta M_2 + (\partial_s \boldsymbol{r})(\partial_s M_1) + \kappa\eta(\partial_s \boldsymbol{r})(\partial_s M_0) = \eta(\mathbf{H}\mu_0)\boldsymbol{\nu} + \nabla\mu_1 \tag{4.74}$$

as $\eta \to \pm\infty$, where $\mathbf{H}$ denotes the Hessian operator. By taking the inner product of this equation with the normal vector $\boldsymbol{\nu}$, noting that $\partial_s \boldsymbol{r}$ is the tangent vector and using $\mu_0 \equiv 0$, we obtain

$$\partial_\eta M_2 = \nabla\mu_1 \cdot \boldsymbol{\nu}. \tag{4.75}$$

Therefore, (4.73) can be written as

$$v_n = \frac{1}{2}[-\nabla\mu_1 \cdot \boldsymbol{\nu}]_-^+, \tag{4.76}$$

where $[\cdot]_-^+$ denotes the jump across the interface. The boundary conditions (4.71) and (4.76) are sufficient to close the $O(\delta)$ outer problem.

In the solution of the inner problem we have implicitly assumed that the transition region does not come into contact with the walls. In the stationary version of the problem, the results of Modica [106] indicate that the sharp interface forms an angle given by $\theta = \cos^{-1}(\hat{\beta})$ with the walls. However, it is unclear what the dynamic boundary conditions are at the contact line and determining these is an area of future work.

4.4.1.3 Approximation of the free energy

To understand which physical processes govern the evolution of the sharp-interface model, we examine the expression for the free energy of the system. To simplify the discussion slightly, we neglect the surface energy contributions due to the walls. In this case, the free energy associated with the governing system of equations (4.59) can be written as

$$F = \int_{\Omega} \left[f(\phi) + \frac{1}{2}\delta^2 |\nabla \phi|^2 \right] \mathrm{d}x\mathrm{d}z, \tag{4.77}$$

where Ω denotes the spatial domain and the function f is given by

$$f(\phi) = \frac{1}{2}\left(\phi^2 - 1\right)^2. \tag{4.78}$$

The contribution to the free energy from the outer region can be estimated by inserting the outer solution into the integrand and then expanding about small δ. Using the fact that $f(\phi_0) = f'(\phi_0) \equiv 0$, we find

$$f(\phi) + \frac{1}{2}\delta^2 |\nabla \phi|^2 = O(\delta^2), \tag{4.79}$$

which suggests the outer region only contributes $O(\delta^2)$ amounts to F. On the other hand, the free energy in the inner region can be written as

$$F = \delta \int_{s_1}^{s_2} \int_{-\infty}^{\infty} \left[f(\Phi_0) + \frac{1}{2}(\partial_\eta \Phi_0)^2 \right] \mathrm{d}\eta\mathrm{d}s + O(\delta^2), \tag{4.80}$$

which dominates the contribution from the outer region. This expression can be written in a physically enlightening form by making use of the fact that Φ_0 satisfies the equation $f'(\Phi_0) = \partial_\eta^2 \Phi_0$ (see (4.65b)), from which it follows that $f(\Phi_0) = (1/2)(\partial_\eta \Phi_0)^2$. Therefore, (4.80) can be written as

$$F = \delta \int_{s_1}^{s_2} \int_{-\infty}^{\infty} (\partial_\eta \Phi_0)^2 \, \mathrm{d}\eta\mathrm{d}s + O(\delta^2). \tag{4.81}$$

Using the definition of the surface energy (4.70), it follows that the leading-order contribution to the free energy is given by

$$F = \delta\sigma(s_2 - s_1). \tag{4.82}$$

In physical terms, this expression is equivalent to saying that the free energy is the product of surface energy and interface length. Therefore, the free energy in the sharp-interface limit is simply equal to the total energy of all of the interfaces. Moreover, since the free energy decreases with time, we can conclude that the sharp-interface model (in the absence of wall interactions) is driven by interface minimisation.

4.4.1.4 Summary of sharp-interface model

The leading-order composite solution to (4.59) can be written as

$$\phi_0(\boldsymbol{x},\tau) = \tanh\left(\frac{[\boldsymbol{x}-\boldsymbol{r}(\tau)]\cdot\boldsymbol{\nu}(\tau)}{\delta}\right), \tag{4.83a}$$

$$\mu_0(\boldsymbol{x},\tau) \equiv 0. \tag{4.83b}$$

The solution ϕ_0 describes how the mixture concentration smoothly changes from one domain to the other. The transition region between these domains is approximated by the sharp interface $\boldsymbol{r}(\tau)$ and its evolution is obtained by solving the $O(\delta)$ outer problem, which reads

$$\nabla^2\mu_1 = 0 \tag{4.84a}$$

with boundary conditions

$$\partial_z\mu_1 = 0 \tag{4.84b}$$

along the walls at $z = 0, 1$ and

$$2\mu_1 = \sigma\kappa, \tag{4.84c}$$

$$v_n = \frac{1}{2}\left[-\nabla\mu_1\cdot\boldsymbol{\nu}\right]_-^+, \tag{4.84d}$$

on the interface $\boldsymbol{x} = \boldsymbol{r}(\tau)$.

4.4.1.5 Reformulation of the sharp-interface model

We now consider the case when the interface can be written as a function of the horizontal coordinate x. In particular, we let the function $h(x,\tau)$ represent the vertical position of the sharp interface at the point x. The bulk equations for the chemical potential are given by

$$\nabla^2\mu_1 = 0 \tag{4.85a}$$

which hold in the regions $0 < z < h(x,\tau)$ and $h(x,\tau) < z < 1$. The boundary conditions at the walls remain unchanged,

$$\partial_z\mu_1 = 0, \tag{4.85b}$$

at $z = 0, 1$. The corresponding boundary conditions at the interface, (4.84c) and (4.84d), become

$$2\mu_1 = \frac{\sigma\partial_x^2 h}{(1+(\partial_x h)^2)^{3/2}}, \tag{4.85c}$$

$$\partial_\tau h = \frac{1}{2}\left([\partial_x\mu_1]_-^+\partial_x h - [\partial_z\mu_1]_-^+\right), \tag{4.85d}$$

on $z = h(x, \tau)$. By integrating (4.85a) with respect to z and applying the boundary conditions (4.85b) and (4.85d), an evolution equation for the interface emerges, namely

$$\partial_\tau h + \partial_x q = 0, \tag{4.85e}$$

where the flux q is given by

$$q = \frac{1}{2}\int_0^1 \partial_x \mu_1 \, \mathrm{d}z. \tag{4.85f}$$

If the sharp interface comes into contact with the bottom wall, we assume that the equilibrium contact angle condition holds at the contact point $x = s(\tau)$; that is, we set

$$\partial_x h = \tan\theta, \tag{4.86}$$

where $\theta = \cos^{-1}(\hat{\beta})$. Moreover, we also impose

$$h(s(\tau), \tau) = 0, \quad q(s(\tau), \tau) = 0, \tag{4.87}$$

the first of which defines the contact point, and the second of which represents conservation of mass at this point. Analogous conditions can be derived in the case when there is a contact point on the top wall.

4.4.2 Reduction to a thin-film problem

If there is a separation between the horizontal and vertical length scales, which can arise, for example, if the contact angle is small, then the sharp-interface model given by (4.85)–(4.87) can be further simplified. We assume that the solution varies slowly on the horizontal length scale; thus, we let $x = \epsilon^{-1}\bar{x}$, where $\epsilon \ll 1$. Through a process of balancing terms, we can obtain scales for time and the chemical potential. In particular, we let $\tau = \epsilon^{-4}\bar{\tau}$ and $\mu_1 = \epsilon^2\bar{\mu}$. With this scaling, the sharp-interface model in (4.85) becomes

$$\left(\epsilon^2\partial_{\bar{x}}^2 + \partial_z^2\right)\bar{\mu} = 0 \tag{4.88a}$$

in $0 < z < h(\bar{x}, \bar{\tau})$ and $h(\bar{x}, \bar{\tau}) < z < 1$, with boundary conditions

$$\partial_z \bar{\mu} = 0, \tag{4.88b}$$

at $z = 0, 1$, and

$$2\bar{\mu} = \frac{\sigma\partial_{\bar{x}}^2 h}{(1 + \epsilon^2(\partial_{\bar{x}} h)^2)^{3/2}}, \tag{4.88c}$$

$$\epsilon^2\partial_{\bar{\tau}} h = \frac{1}{2}\left(\epsilon^2[\partial_{\bar{x}}\bar{\mu}]_-^+\partial_{\bar{x}} h - [\partial_z\bar{\mu}]_-^+\right), \tag{4.88d}$$

at $z = h(\bar{x}, \bar{\tau})$. The evolution equation for the interface reads

$$\partial_{\bar{\tau}} h + \partial_{\bar{x}} \bar{q} = 0, \quad \bar{q} = \frac{1}{2} \int_0^1 \partial_{\bar{x}} \bar{\mu} \, \mathrm{d}z. \tag{4.88e}$$

The leading-order problem can be obtained by taking the limit $\epsilon \to 0$ in (4.88). We find that the corresponding solution for the rescaled chemical potential is $\bar{\mu} = (\sigma/2)\partial_{\bar{x}}^2 h$. This can be inserted into (4.88e) to yield the thin-film equation

$$\partial_{\bar{\tau}} h + \frac{\sigma}{4} \partial_{\bar{x}}^4 h = 0. \tag{4.89}$$

The corresponding flux is $\bar{q} = (\sigma/4)\partial_{\bar{x}}^3 h$. In the case when the contact angle is small, we let $\epsilon = \theta$, in which case the leading-order boundary conditions at the scaled contact point $\bar{x} = \bar{s}(\bar{\tau})$ are given by

$$h = 0, \quad \partial_{\bar{x}} h = 1, \quad \bar{q} = 0. \tag{4.90}$$

4.4.3 Linear stability of a bilayer

Using the sharp-interface model (4.85), it is straightforward to compute the linear stability of a bilayer with a thin transition region. We suppose the bilayer interface is located at $z = 1/2$. This corresponds to setting $h(x, \tau) \equiv 1/2$ in the system (4.85), from which it trivially follows that $\mu_1 \equiv 0$. We then linearise the system (4.85) about this state by writing

$$\hat{\mu}_1(x, z, \tau) = \tilde{\mu}(z) e^{\lambda\tau + ikx} \tag{4.91}$$

$$h(x, \tau) = 1/2 + \tilde{h} e^{\lambda\tau + ikx}, \tag{4.92}$$

where $|\tilde{\mu}| \ll 1$, $|\tilde{h}| \ll 1$, and λ and k denote the growth rate and wavenumber of perturbations to the bilayer. The governing equation for $\tilde{\mu}$ is

$$(-k^2 + \partial_z^2)\tilde{\mu} = 0, \tag{4.93a}$$

which holds in the regions $0 < z < 1/2$ and $1/2 < z < 1$. The usual no-flux conditions apply at the walls, namely

$$\partial_z \tilde{\mu} = 0 \tag{4.93b}$$

at $z = 0, 1$. The conditions at the linearised position of the bilayer interface are

$$2\tilde{\mu} = -\sigma k^2 \tilde{h}, \tag{4.93c}$$

$$\lambda \tilde{h} = -\frac{1}{2}[\partial_z \tilde{\mu}]_-^+, \tag{4.93d}$$

which hold at $z = 1/2$.

The solution for the chemical potential can be written as

$$\tilde{\mu}(z) = \begin{cases} A\cosh(kz), & 0 < z < 1/2, \\ A\cosh(k(z-1)), & 1/2 < z < 1, \end{cases} \tag{4.94}$$

where A is a constant of integration. By inserting this solution into the boundary conditions (4.93c), we find that $A = -(\sigma/2)k^2\mathrm{sech}(k/2)\tilde{h}$. This can be used in (4.93d) to deduce that the perturbation growth rate is

$$\lambda = -\frac{\sigma}{2}\, k^3 \tanh(k/2). \tag{4.95}$$

Inserting $\sigma = 4/3$ (see (4.70)) into this result yields the expression for the growth rate that is presented in (4.58c) once the difference in time scales is taken into account. Since $\lambda < 0$, the bilayer is linearly stable to small perturbations. When $k \ll 1$, we find that $\lambda \simeq -(\sigma/4)k^4$, and this agrees with the growth rate that would be obtained by performing an analogous linear stability analysis of the thin-film equation (4.89).

4.4.4 Dynamics of a punctured bilayer

The energy estimate given in (4.82) states that the lowest-energy configuration will be that which has a minimal A-B interface when the energetic contributions from the walls are neglected. This means that the bilayer, with its large interface, is not expected to be the global energetic minimum of the system. For a mixture with 50:50 composition ratio, the global minimum instead corresponds to laterally separated configuration with a column of A beside a column B. When energetic contributions from the walls are considered, the two-column configuration can still be energetically favourable compared with the bilayer if having shorter A-B interfaces can offset the energy penalty of having non-preferred materials near the walls. Since the bilayer is not the configuration that leads to a global energetic minimum, it is a metastable state; thus, a perturbation of sufficient magnitude will lead to its breakup. This does not contradict the linear stability results of the previous section, as the infinitesimal perturbations considered there are too small to kick the system out of the energy well where the bilayer state is the local energetic minimum.

We now study how the bilayer responds to a large, but local, perturbation that brings its interface in contact with one of the walls. This effectively creates a hole in one of the layers that is filled with material from its counterpart. Furthermore, this introduces a pair of contact lines that may come together to restore the bilayer, or spread apart to widen the hole.

We first use the phase-field model (4.29) to study the dynamics of a punctured bilayer when there are no energetic contributions from the walls. That is, we set $\beta = 0$ which

is equivalent to the equilibrium contact angle being equal to 90°. The initial condition for the order parameter is constructed using a two-step process. First, a sharp-interface representation of the punctured bilayer interface is defined. When the contact angle is 90°, this is given by

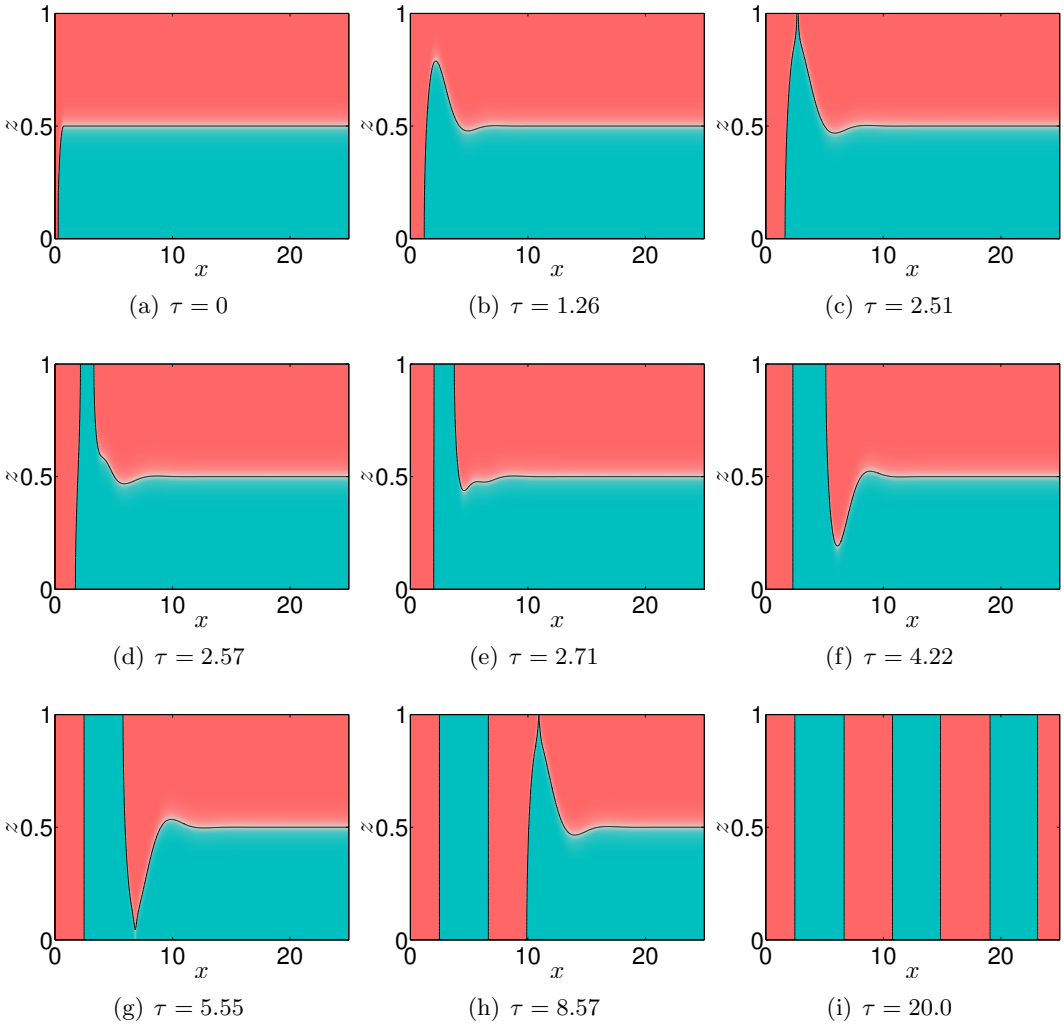
$$h_i(x) = \begin{cases} \sqrt{h_\infty^2 - (x - s_0 - h_\infty)^2}, & s_0 < x < s_0 + h_\infty, \\ h_\infty, & x > s_0 + h_\infty, \end{cases} \tag{4.96}$$

where s_0 denotes the initial location of the contact point and $h_\infty < 1$ is the far-field height of the bilayer interface. The interface profile h_i is assumed to be symmetric about $x = 0$. Using this profile, we then construct the initial condition for ϕ using the leading-order composite solution to the sharp-interface model (4.83a).

The results of a numerical simulation of (4.29), using (4.96) as the initial condition with $h_\infty = 1/2$, $s_0 = 1/5$, $\delta = 0.06$, and $\beta = 0$ ($\theta = 90°$), are shown in Figure 4.12. The initial condition is shown in panel (a), where red denotes material A and blue denotes material B. The solid line represents the hypothetical sharp interface that separates the two layers. We see that the contact line retracts to widen the hole and the displaced mass creates a growing ridge of material B (panel (b)). Eventually, this ridge grows so large that it comes into contact with the upper wall (panel (c)) and two new contact lines are created. The new hole rapidly opens, thus dividing the top A layer into two physically separated domains; see panels (d)–(e). The left domain becomes a perfect rectangular column owing to the equilibrium contact angle being 90°. The rightwards motion of the rightmost contact line creates a dip of material A that grows in size (panel (f)) until it hits the bottom wall (panel (g)). This again creates two new contact lines and the process repeats itself (panel (h)) until the bilayer has been completely transformed into columns (panel (i)).

After the first couple of topological transformations, the system settles into a self-similar evolution where the interface profiles are essentially just translations and reflections of a "master" set of profiles. This means that the widths of the columns converge to a fixed value. A theoretical prediction for this width based on geometric arguments is given in Hennessy *et al.* [72], who find that the width should be 4.4 when the contact angle is 90°. We compare this value to the widths of the first five columns (from left to right) in the simulation, which are are 2.4, 4.2, 4.1, 4.1, and 4.2. The last two columns are not included because they are influenced by the finite geometry of the simulation. The first two widths are strongly affected by the form of the initial condition. The second to fifth widths are in good agreement with the theoretical prediction and the improvement that occurs from the third to fifth width is attributed to the decreasing influence of the initial condition.

The evolution of the non-dimensional free energy defined in (4.77) with $\Omega = \{(x, z) : 0 < x < 25,\ 0 < z < 1\}$ is shown in Figure 4.13. As expected, the free energy monotonically



(a) $\tau = 0$ (b) $\tau = 1.26$ (c) $\tau = 2.51$

(d) $\tau = 2.57$ (e) $\tau = 2.71$ (f) $\tau = 4.22$

(g) $\tau = 5.55$ (h) $\tau = 8.57$ (i) $\tau = 20.0$

Figure 4.12: Dynamics of a punctured bilayer when the walls are not biased. In this case, the equilibrium contact angle is $\theta = 90°$ ($\beta = 0$). The motion of the initial contact line displaces material B (blue) and forms a growing ridge (b) that eventually hits the top wall (c). This creates a hole in the upper layer of material A (red) which rapidly opens (d)–(e). The rightmost of the newly created contact lines moves further to the right, displacing material A and creating a dip (f) that grows until it hits the bottom wall (g). The process repeats itself (h) until the bilayer is transformed into a sequence of columns (i). The other parameter values are $\delta = 0.06$ and $\chi = 1$. The figure is assumed to be symmetric about $x = 0$. The black line corresponds to the $\phi = 0$ contour.

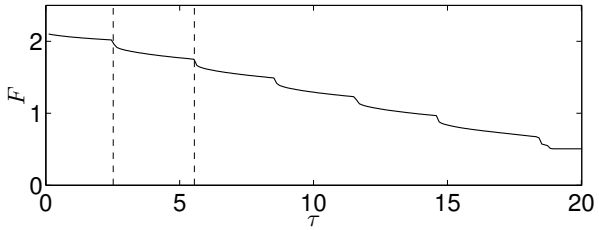


Figure 4.13: Evolution of the rescaled free energy (4.77) during the sequence of topological transformations shown in Figure 4.12. The dashed lines correspond to the times shown in panels (c) and (g) in this figure. Each sharp change in the free energy marks the creation of new contact lines and the rapid opening of the associated hole.

decreases. The rapid changes in F that periodically occur mark the creation of new contact lines and the topological transformations. The final energy of the system is given by $F = 0.506$, which is in exact agreement (to three decimal places) with the estimate using the sharp-interface approximation (4.82).

The same self-sustaining cascade of topological transformations occurs when the bias of the walls is non-zero and the contact angle is less than 90°. In this case, however, the laterally separated domains that emerge are trapezoidal instead of rectangular due to the contact angle condition and our choice of anti-symmetric walls. Furthermore, the trapezoids are always oriented so that their largest horizontal edge is in contact with the preferred wall. These features are illustrated in Figure 4.14, which shows the final morphology obtained from a numerical simulation of the phase-field model when a hole is introduced into a bilayer and the equilibrium contact angle is set to 50°. Due to the aspect ratio of Figure 4.14, the contact angles appear to be greater that 50°. However, numerical calculations of the contact angles from the phase-field simulation confirm they are, indeed, equal to 50°. For contact angles less than 90°, an appropriate sharp-interface representation of the initial punctured layer is

$$h_i(x) = \begin{cases} \tan\theta(x - s_0) - \dfrac{1}{4h_\infty}\tan^2\theta(x - s_0)^2, & s_0 < x < s_0 + 2h_\infty/\tan\theta, \\ h_\infty, & x > s_0 + 2h_\infty/\tan\theta. \end{cases} \tag{4.97}$$

The other parameters used in the simulation are taken to be $h_\infty = 1/2$, $s_0 = 1/5$, and $\delta = 0.1$.

The conditions that are required for a single hole in the bilayer to initiate the self-sustaining sequence of topological transformations are formulated in Hennessy *et al.* [72] using fairly general energy arguments. In summary, the cascade of transformations will happen so long as the walls are partially wetting, that is, if $0 < \theta \leq \pi/2$. In terms the parameter β in this model, these inequalities imply $0 \leq \beta < 1$ when $\chi = 1$. If the walls are perfectly wetting, *i.e.*, $\theta = 0$ or $\beta \geq 1$, then any hole in the bilayer will close up. This is

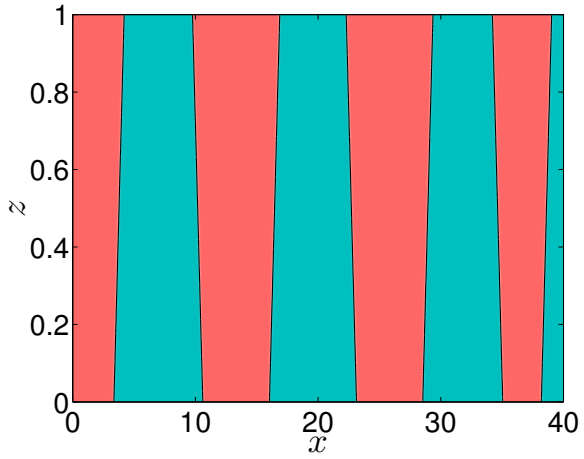


Figure 4.14: When the walls are biased ($\beta \neq 0$), introducing a hole in the bilayer results in a sequence of topological transformations that is similar to that shown in Figure 4.12. As shown here, however, the columns that emerge are now trapezoidal instead of rectangular because the equilibrium contact angle is less than 90°. The trapezoids are always oriented so the long horizontal edge is in contact with the preferred wall. The irregularities in the widths of the last two columns are due to the finite length of the computational domain. Parameter values are $\beta = 0.64$, corresponding to $\theta = 50°$, and $\delta = 0.1$. The solution is shown at time $\tau = 107$. Red and blue corresponds to material A and B, respectively. The black line denotes the $\phi = 0$ contour.

also found to happen if the initial hole is too thin. Generally, the width of the hole has to be greater than the thickness of the diffuse interface, $O(\delta)$, otherwise the layers on either side of the hole are not fully separated.

If an equilibrium contact angle of 50° is considered small, then we can compare the topological transitions that are computed using the phase-field model (4.29) and the thin-film equation (4.89). A numerical simulation of the thin-film equation and a detailed comparison with the phase-field model is given in Hennessy *et al.* [73], so we only summarise the key results here. The geometric aspects of the two models, which are characterised by the widths of the columns, are in good agreement. The relative difference between the width of the second column is roughly 12% and for subsequent columns it is less than 10%. However, there are significant discrepancies between the times at which new contact lines are created.

To further investigate the source of these errors, the first topological transformation has been computed using both the phase-field and thin-film model when the contact angle is 20°. The reduction in the contact angle is used to minimise errors that might arise due to the phase-field model being outside of the thin-film limit. To simulate the thin-film equation (4.89), the spatial domain is truncated at $x = L$ and transformed to the unit interval via the change of variable $\zeta = (x - s(t))/(L - s(t))$, where s is the position of the contact line. Implicit time stepping is used and spatial derivatives are computed with Chebyshev spectral methods. A comparison of the interface profiles obtained using the two models is

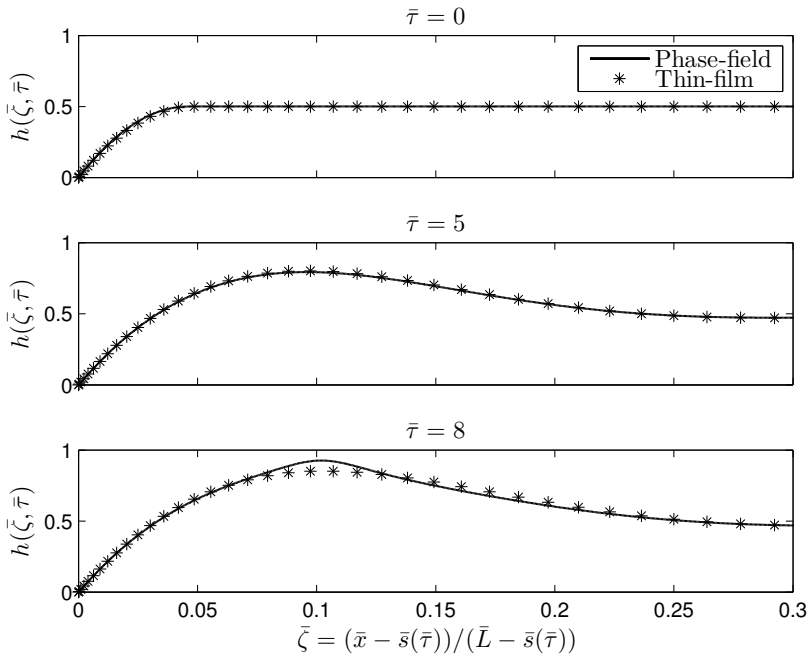


Figure 4.15: Comparison of the perturbed bilayer interface computed using the phase-field model (line) and the thin-film equation (stars) when the equilibrium contact angle is 20° and $\delta = 0.1$. The agreement between the two models is excellent before the system is close to a topological transformation (a)–(b). However, the two models begin to differ significantly when the ridge gets within an $O(\delta)$ distance from the upper wall (c). The source of this discrepancy is a "suction" effect in the phase-field model that is not present in the thin-film equation. This causes the bilayer interface to be rapidly pulled towards the upper wall in the phase-field model, thus accelerating the topological transformation. Here, $\bar{x} = \theta x$, $\bar{s} = \theta s$, $\bar{L} = \theta L$, and $\bar{\tau} = \theta^4 \tau$.

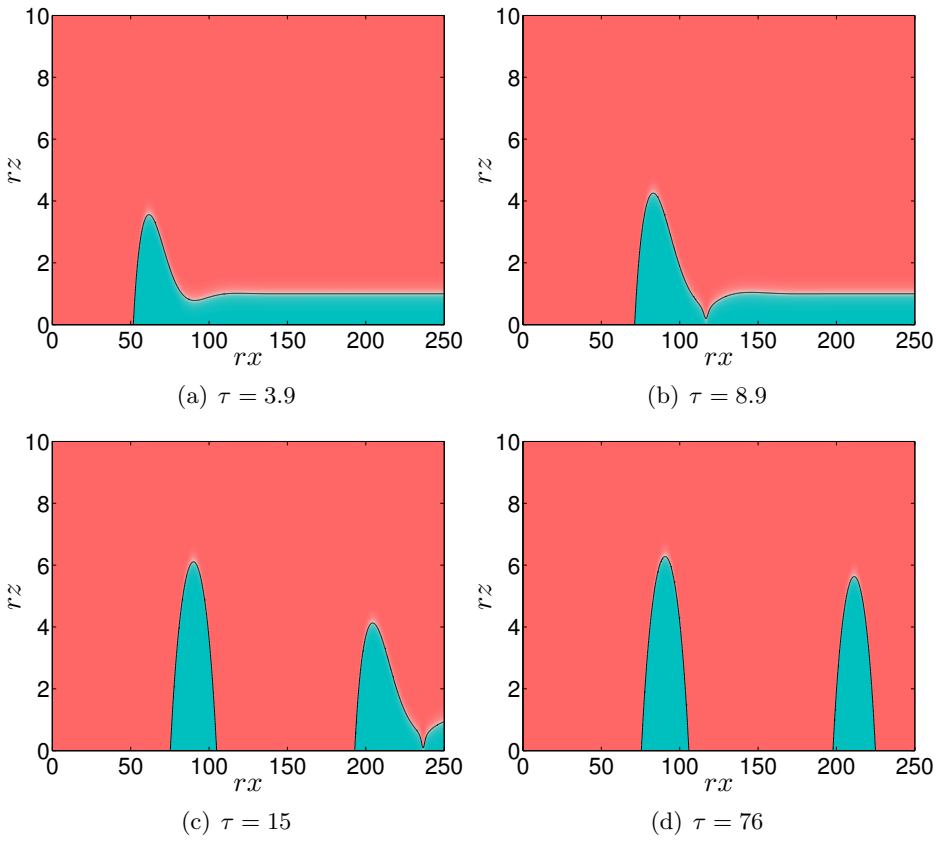
shown in Figure 4.15; a value of $\delta = 0.1$ is used in the phase-field model. For early times, *i.e.,* before the ridge is close to the upper wall, the agreement between the two models is excellent. However, a clear difference in the bilayer profiles begins to emerge for later times, as shown in the bottom panel when $\bar{\tau} = 8$. The source of the discrepancy seems to be a "suction" effect in the phase-field model that occurs when the distance between the ridge and the upper wall is of size $O(\delta)$. This suction force rapidly pulls the ridge towards the upper wall, making the topological transition occur much sooner in the phase-field model than in the thin-film model where this effect is absent. The reason the suction effect is not present in the thin-film model is due to our underlying assumption that the inner region of the sharp-interface problem is always far away from the walls.

The analysis so far has focused on the case of 50:50 mixtures and bilayers that are made from two layers of equal thickness. This does not always have to be the case, however, so we now use the phase-field model to explore how a punctured bilayer with an unequal composition ratio evolves in time. In particular, we assume that the height ratio of the upper layer to the lower layer, as measured from the substrate at $z = 0$, is $r : 1$. This

corresponds to a composition ratio, or equivalently a layer thickness ratio, of $(r-1):1$. We focus on the case of $r > 2$ so the upper layer is thicker than the bottom; note that the bilayers considered previously had $r = 2$. The results of a numerical simulation of the phase-field model (4.29), with $r = 10$, $\delta = 0.03$, and $\theta = \pi/4$, are shown in Figure 4.16. The spatial variables have been multiplied by r so that the height of the undisturbed lower layer is equal to unity and the aspect ratio of the figure is maintained. The system evolves in the usual fashion initially; the hole opens and leads to a growing ridge (panel (a)). However, for this thickness ratio the dip in front of the ridge comes into contact with the bottom wall before the ridge hits the upper wall (panel (b)). This causes the ridge to detach from the retracting layer and the shedded material subsequently develops into the shape of a spherical cap (panel (c)). The main layer continues to retract and the process continues, leading to an array of droplets embedded within the majority phase (panel (d)). The height of the ridge relative to the height of the undisturbed lower layer is approximately 4.3 when it detaches from the main layer. This means that for ratios with $r > 4.3$, the ridge detaches instead of coming into contact with the upper wall. The formation of columns may still be possible for such ratios, however, as the droplets that form from the shedded material grow taller than the ridges are when they detach. This is clearly seen in panels (b)–(d). In this simulation, the steady-state height of the first droplet relative to the initial thickness of the lower layer is roughly 6.3. Therefore, it is conceivable that for ratios with $4.3 < r < 6.3$, the droplets will come into contact with the upper wall. This will ultimately produce a laterally separated columnar morphology, but now this develops through the intermediate processes of ridge detachment and droplet motion.

The topological transformation in bilayers with unequal composition has been studied using the thin-film equation by Hennessy *et al.* [73]. They find that the ridge detaches from the main layer for thickness ratios that satisfy $r > 7.91$ as opposed to $r > 4.3$. The source of this discrepancy is again the suction effect that occurs in the phase-field model. This is clearly shown in Figure 4.16 (b); notice the dip appears to be pinched off at the lower wall. The rapid detachment of the ridge in the phase-field model means that its growth is stunted compared to in the thin-film model. Therefore, the upper layer does not need to be as thick for the ridge to detach before it comes into contact with the upper wall.

There are some quantitative similarities between the phase-field and thin-film models, however. By monitoring the evolution of the contact line in the phase-field model, we find that it converges to the $s(t) \sim t^{2/5}$ behaviour that is predicted from an asymptotic analysis of the thin-film equation by Flitton & King [65].



(a) $\tau = 3.9$ (b) $\tau = 8.9$

(c) $\tau = 15$ (d) $\tau = 76$

Figure 4.16: Topological transformations in a bilayer with unequal composition ratios. In this case, the height ratio of the upper to lower layer is $r : 1$ with $r = 10$. The corresponding composition ratio is $9 : 1$. Distances have been scaled by r so that the height of the undisturbed lower layer has unity thickness. When a hole is introduced into the lower layer, it opens further to create a growing ridge (a). However, the dip in front of the ridge now comes into contact with the lower wall before the ridge hits the upper wall (b). The ridge then detaches from the retracting layer and forms a drop (c). The process repeats itself resulting in an array of droplets (d). Parameter values are $\delta = 0.03$ and $\theta = 45°$. Red and blue corresponds to material A and B, respectively. The black line denotes the $\phi = 0$ contour.

4.4.4.1 Extensions to three dimensions

The phase-field model can easily be extended to include the second horizontal dimension, which up to this point has been neglected. This new coordinate will be denoted by y and we will assume that it extends indefinitely so that the channel remains unbounded in the horizontal plane. With this extended model, we now examine the three-dimensional evolution of a punctured bilayer when the contact angle is 90°. The initial condition is assumed to be radially symmetric, which implies that the initial contact line will take the form of a circle. We write the sharp-interface representation of the perturbed bilayer interface as

$$h_i(r) = \begin{cases} \sqrt{h_\infty - (r - r_0 - h_\infty)^2}, & r_0 < r < r_0 + h_\infty, \\ h_\infty, & r > r_0 + h_\infty, \end{cases} \tag{4.98}$$

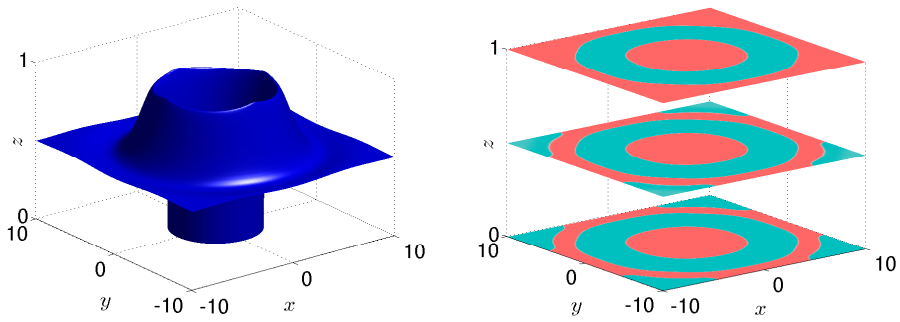
where $r^2 = x^2 + y^2$ and r_0 denotes the radius of the initial hole. We then use the three-dimensional analogue of the leading-order sharp-interface solution (4.83a) to construct the initial condition for the order parameter; in particular, we let

$$\phi_i(r, z) = \tanh\left(\frac{z - h_i(r)}{\delta[1 + (\partial_r h_i)^2]^{1/2}}\right). \tag{4.99}$$

The results of a simulation that begins from this initial condition are shown in Figure 4.17. The parameter values are $\delta = 0.06$ and $\beta = 0$. The contact line recedes in a manner similar to the two-dimensional case and it leads to the formation of a growing ridge. As the ridge gets closer to the upper wall, its axisymmetry is broken; see panel (a). However, the solution is still four-fold symmetric, which may suggest the Cartesian grid used in the simulation is influencing the morphology. The sequence of events that follows the first topological transformation is analogous to the two-dimensional case. Two topological transformations were captured in the simulation. Slices of the final solution are shown in panel (b). Instead of producing columns, the topological transformations lead to the formation of a cylinder of material A (red) that is surrounded by an annulus of material B (blue). Outside of this annulus is mostly material A; however, there are small bumps of material B in the corners. Had a longer computational domain been used, we would expect a sequence of alternating, cylindrical annuli to form. For contact angles that are less than 90°, we anticipate that these annuli would be tapered in the same way that the two-dimensional trapezoidal columns shown in Figure 4.14 are.

4.5 Discussion and conclusion

In this chapter we have studied the dynamics of a binary mixture that is confined between two horizontal walls. The motivation for this problem comes from experiments of spin



(a) $\tau = 7.1$ (b) $\tau = 11.3$

Figure 4.17: Three-dimensional simulation of a punctured bilayer when the equilibrium contact angle is 90°. (a): The two-dimensional sharp interface that separates the two layers, defined implicitly by the equation $\phi(x, y, z) = 0$, just before the first topological transformation occurs. (b): Two-dimensional slices of the solution along the bottom wall ($z = 0$), the top wall ($z = 1$), and at mid-height ($z = 1/2$) showing a cylinder of material A (red) surrounded by annulus of material B (blue). The material in the corners corresponds to developing ridges. Parameter values are $\delta = 0.06$ and $\beta = 0$.

coating solvent-polymer blends. Experimentalists report that the final polymer film often takes one of two morphologies: either the polymers form a bilayer or a laterally separated structure. Using a phase-field model that takes into account the energetic interactions of the confining surfaces, we examined the conditions under which a bilayer can form and studied how such a bilayer responds to perturbations of finite size.

If the mixture is slowly pushed into the spinodal region by slowly cooling it, the growth of small domains within the bulk was suppressed and a bilayer was formed. This was possible even when the bias of the walls was considered to be weak, which was not always the case if the temperature was fixed at a value below the bulk critical point. Slowly cooling the system is thermodynamically similar to slowly removing solvent from a ternary solvent-polymer blend; therefore, if the process of evaporation is slow enough in spin coating, it seems likely that the polymer-substrate interactions can induce the formation of a bilayer.

When the bilayer was manually punctured so that the top layer came into contact with the bottom wall, a cascade of rupturing events could be induced that transformed the topology into a series of trapezoidal columns. The geometrical aspects of nearly all of the columns are identical, the exception being in the first few that form because these are affected by the shape of the puncture. These results support the hypothesis that if the bilayer interface becomes deformed due to an instability and new contact lines are created, the system will undergo a transformation to a laterally separated configuration.

The thin-film equation that is obtained from a systematic reduction of the phase-field model offers many computational benefits over the full phase-field model, particularly when

studying the topological transformation at small contact angles. However, the derivation of this equation is based on the assumption that the sharp interface remains well separated from the walls, and this is believed to cause discrepancies between the two models. As expected, these become particularly apparent when the diffuse interface of the phase-field model is near a wall. Therefore, it would be interesting to carry out an asymptotic analysis of the case when the sharp interface is close to a wall to determine whether these discrepancies can be resolved. Such a study would likely shed light on the "suction" effect that is found to occur in the phase-field model. A related assumption that was made in our thin-film model is that the contact angle is static and equal to its equilibrium value. A consideration of the case when the sharp interface comes in contact with a wall should yield dynamic boundary conditions at the contact line that are more consistent with the phase-field model.

Interestingly, several authors have studied the motion of contact lines by taking sharp-interface limits of models that couple the Cahn–Hilliard and Navier–Stokes equations, where it is found that the stress singularity is regularised by mass diffusion; see, for example, Jacqmin [81] and Yue *et al.* [162]. Such studies might be a helpful resource when attempting to compute the sharp-interface limit of a purely diffusive phase-field model near a contact line.

Several interesting comments can be made about the time scales of the various processes in this problem. The asymptotic analysis in the case of strong walls predicted that the layers satisfy a $t^{1/4}$ growth law for early times. This appears to contradict the $t^{1/3}$ Lifshitz–Slyozov law that is found experimentally. The discrepancy is likely due to our modelling of the wall interactions. The model we considered uses short-range interactions which may not adequately describe the experiments where the $t^{1/3}$ law was found.

When the contact angle is small, the thin-film equation can be used to determine the functional relationship between the physical parameters and the time scale of topological transformations. This is possible because the thin-film equation is parameter free; recall that the prefactor σ in (4.89) is just a numerical constant. Therefore, all of the dynamics of the topological transformations when the contact angle is small can be inferred from a single simulation of this equation. If we let $\bar{\tau}_{\text{trans}}$ correspond to the dimensionless time between topological transformations computed using the thin-film equation, then by redimensionalising this quantity we have that

$$t_{\text{trans}} \propto \frac{d^3}{a\theta^4 D} \frac{T/T_c}{\sqrt{1-T/T_c}} \bar{\tau}_{\text{trans}}. \tag{4.100}$$

From the paper by Hennessy *et al.* [72], the number of columns that emerge can be estimated as $N = 0.15\theta(L/d)$, where L is the (dimensional) horizontal length of the channel. Moreover, it is reported that $\bar{\tau}_{\text{trans}} \simeq 21$. Therefore, the quantity Nt_{trans} gives an estimate of how long

it would take to transform a bilayer into a laterally separated state. The strongly nonlinear dependence of (4.100) on the thickness d and the contact angle θ means even small changes in these values will significantly alter the time needed for a single transformation to occur.

The transformation from a bilayer to alternating columns is driven by interface minimisation. With this in mind, it becomes clear that the laterally separated states which emerge from the transformation may not be the lowest-energy configurations either, as configurations with fewer columns have fewer interfaces and possibly less energy. This is certainly true when the walls are not biased and the columns are rectangular. Thus, it seems reasonable to expect that the columns may eventually coarsen. However, the flatness of the sharp interfaces between the phases suggests that gradients in the chemical potential will be very small; therefore, the coarsening of these domains will be a remarkably slow process. As mentioned by Sun & Ward [145], the coarsening of internal layers in one-dimensional models can be exponentially slow. Attempts to capture the coarsening of the laterally separated domains in numerical simulations were not successful. This gives some indication that if this coarsening were to happen, it may be too slow to be of practical interest.

An important question that has not been addressed in this work is whether an instability can occur at the interface of the bilayer as solvent evaporates from the system. Examining this is a primary area of future work. In order to make progress on this question, several modelling challenges must first be overcome. These relate to the fact that the bilayer is suspected to be dilute when the instability sets in. That is, the volume fraction of the bilayer is much smaller than the volume fraction of solvent. This makes it difficult to precisely define the location of the bilayer interface and to impose physically accurate boundary conditions there. We believe that the correct conditions at this interface can be obtained by first formulating a hydrodynamic version of a three-component phase-field model and then taking an appropriate sharp-interface limit of it. This is motivated by the fact that the usual stress and kinematic boundary conditions at a fluid-fluid interface can be recovered from a sharp-interface reduction of hydrodynamically coupled phase-field model of a binary mixture [1].

Obtaining a hydrodynamic, three-component phase-field model would be particularly useful for studying the alternative hypothesis of lateral domain formation, where an instability occurs at the free surface of the mixture. This, in turn, initiates phase separation that proceeds from the surface down to the substrate. In this situation, the dynamics of phase separation are coupled to those of the instability and therefore, hydrodynamic and thermodynamic processes must be considered simultaneously.

Chapter 5

Conclusions

Motivated by recent experiments of spin-cast polymer films and their application to the fabrication of organic solar cells, we explored several problems relating to the drying and evolution of multicomponent fluids in this thesis. Each of these problems was meant to represent a simplification of a sub-process that is suspected to occur during spin coating. The overall goal of this thesis was to use the results of these problems to build a picture that describes how spin-cast polymer films obtain their morphologies.

5.1 Summary and discussion of thesis

In Chapter 2, we assessed the roles of solutal Marangoni instabilities in evaporating mixtures. These instabilities are caused by composition-induced gradients in the surface tension. In the context of spin coating, solutal Marangoni instabilities are extremely relevant because they are believed to play a primary role in initiating the transition to a laterally separated distribution of polymer.

To conduct our study of solutal Marangoni instabilities, we considered a layer of isothermal fluid consisting of a volatile solvent and a single non-volatile polymer. Although this is a simplification of the ternary systems often used in spin-coating experiments, this problem still proved to be challenging, insightful, and rich in interesting dynamics. The main difficulty of the problem stemmed from the time dependence of the one-dimensional solution, called the base state, that was subsequently used in a linear stability analysis. The system of equations that resulted from a linearisation about the base state were non-autonomous in the time variable. As a consequence, the traditional approaches for stability problems based on normal-mode solutions of the form $\exp(\lambda t)$ could not be directly applied.

In many solvent-polymer systems, the rate of evaporation is small compared to the rate of mass diffusion. This leads to a separation of time scales in the linear stability problem because the base state evolves on the evaporative time scale, whereas the instability evolves

on the diffusive time scale. This allowed the stability problem to be tackled using a frozen-time approach, which is based on neglecting the time dependence of the base state because it evolves much slower than perturbations to it. This method proved to be particularly useful for determining parameter regimes where an instability instantaneously occurred, but it was unable to provide information about how such an instability might develop over the long time scale on which the base state evolves. This led to the question of whether a systematic asymptotic analysis could be performed that captures how the instability evolves on both the evaporative and diffusive time scales. By answering this question, a fairly general asymptotic solution was derived that can be applied to linear stability problems with slowly evolving base states. A comparison of the asymptotic solution with numerical simulations of the linearised problem showed that the two were in excellent agreement.

Carrying out the linear stability analysis using a combination of the frozen-time method, the asymptotic solution to the linearised problem, and numerical simulations, revealed that not one but two modes of instability can occur during the drying process. One of these modes corresponds to the onset of stationary convection cells within the bulk of the layer; the other corresponds to the onset of oscillating deflections at the free surface. These two instabilities compete with each other and from our analysis we could identify parameter regimes where each mode is dominant. These regimes were used to determine experimental conditions that may be used to observe the oscillatory instability.

A comparison of our theoretical results with the experimental data provided by Bassou & Rharbi [8] showed that, in the limit of strong surface tension and gravity, our model predicts stable quiescent films when convection is observed in reality. This suggests that there is another destabilising mechanism in the system other than surface-tension gradients that are induced by variations in the surface composition. Computing the time scale of thermal diffusion showed that it is much smaller than that of mass diffusion, indicating that thermal gradients develop much more rapidly than composition gradients. It seems likely that thermal effects, which might not be strong enough to induce an instability on their own, act in conjunction with the solutal Marangoni instability and lead to additional destabilisation. The relevance of compositional buoyancy was estimated and this may be important for taller films with thicknesses on the order of millimetres.

In spin-coating experiments, the initial mixture thickness is generally on the order of 10 microns [58, 107]. The cubic dependence of the Galileo number (see (2.16)) on the film height suggests that the stabilising effects of gravity are weak in these experiments. Surface tension and Marangoni stresses can still be strong in such films, with the latter being due to the enhanced evaporation rate caused by spinning. Our mathematical analysis predicts that in

this parameter regime, the system will be most susceptible to long-wavelength Marangoni instabilities associated with surface deformations. The experimental data provided by Ebbens *et al.* [60], which examines the evolution of two-dimensional Fourier transforms of the surface and sub-surface film morphologies, shows that long-wavelength structures do indeed emerge during the drying process, and these are attributed to the onset a solutal Marangoni instability driven by evaporation.

In Chapter 3, we explored the use of multicomponent fluid models in studying the evolution of evaporating solvent-polymer mixtures. Starting from a microscopic description of the mixture, the governing equations were systematically averaged to obtain a model that describes the macroscopic composition and flow. On one hand, macroscopic models offer additional mathematical tractability because there is no need to track the geometry and interfaces of microscopic single-phase domains. On the other, this simplification comes at the cost of bulk equations that are more complicated than their microscopic counterparts.

The macroscopic model was used to study two different physical situations. First, the role of compositional buoyancy, which arises from the density differences between the solvent and polymers, was investigated in a one-dimensional setting. When gravity is strong compared to the drag forces between solvent and polymer, the polymers rapidly settle on the substrate to form a bilayer. The upper layer is rich in solvent and it evaporates at a constant and maximal rate, enabling the film to dry in a short amount of time. If drag is the dominant force, the rapid formation of a polymer-rich skin at the free surface significantly reduces the evaporation rate, leading to a very slow thinning that occurs at a roughly uniform rate. The constant downwards force of gravity is suspected to eventually pull the polymer that forms the skin to the substrate, which would allow the remaining solvent to be liberated from the fluid layer.

Second, we investigated the relationship between evaporation and phase separation using a model of a three-component fluid consisting of a volatile solvent, dispersed or partially dissolved polymers, and demixed polymers that have separated from the solvent. Gravitational effects were neglected. Strong drag forces between the solvent and the dispersed polymers caused these phases to travel together. Thus, the dispersed polymers were transported to the free surface by the solvent, where they accumulate over time because they are not volatile. The build up of dispersed polymers increased the rate at which they could demix from the solvent, leading to localised phase separation and the generation of a polymer-rich structure below the free surface. Neglecting gravity in the model meant there was no mechanism to mediate the accumulation of polymer at the free surface; thus, the rate of evaporation decreased until it was effectively equal to zero. When the build up of

polymer was sufficiently rapid, the drying process would end prematurely, resulting in a large proportion of the solvent being trapped within the bulk.

The formation of a polymer-rich skin at the free surface of a mixture is particularly important in the context of spin coating, as many industrial applications seek to produce films that are pure in polymer with minimal residual solvent. In addition, the polymer skin is often very viscous and its formation can freeze the evolution of the surface, thus locking in undesirable transient morphologies. The coupling between evaporation and phase separation is especially relevant to structure formation in spin-cast polymer blends. Although we studied this in a highly idealised context, our results do give further evidence to suggest that laterally separated, polymer-rich structures can be grown from the surface down to the substrate.

The final set of problems were considered in Chapter 4 of this thesis. The aims were to determine the conditions under which a mixture can separate into a vertically stratified bilayer and to examine whether such a bilayer can destabilise into laterally separated structures. The mathematical model was based on phase-field description of a binary mixture. The two components of the mixture were meant to represent two species of polymer. The solvent was not considered, nor were any hydrodynamic effects. Instead, the motion of the two phases was driven purely by diffusion. The thermodynamic effects of the solvent were modelled through a time-dependent temperature field. The mixture was confined between two long horizontal walls. Each component of the mixture was assumed to be preferentially attracted to one, but not the same, wall.

When the temperature of the system was fixed below the bulk critical point of the mixture and the wall-material attraction was not too strong, the onset of spinodal decomposition led directly to the formation of laterally separated structures that resemble columns. The small length of the interfaces that form between adjacent columns allows the laterally separated state to achieve a significantly lower energy in comparison to the bilayer, thus making it favourable for the system to form columns rather than long horizontal layers. However, when the attraction between the walls and materials was increased, a bilayer morphology emerged due to the onset of *surface-directed* spinodal decomposition. By slowly reducing the temperature from the bulk critical value, the onset of spinodal decomposition could be avoided and this led to the formation of a bilayer even when the wall-material interaction was relatively weak. In both cases, the resulting bilayer, with its long interface and high energy, was predicted to be metastable.

In the remainder of the chapter, we focused on the response of the bilayer to a localised perturbation of finite size that brings the bilayer interface in contact with one of the walls. It was shown that such a perturbation can initiate a cascade of ruptures that transforms

the system into a laterally separated repeating array of trapezoidal columns with alternating compositions. The columns were regularly spaced and their widths tended towards a constant as the distance from the initial perturbation increased. This is in contrast to column formation via spinodal decomposition, which generally produced laterally separated structures with irregular spacing. The sequence of topological transformations was efficiently studied by deriving a thin-film equation from a sharp-interface approximation of the phase-field model.

The thermodynamic roles of the temperature field in a binary mixture and the solvent in a ternary mixture are qualitatively similar. For example, the critical solvent concentration of a ternary mixture, below which the polymers undergo phase separation, mimics the critical temperature of a binary mixture. By making some analogies between these two systems, the results from Chapter 4 for binary mixtures can be loosely interpreted in the context of evaporating ternary mixtures. A high evaporation rate will often result in the rapid removal of solvent and quickly push the system below the critical point. Based on our analysis of a binary system that begins below the critical temperature, we can expect the ternary mixture to undergo spinodal decomposition and evolve towards a laterally separated configuration. On the other hand, if evaporation is slow compared to mass diffusion, the system may behave as if it is being slowly cooled. In this case, a transient bilayer morphology may arise. Our analysis suggests that a single localised perturbation to the bilayer interface, which may be due to a hydrodynamic instability, is sufficient to initiate the break up of the bilayer and the formation of laterally separated structures.

The theory developed in this thesis may provide a foundation for understanding why the formation of a transient or persisting bilayer is observed in some spin-coating experiments [58, 76, 107], while others find that the mixture separates directly into lateral structures [60]. In particular, this seems to be determined by the rate of evaporation, with bilayers occurring at low evaporation rates, and lateral structures directly forming at high evaporation rates. In the latter case, we suspect that evaporation either triggers the onset of spinodal decomposition within the bulk, or it localises it to a thin layer near the free surface that grows towards the substrate. There is also likely to be an intermediate regime, where evaporation is slow enough to allow a bilayer to form, yet strong enough to induce a hydrodynamic instability which is responsible for the break up of this bilayer. This conjecture is backed up by the experimental data of Mokarian–Tabari *et al.* [107], which shows that slow evaporation rates typically produce bilayers, whereas high evaporation rates lead to laterally separated morphologies.

5.2 Future directions

Creating a thin polymer film with a given morphology from a solvent-rich blend is a remarkably complex problem that is not fully understood. The investigations carried out in this thesis provide some novel insights into the key processes that can occur as solvent-mixture mixtures dry. However, they have also led to several interesting questions which remain unanswered.

The results of Chapter 2 revealed that an oscillatory mode of instability can occur in evaporating binary mixtures. A useful avenue of future research could be to better assess how physically relevant this is. There are two approaches that could be taken. One is to carry out an analogous linear stability analysis using a mathematical model with realistic fluid rheologies that include, for example, non-Newtonian effects or composition-dependent viscosities. The other approach is to perform a nonlinear analysis or two- or three-dimensional numerical simulations to obtain estimates for the amplitude of surface deflections arising from the instability. The paint drying experiments by Overdiep [120], which clearly show some form of oscillatory behaviour in the film profile, give evidence to suggest that this instability is not only relevant in a purely scientific context, but also in practical ones.

Using the results from the linear stability analysis in Chapter 2, it was possible to determine experimental conditions that might lead to the onset of an oscillatory instability. It would be particularly interesting to work with an experimental collaborator to determine whether the instability occurs when our theory predicts it should. Such a study could also be used to refine the model and, in particular, it may provide further clues about other contributing factors to the instability, such as those from thermal effects.

When considering possible mechanisms of instability in Chapter 2, it was suggested that compositional buoyancy may become important in millimetre-thick films. This partly motivated the studies using multiphase fluid models for evaporating mixtures in Chapter 3. The removal of solvent from the upper surface naturally leads to an unstable density stratification, whereby a heavier layer fluid forms on top of a lighter fluid. Such systems are often subject to a Rayleigh–Taylor instability. This leads to a fingering pattern emerging at the interface of the two fluids which can subsequently develop into plumes that sink. In the context of structure formation in polymer films, the formation and sinking of polymer-rich plumes provides yet another mechanism by which laterally separated configurations can emerge. While gravity may act too weakly for this to be relevant in the micron-thick fluids used in spin-coating experiments, it may be relevant in other coating processes that make use of thicker films.

The question of whether a Rayleigh–Taylor instability can occur in evaporating mixtures was not addressed, making this a prime topic for future work. A linear stability analysis will present the same challenges associated with a time-dependent base state that were encountered in Chapter 2. However, if there is a separation of time scales in the linear stability problem, the machinery that was developed in Chapter 2 can be applied. Two-dimensional numerical simulations of the full problem might also be useful for understanding the long-term evolution of the instability and, in particular, the development of plumes.

In Chapter 4 we studied the interesting situation where a bilayer breaks up due to a localised perturbation of finite size. This investigation was based on a phase-field model of binary mixture that flows via diffusion. In many real-world systems, the two components of the mixture will have a hydrodynamic component of flow. Thus, an interesting and important extension of this work is to introduce hydrodynamics into the phase-field model and investigate whether a similar sequence of topological transitions can occur. From a physical standpoint, the break up of the bilayer is driven by energy minimisation through a reduction of interfacial area, which is a process that is expected to persist when hydrodynamics are included. However, the kinetics of the rupturing process are likely to change, potentially making the transformation from bilayer to laterally separated configuration occur more rapidly than in the purely diffusive case.

An interesting application of the phase-field model and its extensions is to study the dynamics of dewetting liquid films and the instability that can occur at the receding contact line. Recent efforts to study such instabilities have been based on thin-film-type equations and linear stability analyses [65, 94, 113]. Dziwnik *et al.* [59], for example, examine the contact line instability in the same thin-film equation that was derived in Chapter 4. They also compute the dominant wavenumber of the fingering pattern that emerges at the contact line. Given that this thin-film equation can be systematically derived from a phase-field model, one would expect that a similar instability appears in the latter model as well. Thus, an interesting future study would aim to determine whether the phase-field model can capture this instability and if the same dominant wavenumber emerges. From a computational standpoint, phase-field models may be a very effective tool for studying the contact line instability because they avoid the need to solve a multidimensional free boundary problem numerically.

A related area of future research is to examine sharp-interface limits of phase-field models when the diffuse interface comes in contact with a boundary. Such an analysis may produce novel insights into the dynamics that occur at contact lines and provide new boundary conditions that can be used in thin-film equations.

A primary topic that has yet to be considered is the onset of an instability at the bilayer interface. This is thought to create the deformations in the interface that later develop into laterally separated structures. There is a fairly strong consensus among experimentalists that this instability is caused by solutal Marangoni effects [8, 22, 76, 104]. Thus, it is tempting to extend the model presented in Chapter 2 to a two-layer configuration and carry out a similar analysis. However, the dilute nature of the bilayer makes it difficult to apply such a model, at least immediately, because defining the bilayer interface is not trivial nor is it obvious what the correct boundary conditions there would be. One means of overcoming this issue is by treating the bilayer interface as diffuse, which is possible through the use of a three-component multiphase fluid model or a hydrodynamically coupled ternary phase-field model. The multiphase model would have to consider bulk effects due to surface tension and surface-tension gradients, and deriving a model that takes these into account would be an interesting problem in its own right. The approach of Abels *et al.* [1] was used to start the construction of a hydrodynamic, ternary phase-field model, but this only reached preliminary stages of development so it was not discussed in this thesis.

The derivation of a thermodynamically consistent, hydrodynamically coupled, ternary phase-field model would not only facilitate an investigation of the destabilisation of the bilayer, but it could also be used to study many other aspects of the drying process. For example, such a model could be used to revisit the problem of bilayer formation and verify the conclusions that were made from the simplified model of a binary mixture. Moreover, it could be used to further investigate whether a high evaporation rate will localise the onset of phase separation to a thin layer near the surface, causing laterally separated structures to grow from the top down. This phenomenon was captured in a purely diffusive phase-field model of a ternary mixture by Buxton and Clarke [31]; thus, carrying out a similar study with hydrodynamics would be an interesting extension of their work.

An interesting avenue of research that could be pursued in the future is the further use of multiphase fluid models for studying the coupling between hydrodynamic effects and phase separation. This approach would be somewhat non-traditional, as there is a long history of investigating phase separation using phase-field models. In addition, some effort would be required to derive interfacial mass transfer terms that accurately capture the physics of phase separation. That being said, multiphase models offer a straightforward approach for incorporating a wide variety of hydrodynamic effects and they are easily generalised for mixtures with arbitrary numbers of components, thus making them particularly suitable for preliminary investigations on the subject. It would be interesting to use such a model to study a five-phase system consisting of one solvent, two species of dispersed polymer,

and two species of demixed polymer, as this would describe the ternary mixtures that are encountered in experiments.

Last but not least, spinning could be introduced into the various models that were considered in this thesis. This is expected to influence the dynamics in several interesting ways. For example, there may be two distinct thinning regimes: the first of which is driven by the outwards flow of fluid, and the second of which is caused by slow evaporation. In the context of Chapter 2, the dynamics of the Marangoni instability are likely to be tied to centrifugal effects. Surface deformations that appear in the azimuthal direction may be advected outwards, giving rise to striation patterns that are sometimes observed experimentally [159]. Centrifugal forces can be naively thought of as gravitational forces that act in the radial direction and, therefore, they may lead to interesting dynamics in multiphase models that have mixture components with different densities. In particular, chemical species with higher densities will experience a stronger centrifugal force, which may act as an additional mechanism for lateral separation. The theoretical work on spin coating by Reisfeld *et al.* [129] has shown that surface deformations can arise from centrifugal-inertial effects in the absence of Marangoni stresses. This may have important consequences for the polymer-polymer bilayer that can form during spin coating, as it suggests another mechanism that can contribute to its breakup. Furthermore, rotational effects are likely to influence the kinetics of the topological transformation that was studied in Chapter 4. To investigate this latter point, hydrodynamics would have to be included in the phase-field model, thus highlighting yet another interesting problem that could be tackled with such a model.

5.3 Final thoughts

The overall goal of this thesis was to build an understanding of the physical processes that occur during spin coating and to determine how these may influence the morphology of the resulting polymer film. By drawing upon a combination of mathematical modelling, analysis, and computation, valuable insights into the dynamics of evaporating mixtures were obtained from studying a collection of simpler, yet relevant, problems. Thus, the goal of this thesis was, indeed, realised. That being said, several interesting and important questions remain unanswered. Therefore, it is hoped that this thesis will act as a source of inspiration to continue research in this area and provide a solid foundation for future studies. By systematically working towards a complete mathematical description of the drying process, new and fundamental insights can be made into the dynamics of structure formation and self-assembly in evaporating solvent-polymer blends. This knowledge can aid

experimentalists in fabricating thin polymer films with optimal morphologies, thus yielding a new generation of efficient and versatile polymer-based technologies.

Appendix A

Supplementary material for Chapter 2

A.1 Derivation of the asymptotic solution

We seek to construct a uniformly valid asymptotic solution to the non-autonomous linear problem given by

$$\partial_t U = L(\tau)U, \tag{A.1}$$

where $\tau = \delta t$ is a slow time with $\delta \ll 1$, and L is a slowly varying linear operator. The solution U can be a function of time if this problem corresponds to a system of ODEs, or it can be a function of space and time if this problem involves a system of PDEs. As we are only interested in the temporal behaviour of the solution U, we shall write $U = U(t)$. Any dependence on other variables, such as space, will not be written explicitly. The initial condition for this problem is given by $U(0) = U_i$. In the case where (A.1) is a PDE system, we suppose the boundary conditions can be written as $B(\tau)U = 0$.

The asymptotic solution to this problem will first be derived using the method of multiple scales. An introductory discussion on this method can be found in Bender & Orszag [12], whereas an advanced treatment can be found in Kevorkian & Cole [91]. The derivation presented here will be similar to the two-step approach taken by Hennessy & Münch [74], where the solution U is first projected into the eigenfunctions of L and then the resulting system of ODEs is approximately solved using multiple scales. However, we are able to obtain a slightly more general result by not restricting our derivation to the top two eigenmodes, *i.e.*, we consider all of the modes and not just the two corresponding to the eigenvalues with largest and second-largest real parts. Furthermore, we consider the case when the eigenvalues are complex.

To begin the derivation, we assume that the spectrum of L (with possibly B) is discrete, that the eigenvalues are distinct for each value of τ, and that the eigenfunctions form a

complete set. Under these assumptions, we can write the solution U as

$$U(t) = \sum_{l=1}^{\infty} \alpha_l(t) v_l(\tau), \tag{A.2}$$

where v_l is a slowly varying eigenfunction given by

$$L(\tau) v_l(\tau) = \lambda_l(\tau) v_l(\tau), \tag{A.3}$$

and possibly $B(\tau) v_l = 0$. Here, λ_l denotes the l-th eigenvalue. We order the eigenvalues according to the size of their real part so that $\mathrm{Re}\{\lambda_1\} > \mathrm{Re}\{\lambda_2\} > \ldots > \mathrm{Re}\{\lambda_n\}$ as $n \to \infty$. The adjoint eigenvalue problem is given by

$$L^\dagger(\tau) v_l^\dagger(\tau) = \lambda_l^*(\tau) v_l^\dagger(\tau), \tag{A.4}$$

where the star denotes complex conjugation, $L^\dagger$ is the adjoint of the linear operator in (A.1), and $v_l^\dagger$ denotes the adjoint eigenfunction. The eigenfunctions and their adjoints are normalised according to

$$\langle v_l, v_l \rangle(\tau) \equiv 1, \quad \langle v_k^\dagger, v_l \rangle(\tau) \equiv \delta_{kl}, \tag{A.5}$$

where δ_{kl} denotes the Kronecker delta and $\langle \cdot, \cdot \rangle$ denotes a possibly τ-dependent inner product. We assume that the second argument in the inner product is complex conjugated in the operation.

By inserting the solution in (A.2) into (A.1) and taking the inner product with the adjoint eigenfunctions, we find that the functions α_l satisfy system of ODEs given by

$$\frac{\mathrm{d}\alpha_l}{\mathrm{d}t} - \left[\lambda_l(\tau) + \delta\gamma_{ll}(\tau)\right] \alpha_l(t) = \delta \sum_{j \neq l}^{\infty} \gamma_{lj}(\tau) \alpha_j(t), \quad l \in \mathbb{N}, \tag{A.6}$$

where the γ_{jl} are defined as

$$\gamma_{jl}(\tau) = -\langle v_j^\dagger, \partial_\tau v_l \rangle^*(\tau), \quad j, l \in \mathbb{N}. \tag{A.7}$$

The initial conditions for this system are given by $\alpha_l(0) = \alpha_{li} = \langle v_l^\dagger, U_i \rangle^*(0)$.

We now invoke the method of multiple scales to obtain an approximate solution to the ODE system in (A.6). However, the application of the method is not straightforward for this system because the time t is not an appropriate time variable; see page 558 of Bender & Orszag [12] for an exemplary discussion about this. Therefore, we introduce several new times T_l, $l \in \mathbb{N}$, that will replace t. These are defined as

$$T_l = \delta^{-1} \int_0^{\delta t} \left[\lambda_l(s) + \delta\gamma_{ll}(s)\right] \mathrm{d}s, \quad l \in \mathbb{N}. \tag{A.8}$$

Using these new time variables, we write $\alpha_l(t)$ as $\alpha_l(\tau, T)$, where the argument T without any subscript denotes dependence on each of the times T_l. By applying the chain rule, the ODE system in (A.6) can be written as

$$\delta \frac{\partial \alpha_l}{\partial \tau} + \sum_{j=1}^{\infty} \left[\lambda_j(\tau) + \delta \gamma_{jj}(\tau)\right] \frac{\partial \alpha_l}{\partial T_j} - \left[\lambda_l(\tau) + \delta \gamma_{ll}(\tau)\right] \alpha_l = \delta \sum_{j \neq l}^{\infty} \gamma_{lj}(\tau) \alpha_j, \quad l \in \mathbb{N}, \tag{A.9}$$

where the initial condition now reads $\alpha_l(0,0) = \alpha_{li}$. We now treat all of the time variables, namely τ, T_1, T_2, ..., T_n, $n \to \infty$, as independent variables. Following Kevorkian and Cole [91] (see pg. 395), we expand each α_l as an asymptotic series of the form

$$\alpha_l(\tau, T) = \alpha_l^{(0)}(\tau, T_l) + \sum_{n=1}^{\infty} \delta^n \alpha_l^{(n)}(\tau, T), \quad l \in \mathbb{N}. \tag{A.10}$$

The initial conditions now read $\alpha_l^{(0)}(0,0) = \alpha_{li}$ and $\alpha_l^{(n)}(0,0) = 0$ for all $l, n \in \mathbb{N}$. We insert this expansion into the system (A.9), collect powers of δ, and solve each problem sequentially.

For each value of $l \in \mathbb{N}$, the leading-order problem is given by

$$\frac{\partial \alpha_l^{(0)}}{\partial T_l} - \alpha_l^{(0)} = 0, \tag{A.11}$$

which has the solution

$$\alpha_l^{(0)}(\tau, T_l) = P_l(\tau) e^{T_l}, \tag{A.12}$$

where $P_l(0) = \alpha_{li}$. The determination of P_l comes from eliminating secular terms in the $O(\delta)$ problem. This problem is given by

$$\sum_{j=1}^{\infty} \lambda_j(\tau) \frac{\partial \alpha_l^{(1)}}{\partial T_j} - \lambda_l(\tau) \alpha_l^{(1)} = -\frac{\mathrm{d}P_l}{\mathrm{d}\tau} e^{T_l} + \sum_{j \neq l}^{\infty} \gamma_{lj}(\tau) P_j(\tau) e^{T_j}. \tag{A.13}$$

We can treat this equation as a first-order hyperbolic PDE and hence we can rewrite it in terms of its characteristics. Therefore, we let $\mathrm{d}T_i/\mathrm{d}\xi = \lambda_i(\tau)$ and write (A.13) as

$$\frac{\partial \alpha_l^{(1)}}{\partial \xi} - \lambda_l(\tau) \alpha_1^{(1)} = -\frac{\mathrm{d}P_l}{\mathrm{d}\tau} e^{\lambda_l(\tau)\xi} + \sum_{j \neq l}^{\infty} \gamma_{lj}(\tau) P_j(\tau) e^{\lambda_j(\tau)\xi}, \tag{A.14}$$

where we make the remark that the ξ derivative of $\alpha_l^{(1)}$ is only a partial derivative because this function still depends on τ. From this new equation, it is easy to see that any terms that are proportional to $\exp(\lambda_l \xi)$ will lead to secular terms in the solution for $\alpha_l^{(1)}$ and hence they need to be eliminated. This implies that the functions P_l are constants given by

$$P_l(\tau) \equiv \alpha_{li}. \tag{A.15}$$

The equation in (A.14) can be solved using an integrating factor and the solution, upon rewriting it in terms of the times T_l, is given by

$$\alpha_l^{(1)}(\tau, T) = \sum_{j\neq l}^{\infty} \frac{\alpha_{ji}\gamma_{lj}(\tau)}{\lambda_j(\tau) - \lambda_l(\tau)} e^{T_j} + Q_l(\tau) e^{T_l}. \tag{A.16}$$

The functions Q_l have initial conditions given by

$$Q_l(0) = -\sum_{j\neq l}^{\infty} \frac{\alpha_{ji}\gamma_{lj}(0)}{\lambda_j(0) - \lambda_l(0)}, \tag{A.17}$$

and they are determined by eliminating the secular terms that otherwise occur in the $O(\delta^2)$ problem. This problem is given by

$$\begin{aligned} \sum_{j=1}^{\infty} \lambda_j(\tau) \frac{\partial \alpha_l^{(2)}}{\partial T_j} - \lambda_l(\tau)\alpha_l^{(2)} = &-\frac{\partial \alpha_l^{(1)}}{\partial \tau} - \gamma_{ll}(\tau)\alpha_l^{(1)} \\ &+ \sum_{j\neq l}^{\infty} \gamma_{lj}(\tau)\alpha_j^{(1)} + \sum_{j=1}^{\infty} \gamma_{jj}(\tau) \frac{\partial \alpha_l^{(1)}}{\partial T_j}. \end{aligned} \tag{A.18}$$

Using the same approach as before, the terms that lead to secularity in the solution for $\alpha_l^{(2)}$ can be identified as the terms that are proportional to $\exp(\lambda_l \xi)$ once (A.16) is inserted into this equation and it is written in terms of its characteristics. The elimination of these terms yields the following differential equation for Q_l:

$$\frac{\mathrm{d}Q_l}{\mathrm{d}\tau} = \alpha_{li} \sum_{j\neq l}^{\infty} \frac{\gamma_{lj}(\tau)\gamma_{jl}(\tau)}{\lambda_l(\tau) - \lambda_j(\tau)}, \tag{A.19}$$

which can be solved to obtain

$$Q_l(\tau) = \sum_{j\neq l}^{\infty} \left[\alpha_{li} \int_0^{\tau} \frac{\gamma_{lj}(s)\gamma_{jl}(s)}{\lambda_l(s) - \lambda_j(s)} \,\mathrm{d}s - \frac{\alpha_{ji}\gamma_{lj}(0)}{\lambda_j(0) - \lambda_l(0)} \right]. \tag{A.20}$$

Therefore, the asymptotic solution for the α_l, $l \in \mathbb{N}$, can be written as

$$\begin{aligned} \alpha_l(t) = \alpha_{li} e^{T_l} &+ \delta \sum_{j\neq l}^{\infty} \frac{\alpha_{ji}\gamma_{lj}(\tau)}{\lambda_j(\tau) - \lambda_l(\tau)} e^{T_j} \\ &+ \delta \sum_{j\neq l}^{\infty} \left[\alpha_{li} \int_0^{\tau} \frac{\gamma_{lj}(s)\gamma_{jl}(s)}{\lambda_l(s) - \lambda_j(s)} \,\mathrm{d}s - \frac{\alpha_{ji}\gamma_{lj}(0)}{\lambda_j(0) - \lambda_l(0)} \right] e^{T_l} + O(\delta^2), \end{aligned} \tag{A.21}$$

where $\tau = \delta t$ and the T_l are given in (A.8). When this solution is combined with the eigenfunction expansion in (A.2), we effectively have a multiple-scales approximation to the original linear problem in (A.1).

A.1.1 An alternative derivation using the WKB method

The asymptotic solution presented above can also be derived using the WKB approximation [12]. This may be a more useful approach when trying to resolve the situation when eigenvalues momentarily become identical; however, we do not address this issue here. We start by considering the slowly varying linear problem of the form

$$\frac{\partial U}{\partial t} = L(\delta t)U, \tag{A.22}$$

with $\delta \ll 1$, subject to the initial condition $U(0) = U_i$ and possibly with slowly varying boundary conditions given by $B(\tau)U = 0$. We now write the problem exclusively in terms of the slow time τ by making the change of variable $t = \delta^{-1}\tau$, thus giving

$$\delta\frac{\partial U}{\partial \tau} = L(\tau)U. \tag{A.23}$$

We suppose that the solution U can be written in the form of the usual WKB ansatz, namely

$$U(\tau) = \Phi(\tau)e^{\phi(\tau)/\delta}, \tag{A.24}$$

where it is assumed that ϕ depends only on τ and satisfies the initial condition $\phi(0) = 0$. The function Φ can depend on other independent variables such as space, but we do not explicitly write this dependence. By inserting (A.24) into (A.23), the problem becomes

$$\delta\frac{\partial \Phi}{\partial \tau} + \frac{\mathrm{d}\phi}{\mathrm{d}\tau}\,\Phi = L\Phi. \tag{A.25}$$

The functions Φ and ϕ are expanded as asymptotic series of the form

$$\Phi(\tau) = \Phi^{(0)}(\tau) + \delta\Phi^{(1)}(\tau) + \delta^2\Phi^{(2)}(\tau) + O(\delta^3), \tag{A.26a}$$

$$\phi(\tau) = \phi^{(0)}(\tau) + \delta\phi^{(1)}(\tau) + \delta^2\phi^{(2)}(\tau) + O(\delta^3), \tag{A.26b}$$

where $\phi^{(n)}(0) = 0$ for all values of n. By collecting powers of δ after this expansion has been inserted into (A.25), a sequence of sub-problems can be formulated.

The $O(1)$ problem is given by

$$\frac{\mathrm{d}\phi^{(0)}}{\mathrm{d}\tau}\Phi^{(0)} = L\Phi^{(0)}, \tag{A.27}$$

and it follows that $\Phi^{(0)}$ is an eigenfunction of L and $\partial_\tau\phi^{(0)}$ is equal to the corresponding eigenvalue. We let

$$\Phi^{(0)}(\tau) = \alpha_{li}v_l(\tau), \quad \phi^{(0)}(\tau) = \int_0^\tau \lambda_l(s)\,\mathrm{d}s, \tag{A.28}$$

where v_l is the l-th eigenfunction of L that satisfies $\langle v_l, v_l \rangle = 1$, λ_l is the corresponding eigenvalue, and α_{li} is a normalisation factor.

The leading-order solution for U is obtained by summing over all of the eigenmodes to give

$$U(\tau) = \sum_{l=1}^{\infty} \alpha_{li} \exp\left[\int_0^\tau \lambda_l(s)\,\mathrm{d}s\right] v_l(\tau) + O(\delta). \tag{A.29}$$

By imposing the initial condition and taking the inner product with the (normalised) adjoint eigenfunctions, it follows that

$$\alpha_{li} = \langle v_l^\dagger, U_i \rangle^*(0). \tag{A.30}$$

Here we have assumed that the adjoint eigenfunctions are normalised according to $\langle v_j^\dagger, v_k \rangle = \delta_{jk}$, where δ_{jk} is the Kronecker delta.

Proceeding further, the $O(\delta)$ problem is given by

$$\frac{\partial \Phi^{(0)}}{\partial \tau} + \frac{\mathrm{d}\phi^{(1)}}{\mathrm{d}\tau}\,\Phi^{(0)} + \frac{\mathrm{d}\phi^{(0)}}{\mathrm{d}\tau}\,\Phi^{(1)} = L\Phi^{(1)}. \tag{A.31}$$

By making use of (A.28), this problem can be written as

$$(L - \lambda_l I)\Phi^{(1)} = \frac{\partial v_l}{\partial \tau} + \frac{\mathrm{d}\phi^{(1)}}{\mathrm{d}\tau}\,v_l, \tag{A.32}$$

where I is the identity operator. The operator on the left-hand side of this equation is clearly singular; thus, for a solution to exist, the Fredholm solvability condition must be satisfied. Imposing this condition provides an equation for $\phi^{(1)}$. More specifically, we take the inner product of the right-hand side of (A.32) with $v_l^\dagger$ and we find that

$$\phi^{(1)}(\tau) = \int_0^\tau \gamma_{ll}(s)\,\mathrm{d}s, \tag{A.33}$$

where $\gamma_{jk}(\tau) = -\langle v_j^\dagger, \partial_\tau v_k \rangle^*(\tau)$ for all $j, k \in \mathbb{N}$.

The solution for $\Phi^{(1)}$ can be found via an eigenfunction expansion. We let

$$\Phi^{(1)}(\tau) = \alpha_{li} \sum_{j=1}^{\infty} a_j(\tau) v_j(\tau) \tag{A.34}$$

and by inserting this into (A.32), the coefficient functions can straightforwardly be obtained. In particular, we find

$$a_j(\tau) = -\frac{\gamma_{jl}(\tau)}{\lambda_j(\tau) - \lambda_l(\tau)}, \quad j \neq l. \tag{A.35}$$

The function $a_l(\tau)$ cannot be determined from this problem, so we proceed to the next order.

The $O(\delta^2)$ problem is given by

$$(L-\lambda_l I)\Phi^{(2)} = \frac{\partial \Phi^{(1)}}{\partial \tau} + \frac{\mathrm{d}\phi^{(2)}}{\mathrm{d}\tau}\,\Phi^{(0)} + \frac{\mathrm{d}\phi^{(1)}}{\mathrm{d}\tau}\,\Phi^{(1)}, \tag{A.36}$$

and for this equation to admit a solution, the right-hand side must satisfy a similar Fredholm solvability condition. Taking the inner product of the right-hand side of (A.36) with $v_l^\dagger$ yields a differential equation for $\phi^{(2)}$, which can be solved to obtain

$$\phi^{(2)}(\tau) = a_l(0) - a_l(\tau) - \sum_{j\neq l}\int_0^\tau \frac{\gamma_{jl}(s)\gamma_{lj}(s)}{\lambda_j(s)-\lambda_l(s)}\,\mathrm{d}s. \tag{A.37}$$

To proceed further, we insert the $O(1)$ and $O(\delta)$ solutions along with (A.37) into the WKB ansatz (A.24) and we expand the exponential as

$$\exp\left(\delta^{-1}\phi^{(0)} + \phi^{(1)} + \delta\phi^{(2)} + O(\delta^2)\right) = (1+\delta\phi^{(2)})\exp\left(\delta^{-1}\phi^{(0)} + \phi^{(1)}\right) + O(\delta^2). \tag{A.38}$$

This allows the unknown function $a_l(\tau)$ to be eliminated from the problem. However, its initial value $a_l(0)$ still appears, and this is chosen below to satisfy the initial condition.

The solution U is obtained by summing over all of the modes to obtain

$$\begin{aligned} U(\tau) = \sum_{l=1}^\infty \alpha_{li}\Bigg[&(1+\delta a_l(0))v_l(\tau) + \delta\sum_{j\neq l}^\infty \frac{\gamma_{jl}(\tau)}{\lambda_l(\tau)-\lambda_j(\tau)}\,v_j(\tau) \\ &+ \left(\sum_{j\neq l}^\infty \int_0^\tau \frac{\gamma_{lj}(s)\gamma_{jl}(s)}{\lambda_l(s)-\lambda_j(s)}\,\mathrm{d}s\right)v_l(\tau)\Bigg]e^{T_l(\tau)} + O(\delta^2), \end{aligned} \tag{A.39}$$

where T_l is defined as

$$T_l(\tau) = \delta^{-1}\int_0^\tau \left[\lambda_l(s) + \delta\gamma_{ll}(s)\right]\,\mathrm{d}s, \quad l\in\mathbb{N}. \tag{A.40}$$

To simplify this solution, we write it as an eigenfunction expansion of the form

$$U(\tau) = \sum_{l=1}^\infty \alpha_l(\tau)v_l(\tau), \tag{A.41}$$

where $\alpha_l(0) = \alpha_{li}$ for all values of l. Using the fact that

$$\sum_{l=1}^\infty \alpha_{li}\left(\sum_{j\neq l}\frac{\gamma_{jl}}{\lambda_l-\lambda_j}\,v_j\right)e^{T_l} = \sum_{j=1}^\infty\left(\sum_{l\neq j}^\infty \frac{\alpha_{li}\gamma_{jl}}{\lambda_l-\lambda_j}\,e^{T_l}\right)v_j, \tag{A.42}$$

we find that the functions α_l in (A.41) are given by

$$\begin{aligned} \alpha_l(\tau) = \alpha_{li}(1+\delta a_l(0))e^{T_l(\tau)} &+ \delta\sum_{j\neq l}^\infty \frac{\alpha_{ji}\gamma_{lj}(\tau)}{\lambda_j(\tau)-\lambda_l(\tau)}\,e^{T_j(\tau)} \\ &+ \delta\left(\sum_{j\neq l}^\infty \alpha_{li}\int_0^\tau \frac{\gamma_{jl}(\tau)\gamma_{lj}(\tau)}{\lambda_l(\tau)-\lambda_j(\tau)}\,\mathrm{d}s\right)e^{T_l(\tau)} + O(\delta^2). \end{aligned} \tag{A.43}$$

By imposing the initial condition $\alpha_l(0) = \alpha_{li}$ we can solve for $a_l(0)$, thus yielding

$$\alpha_l(\tau) = \alpha_{li} e^{T_l(\tau)} + \delta \sum_{j \neq l}^{\infty} \frac{\alpha_{ji}\gamma_{lj}(\tau)}{\lambda_j(\tau) - \lambda_l(\tau)} e^{T_j(\tau)} + \delta \Bigg(\sum_{j \neq l}^{\infty} \alpha_{li} \int_0^{\tau} \frac{\gamma_{jl}(\tau)\gamma_{lj}(\tau)}{\lambda_l(\tau) - \lambda_j(\tau)} \, \mathrm{d}s - \frac{\alpha_{ji}\gamma_{lj}(0)}{\lambda_j(0) - \lambda_l(0)} \Bigg) e^{T_l(\tau)} + O(\delta^2), \quad \text{(A.44)}$$

which is equivalent to the expression obtained using the method of multiple scales.

A.2 The adjoint problem

Using the asymptotic solution presented in Appendix A.1 requires taking inner products with adjoint eigenfunctions. The rescaled eigenvalue problem given in (2.52) is not self-adjoint and so the adjoint problem must be formulated before this solution can be used. An additional benefit of formulating the adjoint problem is that in this case, it offers a straightforward approach for calculating the characteristic equation associated with the eigenvalues. This can be used to easily obtain a small-wavenumber expansion of the top eigenvalue.

Before calculating the adjoint problem, we recall its precise definition. Let L be a linear operator with boundary conditions B. Suppose that U is a solution of the regular problem so that $LU = 0$ and $BU = 0$. The associated adjoint problem, with operator $L^\dagger$, boundary conditions $B^\dagger$, and solution $U^\dagger$, is given by $L^\dagger U^\dagger = 0$ and $B^\dagger U^\dagger = 0$. The adjoint operator and boundary conditions are chosen so that

$$\langle LU, U^\dagger \rangle = \langle U, L^\dagger U^\dagger \rangle \quad \text{(A.45)}$$

holds for all U and $U^\dagger$. Here, $\langle \cdot, \cdot \rangle$ is an appropriate inner product for the space on which U and $U^\dagger$ are defined. For an eigenvalue problem given by $Lv = \sigma v$ with $Bv = 0$, the associated adjoint eigenvalue problem is given by $L^\dagger v^\dagger = \sigma^* v^\dagger$ with $B^\dagger v^\dagger = 0$, where the star is used to denote complex conjugation.

A.2.1 Formulation

The (rescaled) eigenvalue problem (2.52) that forms the basis of the analysis in Chapter 2 can be written as (upon dropping the checks)

$$(\partial_\zeta^2 - a^2)^2 w = 0, \quad \text{(A.46a)}$$

$$\sigma c - \zeta w = -a^2 c + \partial_\zeta^2 c. \quad \text{(A.46b)}$$

The boundary conditions at the substrate are given by

$$w = \partial_\zeta w = \partial_\zeta c = 0, \quad \zeta = 0, \quad \text{(A.46c)}$$

and at the surface they are

$$w - \sigma h = 0, \qquad \zeta = 1, \tag{A.46d}$$

$$-h + \partial_\zeta c = 0, \qquad \zeta = 1, \tag{A.46e}$$

$$-\partial_\zeta^3 w + 3a^2 \partial_\zeta w = -a^2(a^2 C^{-1} + G)h, \quad \zeta = 1, \tag{A.46f}$$

$$\partial_\zeta^2 w + a^2 w = -a^2 M(c - h), \qquad \zeta = 1. \tag{A.46g}$$

The velocity w can, in theory, be eliminated from this problem. Therefore, we write $w(\zeta) = W_c(\zeta)c(1) + W_h(\zeta)h$. The eigenvalue problem then simplifies to

$$\sigma c = \zeta W_c(\zeta)c(1) + \zeta W_h(\zeta)h - a^2 c + \partial_\zeta^2 c, \tag{A.47a}$$

$$\sigma h = W_c(1)c(1) + W_h(1)h, \tag{A.47b}$$

subject to the boundary conditions

$$\partial_\zeta c = 0, \quad \zeta = 0, \tag{A.47c}$$

$$\partial_\zeta c - h = 0, \quad \zeta = 1. \tag{A.47d}$$

To proceed with the derivation of the adjoint problem, an inner product needs to be specified. We let $U_i = [c_i(\zeta), h_i]^T$, $i = 1, 2$, denote two vector functions and we define the inner product of these to be

$$\langle U_1, U_2 \rangle = \int_0^1 c_1(\zeta) c_2^*(\zeta)\, \mathrm{d}\zeta + h_1 h_2^*. \tag{A.48}$$

Using this, the adjoint problem can be obtained by a simple application of integration by parts. Eliminating the boundary terms provides extra conditions that are required to determine the constants of integration in the adjoint problem. We find that the adjoint eigenvalue problem is given by

$$\sigma^* c^\dagger = -a^2 c^\dagger + \partial_\zeta c^\dagger, \tag{A.49a}$$

$$\sigma^* h^\dagger = W_h(1)h^\dagger + c^\dagger(1) + \int_0^1 \zeta W_h(\zeta) c^\dagger(\zeta)\, \mathrm{d}\zeta, \tag{A.49b}$$

subject to the conditions

$$\partial_\zeta c^\dagger(0) = 0, \tag{A.49c}$$

$$\partial_\zeta c^\dagger(1) = W_c(1)h^\dagger + \int_0^1 \zeta W_c(\zeta) c^\dagger\, \mathrm{d}\zeta. \tag{A.49d}$$

Thus, unlike the regular eigenvalue problem, the adjoint problem is non-local. Despite this complication, it is straightforward to determine the characteristic equation for the eigenvalues σ. By solving (A.49a) subject to the condition (A.49c), we find that $c^\dagger =$

$A^\dagger \cosh(\sqrt{a^2+\sigma}\zeta)$, where $A^\dagger$ is a constant of integration. Inserting this solution into (A.49d) yields the relation

$$\sqrt{a^2+\sigma}\sinh(\sqrt{a^2+\sigma})A^\dagger = W_c(1)h^\dagger + A^\dagger \int_0^1 \zeta W_c(\zeta)\cosh(\sqrt{a^2+\sigma}\zeta)\,\mathrm{d}\zeta. \tag{A.50}$$

Thus, (A.49b) and (A.50) define a two-dimensional linear system for $A^\dagger$ and $h^\dagger$. Setting the determinant of the corresponding matrix equal to zero provides the characteristic equation for the eigenvalues. In particular, if we define

$$\chi_c(\sigma;a) := \int_0^1 \zeta W_c(\zeta;a)\cosh(\sqrt{a^2+\sigma}\zeta)\,d\zeta, \tag{A.51a}$$

$$\chi_h(\sigma;a) := \int_0^1 \zeta W_h(\zeta;a)\cosh(\sqrt{a^2+\sigma}\zeta)\,d\zeta, \tag{A.51b}$$

then the characteristic equation determining the eigenvalues is given by

$$\begin{aligned}[W_h(1;a)-\sigma]\left[\chi_c(\sigma;a) - \sqrt{a^2+\sigma}\sinh(\sqrt{a^2+\sigma})\right]\\ -W_c(1;a)\left[\cosh(\sqrt{a^2+\sigma}) + \chi_h(\sigma;a)\right] = 0.\end{aligned} \tag{A.52}$$

A.2.2 Small-wavenumber asymptotics

The eigenvalues for $a \ll 1$ can be easily obtained using the characteristic equation (A.52). By seeking an asymptotic solution for the velocity w in (A.46), we find that

$$W_c(\zeta) = -\frac{1}{2}a^2 M\zeta^2 + O(a^4), \tag{A.53a}$$

$$W_h(\zeta) = \frac{1}{2}a^2\left[\left(\frac{1}{3}\zeta - 1\right)G + M\right]\zeta^2 + O(a^4). \tag{A.53b}$$

By naively seeking an expansion of the form $\sigma = \sigma_0 + o(1)$, it follows from (A.51a) and (A.51b) that $\chi_c, \chi_h = O(a^2)$. Using these facts in (A.52) yields $\sigma_0 = 0$ or $\sigma_0 = -n^2\pi^2$ for $n \in \mathbb{N}$. The former result implies that the top eigenvalue is small. Through a process of balancing terms in the characteristic equation (A.52) under the assumption $\sigma \ll 1$, we find that an appropriate expansion of the top eigenvalue takes the form $\sigma = a\sigma_1 + a^2\sigma_2 + O(a^3)$. By carrying out the relevant expansions in (A.52), one finds that

$$\sigma_1 = \pm i\left(\frac{M}{2}\right)^{1/2}, \quad \sigma_2 = \frac{5}{48}M - \frac{1}{6}G - \frac{1}{2}, \tag{A.54}$$

which agrees with the calculation presented in Section 2.5.1.

Appendix B

Supplementary material for Chapter 3

B.1 Properties of the indicator function

The indicator function X_k, defined as

$$X_k(\boldsymbol{x}, t) = \begin{cases} 1, & \boldsymbol{x} \in R_k(t), \\ 0, & \text{otherwise}, \end{cases} \tag{B.1}$$

and its derivatives play a major role in the averaging process and in the derivation of the macroscopic equations. Many of its properties were stated without proof in Chapter 3; hence, the goal of this appendix is to present the mathematical details of these.

We treat the indicator function within the framework of generalised functions and distributions. This enables us to rigorously define the derivatives of X_k despite the fact that this function is clearly discontinuous. We let ϕ denote an infinitely smooth test function with compact support on the set $R \times \mathbb{R}$ in space and time, where R denotes a sufficiently large spatial domain. Thus, we may write $\phi \in \mathcal{C}_0^\infty(R \times \mathbb{R})$. Using this test function, we define the derivatives of X_k in a distributional sense:

$$\int_{\mathbb{R}} \int_R (\partial_t X_k)\phi \,\mathrm{d}V\mathrm{d}t = -\int_{\mathbb{R}} \int_R X_k \partial_t \phi \,\mathrm{d}V\mathrm{d}t, \quad \forall \phi \in \mathcal{C}_0^\infty(R \times \mathbb{R}), \tag{B.2a}$$

$$\int_{\mathbb{R}} \int_R (\nabla X_k)\phi \,\mathrm{d}V\mathrm{d}t = -\int_{\mathbb{R}} \int_R X_k \nabla \phi \,\mathrm{d}V\mathrm{d}t, \quad \forall \phi \in \mathcal{C}_0^\infty(R \times \mathbb{R}). \tag{B.2b}$$

One interesting property of the indicator function is that its gradient acts as a delta function, picking out values on the interface of the k-th domain. To formalise this statement, consider a test function $\phi \in \mathcal{C}_0^\infty(R \times \mathbb{R})$. Then, from above definitions and the divergence

theorem, we have

$$\begin{aligned}\int_{\mathbb{R}}\int_{R}(\nabla X_k)\phi\,\mathrm{d}V\mathrm{d}t &= -\int_{\mathbb{R}}\int_{R} X_k\nabla\phi\,\mathrm{d}V\mathrm{d}t \\ &= -\int_{\mathbb{R}}\int_{R_k}\nabla\phi\,\mathrm{d}V\mathrm{d}t \\ &= -\int_{\mathbb{R}}\oint_{\partial R_k}\phi\,\boldsymbol{e}_n^k\,\mathrm{d}s\mathrm{d}t, \quad \forall\phi\in\mathcal{C}_0^\infty(R\times\mathbb{R}).\end{aligned} \tag{B.3}$$

We introduce the interfacial delta function, $\delta_{\partial R_k}(\boldsymbol{x})$, which is defined through the relation

$$\int_R \phi(\boldsymbol{x}')\delta_{\partial R_k}(\boldsymbol{x}'-\boldsymbol{x})\,\mathrm{d}V' = \int_{\partial R_k}\phi(\boldsymbol{x})\,\mathrm{d}s. \tag{B.4}$$

Using this definition, it follows that

$$\int_{\mathbb{R}}\int_{R}(\nabla X_k)\phi\,\mathrm{d}V\mathrm{d}t = \int_{\mathbb{R}}\int_{R}\phi(\boldsymbol{x}')\delta_{\partial R_k}(\boldsymbol{x}'-\boldsymbol{x})\boldsymbol{e}_n^k(\boldsymbol{x}')\,\mathrm{d}V'\mathrm{d}t, \quad \forall\phi\in\mathcal{C}_0^\infty(R\times\mathbb{R}). \tag{B.5}$$

Therefore, we may say that

$$\nabla X_k = -\delta_{\partial R_k}(\boldsymbol{x}-\boldsymbol{x}')\boldsymbol{e}_n^k \tag{B.6}$$

in a distributional sense.

Another important property of the indicator function is that it satisfies the topological equation given by

$$\partial_t X_k + \boldsymbol{v}\cdot\nabla X_k = 0 \tag{B.7}$$

in a distributional sense. Here, $\boldsymbol{v}$ is the interfacial velocity that has been smoothly extended into the domain $R_k(t)$. To prove this claim, consider a test function $\phi\in\mathcal{C}_0^\infty(R\times\mathbb{R})$. From the definition of distributional derivatives, we have

$$\begin{aligned}\int_{\mathbb{R}}\int_{R}\left(\partial_t X_k + \boldsymbol{v}\cdot\nabla X_k\right)\phi\,\mathrm{d}V\mathrm{d}t &= -\int_{\mathbb{R}}\int_{R}\left[\partial_t\phi+\nabla\cdot(\boldsymbol{v}\phi)\right]X_k\,\mathrm{d}V\mathrm{d}t \\ &= -\int_{\mathbb{R}}\int_{R_k(t)}\left[\partial_t\phi+\nabla\cdot(\boldsymbol{v}\phi)\right]\mathrm{d}V\mathrm{d}t, \\ &= -\int_{\mathbb{R}}\left[\int_{R_k(t)}\partial_t\phi\,\mathrm{d}V + \oint_{\partial R_k(t)}\phi\boldsymbol{v}\cdot\boldsymbol{e}_n^k\,\mathrm{d}s\right]\mathrm{d}t,\end{aligned} \tag{B.8}$$

for all $\phi\in\mathcal{C}_0^\infty(R\times\mathbb{R})$. By using the Reynolds Transport theorem on the terms inside the brackets, we then obtain

$$\begin{aligned}\int_{\mathbb{R}}\int_{R}\left(\partial_t X_k + \boldsymbol{v}\cdot\nabla X_k\right)\phi\,\mathrm{d}V\mathrm{d}t &= -\int_{\mathbb{R}}\frac{\mathrm{d}}{\mathrm{d}t}\left(\int_{R_k(t)}\phi\,\mathrm{d}V\right)\mathrm{d}t \\ &= -\left[\int_{R_k(t)}\phi\,\mathrm{d}V\right]_{t=-\infty}^{t=+\infty} \\ &= 0,\end{aligned} \tag{B.9}$$

for all $\phi \in \mathcal{C}_0^\infty(R \times \mathbb{R})$, due to the fact that ϕ has compact support in time.

The indicator function also satisfies the product rule. In the case of a scalar function f, we have

$$\begin{aligned}\int_R \nabla(X_k f)\phi \,\mathrm{d}V &= -\int_R X_k f \nabla\phi \,\mathrm{d}V \\ &= -\int_{R_k} f\nabla\phi \, dV \\ &= \int_{R_k} \left[\phi\nabla f - \nabla(f\phi)\right] \mathrm{d}V \\ &= \int_R X_k(\nabla f)\phi \,\mathrm{d}V - \oint_{\partial R_k} f\phi \boldsymbol{e}_n^k \,\mathrm{d}s.\end{aligned} \tag{B.10}$$

for all $\phi \in \mathcal{C}_0^\infty(R \times \mathbb{R})$. By integrating both side with respect to time and using the results of (B.3), we have that

$$\int_{\mathbb{R}}\int_R \nabla(X_k f)\phi \,\mathrm{d}V\mathrm{d}t = \int_{\mathbb{R}}\int_R \left[X_k(\nabla f) + f\nabla X_k\right]\phi \,\mathrm{d}V\mathrm{d}t, \quad \forall\phi \in \mathcal{C}_0^\infty(R \times \mathbb{R}). \tag{B.11}$$

Therefore,

$$\nabla(X_k f) = X_k \nabla f + f\nabla X_k \tag{B.12}$$

holds in a distributional sense. A similar sequence of steps can be used to prove the product rule when f is replaced by a vector quantity $\boldsymbol{w}$ or a tensor quantity $\mathbf{Q}$:

$$\nabla \cdot (X_k \boldsymbol{w}) = X_k \nabla \cdot \boldsymbol{w} + \boldsymbol{w} \cdot \nabla X_k, \tag{B.13a}$$

$$\nabla \cdot (X_k \mathbf{Q}) = X_k \nabla \cdot \mathbf{Q} + \mathbf{Q} \cdot \nabla X_k, \tag{B.13b}$$

Appendix C

Supplementary material for Chapter 4

C.1 Proof of monotonically decreasing energy

We now prove that the phase-field evolution equations monotonically decrease the energy of the system. We recall that these equations can be written in non-dimensional form as

$$\partial_t \phi = \nabla \cdot ((1-\phi^2)\nabla \mu), \tag{C.1a}$$

$$\mu = f'(\phi) - \varepsilon^2 (T_c/T)\nabla^2 \phi. \tag{C.1b}$$

The non-dimensional boundary conditions for this problem are given by

$$\varepsilon \partial_z \phi = g_0'((1+\phi)/2), \quad z = 0, \tag{C.1c}$$

$$\varepsilon \partial_z \phi = g_0'((1-\phi)/2), \quad z = 1, \tag{C.1d}$$

together with

$$\partial_z \mu = 0, \quad z = 0, 1. \tag{C.1e}$$

The non-dimensional energy can be written as

$$\begin{aligned} F = &\int_\Omega \left[f(\phi) + \frac{1}{2}\varepsilon^2 (T_c/T)|\nabla \phi|^2 \right] \mathrm{d}x\mathrm{d}z \\ &+ 2\varepsilon (T_c/T) \int_{z=0} g_0((1+\phi)/2)\,\mathrm{d}x + 2\varepsilon (T_c/T) \int_{z=1} g_0((1-\phi)/2)\,\mathrm{d}x. \end{aligned} \tag{C.2}$$

Differentiating this expression in time and applying the divergence theorem gives

$$\begin{aligned} \frac{\mathrm{d}F}{\mathrm{d}t} = &\int_\Omega \left[f'(\phi) - \varepsilon^2 (T_c/T)\nabla^2 \phi \right] \partial_t \phi \,\mathrm{d}x\mathrm{d}z \\ &+ \varepsilon (T_c/T) \int_{z=0} \left[-\varepsilon \partial_z \phi + g_0'((1+\phi)/2) \right] \partial_t \phi \,\mathrm{d}x \\ &+ \varepsilon (T_c/T) \int_{z=1} \left[\varepsilon \partial_z \phi - g_0'((1-\phi)/2) \right] \partial_t \phi \,\mathrm{d}x. \end{aligned} \tag{C.3}$$

The boundary terms in this expression vanish due to the boundary conditions for ϕ given in (C.1c) and (C.1d). By using (C.1a) and (C.1b) in the remaining integral, the rate of change of energy can be written as

$$\frac{\mathrm{d}F}{\mathrm{d}t} = \int_\Omega \mu\nabla\cdot((1-\phi^2)\nabla\mu)\,\mathrm{d}x\mathrm{d}z. \tag{C.4}$$

Another application of the divergence theorem yields

$$\frac{\mathrm{d}F}{\mathrm{d}t} = -\int_\Omega (1-\phi^2)|\nabla\mu|^2 + \int_{z=0}(1-\phi^2)\mu\partial_z\mu\,\mathrm{d}x + \int_{z=1}(1-\phi^2)\mu\partial_z\mu\,\mathrm{d}x. \tag{C.5}$$

The boundary terms now vanish due the to the no-flux conditions on the substrate (C.1e). Based on physical grounds, the order parameter is assumed to satisfy $-1<\phi<1$; therefore, we have

$$\frac{\mathrm{d}F}{\mathrm{d}t} \leq 0, \tag{C.6}$$

which completes the proof.

C.2 Calculation of the equilibrium contact angle

The parameter β that appears in the boundary conditions for the order parameter (4.29d) can be related to the equilibrium contact angle θ by applying the results of Modica [106]. To begin, we first formulate the energy minimisation problem for the stationary states of the system in the near-criticality limit (4.29). This requires writing the boundary conditions for the order parameter as

$$\delta\nabla\phi\cdot\boldsymbol{e}_n + g'(\phi) = 0, \quad z=0,1, \tag{C.7}$$

where $\boldsymbol{e}_n$ denotes the unit normal vector to the boundary and the function g is defined as

$$g(s) = \begin{cases} \beta(s-s^3/3), & z=0,\\ -\beta(s-s^3/3), & z=1. \end{cases} \tag{C.8}$$

With these definitions, the energy minimisation problem can be written as

$$\min\left\{\int_\Omega \left[2f(\phi)+\delta^2|\nabla\phi|^2\right]\,\mathrm{d}x\mathrm{d}z + \int_\omega 2\delta g(\phi)\,\mathrm{d}x\right\}, \tag{C.9}$$

where ω denotes the walls and $f(\phi)=(1/2)(\phi^2-\chi)^2$. We can now use Modica's expression for the contact angle which bears a distinct similarity to Young's law:

$$\cos\theta = \frac{\sigma_{WM}(\sqrt{\chi}) - \sigma_{WM}(-\sqrt{\chi})}{\sigma_{AB}}. \tag{C.10}$$

In this expression, the function σ_{WM} is defined according to

$$\sigma_{WM}(u) = \inf_v \left\{ g(v) + \left| \int_v^u (2f(r))^{1/2} \, \mathrm{d}r \right| \right\}. \tag{C.11}$$

It represents a surface energy between the walls and the materials that takes into account the effects of possible compositional boundary layers. The parameter σ_{AB} denotes the surface energy associated with an A-B interface and it is given by

$$\sigma_{AB} = \int_{-\sqrt{\chi}}^{\sqrt{\chi}} (2f(r))^{1/2} \, \mathrm{d}r = \frac{4}{3} \chi^{3/2}. \tag{C.12}$$

Note this expression is a generalisation of (4.70) for $\chi \leq 1$. The calculation of the equilibrium contact angle is now a matter of solving two minimisation problems that result from evaluating σ_{WM}. We will write $\sigma_{WM}(\pm\sqrt{\chi}) = \inf_v\{S_\pm(v)\}$, where the objective function $S_\pm$ is given by

$$S_\pm(v) = \beta(v - v^3/3) + \left| \int_v^{\pm\sqrt{\chi}} |r^2 - \chi| \, \mathrm{d}r \right|. \tag{C.13}$$

Moreover, we will assume that $\beta \leq 1$ and $\chi \leq 1$.

We first calculate $\sigma_{WM}(-\sqrt{\chi}) = \inf_v\{S_-(v)\}$. Upon evaluating the integral in (C.13), we find that

$$S_-(v) = \begin{cases} \beta(v - v^3/3) - v^3/3 + \chi v + (2/3)\chi^{3/2}, & v < \sqrt{\chi}, \\ \beta(v - v^3/3) + v^3/3 - \chi v + 2\chi^{3/2}, & v \geq \sqrt{\chi}. \end{cases} \tag{C.14}$$

Although this function and its first derivative with respect to v are continuous everywhere, some care still needs to be taken when minimising it. The overall minimisation procedure is straightforward and one finds that the minimum is located at $v_1 = -\sqrt{(\chi+\beta)/(1+\beta)} < -\sqrt{\chi}$. Therefore, we have that

$$\sigma_{WM}(-\sqrt{\chi}) = S_-(v_1) = \frac{2}{3}\frac{(\chi+\beta)^{3/2}}{(1+\beta)^{1/2}} + \frac{2}{3}\chi^{3/2}. \tag{C.15}$$

We follow the same procedure for calculating $\sigma_{WM}(\sqrt{\chi})$. In this case, the objective function S_+ can be written as

$$S_+(v) = \begin{cases} \beta(v - v^3/3) + v^3/3 - \chi v + (2/3)\chi^{3/2}, & v > -\sqrt{\chi}, \\ \beta(v - v^3/3) - v^3/3 + \chi v + 2\chi^{3/2}, & v \leq -\sqrt{\chi}, \end{cases} \tag{C.16}$$

which is again continuous and differentiable everywhere. However, there are now two potential minimisers. One of these occurs when $v = v_1$, with v_1 given above. The other only occurs when $\chi \geq \beta$ and, in this case, is given by $v_2 = \sqrt{(\chi-\beta)/(1-\beta)} > -\sqrt{\chi}$. To determine the global minimiser, we consider the function

$$H(\beta) = S_+(v_1) - S_+(v_2) = \frac{4}{3}\chi^{3/2} + \frac{2}{3}\frac{(\chi-\beta)^{3/2}}{(1-\beta)^{1/2}} - \frac{2}{3}\frac{(\chi+\beta)^{3/2}}{(1+\beta)^{1/2}} \tag{C.17}$$

which is defined on the interval $0 \leq \beta \leq \chi$. The derivative of this function is given by

$$H'(\beta) = -\left(\frac{\chi-\beta}{1-\beta}\right)^{1/2}\left(1-\frac{1}{3}\frac{\chi-\beta}{1-\beta}\right) - \left(\frac{\chi+\beta}{1+\beta}\right)^{1/2}\left(1-\frac{1}{3}\frac{\chi+\beta}{1+\beta}\right). \tag{C.18}$$

All of the terms in brackets are positive and hence $H'(\beta) < 0$. Furthermore, by direct calculation we have that $H(0) > 0$ and $H(\chi) < 0$ if $0 < \chi < 1$. Therefore, the function H has a unique root, denoted by β_w, that lies in the interval $0 < \beta_w < \chi$. If $\beta < \beta_w$ then $H(\beta) > 0$ and hence $\sigma_{WM}(\sqrt{\chi}) = S_+(v_2)$. Alternatively, if $\beta > \beta_w$ then $\sigma_{WM}(\sqrt{\chi}) = S_+(v_1)$.

We are now in a position to evaluate the equilibrium contact angle using the expression in (C.10). There are two cases to consider. If $\beta < \beta_w < \chi$ then the contact angle satisfies

$$\cos\theta = \frac{1}{2}\frac{(1+\beta/\chi)^{3/2}}{(1+\beta)^{1/2}} - \frac{1}{2}\frac{(1-\beta/\chi)^{3/2}}{(1-\beta)^{1/2}}. \tag{C.19}$$

When $\beta > \beta_w$ the contact angle is given by $\theta = 0$. The parameter $\beta_w = \beta_w(\chi)$, therefore, corresponds to the critical value of β for a given temperature χ at which the walls become perfectly wetting. Calculating this value amounts to setting $\cos\theta = 1$ and $\beta = \beta_w$ in (C.19), and then solving for β_w.

Many of the calculations in Chapter 4 were concerned with the case when $\chi = 1$. When this is true, the expression for the equilibrium contact angle (C.19) simplifies significantly and becomes

$$\cos\theta = \begin{cases} \beta, & \beta < 1, \\ 1, & \beta \geq 1. \end{cases} \tag{C.20}$$

When the temperature is close to the critical point, $\chi \ll 1$, an asymptotic solution for β_w can be obtained. This can be found by writing $\beta = \beta_w$, $\beta_w = \chi B + o(\chi)$ in (C.19) with $\cos\theta = 1$. The leading-order equation that results after expanding around small χ is

$$(1+B)^{3/2} - (1-B)^{3/2} = 2, \tag{C.21}$$

which has solution $B \simeq 0.68125$. The fact that β_w scales like χ when $\chi \ll 1$ implies that even small values of β will correspond to strongly-biased walls when the system is sufficiently close to the bulk critical point.

C.3 Details of the sharp-interface limit

In this appendix the details of the change of variable that is used in the sharp-interface limit will be presented. This change of variable is given by

$$x = r_1(s,\tau') - \delta\eta\partial_s r_2(s,\tau'), \tag{C.22a}$$

$$z = r_2(s,\tau') + \delta\eta\partial_s r_1(s,\tau'), \tag{C.22b}$$

$$\tau = \tau'. \tag{C.22c}$$

The curve $\boldsymbol{r} = r_1\boldsymbol{e}_x + r_2\boldsymbol{e}_z$ is parameterised by its arclength s which leads to the identity $(\partial_s r_1)^2 + (\partial_s r_2)^2 \equiv 1$. By applying the chain rule we obtain

$$\partial_s = (\partial_s r_1 - \delta\eta\partial_{ss} r_2)\,\partial_x + (\partial_s r_2 + \delta\eta\partial_{ss} r_1)\,\partial_z, \tag{C.23a}$$

$$\partial_\eta = -\delta(\partial_s r_2)\partial_x + \delta(\partial_s r_1)\partial_z, \tag{C.23b}$$

$$\partial_{\tau'} = (\partial_{\tau'} x)\partial_x + (\partial_{\tau'} z)\partial_z + \partial_\tau, \tag{C.23c}$$

where $\partial_{ss} = (\partial_s)^2$ denotes the second derivative with respect to the arclength. In theory, this system can be inverted directly to obtain explicit solution for ∂_x, ∂_z, and ∂_τ; however, these expressions are very cumbersome and impractical to use, especially when building operators that are based on higher derivatives such as the Laplacian. Instead, we solve this system asymptotically by expanding its solution in powers of δ:

$$\partial_x = \delta^{-1}\partial_x^{(-1)} + \partial_x^{(0)} + \delta\partial_x^{(1)} + O(\delta^2), \tag{C.24a}$$

$$\partial_z = \delta^{-1}\partial_z^{(-1)} + \partial_z^{(0)} + \delta\partial_z^{(1)} + O(\delta^2), \tag{C.24b}$$

$$\partial_\tau = \delta^{-1}\partial_\tau^{(-1)} + O(1). \tag{C.24c}$$

By inserting this expansion into (C.23) and solving the subproblems at each power of δ, we obtain

$$\partial_x^{(-1)} = -(\partial_s r_2)\partial_\eta, \quad \partial_x^{(0)} = (\partial_s r_1)\partial_s, \quad \partial_x^{(1)} = \kappa\eta(\partial_s r_1)\partial_s, \tag{C.25a}$$

$$\partial_z^{(-1)} = (\partial_s r_1)\partial_\eta, \quad \partial_z^{(0)} = (\partial_s r_2)\partial_s, \quad \partial_z^{(1)} = \kappa\eta(\partial_s r_2)\partial_s, \tag{C.25b}$$

$$\partial_\tau^{(-1)} = -v_n\partial_\eta, \tag{C.25c}$$

where $\kappa = (\partial_s r_1)(\partial_{ss} r_2) - (\partial_s r_2)(\partial_{ss} r_1)$ and $v_n = (\partial_{\tau'}\boldsymbol{r})\cdot\boldsymbol{\nu}$ denote the curvature and the normal velocity of $\boldsymbol{r}$, respectively, where $\nu = -(\partial_s r_2)\boldsymbol{e}_x + (\partial_s r_1)\boldsymbol{e}_z$ is the normal vector to this curve. The tangent vector is given by $\boldsymbol{t} = (\partial_s r_1)\boldsymbol{e}_x + (\partial_s r_2)\boldsymbol{e}_z$. In deriving (C.25), we have used the Serret–Frenet relation $\partial_s\boldsymbol{t} = \kappa\boldsymbol{\nu}$, which holds because an arclength parameterisation is used.

Using the asymptotic expressions for the first derivatives, the gradient operator can now be asymptotically constructed. To begin, we first expand it as

$$\nabla = \delta^{-1}\nabla^{(-1)} + \nabla^{(0)} + \delta\nabla^{(1)} + O(\delta^2). \tag{C.26}$$

Then, by making use of the definitions of the tangent and normal vectors, and the asymptotic solutions in (C.25), we find that

$$\nabla^{(-1)} = \boldsymbol{\nu}\,\partial_\eta, \quad \nabla^{(0)} = \boldsymbol{t}\,\partial_s, \quad \nabla^{(1)} = \kappa\eta\,\boldsymbol{t}\,\partial_s. \tag{C.27}$$

The Laplacian operator, which in this context is most conveniently denoted by Δ, can be determined directly from the asymptotic expansion of the gradient using the fact that $\Delta = \nabla \cdot \nabla$. By writing

$$\Delta = \delta^{-2}\Delta^{(-2)} + \delta^{-1}\Delta^{(-1)} + \Delta^{(0)} + O(\delta) \tag{C.28}$$

and then using (C.27), we find that

$$\Delta^{(-2)} = \partial_{\eta\eta}, \quad \Delta^{(-1)} = -\kappa\,\partial_{\eta}, \quad \Delta^{(0)} = \partial_{ss} - \kappa^2\eta\,\partial_{\eta}. \tag{C.29}$$

Bibliography

[1] H. Abels, H. Garcke, and G. Grün. Thermodynamically consistent, frame indifferent diffuse interface models for incompressible two-phase flows with different densities. *Math. Models Methods Appl. Sci.*, 22(3):1150013, 2012.

[2] A. Acrivos, M. J. Shah, and E. E. Petersen. On the flow of a non-Newtonian liquid on a rotating disk. *J. Appl. Phys.*, 31(6):963–968, 2004.

[3] T. Ahnert, A. Münch, and B. Wagner. Two-phase flow model for concentrated suspensions. WIAS Preprint No. 1901, 2013.

[4] Satish Balay, Mark F. Adams, Jed Brown, Peter Brune, Kris Buschelman, Victor Eijkhout, William D. Gropp, Dinesh Kaushik, Matthew G. Knepley, Lois Curfman McInnes, Karl Rupp, Barry F. Smith, and Hong Zhang. PETSc users manual. Technical Report ANL-95/11 - Revision 3.4, Argonne National Laboratory, 2013.

[5] Satish Balay, Mark F. Adams, Jed Brown, Peter Brune, Kris Buschelman, Victor Eijkhout, William D. Gropp, Dinesh Kaushik, Matthew G. Knepley, Lois Curfman McInnes, Karl Rupp, Barry F. Smith, and Hong Zhang. PETSc Web page, 2014.

[6] Satish Balay, William D. Gropp, Lois Curfman McInnes, and Barry F. Smith. Efficient management of parallelism in object oriented numerical software libraries. In E. Arge, A. M. Bruaset, and H. P. Langtangen, editors, *Modern Software Tools in Scientific Computing*, pages 163–202. Birkhäuser Press, 1997.

[7] R. C. Ball and R. L. H. Essery. Spinodal decomposition and pattern formation near surfaces. *J. Phys.: Condens. Matter*, 2(51):10303, 1990.

[8] N. Bassou and Y. Rharbi. Role of Bénard-Marangoni instabilities during solvent evaporation in polymer surface corrugations. *Langmuir*, 25(1):624–632, 2009.

[9] H. Bénard. Les tourbillons cellulaires dans une nappe liquide. *Rev. Gen. Sci. Pures Appl.*, 11:1261–1271, 1900.

[10] H. Bénard. Les tourbillons cellulaires dans une nappe liquide: Méthodes optiques d'observation et d'enregistrement. *J. Phys. Theor. Appl.*, 10(1):254–266, 1901.

[11] H. Bénard. Les tourbillons cellulaires dans une nappe liquide transportant de la chaleur par convection en regime permanent. *Ann. Chim. Phys.*, 23:62–144, 1901.

[12] C. Bender and S. Orszag. *Advanced Mathematical Methods for Scientists and Engineers*. Springer, 1999.

[13] D. J. Benney and S. Rosenblat. Stability of spatially varying and time-dependent flows. *Phys. Fluids*, 7(8):1385–1386, 1964.

[14] J. C. Berg, M. Boudart, and A. Acrivos. Natural convection in pools of evaporating liquids. *J. Fluid. Mech.*, 24(4):721–735, 1966.

[15] G. W. Bergantz and J. Ni. A numerical study of sedimentation by dripping instabilities in viscous fluids. *Int. J. Multiphase Flow*, 25(2):307–320, 1999.

[16] R. Bhandari and I. Stadler. Grid parity analysis of solar photovoltaic systems in Germany using experience curves. *Solar Energy*, 83(9):1634–1644, 2009.

[17] K. Binder. Surface effects on polymer blends and block copolymer melts: theoretical concepts of surface enrichment, surface induced phase separation and ordering. *Acta Polymer.*, 46(3):204–225, 1995.

[18] K. Binder. Spinodal decomposition in confined geometry. *J. Non-Equilib. Thermodyn.*, 23(1):1–44, 1998.

[19] K. Binder. *Kinetics of Phase Transitions*, chapter 2: Spinodal Decomposition versus Nucleation and Growth. CRC Press, 2009.

[20] K. Binder, C. Billotet, and P. Mirold. On the theory of spinodal decomposition in solid and liquid binary mixtures. *Z. Phys. B Con. Mat.*, 30(2):183–195, 1978.

[21] K. Binder, S. Puri, S. K. Das, and J. Horbach. Phase separation in confined geometries. *J. Stat. Phys.*, 138:51–84, 2010.

[22] D. P. Birnie III. Rational solvent selection strategies to combat striation formation during spin coating of thin films. *J. Mater. Res*, 16(4):1145–1154, 2001.

[23] M. J. Block. Surface tension as the cause of Bénard cells and surface deformation in a liquid film. *Nature*, 178:650–651, 1956.

[24] E. Bodenschatz, W. Pesch, and G. Ahlers. Recent developments in Rayleigh–Bénard convection. *Ann. Rev. Fluid Mech.*, 32(1):709–778, 2000.

[25] C. S. Bohun and C. Breward. Yolk dynamics in amphibian embryos. *Mathematics-in-Industry Case Studies*, 1:99–119, 2009.

[26] D. E. Bornside, C. W. Macosko, and L. E. Scriven. Spin coating: One-dimensional model,. *J. Appl. Phys.*, 66(11):5185–5193, 1989.

[27] BP. BP Statistical Review of World Energy June 2011. Microsoft Excel spreadsheet data, June 2011. Available online at `www.bp.com/statisticalreview`.

[28] A. J. Bray. Theory of phase-ordering kinetics. *Advances in Physics*, 43(3):357–459, 1994.

[29] C. J. W. Breward, H. M. Byrne, and C. E. Lewis. The role of cell-cell interactions in a two-phase model for avascular tumour growth. *J. Math. Biol.*, 45(2):125–152, 2002.

[30] J. P. Burelbach, S. G. Bankoff, and S. H. Davis. Nonlinear stability of evaporating/condensing liquid films. *J. Fluid Mech.*, 195(1):463–494, 1988.

[31] G. A. Buxton and N. Clarke. Ordering polymer blend morphologies via solvent evaporation. *Europhys. Lett*, 78(5):56006, 2007.

[32] J. W. Cahn. On spinodal decomposition. *Acta Metall.*, 9:795–801, 1961.

[33] J. W. Cahn. Phase separation by spinodal decomposition in isotropic systems. *J. Chem. Phys.*, 42(1):93–99, 1965.

[34] J. W. Cahn. Critical point wetting. *J. Chem. Phys.*, 66:3667–3672, 1977.

[35] J. W. Cahn and J. E. Hilliard. Free energy of a nonuniform system. I. Interfacial free energy. *J. Chem. Phys.*, 28(8):258–267, 1958.

[36] A. H. Carter. *Classical and Statistical Thermodynamics*. Prentice Hall, 2001.

[37] W. C. Carter, J. E. Taylor, and J. W. Cahn. Variational methods for microstructural-evolution theories. *JOM*, 49(12):30–36, 1997.

[38] S. Cataldo, C. Sartorio, F. Giannazzo, A. Scandurra, and B. Pignataro. Self-organization and nanostructural control in thin film heterojunctions. *Nanoscale*, 2014.

[39] D. M. Chapin, C. S. Fuller, and G. L. Pearson. A new silicon p-n junction photocell for converting solar radiation into electrical power. *J. Appl. Phys.*, 25(5):676–677, 1954.

[40] J. P. F. Charpin, M. Lombe, and T. G. Myers. Spin coating of non-Newtonian fluids with a moving front. *Phys. Rev. E*, 76(1):016312, 2007.

[41] F. Chauvet, S. Dehaeck, and P. Colinet. Threshold of Bénard–Marangoni instability in drying liquid films. *Europhys. Lett.*, 99(3):34001, 2012.

[42] L.-M. Chen, Z. Hong, G. Li, and Y. Yang. Recent progress in polymer solar cells: manipulation of polymer: fullerene morphology and the formation of efficient inverted polymer solar cells. *Adv. Mater.*, 21(14-15):1434–1449, 2009.

[43] L.-Q. Chen. Phase-field models for microstructure evolution. *Annu. Rev. Mater. Res.*, 32(1):113–140, 2002.

[44] R. P. Chhabra and J. F. Richardson. *Non-Newtonian Flow and Applied Rheology: Engineering Applications*. Elsevier, second edition, 2008.

[45] P. Colinet, J. C. Legros, and M. G. Velarde. *Nonlinear Dynamics of Surface-Tension-Driven Instabilities*. Wiley-VCH, 2001.

[46] H. E. Cook. Brownian motion in spinodal decomposition. *Acta Metall.*, 18(3):297–306, 1970.

[47] F. Coquel, K. El Amine, E. Godlewski, B. Perthame, and P. Rascle. A numerical method using upwind schemes for the resolution of two-phase flows. *J. Comput. Phys.*, 136(2):272–288, 1997.

[48] S. Coveney and N. Clarke. Breakup of a transient wetting layer in polymer blend thin films: Unification with 1D phase equilibria. *Phys. Rev. Lett.*, 111(12):125702, 2013.

[49] R. V. Craster and O. K. Matar. Dynamics and stability of thin liquid films. *Rev. Mod. Phys.*, 81(3):1131–1198, 2009.

[50] S. K. Das, J. Horbach, and K. Binder. Kinetics of phase separation in thin films: Lattice versus continuum models for solid binary mixtures. *Phys. Rev. E*, 79(2):021602, 2009.

[51] S. K. Das, S. Puri, J. Horbach, and K. Binder. Kinetics of phase separation in thin films: Simulations for the diffusive case. *Phys. Rev. E*, 72:061603, 2005.

[52] S. H. Davis. The stability of time-periodic flows. *Ann. Rev. Fluid Mech.*, 8(1):57–74, 1976.

[53] S. H. Davis. *Theory of Solidification*. Cambridge Monographs on Mechanics. Cambridge University Press, 2001.

[54] B.-J. de Gans, P. C. Duineveld, and U. S. Schubert. Inkjet printing of polymers: State of the art and future developments. *Adv. Mater.*, 16(3):203–213, 2004.

[55] F. Doumenc, T. Boeck, B. Guerrier, and M. Rossi. Transient Rayleigh–Bénard–Marangoni convection due to evaporation: a linear non-normal stability analysis. *J. Fluid Mech.*, 648:521–539, 2010.

[56] D. A. Drew. Mathematical modeling of two-phase flow. *Ann. Rev. Fluid Mech.*, 15(1):261–291, 1983.

[57] D. A. Drew and S. L. Passman. *Theory of Multicomponent Fluids*. Springer, 1999.

[58] A. D. F. Dunbar, P. Mokarian-Tabari, A. J. Parnell, S. J. Martin, M. W. A. Skoda, and R. A. L. Jones. A solution concentration dependent transition from self-stratification to lateral phase separation in spin-cast PS:d-PMMA thin films. *Eur. Phys. J. E*, 31(4):369–375, 2010.

[59] M. Dziwnik, M. Korzec, A. Münch, and Wagner B. Stability analysis of non-constant base states in thin film equations. *SIAM J. Appl. Math.*, 12(2):755–780, 2014.

[60] S. Ebbens, R. Hodgkinson, A. J. Parnell, A. Dunbar, S. J. Martin, P. D. Topham, N. Clark, and J. R. Howse. *In situ* imaging and height reconstruction of phase separation processes in polymer blends during spin coating. *ASC Nano*, 5(6):5124–5131, 2011.

[61] A. Einstein. Eine neue Bestimmung der Moleküldimensionen. *Annalen der Physik*, 324(2):289–306, 1906.

[62] A. G. Emslie, F. T. Bonner, and L. G. Peck. Flow of a viscous liquid on a rotating disk. *J. Appl. Phys.*, 29(5):858–862, 1958.

[63] M. H. Eres, D. E. Weidner, and L. Schwartz. Three-dimensional direct numerical simulation of surface-tension-gradient effects on the leveling of an evaporating multicomponent fluid. *Langmuir*, 15(5):1859–1871, 1999.

[64] M. C. Flemings. Solidification processing. *Metall. Trans.*, 5(10):2121–2134, 1974.

[65] J. C. Flitton and J. R. King. Surface-tension-driven dewetting of Newtonian and power-law fluids. *J. Eng. Math.*, 50(2–3):241–266, 2004.

[66] T. D. Foster. Stability of a homogeneous fluid cooled uniformly from above. *Phys. Fluids*, 8(7):1249–1257, 2004.

[67] A. C. Fowler. *Mathematical Models in the Applied Sciences*. Cambridge University Press, 1997.

[68] M. Geoghegan and G. Krausch. Wetting at polymer surfaces and interfaces. *Prog. Polym. Sci.*, 28(2):261–302, 2003.

[69] A. Goetzberger, C. Hebling, and H.-W. Schock. Photovoltaic materials, history, status and outlook. *Mat. Sci. Eng. R*, 40(1):1–46, 2003.

[70] S. Günes, H. Neugebauer, and N. S. Sariciftci. Conjugated polymer-based organic solar cells. *Chem. Rev.*, 107(4):1324–1338, 2007.

[71] B. Haut and P. Colinet. Surface-tension-driven instabilities of a pure liquid layer evaporating into an inert gas. *J. Colloid Interf. Sci.*, 285(1):296–305, 2005.

[72] M. G. Hennessy, V. M. Burlakov, , A. Münch, B. Wagner, and A. Goriely. Propagating topological transformation in thin immiscible bilayer films. *Europhys. Lett.*, 105(6):66001, 2014.

[73] M. G. Hennessy, V. M. Burlakov, A. Goriely, A. Münch, and B. Wagner. Controlled topological transitions in thin film phase separation. *Submitted*, 2014. Preprint available at arXiv:1402.6890.

[74] M. G. Hennessy and A. Münch. A multiple-scale analysis of evaporation induced Marangoni convection. *SIAM J. Appl. Math.*, 73(2):974–1001, 2013.

[75] M. G. Hennessy and A. Münch. Dynamics of a slowly evaporating solvent–polymer mixture with a deformable upper surface. *IMA J. Appl. Math.*, 2014. In press.

[76] S. Y. Heriot and R. A. L. Jones. An interfacial instability in a transient wetting layer leads to lateral phase separation in thin spin-cast polymer-blend films. *Nat. Mater.*, 4(10):782–786, 2005.

[77] H. Hoppea and N. S. Sariciftci. Organic solar cells: An overview. *J. Mater. Res*, 19(7):1924–1945, 2004.

[78] P. Howell and M. Muldoon. Two-phase modelling of air bubbles in ice cream. Technical report, ESGI 46, 2003. Available at `www.maths-in-industry.org`.

[79] S. D. Howison, J. A. Moriarty, J. R. Ockendon, E. L. Terrill, and S.K. Wilson. A mathematical model for drying paint layers. *J. Engrg. Math.*, 32(4):377–394, 1997.

[80] M Ishii and T. Hibiki. *Thermo-Fluid Dynamics of Two-Phase Flow*. Springer, second edition, 2011.

[81] D. Jacqmin. Contact-line dynamics of a diffuse fluid interface. *J. Fluid Mech.*, 402:57–88, 2000.

[82] J. Jaczewska, A. Budkowski, A. Bernasik, E. Moons, and J. Rysz. Polymer vs solvent diagram of film structures formed in spin-cast poly(3-alkylthiophene) blends. *Macromolecules*, 41(13):4802–4810, 2008.

[83] P. K. Jaiswal, K. Binder, and S.Puri. Formation of metastable structures by phase separation triggered by initial composition gradients in thin films. *J. Chem. Phys.*, 137:064704, 2012.

[84] P. K. Jaiswal, S. Puri, and K. Binder. Phase separation in thin films: Effect of temperature gradients. *Europhys. Lett.*, 103(6):66003, 2013.

[85] P. K. Jaiswal, S. Puri, and S. K. Das. Hydrodynamic crossovers in surface-directed spinodal decomposition and surface enrichment. *Europhys. Lett.*, 97(1):16005, 2012.

[86] R. A. L. Jones, L. J. Norton, E. J. Kramer, F. S. Bates, and P. Wiltzius. Surface-directed spinodal decomposition. *Phys. Rev. Lett.*, 66(10):1326–1329, 1991.

[87] P. C. Jukes, S. Y. Heriot, J. S. Sharp, and R. A. L. Jones. Time-resolved light scattering studies of phase separation in thin film semiconducting polymer blends during spin-coating. *Macromolecules*, 38(6):2030–2032, 2005.

[88] K. H. Kang and C. K. Choi. A theoretical analysis of the onset of surface-tension-driven convection in a horizontal liquid layer cooled suddenly from above. *Phys. Fluids*, 9(7):7–15, 1997.

[89] A. Karim, J. F. Douglas, B. P. Lee, S. C. Glotzer, J. A. Rogers, R. J. Jackman, E. J. Amis, and G. M. Whitesides. Phase separation of ultrathin polymer-blend films on patterned substrates. *Phys. Rev. E*, 57(6):R6273–R6276, 1998.

[90] R. F. Katz and Y. Takei. Consequences of viscous anisotropy in a deforming, two-phase aggregate. Part 2. Numerical solutions of the full equations. *J. Fluid. Mech.*, 734:456–485, 2013.

[91] J. Kevorkian and J. D. Cole. *Multiple Scale and Singular Perturbation Methods.* Springer, 1996.

[92] L. S. Kimpton, J. P. Whiteley, S. L. Waters, J. R. King, and J. M. Oliver. Multiple travelling-wave solutions in a minimal model for cell motility. *Math. Med. Biol.*, 30(3):241–272, 2013.

[93] L. S. Kimpton, J. P. Whiteley, S. L. Waters, and J. M. Oliver. On a poroviscoelastic model for cell crawling. *J. Math. Biol.*, pages 1–39, 2014.

[94] A. King, J. R. Munch and B. Wagner. Linear stability of a ridge. *Nonlinearity*, 19(12):2813–2832, 2006.

[95] J. R. King and J. M. Oliver. Thin-film modelling of poroviscous free surface flows. *Eur. J. Appl. Math.*, 16(4):519–553, 2005.

[96] S. Kojima, T. Moriga, and K. Takenouchi. The leveling of thermosetting water-borne coatings. Part III: Leveling under controlled conditions. *Polym. Eng. Sci.*, 35(24):1949–1954, 1995.

[97] E. L. Koschmieder. *Bénard Cells and Taylor Vortices.* Cambridge University Press, 1993.

[98] G. Krausch. Surface induced self assembly in thin polymer films. *Mater. Sci. Eng.: R: Reports*, 14(1–2), 1995.

[99] G. Krausch, C.-A. Dai, E. J. Kramer, and F. S. Bates. Real space observation of dynamic scaling in a critical polymer mixture. *Phys. Rev. Lett.*, 71:3669–3672, 1993.

[100] W.-M. Kulicke and R. Kniewske. The shear viscosity dependence on concentration, molecular weight, and shear rate of polystyrene solutions. *Rheol. Acta*, 23(1):75–83, 1984.

[101] J. H. Lai. An investigation of spin coating of electron resists. *Polym. Eng. Sci.*, 19(15):1117–1121, 1979.

[102] C. J. Lawrence and W. Zhou. Spin coating of non-Newtonian fluids. *J. Non-Newton. Fluid*, 39(2):137–187, 1991.

[103] W. Lick. The instability of a fluid layer with time-dependent heating. *J. Fluid Mech.*, 21(3):565–576, 1965.

[104] H. Machrafi, A. Rednikov, P. Colinet, and P. C. Dauby. Bénard instabilities in a binary-liquid layer evaporating into an inert gas. *J. Colloid Interf. Sci.,*, 349(1):331–353, 2010.

[105] H. Machrafi, A. Rednikov, P. Colinet, and P. C. Dauby. Bénard instabilities in a binary-liquid layer evaporating into an inter gas: Stability of quasi-stationary and time-dependent reference profiles. *Eur. Phys. J. Special Topics*, 192(1):71–81, 2011.

[106] L. Modica. Gradient theory of phase transitions with boundary contact energy. *Ann. I. H. Poincaré-A.N.*, 4(5):487–512, 1987.

[107] P. Mokarian-Tabari, M. Geoghegan, J. R. Howse, S. Y. Heriot, R. L. Thompson, and R. A. L. Jones. Quantitative evaluations of evaporation rate during spin-coating of polymer blend films: Control of film structure through defined-atmosphere solvent-casting. *Eur. Phys. J. E*, 33(4):283–289, 2010.

[108] E. Moons. Conjugated polymer blends: linking film morphology to performance of light emitting diodes and photodiodes. *J. Phys.: Condens. Matter*, 14(47):12235–12260, 2002.

[109] J. A. Moriarty, L. W. Schwartz, and E. O. Tuck. Unsteady spreading of thin liquid films with small surface tension. *Phys. Fluids*, 3(5):733–742, 1991.

[110] O. Morton. Solar energy: A new day dawning?: Silicon Valley sunrise. *Nature*, 443(7107):19–22, 2006.

[111] W. W. Mullins and R. F. Sekerka. Morphological stability of a particle growing by diffusion or heat flow. *J. Appl. Phys.*, 34(2):323–329, 1963.

[112] A. Münch, C. P. Please, and B. Wagner. Spin coating of an evaporating polymer solution. *Phys. Fluids*, 23(10):102101, 2011.

[113] A. Münch and B. Wagner. Contact-line instability of dewetting thin films. *Physica D*, 209(1):178–190, 2005.

[114] A. Münch and B. Wagner. Impact of slippage on the morphology and stability of a dewetting rim. *J. Phys.: Condens. Matter*, 23(18):184101, 2011.

[115] T. G. Myers. Thin films with high surface tension. *SIAM Review*, 40(3):441–462, 1998.

[116] T. G. Myers. Application of non-Newtonian models to thin film flow. *Phys. Rev. E*, 72(6):066302, 2005.

[117] B. NaNagara, R. D. O'Connor, and F.D. Blum. Mobility of toluene in polystyrene-toluene solutions: a NMR study. *J. Chem. Phys.*, 96(15):6417–6423, 1992.

[118] A. Novick-Cohen. *Handbook of Differential Equations: Evolutionary Equations*, volume 4, chapter 4: The Cahn–Hilliard Equation. Elsevier, 2008.

[119] A. Oron, S. H. Davis, and S. G. Bankoff. Long-scale evolution of thin liquid films. *Rev. Mod. Phys.*, 69(3):931–980, 1997.

[120] W. S. Overdiep. The levelling of paints. *Prog. Org. Coat.*, 14(2):159–175, 1986.

[121] J. R. A. Pearson. On convective cells induced by surface tension. *J. Fluid Mech.*, 4(5):489–500, 1958.

[122] R. L. Pego. Front migration in the nonlinear Cahn–Hilliard equation. *Proc. R. Soc. Lond. A*, 422(1863):261–278, 1989.

[123] C. Pérez-García and G. Carneiro. Linear stability analysis of Bénard-Marangoni convection in fluids with deformable free surface. *Phys. Fluids A*, 3(2):292–298, 1991.

[124] P. Peumans, S. Uchida, and S. R. Forrest. Efficient bulk heterojunction photovoltatic cells using small-molecular-weight organic thin films. *Nature*, 425(6954):158–162, 2003.

[125] S. Puri. Surface-directed spinodal decomposition. *J. Phys.: Condes. Matter*, 17(3):R101–R142, 2005.

[126] S. Puri and K. Binder. Surface-directed spinodal decomposition: Phenomenology and numerical results. *Phys. Rev. A*, 46(8), 1992.

[127] L. Rayleigh. On convection currents in a horizontal layer of fluid, when the higher temperature is on the under side. *Philos. Mag.*, 32(192):529–546, 1916.

[128] B. Reisfeld, S. G. Bankoff, and S. H. Davis. The dynamics and stability of thin liquid films during spin coating. I. Films with constant rates of evaporation or absorption. *J. Appl. Phys.*, 70(10):5258–5266, 1991.

[129] B. Reisfeld, S. G. Bankoff, and S. H. Davis. The dynamics and stability of thin liquid films during spin coating. II. Films with unit-order and large peclet numbers. *J. Appl. Phys.*, 70(10):5267–5277, 1991.

[130] D. H. Rothman and S. Zaleski. Lattice-gas models of phase separation: interfaces, phase transitions, and multiphase flow. *Rev. Mod. Phys.*, 66(4):1417, 1994.

[131] J. S. Rowlinson. Translation of J. D. van der Waals' "The thermodynamic theory of capiliarity under the hypothesis of a continuous variation of density". *J. Stat. Phys.*, 20(2):197–200, 1979.

[132] L. E. Scriven and C. V. Sternling. On cellular convection driven by surface-tension gradients: effects of mean surface tension and surface viscosity. *J. Fluid Mech.*, 19(3):321–340, 1964.

[133] G. Seminara and P. Hall. Linear stability of slowly varying unsteady flows in a curved channel. *Proc. R. Soc. A*, 346(1646):279–303, 1975.

[134] S. K. Serpetsi and S. G. Yiantsios. Stability characteristics of solutocapillary Marangoni motion in evaporating thin films. *Phys. Fluids*, 24(12):122104, 2012.

[135] S. F. Shen. Some considerations on the laminar stability of time-dependent basic flows. *J. Aerosp. Sci.*, 28(5):397–404, 1961.

[136] O. Shevaleevskiy. The future of solar photovoltaics: A new challenge for chemical physics. *Pure Appl. Chem.*, 80(10):2079–2089, 2008.

[137] S. Shklyaev, A. A. Alabuzhev, and M. Khenner. Long-wave Marangoni convection in a thin film heated from below. *Phys. Rev. E*, 85(1):106328, 2012.

[138] S. Shklyaev, M. Khenner, and A. A. Alabuzhev. Oscillatory and monotonic modes of long-wave Marangoni convection in a thin film. *Phys. Rev. E*, 82(2):025302, 2010.

[139] K. A. Smith. On convective instability induced by surface-tension gradients. *J. Fluid Mech.*, 24(2):401–414, 1966.

[140] L. B. Smolka and T. P. Witelski. On the planar extensional motion of an inertially driven liquid sheet. *Phys. Fluids*, 21(4):042101, 2009.

[141] M. Souche and N. Clarke. Phase equilibria in polymer blend thin films: A Hamiltonian approach. *J. Chem. Phys.*, 131:244903, 2009.

[142] M. Sprenger, S. Walheim, A. Budkowski, and U. Steiner. Hierarchic structure formation in binary and ternary polymer blends. *Interface Science*, 11(2):225–235, 2003.

[143] I. Steinbach. Phase-field models in materials science. *Modelling Simul. Mater. Sci. Eng.*, 17(7):1–31, 2009.

[144] E. Sultan, A. Boudaoud, and M. B. Amar. Evaporation of a thin film: diffusion of the vapour and Marangoni instabilities. *J. Fluid Mech.*, 543:183–202, 2005.

[145] X. Sun and M. J. Ward. Dynamics and coarsening of interfaces for the viscous cahnhilliard equation in one spatial dimension. *Studies in Applied Mathematics*, 105(3):203–234, 2000.

[146] M. Takashima. Surface tension driven instability in a horizontal liquid layer with a deformable free surface. II. Overstability. *J. Phys. Soc. Japan*, 50(8):2751–2756, 1981.

[147] Y. Takei and R. F. Katz. Consequences of viscous anisotropy in a deforming, two-phase aggregate. Part 1. Governing equations and linearized analysis. *J. Fluid. Mech.*, 734:424–455, 2013.

[148] C. W. Tang and S. A. VanSlyke. Organic electroluminescent diodes. *Appl. Phys. Lett.*, 51(12):913–915, 1987.

[149] G. Toussaint, H. Bodiguel, F. Doumenc, B. Guerrier, and C. Allain. Experimental characterization of buoyancy-and surface tension-driven convection during the drying of a polymer solution. *Int. J. Heat Mass Tran.*, 51(17):4228–4237, 2008.

[150] L. N. Trefethen. *Spectral methods in MATLAB*, volume 10. SIAM, 2000.

[151] A. Vidal and A. Acrivos. Nature of the neutral state in surface-tension driven convection. *Phys. Fluids*, 9(3):615–616, 1966.

[152] N. Vladimirova, A. Malagoli, and R. Mauri. Diffusion-driven phase separation of deeply quenched mixtures. *Phys. Rev. E*, 58(6):7691–7699, 1998.

[153] J. S. Vrentas and C. M. Vrentas. Exchange of stabilities for surface tension driven convection,. *Chem. Eng. Sci.*, 59(21):4433–4436, 2005.

[154] S. Walheim, M. Böltau, J. Mlynek, G. Krausch, and U. Steiner. Structure formation via polymer demixing in spin-cast films. *Macromolecules*, 30(17):4995–5003, 1997.

[155] M. R. E. Warner, R. V. Craster, and O. K. Matar. Unstable van der waals driven line rupture in marangoni driven thin viscous films. *Phys. Fluids*, 14(5):1642–1654, 2002.

[156] S. K. Wilson. The levelling of paint films. *IMA J. Appl. Math.*, 50(2):149–166, 1993.

[157] H. F. Winstanley, M. Chapwanya, M. J. McGuinness, and A. Fowler. A polymer-solvent model of biofilm growth. *Proc. R. Soc. A*, 467:1449–1467, 2010.

[158] O. Wodo and B. Ganapathysubramanian. Modeling morphology evolution during solvent-based fabrication of organic solar cells. *Comp. Mat. Sci.*, 55:113–126, 2012.

[159] K.-H. Wu, S.-Y. Lu, and H.-L. Chen. Formation of parallel strips in thin films of polystyrene/poly(vinyl pyrrolidone) blends via spin coating on unpatterned substrates. *Langmuir*, 22(19):8029–8035, 2006.

[160] X. Xu and X. Wang. Analysis of wetting and contact angle hysteresis on chemically patterned surfaces. *SIAM J. Appl. Math.*, 71(5):1753–1779, 2011.

[161] L.-T. Yan and X.-M. Xie. Wetting-layer formation mechanisms of surface-directed phase separation under different quench depths with off-critical compositions in polymer binary mixture. *J. Chem. Phys.*, 126(6):064908, 2007.

[162] P. Yue, C. Zhou, and J. J. Feng. Sharp-interface limit of the Cahn–Hilliard model for moving contact lines. *J. Fluid Mech.*, 645:279–294, 2010.